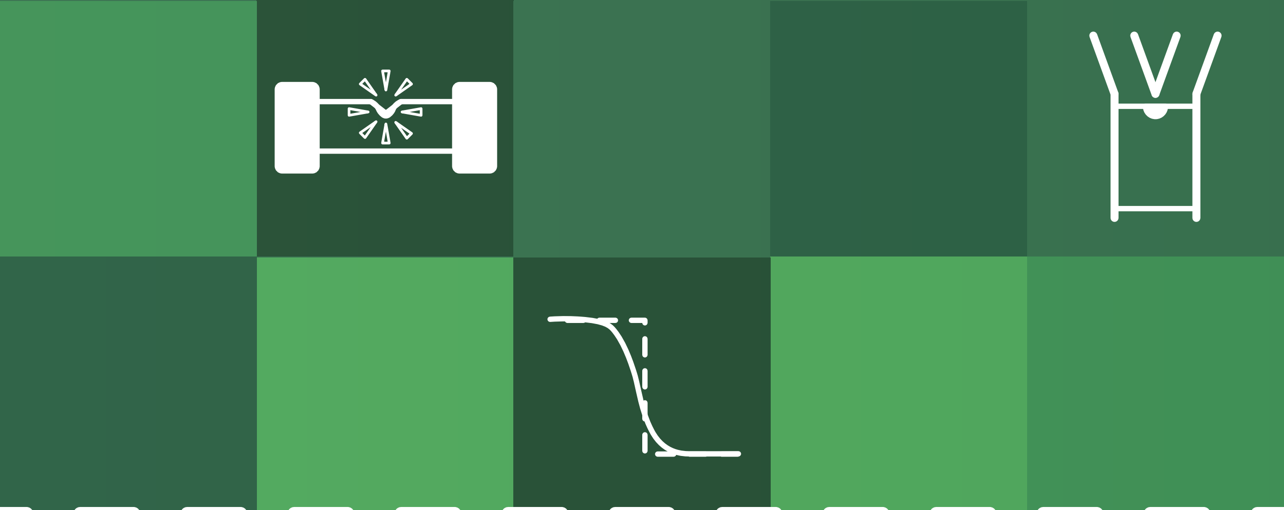

The strong and the weak:

Nucleating insight into the role of mechanical heterogeneity on material failure

J.N.M. Boots

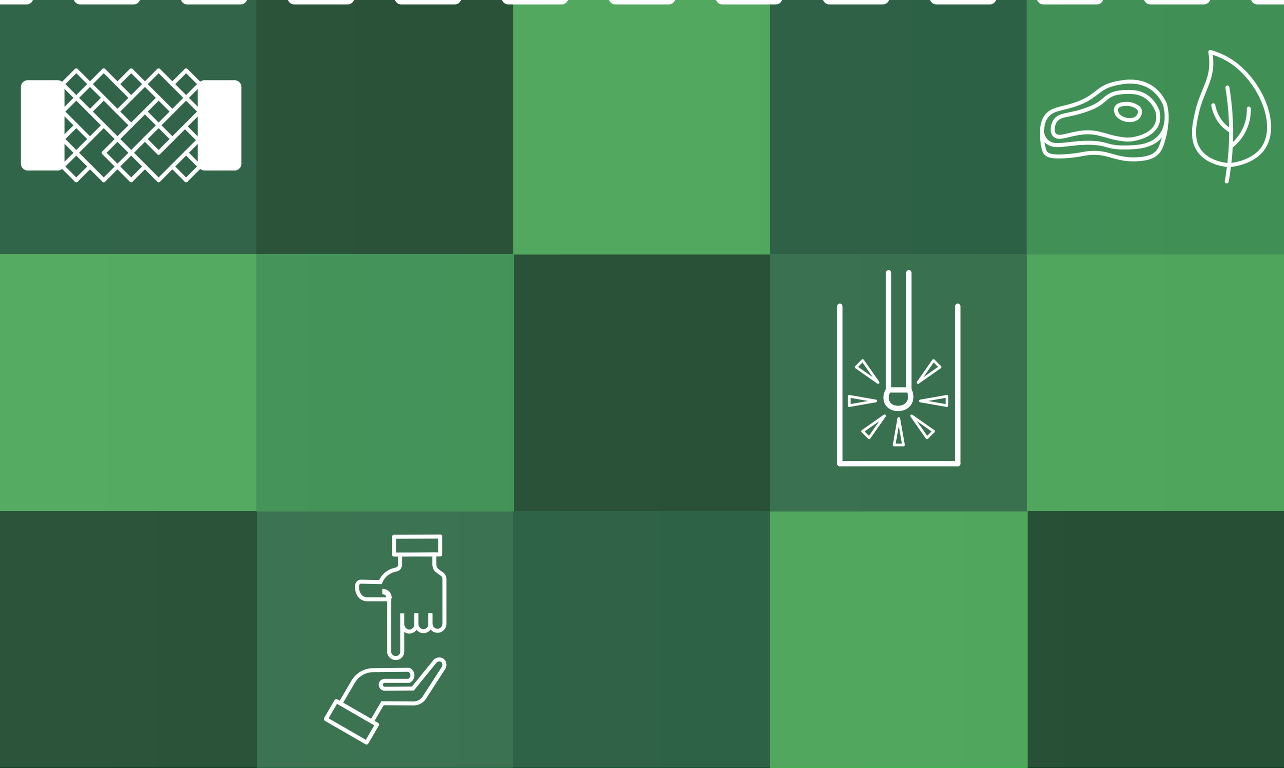

PROPOSITIONS

1. Because the microscopic processes governing fracture mechanics span multiple length scales, obtaining understanding of these processes requires a team of researchers that span multiple backgrounds. (this thesis)
2. While mechanosensors enhance the scientific understanding, they also enhance the experimental complexity. (this thesis)
3. As science progresses, so does the challenge of first acquiring existing knowledge before building on that knowledge.
4. Science would benefit from publishing failed scientific approaches.
5. Innovative technologies could help solve climate change, but innovating our behaviour is equally important.
6. In the absence of major problems, people tend to turn minor issues into major problems.
7. One of humankind's pitfalls is our inability to signal problems in our daily routines.
8. Anonymous communication through the internet leads to increasingly severe problems.

Propositions belonging to the thesis entitled:

THE STRONG AND THE WEAK:
NUCLEATING INSIGHT INTO THE ROLE OF MECHANICAL HETEROGENEITY ON MATERIAL FAILURE

J,N.M. Boots
Wageningen, 8 April 2022

The strong and the weak:

Nucleating insight into the role of mechanical heterogeneity on material failure

J.N.M. Boots

Thesis committee

Promotor
Jasper van der Gucht
Professor of Physical Chemistry and Soft Matter
Wageningen University

Co-promotor
Thomas Kodger
Assistant Professor of Physical Chemistry and Soft Matter
Wageningen University

Other members
Prof. Remko Boom, Wageningen University & Research
Prof. Rint Sijbesma, Eindhoven University of Technology
Dr Santiago Garcia Espallarges, Technical University Delft
Dr Jasper Landman, Wageningen University & Research

This research was conducted under the auspices of Graduate School VLAG (Advanced studies in Food Technology, Agrobiotechnology, Nutrition and Health Sciences).

THE STRONG AND THE WEAK:

NUCLEATING INSIGHT INTO THE ROLE OF MECHANICAL HETEROGENEITY ON MATERIAL FAILURE

J.N.M. Boots

Thesis
submitted in fulfillment of the requirements for the degree of doctor
at Wageningen University
by the authority of the Rector Magnificus,
A.P.J. Mol,
in the presence of the
Thesis Committee appointed by the Academic Board,
to be defended in public
on Friday 8 April 2022
at 1.30 p.m. in the Aula.

J.N.M. Boots
The strong and the weak: Nucleating insight into the role of mechanical heterogeneity on material failure
247 pages

PhD thesis, Wageningen University, Wageningen, The Netherlands (2022)
with references, with summary in English.

ISBN: 978-94-6447-072-7
DOI: `https://doi.org/10.18174/560972`

“It is not our abilities that show who we truly are, it is our choices.”

J.K. Rowling - Harry Potter and the Chamber of Secrets (1998)

CONTENTS

Part I: Production and mechanical characterization of mechanically heterogeneous polymer networks

Part II: Using mechanosensors to obtain detailed microscopic information on material failure

Chapter 1

General Introduction

Leonardo da Vinci (1452-1519) was the first to document about a fracture experiment. In this experiment, da Vinci slowly added sand to a bag attached at the end of an iron wire and found that longer wires break with less sand in the bag[1,2]. This is a remarkable finding in a time where little is known about mechanics (i.e. before the pioneering work of Isaac Newton, 1642 – 1727)[3].
How can the fracture strength depend on the length of the wire?
And why is the answer to this question relevant to modern day science?

Da Vinci's finding that the a longer metal wire with equal cross-sectional area fails earlier upon equal load actually has a logical explanation; heterogeneity. In other words, on the atomic level, the material is not homogeneous but rather holds flaws, where some of the bonds between the atoms are missing. The longer the wire, the more flaws the wire contains. It is at these flaws that the fracture that will break the wire will nucleate due to stress concentration[4]. The result implies that material flaws control the material strength; a longer wire contains more flaws and therefore has a lower load at failure.

Ever since da Vinci's experiment, humankind's understanding of materials, their properties and response to external forces, has drastically increased. Nevertheless, designing (new) materials with improved properties is a continuous challenge pursued in the research field known as material science. Within this field, three sub-disciplines exist:

1. Ceramic engineering, working with inorganic and non-metallic materials, such as stoneware, earthenware, porcelain, silicon, carbides, fired bricks and glass ceramics[5]. These materials are hard, strong in compression, weak in tension and shearing, deform very little before failure, possess excellent temperature resistance and are poorly conductive[5]. Examples of objects made from this class of materials include asphalt, bricks and concrete.

2. Metallurgy, working with metallic materials, either pure or a mixture (known as alloys)[6]. These materials are hard, conductive, deform before failure and malleable[7]. Mixing metals, creating alloys, gives tunability in several mechanical properties, allowing optimization of these properties to create objects with various purposes. Examples of objects made from this class of materials include cutlery and jewellery, and often they are part of objects such as computers, many music instruments, scientific research instruments, medical equipment, building materials and many vehicles.

3. Polymer science and engineering, working with polymeric materials. The research presented in this thesis will be about polymers,

with Section 1.1 introducing them extensively.

Despite working on different materials, all subdisciplines share equal objectives going from developing the process to produce (new) objects from these materials, to understanding and improving the properties (e.g. mechanical, chemical, electrical, thermal, optical and magnetic) and to control and forecast the failure of the produced objects. The latter, material failure, is where the work in this thesis aims to add new understanding, as this is both unavoidable and undesirable.

Failure of objects could lead to severe problems, possibly costing financially, creating environmental damage or even costing lives. Examples include:

- Tyre failure in any means of transport, such as trucks, cars and bicycles, leading to accidents and financial expenses.
- (micro)Crack formation in sewage systems, leading to obstruction of the system which might have to be repaired, leading to financial expenses.
- (micro)Crack formation in seals, potentially leading to dangerous situations in case of e.g. flammable, toxic and/or a leaking object under high pressure.

The focus of the scientific research studying material failure is to understand why (under which conditions) and how (what physical processes occur at failure) materials fail, with the eventual goal of reducing the possibility of materials to fail, by e.g. controlling this process and/or forecasting failure. Material failure can occur for a number of reasons, including: when an externally applied load becomes too high and too much energy is being stored in the material to dissipate; when the material is being deformed repeatedly, creating small microcracks in the material which eventually propagate trough the material (i.e. fatigue); a reduction in temperature causing a material to become more brittle. A material deformation can be either elastic, where the material does not experience any permanent damage and upon removal of the applied deformation returns to the initial shape, or plastic, where the material undergoes irreversible deformation and does not return to the initial shape. Between these two cases, the physical processes setting the fracture process, e.g. the formation of force chains, stress localization and fracture energy, vary largely, dependent on the ability of the material to absorb and dissipate energy during deformation. This ability is set by a mixture of a number of factors, e.g. the type of atoms and/or molecules in the material, the absence/presence of solvents, temperature and so-called microstructure. The microstructure is the structure of the material ranging from tens of nanometers in the case of gels to meters in the case of geological media[8]. In most materials, this structure is considered homogeneous, when averaged over some length scale. However, except for the theoretically perfect crystals, virtually all materials have missing bonds, voids or dislocations, in case of crystalline materials, or have an amorphous structure. These material flaws will lead to stress localization in case the material is subjected to a load, just like the metal wire that da Vinci studied, which could lead to fracture nucleation.

The metal wires that da Vinci studied in his experiments hold a relatively low amount of flaws. In other words, the heterogeneity, also called disorder, is relatively low. How will the material fail when the disorder is increased? Will the fracture strength increase or decrease? Intuitively, one would say the fracture strength decreases, as da Vinci observed in his experiments, as there are more weak spots in the material where stresses localize. However, one could also argue that at a higher degree of heterogeneity, propagating cracks are hindered due to crack trapping in low density area's. Clearly, the physical processes during fracture in such mechanically heterogeneous materials can span some orders of magnitude in length. In addition, these processes occur at short time scales, as material fracture typically is a fast process. Therefore, understanding these complex processes, for example by measuring the number of bonds that break or the local stress and strain right before material failure, requires knowledge about the material structure and direct visualization of the fracture process, perfectly facilitated by mechanosensors. Mechanosensors are molecules that can be mechanically coupled in polymeric materials, and are able to, for example, emit light upon fracture or redshift fluorescent light emission upon mechanical stress. Therefore, the research performed in this thesis uses polymer networks doped with various mechanosensors to explore the ingredients necessary to study the role of mechanical heterogeneity on material failure. To do so, as a first step, these heterogeneous materials are produced, with the aim to control the heterogeneity, and, subsequently, mechanically characterized.

This introduction chapter provides general information on both polymer chemistry and polymer physics, as well as background information directed towards the research conducted in this project. Section 1.1 will introduce the material that is used for the production and characterization of mechanically heterogeneous materials, which is required to study fracture of heterogeneous materials, polymers; what are they on a chemical level and what are their physical properties? Then, Section 1.2 will give a general introduction on material mechanics and how these can be measured on length scales from meters to nanometers, which is of major importance for the research conducted in this thesis. This is followed by introducing heterogeneity and the importance of length scale in Section 1.3, and strategies to produce materials with mechanical heterogeneity. Afterwards, Section 1.4 will introduce fracture mechanics and mechanosensors, and show reports from literature in which the effect of mechanical heterogeneity on material failure was studied, both in computer simulations and experiments. Subsequently, in Section 1.5, some open research questions will be formulated regarding the role of mechanical heterogeneity in materials on its mechanical properties and fracture mechanics, which the research in this thesis aims to address. Lastly, the thesis outline is presented in Section 1.6.

1.1 Polymeric materials

Humankind's evolution has always gone hand in hand with the development of new materials and tools. Natural polymers, such as natural rubber, silk, wool, cotton and starch, have already been used for centuries. In the nineteenth century, scientist began to produce new materials from these natural polymers. In 1865, for example, cellulose acetate was prepared by Schützenberg by heating cellulose with acetic anhydride in a sealed tube[9], a material that nowadays is still used for clothing and cigarettes. Up to the early 1920s the standard point of view was that these natural polymers consisted of colloids, held together by some non-covalent bond[10]. It was the pioneering work of Hermann Staudinger that first described these large molecules as macromolecules, consisting of many repeatable covalently bound sub-units called monomers[11]. This view explained why these materials would exhibit colloidal properties in all solvents in which they dissolve. With the general acceptation of this theory in the late 1920s, scientists began to develop new synthetic polymers that would improve the quality of life significantly, and the Polymer Age started.

1.1.1 Polymers in everyday life

In present day, polymers are part of everyday life as they are being used for many applications, such as medicine, transportation, clothing and construction. In fact, present day life is hard to imagine without synthetic polymers. Figure 1.1a shows the worldwide production increase of synthetic polymeric objects, representing society's demand for these materials. The question now is:

Why does the production of synthetic polymeric materials continue to increase since the 1950s?

The answer to this question is that polymeric materials yield some great benefits over the other material classes; ceramics and metals. Polymeric materials offer a wide range of useful properties such as light weight, elasticity and processability[12]. In addition, these materials are able to deform to a relatively large extent before failure, making them suited candidates for the design of future materials such as soft active devices and wearable sensors[13]. Furthermore, new types of polymeric materials are introduced on the market regularly, increasing the use[14]. Nowadays, polymers are used in multiple industries, as shown in Figure 1.1b[15].

Polymeric materials exist both as natural or synthetic, depending on their origin from nature. Natural polymer are mostly used in the textile industry to produce clothing and/or upholstery. The textile industry uses natural protein fibers made from made from cotton, wool and silk. Cotton is produced by the cotton plant and used in for example curtains, upholstery and mattresses as well[17]. Wool is made by animals like sheep, bison and goat and is used for products that directly influence wearer comfort: blankets, carpeting, insulation and upholstery[18]. Silk is produced by the silkworm, *Bombyx mori*, and is used for tissue engineering and suture materials in biomedical industries[19]. Examples of synthetic polymer analogues to natural protein fibers are, for example, Nylon[20]

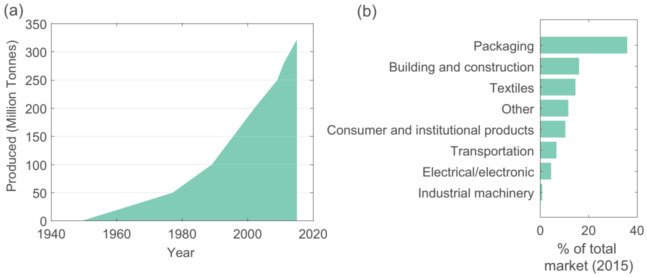

Figure 1.1 – **(a)** Worldwide annual production of synthetic polymeric materials[16]. **(b)** Market share of polymer use per industry[15].

and Kevlar[21], also fiber materials that are used in the textile industry. Synthetic polymeric fibers is the first out of four categories of synthetic plastics[22], typically produced from for example polyester, polyamide, and polyacrylonitrile[20,21]. The second category is thermoplastics, materials that can repeatedly be heated giving it recyclability, and molding and reshaping properties, produced from for example polyvinyl chloride (PVC) to manufacture objects like sewer pipes, single-use medical devices (e.g. blood containers, heart-lung bypass sets[23]) and electric cables. This repeatability comes from the fact that this type of materials does not contain crosslinks, a concept that is elucidated further in Section 1.1.2. However, thermoplastics melt above a melting temperature. Examples are plastic bags and drinking bottles, which are produced from low-density polyethylene (LDPE), and plastic chairs and jerrycans, which are produced from high-density polyethylene (HDPE). For completion, most natural polymers are thermoplastics as well, which is why textiles can be ironed smoothly. The third category of plastics are thermosets, which are resistant to higher temperatures, but can not be molded or reshaped. An example of a thermoset is epoxy resin, which is used in for example resin art or epoxy glue. In contrast to thermoplastics, thermosets do have crosslinks. The fourth category is the elastomer, which is a rubber-like material. Rubbers are polymeric materials that are elastic, whereas plastics (which is actually a rather general term of polymeric materials) typically are not, as will be described in more detail in section 1.1.3.

Synthetic polymeric materials such as teflon, plexiglas and styrofoam are used for applications in, for example, transportation, building and construction or packaging, see Figure 1.1. These materials have some important advantages over materials produced from natural polymers. For example, they have desirable flexibility (depending on the building blocks and linking those together, as will be further introduced in Section 1.1.2), hold specific properties (such as glue), allow for new techniques to arise (3D printing), have relatively low processing temperatures (elucidated in Section 1.1.3), and they show chemical inertness (making them great candidates for the packaging industry). The latter is actually also a major disadvantage of synthetic polymers, illustrated by the decomposition time of some plastic materials shown in Figure 1.2, with detrimental effects for the natural environment.

There are some strategies to reduce the use of synthetic polymeric materials:

1. To not produce and use them anymore. However, this is not really an option as they are used to such a high degree and, as discussed in this Section 1.1, they offer advantages over other materials.

2. Limit the use of single-use plastics[24], reduce the amount of plastic littering[24] and an increasing effort is being done to increase awareness for the consequences of littering[25]. In fact, based on estimations, 60% of plastic ever produced were discarded and are accumulating in landfills or in the natural environment[15].

3. Transformation to a society where all plastics are recyclable[24]. Based on estimations, only 10% of plastics ever produced is recycled[15].

4. Instead of using synthetic polymeric materials with a multi-year decomposition time, as shown in Figure 1.2, transition to synthetic polymeric materials that have a short decomposition time, also known as materials produced with biodegradable polymers with decomposition times ranging from roughly 10-250 days[26].

5. Improve the lifetime of indispensable synthetic materials, like car tyres, rubber conveyor belts and pipelines, such that we will have to produce less. The work in this thesis aims to increase the understanding of fracture of synthetic materials. On the long term,

increasing our understanding of the fracture of these materials will lead to the design of better or new materials that have an enhanced lifetime, eventually reducing the production of these synthetic polymeric materials.

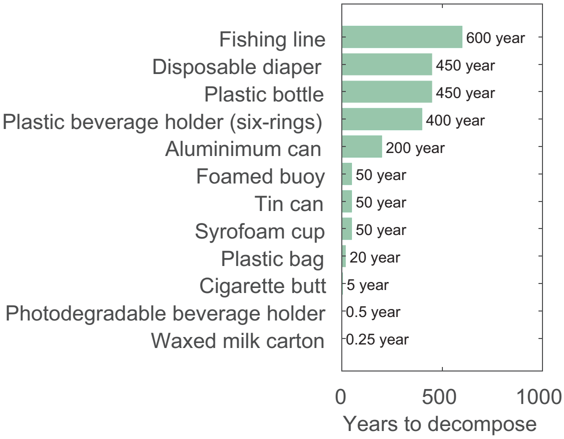

Figure 1.2 – Decomposition time of some common plastic materials[27].

Improving the properties and lifetime of synthetic materials requires knowledge about their building blocks; polymers. What are the chemical and physical properties of polymers? Section 1.1.2 provides an introduction on the chemical and physical properties of polymers.

1.1.2 Chemical and physical properties of polymers

The word polymer is actually a self-explanatory word; (poly)-(mer) literally means (many)-(parts). The parts that are referred to are called (momo)-(mers), literally (single)-(parts). The intermediate form, existing of a few identical repeating sub-units, is called an (oligo)-(mer), from the Greek (few)-(parts). So a polymer is a long chain of repeating units that are connected[10]. The amount of monomers in a polymer is called the degree of polymerisation N, see figure 1.3. Polymers can exist of up to $n \approx 10^{10}$ monomers[10], for one of the largest DNA molecules[I].

For illustrations purposes, suppose that a monomer would have an individual bond length of $l = 1$ cm, then a polymer would have the volume $V = nl^3 = 10^4\ \mathrm{m}^3$, equal to a single room for attractive interactions, a volume equivalent to a university campus for zero net interactions, a city for short-range repulsive interactions and a quarter of the distance from the earth to the moon for long-range repulsive interactions[10]. The actual individual bond length for polymers is on the scale of Angstroms, 10^{-10} m, and, therefore, a polymer with strong interactions occupies a volume of $\sim$100 nm^3. Typically, for synthetic polymers, N varies as it is very challenging to control the amount of monomers that polymerise into a polymer. This distribution in N is called polydispersity. Consequently, the molecular weight M_w of polymers, which is directly proportional to N via $M_w = M_{mon}N$, also also has a distribution in most synthetic polymers. In contrast, many natural polymers are monodisperse, as N is constant. A good example of monodisperse polymers are proteins, which are natural polymers.

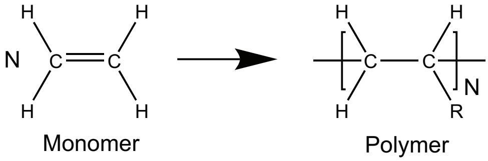

Figure 1.3 – Polymerisation of vinyl into polyethylene, where N, the degree of polymerisation, is the amount of monomers that are linked together in the polymer.

Monomers are bonded with a chemical bond into a polymer. In particular, monomers are bonded with intramolecular, within the polymer molecule, bonds to create a polymer. The lasting intramolecular bond is a state in which the energy between two atoms is lower compared to the unbound state of the two atoms. When this energetically favorable state is reached, a bond is created by the the electrostatic attractive interaction of sharing an electron[29,30]. In case this bond is reached via the complete transfer of one or more electrons of one atom to another, the bond is called ionic. In case this bond is reached when a large number of cations (positively charged atoms) are held together by electrons, the bond is called metallic as most cations are metallic. In case this bond is reached by the sharing of (an) electron(s), the bond is called covalent.

[I] *Deoxyribonucleic acid (DNA)* • DNA is the molecule that comprises the four types of monomers (cytosine, guanine, adenine and thymine), also called nucleotides, that hold the genetic information that is passed on from cell to cell. DNA consists of up to $3.2 \cdot 10^9$ monomers[28].

The process in which monomers are connected together to create a polymer is called polymerisation. There are are two general categories of polymerisation, addition and condensation polymerisation. In addition polymerisation, a polymer is formed by linking monomers together without forming other products. An example is shown in Figure 1.3, where a vinyl monomer is polymerized into polyethylene. A commonly used method to perform this polymerisation is using a free radical. This is a molecule that, upon initiation, creates a free electron that can covalently bind monomers together, called the propagation step, until the polymerisation is terminated by meeting another initiator, when two unfinished chains meet, or quenched by for example present oxygen gas. The free radical polymerisation process is shown in Figure 1.4a,b. This is also a good example of why it is hard to control the degree of polymerisation. Essentially, with free radical polymerisation the degree of polymerisation is a stochastic process, that will result in a distribution of polymer lengths. Initiation of the polymerization is done by degrading the initiator. Depending on the initiator, commonly used methods to initiate polymerization are thermo-initiation using heat (for example using 2,2′-Azobis(2-methylpropionitrile, or AIBN in short[31]) and photo-initiation using UV-light (for example using 2,2-dimethoxy-2-phenyl acetophenone[32]). Addition polymerisation differs from condensation polymerisation, which does generate a co-product. Figure 1.4c shows an example, where Nylon is synthesized from Hexamethylenediamine and Adipic acid, giving water as a byproduct[20].

Polymers, in turn, can also be linked together with either chemical or physical bonds. Physical bonds are intermolecular bonds, bonds between atoms of separate molecules. Examples of physical bonds include hydrogen bonds, hydrophobic interactions and van der Waals interactions and can, for example, be used to create self-healing polymers[33,34]. While chemical bonds can be intramolecular bonds, as described above, they can also be intermolecular bonds, bonding polymer chains together. This process of bonding synthetic polymers together chemically was first discovered, accidentally, in 1839 by Charles Goodyear[35]. In this process, sulfide bridges are formed between adjacent chains, transforming a soft material in a tough and firm material. Since Goodyear's discovery, the vulcanization process has been improved significantly. For example, efficient

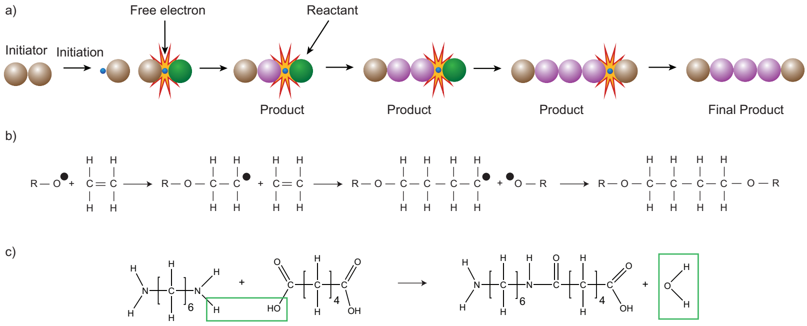

Figure 1.4 – Addition polymerisation of vinyl groups using free radical polymerisation shown (a) schematically and (b) in chemical structures. (c) Condensation polymerisation of a Nylon polymer, where water is a byproduct produced by the -H and -OH group in the green boxes.

methods have been developed to delay the crosslinking reactions, such that a material can first be molded or processed. There are also ways to optimize the curing temperature and time[35]. The optimization requires the addition of additives. Additives are small molecules that alter the properties of a material. Examples of those properties include processing aids[35], antioxidants, plasticizers, heat stablizers, UV stabalizers, but also protection requirements (such as biocides and flame retardants), and mechanical and physical properties (such as fillers[II], glass fibres, impact modifiers, antistats and nucleating agents)[36]. In fact, many materials that are used in daily life would not have their properties without the essential presence of additives[36].

[II] *Fillers* • Fillers are added to rubbers to enhance the mechanical properties, such as tensile strength, elongation at break, and in car tyres to reduce rolling resistance[37].

A polymer that consists of one type of monomer is called a homopolymer, whereas a polymer that consists of more than one monomer is called a heteropolymer or, more often used, copolymer. The use of more than one monomer to construct a polymer can be used to obtain a combination of the properties of the monomers. These properties depend on both the composition, the fraction of each monomer present, and sequence in which the monomers are linked. There are several compositions and sequences in which monomers can be linked together, as can be seen in figure 1.5a. Furthermore, the polymer architecture, shown in figure 1.5b, is another important feature that controls the properties of the polymer[10]. Polymerization of these polymer architectures to each other will result in a so-called sol, as a polymer structure of this size is soluble. As the polymerisation continues, at some point the polymer structure has reached a size where it spans the system size. At this point, the network is called a gel. This transition is called the sol-gel transition and the point at which this occurs is called the gelation point.

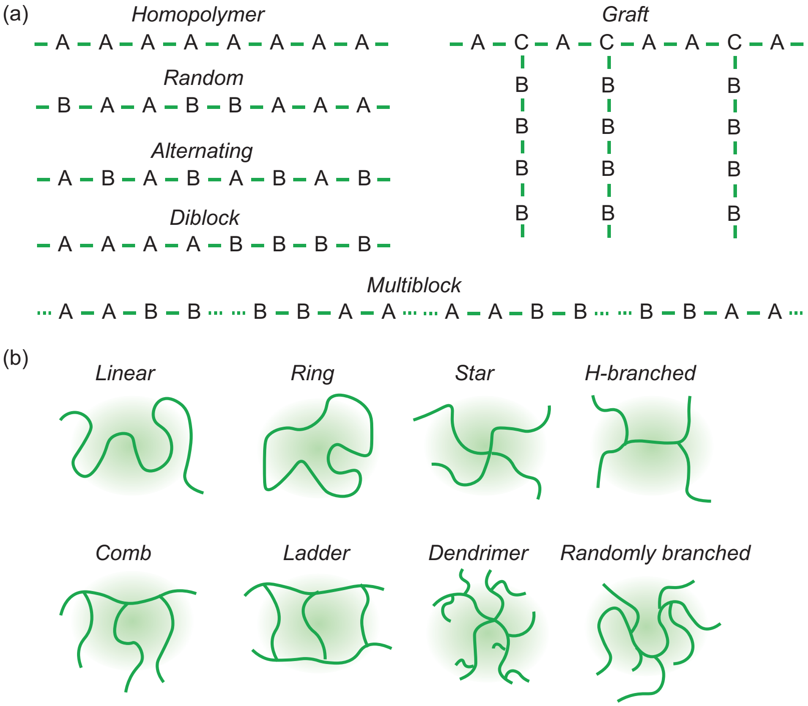

Figure 1.5 – (a) Examples of polymer sequences (b) Examples of polymer architectures.

1.1.3 Types of polymeric states

Before introducing existing polymeric states, let's first introduce the states of the most abundant molecule on earth, water, as an analogy. Water exists in three different states; solid, liquid and gas, as the temperature is increased. These phase transitions can be explained by considering a closed system in which the temperature is slowly increased, and a combination of the first law of thermodynamics and the ideal gas law. For this closed system, the first law of thermodynamics states that the total energy is conserved;

$$\Delta U = Q - W \tag{1.1}$$

where U is the total energy in the system, Q the amount of energy added to the system as heat and W the amount of thermodynamic work done by the system[38]. The ideal gas law describes the relation between temperature and pressure

$$pV = Nk_BT \tag{1.2}$$

with p the pressure, and V the volume of the system, N the number of molecules, k_B the Boltzmann constant and T the temperature[38]. According to the ideal gas law, an increase in temperature results in an increase in pressure. For gasses, this process is well described with the kinetic theory of gasses;

$$k_BT = \frac{m\overline{v^2}}{3} \tag{1.3}$$

with m the mass of the gas and $\overline{v}$ the mean velocity of the gas molecule. Hence, temperature is directly related to the speed of motion of the molecules[38].

As a result, when ice (the solid state of water) is heated, thermal energy is converted into velocity. More particularly, the velocity of water molecules will increase, up to the point where the molecules vibrate to such an extent that the hydrogen bond interactions between the water molecules are insufficient to keep the molecules in close proximity. This is known as the melting temperature, which is 0°C or 273K for water, and at this point the solid transitions into a liquid and the crystalline structure is lost. Increase the temperature even further, and water will start to evaporate. The material will then transition from liquid to gas, as molecules vibrate even more, resulting in more distance between the molecules. This is known as the boiling temperature, and this is 100° C or 373K for water. The transition between these states of matter are known as phase transitions.

For polymeric systems, phase transitions are often not so straightforward. The reason is that many polymeric systems, in contrast to water, often are heterogeneous in composition, structure and architecture, see figure 1.5. In addition, polymer alignment is also important for phase transitions. Polymers can be either aligned, in regions called lamellae, or randomly aligned, a state called amorphous (from the Greek *a-morph*, which means without shape). Materials that have aligned and amorphous regions coexisting are called semi-crystalline, see figure 1.6. Generally, there are two polymeric states; liquid and solid.

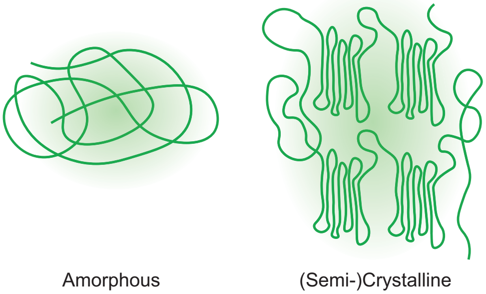

Figure 1.6 – (left) Random alignment of a polymer is known as an amorphous alignment. (right) Ordered alignment of so-called lamellae results in a polymer known as a (semi-)crystalline polymer, as the lamellae are connected by amorphous regions.

Polymer liquids

The first polymer state is polymer liquids, which can be either in presence of solvent, i.e. dissolved in a solvent, called a polymer solvent or in absence of a solvent called a polymer melt. The polymer solution can be dilute, semidilute and overlapping[10], depending on the polymer volume fraction ϕ:

$$\phi = \frac{c}{\rho} \tag{1.4}$$

where c is the polymer mass concentration and ρ is the polymer density. The volume that a polymer spans is known as the pervaded volume V and is roughly described with:

$$V \approx R^3 \tag{1.5}$$

where R is the radius of the chain. In addition, temperature plays a key role in the mixing of polymers with a solvent. This has been described in detail by the theory known as the Flory-Huggins solution theory[10]:

$$\Delta F = \Delta H - T\Delta S = k_B T[\frac{\phi}{N}\ln\phi + (1-\phi)\ln(1-\phi) + \chi\phi(1-\phi)] \tag{1.6}$$

where H is the enthalpy $H = U + pV$, i.e. energy U plus the pressure p multiplied with the volume V, T the temperature, S is the entropy[III], k_B is the Boltzmann constant, ϕ is the volume fraction, N is the number of polymers and χ is the Flory interaction parameter[39]. The interaction parameter χ is defined as

$$\chi \equiv \frac{z}{2}\frac{(2u_{AB} - u_{AA} - u_{BB})}{k_B T} \tag{1.7}$$

where $z = 2d$ is the coordination number with d the lattice dimension, and u the interaction energy between polymer A and solution B. The interaction parameter χ, a dimensionless parameter, promotes mixing ($\chi < 0$), opposes mixing ($\chi > 0$) or neither promotes nor opposes mixing ($\chi = 0$), a situation called ideal mixing. The interaction energy is a function of the distance between two monomers, see Figure 1.7a, such as the Lennard-Jones potential. The magnitude of the potential varies depending on the type of interaction. The probability of finding a second monomer at distance r from a given monomer is obtained using the Boltzmann factor $e^{(\frac{U(r)}{k_B T})}$, which can be used to determine the excluded volume v_e for a polymer:

$$v_e = -\int f(r)^3 dr \tag{1.8}$$

or, in other words, the area under the curve in Figure 1.7b. The excluded volume of a (long) polymer is the volume that is already occupied by another monomer of the polymer, and therefore cannot be occupied. The Mayer f-function shows repulsive (f<0) and attractive (f>0) interactions. A net repulsion between monomers leads to positive $v_e > 0$, whereas a net attraction leads to a negative excluded volume $v_e < 0$. An excluded volume of zero $v_e = 0$ is only true for a so-called ideal chain, which assumes that there are no kind of interactions between monomers

---

[III] *Entropy* S (J/K) • An extensive quantity of a thermodynamic system that describes the amount of configurations (microstates Ω) of a system, described by $S = k_B \ln\Omega$. The second law of thermodynamics states that the entropy of a closed system can never decrease. Only when the system gives/equates entropy to/with another system, entropy can decrease, for example when a hot reservoir comes into contact with a cold reservoir.

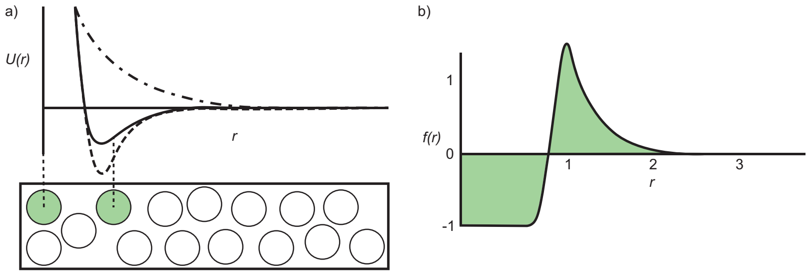

Figure 1.7 – (a) The interaction potential U plotted as a function of the monomer radius r for two monomers in the case of weak attractive interaction (——), strong attractive interaction (- - -) and repulsive interaction (— -). (b) The Mayer f-function and the excluded volume v_e shown by the shaded area.

and every type of conformation of this type of polymer can be described with the mathematical random walk model. This is known to be the case for a so-called θ-solvent[40], which is also captured in the phase diagram for polymer solutions showing an UCST[IV] shown in Figure 1.8.

[IV] *Upper Critical Solution Temperature (UCST) (K)* • The critical temperature above which the all proportions of a mixture are miscible.

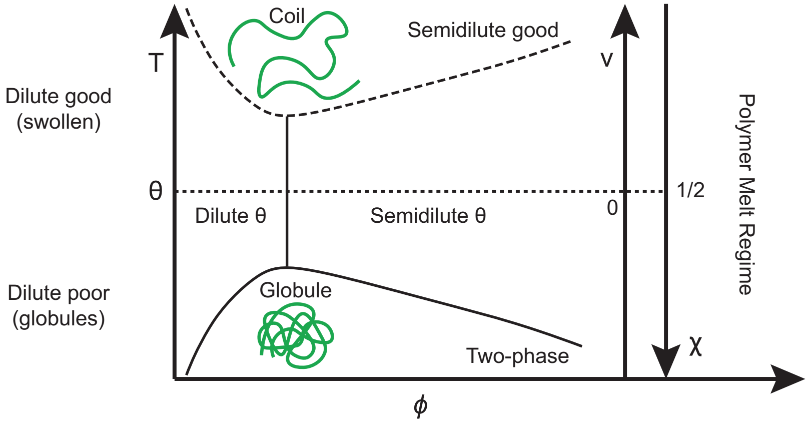

Figure 1.8 – Phase diagram for an UCST polymer, showing the phases for an increasing volume fraction as function of temperature, excluded volume and Flory interaction parameter.

USCT phase separation is an enthalpically driven process, whereas LCST[V] has an entropic driven force for demixing[41]. Note in Figure 1.8 that a polymer in a poor solvent will shrink in volume, a state called a globule. A polymer in a good solvent is in a coiled state.

[V] *Lower Critical Solution Temperature (LCST) (K)* • The critical temperature below which the all proportions of a mixture are miscible

Polymer melts are solvent-free polymers above the glass transition temperature[VI] and melting temperature[VII][42]. Polymer melts can also be cooled below the glass transition state, a state of polymers that is known as glassy polymers[43], which typically are brittle. The latter are solids, which will be introduced further later in this Section. At the same temperature, one type of polymer can be above its T_g, whereas another can be below its T_g. For example, polydimethylsiloxane (PDMS), with a $T_g = 123$ K $< T_{RT}$, is a polymer melt at room temperature T_{RT}, whereas PVC, with a $T_g = 356$ K $> T_{RT}$, is a polymer glass. This transition trough the glass transition temperature T_g of polymers from a glassy to rubbery state is shown in Figure 1.9.

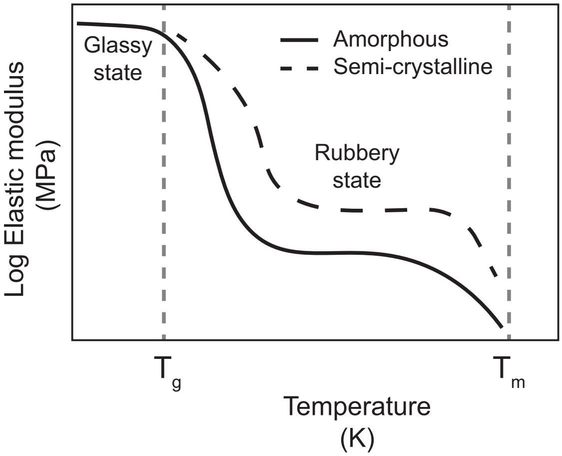

Figure 1.9 – The temperature versus the elastic modulus for amorphous and semi-crystalline polymers, showing the glass-transition temperature T_g and melting temperature T_m indicated with the grey vertical dashed lines[43]. As temperature increase, glassy state polymers cross T_g and go to a rubbery state. While this graph shows the general behavior of polymers, not all polymers follow this graph.

A macroscopic piece of a polymeric melt shows an elastic response, as it remembers its shape on short time scales but shows liquid flow at long time scales. Such time-dependent mechanical properties are called viscoelastic properties. Polymer melts typically have entanglements, which is the topological restriction of molecular motion by other chains[44]. A good analogy would be trying to pull on a single spaghetti string in dish of spaghetti pasta. Moving the single spaghetti string causes the other spaghetti strings to move as well, a process that requires a significant amount of energy. Analogously to a polymer moving in a solvent, movement of a particle is described by the Stokes-Einstein relation:

$$D = \frac{k_b T}{\zeta} = \frac{k_b T}{6\pi\eta R} \tag{1.9}$$

where D is the diffusion coefficient (m^2/s), ζ is the friction coëfficient, R (m) the radius of the particle, and η is the viscosity[10], which describes the resistance of a fluid to flow, is defined as the shear stress $\tau = \frac{F}{A}$ divided over the applied shear rate $\dot{\gamma} = \frac{v}{h}$, leading to dimensions of Ns/m^2.

However, unlike a spaghetti string in a spaghetti mesh, the particle is not hindered by large connected molecules, only by small solvent molecules. For a polymer in a polymer mesh, as is the case in a polymer melt, thermal motion is called reptation, analogous to snakes moving around in a snake pit. The diffusion of a polymer in a polymer melt is described with the Rouse model[45], which describes polymers as N beads connected by springs of root mean square size b, or Kuhn lengths, according to:

$$D = \frac{k_b T}{N\zeta} \tag{1.10}$$

Equation 1.10 shows that the curvilinear diffusion coefficient of a polymer in a polymer melt is inversely proportional to the amount of Kuhn segments N[10]. Hence, the longer the polymer chain, the slower the reptation, as expected intuitively.

Polymer solids

The second type of polymers are polymer solids, which exist in multiple states. For example, when a polymer melt is cooled below the melting temperature T_m, it can transform into a semicrystalline solid, see figure 1.6, or, when cooled even further below the glass transition temperature T_g it can transform into a polymeric glass. Semicrystalline polymers are opaque, due to the multiphase nature of lamellae and amorphous regions. When used above T_g, semicrystalline polymers are deformable and though[10].

[VI] *Glass transition temperature* T_g (K) • The glass transition temperature is the temperature at which an amorphous (or amorphous regions in semi-crystalline materials) material gradually transitions from a glassy state into a viscous or rubbery state, as the temperature is increased. Several factors can affect T_g, like molecular weight, size and intermolecular forces of side groups, plasticizers and presence of solvents. Figure 1.9 schematically depicts T_g.

Crosslinking the chains of a polymer melt results in a so-called polymer network. The chains of a polymer network can move locally, above the T_g. Such polymer networks are called soft solids[10]. Soft solids with a T_g below room temperature are called rubbers. A great example is crosslinked PDMS (e.g. the commercial variant Sylgard 184[46]), a rubber that is used extensively in soft matter research, for example in microfluidics, due to its excellent properties, including its transparency, the almost negligible shrinking ratio upon polymerisation[47] and the sufficient elongation at break to study fracture[48]. Sylgard 184 is polymerised through the reaction of a “base” with a crosslinking agent in the presence of a catalyst[49]. The ”base” is a dimethylvinyl-terminated dimethylsiloxane, the crosslinking agent is actually unknown to the consumer, and the catalyst is a platinum species such as Karsted’s catalyst, or H_2PtCl_6, through a hydrosilylation mechanism[49]. Sylgard 184 is also used in the research performed in this thesis.

Lastly, a polymer network that is swollen in a solvent is called a polymer gel. The more solvent is used, the softer the material becomes. However, it will remain a polymer network, due to the permanent bonds present in the polymer network.

[VII] *Melting temperature* T_m (K) • The temperature at which polymers have gained sufficient thermal energy to slide past one another upon deformation. In all cases, $T_g < T_m$. Figure 1.9 schematically depicts T_m.

1.2 Material mechanics

The previous Section, Section 1.1, has introduced the chemical and physical properties of polymers. This Section will take the next step towards understanding fracture of mechanically heterogeneous materials, introducing material mechanics. Mechanical properties are of crucial importance for most materials, as these properties set what the material can be used for and what not; in other words, mechanical properties largely determine a material’s functionalities and therewith the purpose or reason of material production. Many materials are designed to withstand many and/or large deformation, without losing mechanical integrity. However, deforming a material too much will eventually lead to material failure. Mechanical properties are of great influence for a materials lifetime, i.e. the time that a material can be used for what it was produced. In order to improve the functionalities and lifetime of a material or object, the mechanical properties have to be studied and related to the materials lifetime. Changes in the manufacture process, i.e. building blocks and/or handling, of the material will change the mechanical properties. It is the challenge of material scientists to relate the changes in manufacturing to mechanical properties, and optimize them. However, what are these mechanical properties, and how are they being studied?

1.2.1 Mechanical properties

Mechanical properties of a material are typically measured by deforming a material to a certain degree, called applied strain, and measure the force required to do so. Examples of mechanical properties are toughness, yield, stress, strain, ductility and elastic modulus[50]. These parameters can be described using Figure 1.10, which displays (a) a dogbone shaped sample being stretched and (b) the corresponding stress-strain curve.

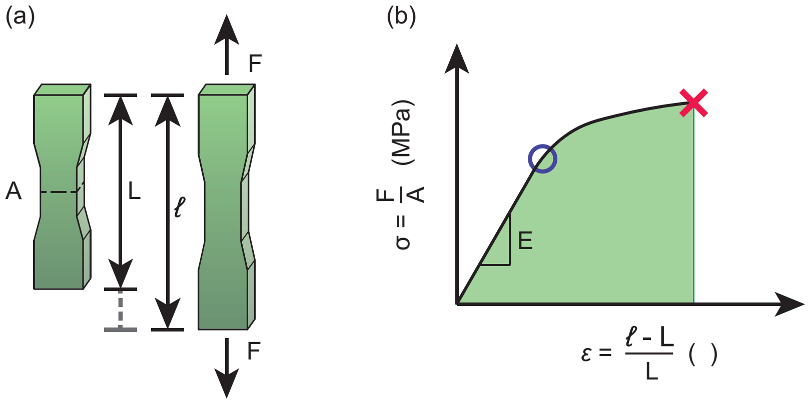

Figure 1.10 – **(a)** Schematic of a dogbone shaped sample with cross-sectional area A (dotted line) and initial length L that is extended with force F to a length ℓ. **(b)** The corresponding stress-strain (σ-ϵ) curve shows the yield stress point (blue circle), which is where the material transitions from elastic (linear response) to plastic or ductile deformation (where bonds start breaking). An increasing strain will lead to fracture of the material (red cross).

The elastic modulus E of a material is the slope of the linear relation between stress σ and strain ϵ, and therefore is a force per unit area, as shown in the stress-strain (σ-ϵ) curve in figure 1.10b. At some point,

Brittle Fracture	Ductile Fracture
Glass	Rubber
Porcelain	Copper
Cement	Aluminum
Stone	Reinforced concrete

Table 1.1 – Examples of some brittle and ductile materials[52]

chemical and/or physical bonds start breaking and the material transitions from elastic to plastic or ductile deformation, until the material fractures. This point is called the yield point. The amount of ductile deformation is called the ductility. Some materials show a (high) degree of ductility, such as copper and rubber[51]. Other materials barely show ductile deformation before fracture, such as glass and stone, and are called brittle materials[51], see table 1.1. The area underneath the σ-ϵ-curve shown in green in Figure 1.10b is the energy absorbed by the material before the material fails, known as toughness. The larger this area, the tougher the material, as it is able to absorb more energy before it fails.

The deformation applied on the dogbone sample in Figure 1.10a is known as uniaxial deformation, as the deformation is applied in one direction. Deforming a material along one axis leads to deformation in the transverse axes as well. This deformation on the other axes is a function of the elasticity of the material, set by the Poisson's ratio:

$$\nu = -\frac{d\varepsilon_{\mathrm{trans}}}{d\varepsilon_{\mathrm{axial}}} = -\frac{d\varepsilon_{\mathrm{y}}}{d\varepsilon_{\mathrm{x}}} = -\frac{d\varepsilon_{\mathrm{z}}}{d\varepsilon_{\mathrm{x}}} \tag{1.11}$$

with ν the Poisson ratio, ε the strain, the axial x-axis being the axis where the deformation is applied and the y/z-axes the transverse axes. Most materials have a Poisson ratio between 0-0.5, with 0 for a material that shows no transverse deformation upon axial strain, such as cork, and 0.5 for a material that shows volume conservation upon axial strain, such as elastomers. Materials with negative Poisson ratio are called auxetics, extending rather than compressing in the transverse direction as opposed to materials with positive Poisson ratio.

Typically, soft materials, like polymer networks, hold a time dependent response to mechanical deformation. In other words, there is some delay between an applied stress and reaching a final deformation. This delayed response is shown in figure 1.11(a), where the stress response to an applied strain can be delayed in time. Typically, these visco-elastic properties are studied with oscillatory measurements. In these measurements, a sample is deformed back and forth, and typically the complex shear modulus G^* is obtained, which is a complex between the elastic and visco-elastic response. The storage modulus G', which describes the elastic component of the shear stress response, is the shear stress $\sigma = \frac{F}{A}$ divided over the applied strain $\epsilon = \frac{s}{h}$, as shown in Figure 1.11(c), multiplied with the cosine of δ; $G' = \frac{\sigma}{\epsilon} \cos \delta$. The loss modulus G", which describes the visco-elastic component of the shear stress response, is defined with $G" = \frac{\sigma}{\epsilon} \sin \delta$. The loss tangent δ is defined as $\delta = \frac{G'}{G"}$, as shown in Figure 1.11(c). There are three cases for the time delay; no delay is called a purely elastic response of the material ($\delta = 0°$), a fully out of phase response of the material is called a purely viscous response ($\delta = 90°$), and the in between response, which is the visco-elastic response ($0° < \delta < 90°$), where the loss tangent δ describes the lag time between applied deformation and stress response.

The above described oscillatory experiments are generally performed with a rheometer, which will be described in more detail in Section 1.2.2. In this experimental setup, a material is deformed with rotational oscillation. The modulus, i.e. a material's elasticity, obtained with this rotational motion is slightly different than the elastic modulus E obtained with e.g. the tensile test in Figure 1.10. To convert the shear modulus G, obtained with rotational motion, to a typical elastic modulus E (also known as the Young's modulus, but in this thesis referred to as the elastic modulus) obtained in uniaxial deformation, one can use the following relation[53]:

$$E = 2G'(1 + \nu) \tag{1.12}$$

An important consequence of visco-elastic behaviour of polymers is the relation between temperature and strain rate, i.e. the time interval at which strain is applied on a material, as both have an effect on the motion of polymers. As a consequence, increased strain rate will result in a higher elastic modulus, but the same elastic modulus will decrease at a decreased temperature. This behaviour is described with the time-temperature su-

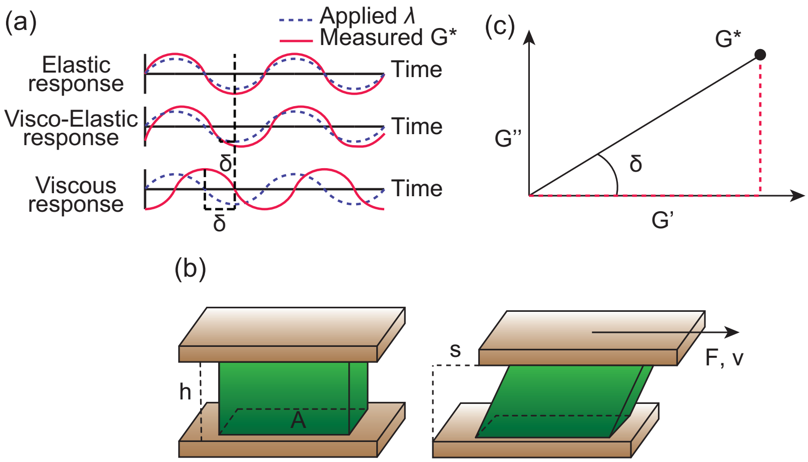

Figure 1.11 – **(a)** Elastic, visco-elastic and viscous response of material, depending on the delayed time at which the material responds. **(b)** Schematic of two plates shearing a sample **(c)** Illustration of diagram showing the relation between complex shear modulus G*, storage modulus G' and loss modulus G''.

perposition principle[54]. Hence, this property of visco-elastic amorphous polymers declares that there is an inverse relation between strain rate and temperature, due to the competition between polymer chain relaxation time, and free volume and thermal motion of the polymer chains[54].

1.2.2 How are mechanical properties measured?

Over the years, several techniques have been developed to study mechanical properties of materials. The choice of the method used to measure mechanical properties is largely dependent on the length scale at which these mechanical properties are measured. In the soft matter field, a typical range of length scales over which mechanical properties are measured are ranging all the way from meters to nanometers, spanning nine orders of magnitude. Figure 1.12 shows some typical examples of experimental setups that can be used to measure mechanical properties on a length scale of interest. Each setup measures mechanical properties at a range of length scales. The length scale at which a setup is able to probe mechanics is set by the area or volume scanned by the load sensor and/or probe.

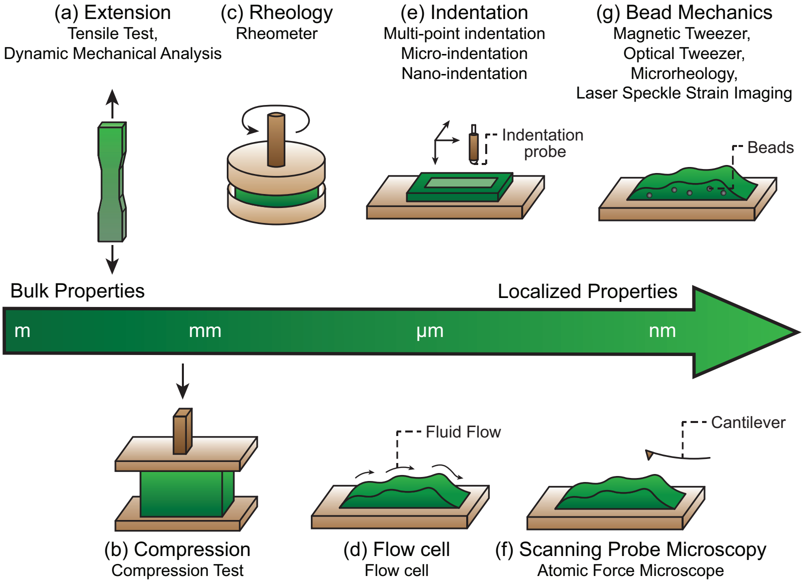

Figure 1.12 – Schematics of experimental techniques used in the soft matter field to measure mechanical properties of materials, spanning multiple orders of magnitude in the length scale that can be probed and, consequently, the level of bulk/local properties that can be probed.

The most widely used methodology in the soft matter field is rheology, which is used to study the flow and deformation of materials, both fluids and soft solids, and has been established in the 1920s[55]. As introduced in Section 1.2.1, rheology is a method in which a material can be (dynamically) sheared, obtaining parameters like shear rate, loss and storage modulus and the viscosity. Therefore, rheology is also known as the study of the flow of matter. With rheology, bulk properties of a material are measured, as the stresses are recorded by a single torque sensor averaging the over the entire loaded sample sizes that are typically on the order of milliliters of volume[56]. The volume of a typical polymer strand is on the order of $\sim$ 100 nm^3, see Section 1.1.2. Therefore, rheometers typically measures the combined mechanical properties of many polymers, leading to a bulk parameter for the whole sample.

On probing comparable to perhaps even larger length scales than rheology, Figure 1.12 shows three other techniques. The first is a compression test, in which a complete sample is compressed while recording the force required and applied displacement, and parameters like elastic modulus and toughness can be obtained[57]. The second is the tensile test, where a material is elongated either to the subcritical stress, or critical stress. In the former, the applied stress does not immediately lead to material failure, but rather it takes some time for a few bonds to break, after which stress redistribution will lead to more bonds to fail, which eventually leads to material failure[58]. This type of experiment is known as a delayed failure test. In the latter, the material is extended until it fails, exceeding the critical stress with the applied stress[59]. The third is the Dynamic Mechanical Analysis test, a technique that is used widely in material science to study for example fatigue and visco-elastic properties in oscillatory measurements, as described in Section 1.2.1.

Figure 1.12 also shows several techniques that allow probing mechanical properties at smaller length scales. The first technique, called flow cell, is mostly used to study mechanical properties of biofilms, thin films of organic material. These flow cells typically have sizes ranging from millimeters to centimeters. The biofilms are present in a variety of ways, for example in sewage treatment[60], but also diseases such as dental plaque and cystic fibrosis[61]. With a flow cell, a fluid is used to deform a biofilm and Digital Image Correlation (DIC) is used to study the shear stress on the biofilm.

The second technique is indentation, where a probe is pushed on a material while recording the normal force response, measuring the local resistance of the material to deformation. Based on the size of the indentation probe and sensitivity of the load sensor, indentation can range from the μm-nm length scale[62]. Probing the material at multiple positions will result in a mechanical map of the material, where each position represents the local stiffness of the material. Furthermore, indentation setups are commonly used to study the adhesion of soft materials. This can be done by retracting the indentation probe from the surface, where the area of negative forces and depth will give the adhesive energy of the material, a parameter that is dependent on the retraction velocity[63]. Indentation is a technique that will be used in Chapters 2-4 in this Thesis, as the length scale used is the length scale of heterogeneity that can be imprinted on soft polymeric material. The latter will be discussed in Section 1.3.2 of this Thesis.

The third technique is Atomic Force Microscopy (AFM), which is a branch of microscopy called Scanning Probe Microscopy, a branch where a physical probe is used to scan the sample surface to produce height or elastic modulus maps of these surfaces. The AFM uses a sharp tip with a diameter of micrometers to tens of nanometers that is mounted on the end of a flexible cantilever. A laser is deflected on this cantilever, which is detected by a photodiode detector. With the spring constant of the cantilever known, i.e. provided by the manufacturer and typically on the order of N/m, the force required to push the sample with a certain depth can be calculated based on the deflection of the laser beam on the detector[64]. These so-called contact mode tests were the first measurements conducted with an AFM. In later use, the tip was oscillated across the interface, thereby obtaining information on interactions between the tip and surface from the damping of the oscillation. An important note is that the height of the probe relative to the surface in Scanning Probes Microscopes is regulated with an electronic feedback mechanism. A typical AFM measurent performs indentations on the order of nanometers, detecting forces on the order of piconewtons. The advantage of AFM over STM is that non-conductive samples can also be measured[65]. The fourth method of measuring mechanical properties below the length scale of rheometers is a set of techniques that use (tracer) beads and are called Bead Mechanics here. Examples hold Magnetic[66] and Optical Tweezers[67], where beads with sizes on the order of micrometers are held by either a magnet or by light. In these techniques, very localized forces can be measured for example by attaching the beads to a part of the sample of which one wishes to obtain mechanical information. By moving either the sample or the bead, the sample is extended and thus experiences a force. The force can be calculated by detecting the displacement of the bead from the center of the trap, after the trap stiffness is known. The trap stiffness κ could be obtained using the equipartition theorem[VIII]:

$$\frac{1}{2}\kappa \left\langle x^2 \right\rangle = \frac{1}{2}k_B T \tag{1.13}$$

where κ is obtained by isolation:

$$\kappa = \frac{k_B T}{\left\langle x^2 \right\rangle} \tag{1.14}$$

Hence, calibration of an optical tweezer can be done by recording the statistical variance of a trapped particle $\left\langle x^2 \right\rangle$. This variance σ can be ob-

[VIII] *Equipartition Theorem* • A theory in classical statistical mechanics that relates temperature to average energy of particles. It predicts that at thermal equilibrium all the atoms in a closed environment have an average translational kinetic energy of $\frac{3}{2}$ k_BT. The theorem is derived from the Maxwell–Boltzmann distribution which predicts the velocity distribution of atoms in a closed environment[38].

tained by fitting the distribution of positions of a trapped particle with a Gaussian fit[68], defined as $f(x) = \frac{1}{\sigma\sqrt{2\pi}} \exp\left(-\frac{1}{2}\frac{(x-\mu)^2}{\sigma^2}\right)$.

The second example of Bead Mechanics is passive Microrheology, which is a field where the location of beads is tracked over time. Often, beads with sizes on the order of micrometers are made visible to microscopes for example by fluorescent labeling. In microrheology, either one or multiple beads are tracked. In case one particle is tracked, information on for example individual proteins are followed over time, by tracking the single fluorescent label that is attached to the object of interest using algorithms[69].

The motion of the beads in microrheology can be driven with or without an externally applied load. In the latter case, in for example passive microrheology, the motion is driven by thermal fluctuations, leading to Brownian motion. From these passive microrheology experiments, parameters like local storage and loss modulus, and the diffusion constant can be deduced. In case an externally applied load is used to set the particles in motion, one speaks of active microrheology. This can be used to, for example, obtain the Péclet number[IX], and a microviscosity[X] of a sample[70]. Microrheology is also studied using optical tweezers[71].

The third and last example of Bead Mechanics is Laser Speckle Strain Imaging (LSSI), where tracer beads are placed in a material. This technique uses linearly polarized light to measure the interference pattern by light scattering from the tracer beads in the illuminated area[72]. The resulting speckle pattern detected by the camera is a grid of superposition of all waves arriving at one pixel, where all the waves are created by scattered light at different depths in the sample. The tracer beads in the material will randomly diffuse by thermal energy, creating a dynamic speckle pattern. Deforming the material will change the dynamics of the speckles. Statistical analysis can be used to estimate the local change in dynamics of the tracer beads, giving an indirect read-out of small-scale deformations in the material[58].

The fifth and final method of measuring mechanical properties below the size of rheometers is a set of techniques using mechanosensors; stimuli-responsive polymers incorporated in the polymer network[73,12,74]. In the past decade, the development of these materials has enabled several new possibilities of studying mechanical processes in biological samples.

[IX] *Péclet number* • The Péclet number is the advective transport rate over the diffusive transport rate. Advection is the transport of a particle, substance or quantity by the bulk, for example when a river is carrying logs or tree branches. Diffusion is the net movement of anything to equilibrate a system, driven purely by a concentration difference in the system.

[X] *Microviscosity* (Pa · s) • In comparison to the bulk parameter viscosity, microviscosity is a parameter that takes into account the local friction in the small volume where the quantity is probed. Therefore, it is a local parameter rather than a bulk parameter[70].

Examples include probing the microviscosity[X] in living plant cells using rotor dyes[75] and with Förster Resonance Energy Transfer (FRET) using fluorescent proteins [XI] Protein[76,77].

In addition, mechanosensors have been used to study mechanics and fracture mechanics in polymeric materials. Examples using physical bonds include monitoring polymer strains using a conjugated polymers strain sensor[80], doping protein polymers that can self-assemble intro triple helices upon cooling with FRET sensors[81], and mechanochemical transductions achieved with metallosupramolecular polymers[82]. An example of using a chemical bond includes recent work by the Creton group on post-mortem confocal imaging of a Diels-Alder adduct of π-extended anthracene[83]. Other examples include two other probes, dioxetane and spiropyran, that act as a bond rupture probe and stress probe, relatively. These will be used in this Thesis, in Chapters 5 and 6, respectively. Therefore, these mechanosensors will be introduced in more detail in Section 1.4.3.

[XI] *Yellow and Green Fluorescent Protein* • Examples of fluorescent proteins that have been expressed in many species, including bacteria, yeasts, fungi, fish and mammals, introduced through transgenic techniques to study the expression of proteins[78,79] and to study mechanical processes using FRET.

1.3 Heterogeneity

With the chemical and physical properties of polymers introduced in Section 1.1 and methods to measure mechanical properties of soft polymeric materials introduced in Section 1.2, this Section will continue by introducing heterogeneity; what is heterogeneity, why are length scales important and how can heterogeneity be controlled?

1.3.1 Heterogeneity and length scale

The work presented in this research is focused around heterogeneous materials, i.e. materials that have multiple properties due to some structural variation, controlled or uncontrolled, in the material, as shown in figure 1.13. This variation can be:

1. Compositional heterogeneity; a material consisting out of multiple building blocks, called a composite, such as steel-fibre reinforced concrete, mattresses and meat analogues.

2. A material that locally has different structures, such as:
    - Crystal structure heterogeneity: crystalline structures with multiple crystals, recognizable by the so-called ’metal flake effect’, called polycrystallines, for example most photovoltaic cells[84].
    - Microstructural heterogeneity: materials with spatial variations in connectivity or density within the material. Except for perfect crystalline structures, all materials posses some degree of microstructural heterogeneity[8].

The list above holds examples of both synthetic materials, such as composites, colloidal systems, gels, foams, and natural heterogeneous materials, such as granular media, animal and plant tissue, cell aggregates and tumors, earth’s crust and wood. Hence, material heterogeneity exist both for synthetic and natural materials.

Heterogeneity is a function of length scale, as shown in Figure 1.13a, which covers heterogeneous materials over several orders of magnitude. Colloidal systems, for example milk and paints, are shown to have heterogeneous structures on the $\sim \mu m$-scale[88,89]. At this same μm length scale the earth’s crust might appear as a homogeneous material, as the different layers of the earth’s crust span on the order of kilometers. However, at a length scale over several hundreds of kilometers, even the earth’s crust will appear to be heterogeneous, as this might span multiple crusts. This concept is shown in Figure 1.13b, where ℓ would represent observing the earth’s crust at a relatively short length scale (for example 1 meter) compared to the system size (the earth has a diameter of $\sim$ 6370 kilometers) and L would represent observing the length scale at several hundreds of kilometers. Therefore, the scale at which heterogeneity is observed, sets the amount of heterogeneity that is found.
The effective properties of a material, such as conductivity, stiffness or viscosity, depend on the heterogeneity of a material. The most straightforward way to describe the heterogeneity of a material is by the volume fraction of the phases present in material. The question arises whether a materials volume fraction is sufficient to predict the effective material properties. To address this question, two examples are given here that are inspired by a book on heterogeneity in materials written by Torquato[8], and a third that

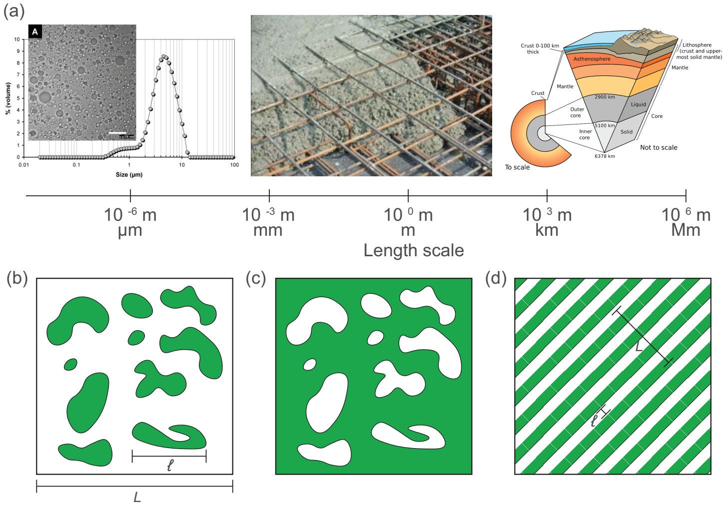

Figure 1.13 – **(a)** Heterogeneity at different length scales, showing mature human milk observed with light microscopy using differential interference contrast[85], steel-fibre reinforced concrete[86], and the earth's crust[87] **(b)** Schematic of a heterogeneous material with a relatively shorter length scale ℓ and larger length scale L. **(c)** Schematic of a heterogeneous material that has a structure identical to panel (b), except that the phases are interchanged. **(d)** Schematic of a ordered heterogeneous material with a relatively shorter length scale ℓ and larger length scale L.

addresses the size of the heterogeneity compared to the sampling size. In the first example, the degree of electrical conductivity of a composite material[90], such as that of steel-fibre reinforced concrete that is designed to increase resistance to tensile stresses and increase ductility, depends on the axis the conductivity is measured. In this example study, the electrical conductivity of steel-fibre reinforced concrete at multiple steel-fibre volume fractions was measured along three axes, all three showing different conductivity at the multiple levels of steel-fibre volume fractions, without a clear dependence on the volume fractions. Although drying of the concrete was shown to affect the electrical conductivity, still the sampling orientation influenced the measured electrical conductivity at the multiple steel-fibre volume fractions. This example, where electrical conductivity is sampled at different volume fractions, shows that the volume fraction by itself is insufficient to describe the effective material properties. Rather, it shows that the orientation at which the material is sampled will largely

affect the sampled property, in this case electrical conductivity, of the material.
In the second example, the volume fraction of the two phases are 50%, but interchanged between Figures 1.13b and c. As an example, it is assumed that the green phase has a higher electrical conductivity compared to the white phase. In this case, although panels b and c of Figure 1.13 have the same volume fraction of material, panel c will have the higher electrical conductivity as a material as a whole, since it spans, or percolates, the system size. Hence, the volume fraction by itself is insufficient to describe the effective property of the material. In this example, the location of the phases is important and largely affects the effective material properties.
In the third example, shown by Figure 1.13d, the two phases are placed in an ordered structure. This example shows that the size over which the material is sampled, depicted with ℓ and L, can either lead to the material's effective property being dominated by one of the two phases, in the case of ℓ, or the effective property being a mix of both phases, in the case of L. Hence, the size over which the material is sampled can affect the measured effective properties. Furthermore, the material in this example can appear to be homogeneous, in case the length scale over which it is sampled is (much) larger than the (average) size of the phases.

The three examples above show that knowledge about volume fraction of the heterogeneous phases are insufficient to accurately describe what the effective properties of the material will be. Rather, the sampling orientation, position, and length of the phases will influence the effective properties of the material.

The heterogeneity shown in 1.13b,c is called random heterogeneity, implying that the location of the heterogeneous structures are not controlled purposely. With the exception of composite materials, most synthetic materials possess a random heterogeneity. This also includes meat analogues, a type of material of which the mechanical characterization will be used to provide the food industry with a methodology to quantify the mechanical texture in Chapter 4 of this thesis. In contrast, few materials exist that have a programmed heterogeneity, where the position and size of the phases are controlled and programmed into the material. In order to study the relation between mechanical heterogeneity/network architecture and fracture, one of the goals of this thesis will be to develop a material with controlled mechanical heterogeneity.

1.3.2 Creating a controlled mechanically heterogeneous material

To create a controlled mechanically heterogeneous material, one has to know how mechanical heterogeneity can actually be obtained. Generally, there are three methods to create heterogeneity into a material;

- Creating a composite material, which is a material that is composed out of two or more constituent materials.
- Creating a material with multiple components (in a non-layered fashion, e.g. by mixing, distinguishing this method from composite materials), where each component has different mechanical properties, including the energy required to extend and fracture it's bonds, the latter called the bond activation energy. For example, in polymeric materials, a material can be produced that is polymerized with two different polymers that polymerize to from a network. The resulting properties are a function of several parameters, including the chemical bond energy between atoms and the amount of segments in a polymer chain. Section 1.4 will elucidate this further. By using multiple types of molecules in a material, the material will be a convolution of all of these mechanical properties, creating a mechanically heterogeneous material.
- By locally varying the density of crosslinkers in the material, a mechanically heterogeneous material is created. This variation can range from a relatively high dense region of crosslinks to the local absence of crosslinks. Chapters 2 and 3 will explore production and mechanical characterization of a material where the local density of polymer crosslinks is controlled.

There are some ways to control the mechanical heterogeneity of a material. Here, two of these are listed, including some examples.

- The first method to control the mechanical heterogeneity of a material is to control the connectivity. By controlling the local connectivity, the number of bonds to which a polymer (e.g. in polymeric materials) or beam is connected, the network topology and with that the mechanical heterogeneity of a material can be controlled. The challenge here is the length scale, as controlling the connectivity at the single polymer level is impractical to achieve. Therefore, this method is more generally applied on the µm-cm scale, for example in metameterials[91]. By using techniques such as laser-cutting a sheet of material and 3D printing a mold, metamaterials are readily produced in 2D. In fact, section 7.2.1 discusses preliminary work from a project conducted during this PhD, where a 3D printer is used to produce molds that are in turn used to produce 2D dimensional triangular networks on the mm-cm scale. With the 3D printer, several network topologies can be printed, enabling the study of (fracture) mechanics as a function of mechanical heterogeneity.

- The second method to control the mechanical heterogeneity of a material is photolithography. With photolithography, a material, containing a photo-initiator, see Section 1.1.2, is illuminated to polymerize the material. The illumination can be applied heterogeneously, triggering the photoinitiators to polymerize the material locally by a higher degree. This heterogeneous illumination can be achieved by exposing areas in the material for multiple times with varying dosages or by using a photomask, blocking part of the UV-light from the light source. The heterogeneous resolution of photolithography is limited by the resolution of the photomask and/or the resolution of the UV illumination source and eventually diffraction-limited, elucidated in Section 1.2.2. The latter is optimized with Extreme Ultraviolet Lithography, which has a resolution of ~ 13.5 nm[92].

  Here, two examples of studies creating mechanically heterogeneous polymeric materials reported in literature are presented.

  The first example uses stereolithography, the layer by layer polymerization of a 3D material by focusing the UV light source at the edge of a material which is submerged in its unpolymerized building blocks[93]. The polymer used is Poly(ethylene glycol)dimethacrylate (Mw 750 g/mol) with photo-initiator lith-

ium phenyl-2,4,6-trimethylbenzoylphosphinate (LAP). In this study, the mechanically heterogeneous material is used to study cellular organization on softer and stiffer parts of the material.
The second example used halftone lithography, the subsequent use of two photomasks, to produce a mechanically heterogeneous material[94]. The polymer used is N-isopropylacrylamide (NIPAm) and Acrylic acid (AAc) copolymer containing the photo-initator benzophenone acrylamide (BPAm). In this study, the mechanically heterogeneous material is demonstrated to be stimuli-responsive to temperature, re-morphing as a function of temperature.

Nevertheless, precise control over the network mechanical heterogeneity or architecture remains challenging, even with the continuous development of experimental techniques, although this development has opened pathways towards control of heterogeneity on the sub-mm scale in the past decade. Furthermore, both the methodologies presented above come along with associated experimental challenges. For example, laser cutting leads to residual stresses, and filling 3D printed molds gives rise to underfilling, adhesion, and inhibition reactions, and photolithography will give rise to blurring of the mechanical features in all three dimensions, depending on the chemistry and optics used.

1.4 Fracture

With the chemical and physical properties of polymers introduced in Section 1.1, methods to measure mechanical properties of soft polymeric materials introduced in Section 1.2, introduction to heterogeneity and methods to create a material with mechanical heterogeneity in Section 1.3, this section will introduce the last step towards studying fracture of mechanically heterogeneous materials: fracture mechanics.

Fracture mechanics is a scientific field that studies the physical concepts that cause material failure, with the natural consequence that this knowledge is used to design materials and structures that resist failure.

Leonardo da Vinci (1452-1519) was the first to document about a fracture experiment, as mentioned at the very beginning of this introduction. At the time, iron, the material on which da Vinci experimented, was not yet used in the construction of buildings, as production methods were insufficient. Rather, buildings at the time were produced with timber, stone, brick and mortar[2], materials that are unreliable for carrying tensile loads. Yet, designs of structures that would withstand failure, found mainly empirically trough trial and error, are still found today. Examples include structures built by ancient societies as the Pharaohs of Egypt or the Roman Empire, showcasing the ability of early architects and engineers. Supposedly, the Roman Empire would make the engineer of a bridge stand underneath its design while the bridge integrity was being tested by chariots crossing over the bridge. This Darwinian approach would accelerate the design of a desirable bridges and would 'naturally select' the best engineers. This lead to the design of a bridge in an arch shape, which causes compressive rather than tensile stress to be transmitted through the bridge structure, enhancing the load that the bridge could bear. With the industrial revolution around 1750, iron and steel could also be used in structures, allowing for the building of structures that carried tensile stresses. However, the use of iron in structures would lead to unexpected material failures, as materials would fail at stresses well below the anticipated tensile strength. It was the pioneering work of he British engineer Griffith (1893-1963) around World War I, in 1920, that explained the seemingly random failure of iron structures, using the first law of thermodynamics. With that, the scientific field of material failure was born.

To understand the origin of material failure, an atomic view on bond failure can be used. In the late 1800s and first decades of the 1900s, linear elastic fracture mechanics (LEFM) was developed, which describes the mechanics of propagating cracks in a material. LEFM is introduced in the next Section, Section 1.4.1.

1.4.1 Linear elastic fracture mechanics

Bonds will break once the dissociation energy, D, that holds two atoms together, is overcome. Figure 1.14 shows the potential energy $U(r)$ of a chemical bond under zero load, described by a Morse potential, showing the dissociation energy D. Applying an external load P will lower $U(r)$ by the work of the external load; $W(r) = P(r' - r_0)$[95]. Under the applied load, the potential energy is lowered to $U(r')$, with a decreased activation barrier D'. The potential energy and the associated D can also be lowered with increasing temperature, as described by the Thermally Activated Barrier to Scission (TABS) model[96]. The stochastic nature of material failure can also be explained with TABS; in case a material is subcritically strained, and therefore the potential energy barrier is slightly too high to break the bond, thermal fluctuations could still cause the bond to break.

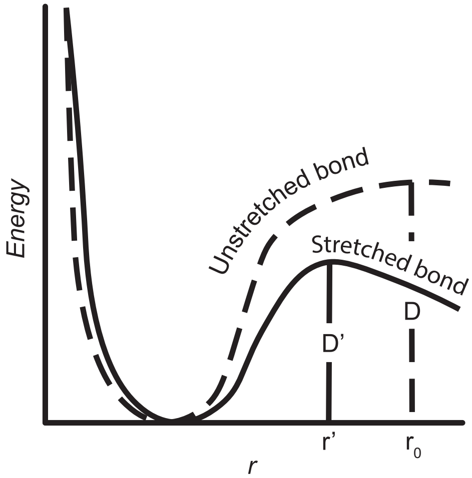

Figure 1.14 – The potential energy landscape for an unstretched and stretched bond, lowering the dissociation energy D[95]

The energy between bonds E_b in one dimension is obtained by[2]:

$$E_b = \int_{x_0}^{\infty} P_c dx \tag{1.15}$$

with x_0 the distance between atoms when in contact and where the cohesive strength P_c between atoms can be estimated with one half-period of a sine wave[2]:

$$P = P_c \sin(\frac{\pi x}{\lambda}) \sim P_c \frac{\pi x}{\lambda} \tag{1.16}$$

for small displacements. Multiplying the relation for the spring constant $k = P_c \frac{\pi}{\lambda}$ with the number of bonds per unit area and x_0 on both sides, the cohesive stress σ_c equals:

$$\sigma_c = \frac{E\lambda}{\pi x_0} \sim \frac{E}{\pi} \tag{1.17}$$

Expressing this in terms of the surface energy per unit area γ_s:

$$\gamma_s = \frac{1}{2} \int_0^{\lambda} \sigma_c \sin(\frac{\pi x}{\lambda}) dx = \sigma_c \frac{\lambda}{\pi} \tag{1.18}$$

leading to a relation to compute the critical stress:

$$\sigma_c = \sqrt{\frac{E\gamma_s}{x_0}} \tag{1.19}$$

However, this theory does not explain the results observed by Leonardo da Vinci, hypothesizing that material flaws would lower the fracture strength. It was the work of Kirsch in 1898 that gave the first qualitative description of fracture with a flaw embedded[97]. In this work, Kirsch studied the stress that is needed to propagate a crack around a spherical hole in an infinite plate, which he postulated in this theory called the Stress Concentrations at Holes[97]. In the early 1900's this theory was expanded for elliptical shaped holes by Inglis[98]. Inglis assumed that the elliptical shaped hole is not influenced by the plate boundary, or $A \gg a$ and $B \gg b$ shown in Figure 1.15, and described stress concentration as:

$$\sigma_c = \sigma \left(1 + 2\frac{2a}{b}\right) = \sigma \left(1 + 2\sqrt{\frac{a}{\rho}}\right) \tag{1.20}$$

where $\rho = \frac{b^2}{a}$ is the radius of the ellipsoid. However, a flaw with infinitesimal small radius ρ would cause the smallest stress to rupture the sample, which obviously is incorrect. This motivated Griffith to develop a fracture theory that is based on energy rather than stress localization. In his theory, Griffith uses the first law of thermodynamics, see Equation 1.1,

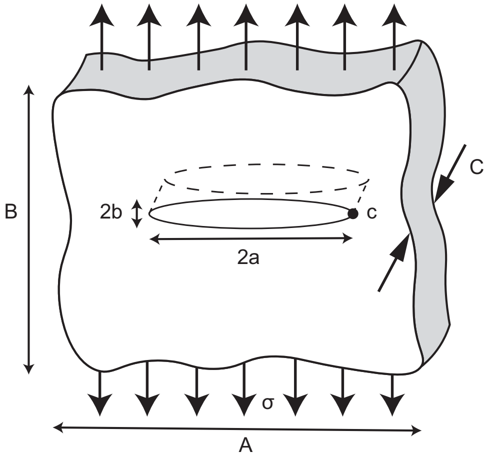

Figure 1.15 – An infinite plate with an elliptical shaped notch subjected to a stress σ with stress concentration at the tip c of the ellipsoid.

which is based on energy conservation, to describe when a material flaw will become unstable and form a crack. He argued that in order for a crack to grow, the potential energy Π supplied by an externally applied stress has to overcome the surface energy W_s of the crack surface energy of the material for an incremental increase in the crack area dA_c:

$$\frac{dE}{dA_c} = \frac{d\Pi}{dA_c} + \frac{dW_s}{dA_c} = 0 \tag{1.21}$$

or

$$-\frac{d\Pi}{dA_c} = \frac{dW_s}{dA_c} \tag{1.22}$$

where E is the total energy. Using the stress analysis of Inglis, Griffith showed that

$$\Pi = \Pi_0 - \frac{\pi\sigma^2 a^2 C}{E} \tag{1.23}$$

The formation of a crack requires the creation of two crack surfaces, W_s, given by:

$$W_s = 4aC\gamma_s \tag{1.24}$$

Plugging equations 1.23 and 1.24 into equation 1.22 results in

$$\sigma_f = \sqrt{\left(\frac{2E\gamma_s}{\pi a}\right)} \tag{1.25}$$

which is the Griffith criterion where σ_f is the fracture stress, the stress at which the material fractures.

Analogous to Griffith's model for fracture, Irwin used the energy release rate G to describe fracture[2]:

$$\mathbf{G} = -\frac{d\Pi}{dA_c} \tag{1.26}$$

with unit Jm^{-2} where the *rate*, here, does not refer to a time derivative but rather to the rate of change in potential energy $d\Pi$ with crack area dA. G also appears in another interesting method to look at fracture, known as the stress intensity factor K, which is defined as:

$$K \sim \sqrt{E\mathbf{G}} \tag{1.27}$$

with E the elastic modulus[99]. The energy release rate at which a material fails is known as the fracture surface energy $\Gamma = \frac{U}{A}$. In LEFM, the fracture surface energy is obtained with an energy balance between the energy required to advance a (steady state) crack by a unit area and the energy to open up a surface λ alongside any plastic work performed: $\Gamma = 2\lambda + w_p$, leading to:

$$\Gamma = \pi\frac{\sigma^2 a}{E} \tag{1.28}$$

In case the energy release rate G in Equation 1.27 is substituted with the fracture surface energy $\Gamma = \frac{U}{A}$, i.e. work done at the point of crack propagation and the surface area of the fracture, one obtains the fracture toughness:

$$K_C \sim \sqrt{E\Gamma} \tag{1.29}$$

which has units Pa·m$^{1/2}$, and a measure of a material's capability to resist crack propagation. Experimental work from 1953 on tearing notched rubbers with various notch lengths showed that Γ is a material dependent parameter[100]. Typically, the fracture toughness is described with K_{IC} for mode I failure, opening mode (e.g. in a tensile test[59]), K_{IIC} for mode II failure, in-plane shear mode (e.g. in a 3-point bending test[101]) and K_{IIIC} for mode III failure, out-of-plane shear mode (e.g. in a tensile test[102])[2].

Irwin also showed that the stress field around a crack can be described with[103]:

$$\sigma(r) \sim \frac{K}{\sqrt{r}} \tag{1.30}$$

with r the distance from the crack tip. From this, also the displacement ϵ and energy u around the crack tip can be derived[99]:

$$\epsilon(r) \sim \frac{\sigma}{E} \sim \frac{K}{E\sqrt{r}} \tag{1.31}$$

$$u(r) \sim \int \epsilon \partial r \sim \frac{K\sqrt{r}}{E} \tag{1.32}$$

The above relations for ϵ and u, however, only hold within close proximity of the crack tip[99]. This criteria is known as small scale yielding (SSY)[104]. Consequently, LEFM only accurately describes any linear and non-linear, e.g. nonlinear elasticity, plasticity, certain thermal phenomena, and time-dependent phenomena such as visco-elasticity[105], deformation that is in close proximity at the crack tip.

1.4.2 Fracture of rubbers

The fracture energy of rubbers[106] is a few orders of magnitude higher compared to silica glass[107]. One reason for this is plastic deformation of the rubber before failure[108], for example caused by visco-elasticity (see Section 1.1 and Section 1.2). The effect of visco-elastiticy can be reduced by increasing the temperature or reducing the strain rate[XII]. In this case, the intrinsic fracture energy Γ_0, i.e. the time-independent fracture energy, can be obtained, as is done in experimental work by Lake and Thomas[109]. This Γ_0 is still higher compared to the fracture energy of, for example, silica glass.

To explain this difference, Lake and Thomas introduced a model that predicts that the intrinsic fracture energy of polymer networks is relatively high because the polymer chains act as entropic springs, with the capacity to change the end-to-end distance significantly before failure. This is in contrast to, for example, silica, where bonds act as an atomic spring, having little room to change the end-to-end distance before the material fails. In the model, Lake and Thomas show that Γ_0 can be estimated by:

$$\Gamma_0 = \frac{U_b a \rho}{M_n} \sqrt{N_x} \tag{1.33}$$

with N_x segments, the length of the monomer a, chemical energy between covalent bonds U_b, monomer density ρ and monomer molar mass M_n. This relation for Γ_0 implies that for a polymer to break, the entire chain is to be stretched. As a consequence, the energy is stored in all bonds in the polymer; breaking one bond then releases all this stored energy, which leads to an increase in fracture energy that relates to the polymer length. This Lake-Thomas theory explains why the fracture energy of rubbers is a few orders of magnitude higher than that of silica glass.

1.4.3 Fracture mechanics of polymer networks studied with mechanosensors

In Section 1.4.1 LEFM was introduced, which is a fracture mechanics model that specifically works well to describe fracture propagation. Unfortunately, the model has a limited capacity to accurately describing physical processes near the crack propagation tip, as these processes are lumped together in one parameter; the fracture energy Γ. In order to relate Γ to the microscopic polymer structure and interactions, understanding what happens at the microscopic scale is key. The fracture energy is a function of the number of bonds broken, as shown in Equation 1.33 in Section 1.4.2. Therefore, obtaining the number of broken bonds in a fracture experiment is an important step towards understanding the processes preceding crack propagation, known as crack nucleation. In the past decade, mechanosensors have been used increasingly to, for example, obtain the number of broken bonds directly from the polymers. Here, previous work reported in literature, for two mechanosensors that are used in this Thesis, will be discussed. These mechanosensors are the 1,2-dioxetane molecule used in Chapter 5 to study bond rupture of covalently crosslinked polymers and the spiropyran molecule used in Chapter 6 to study stress accumulation in elastomers.

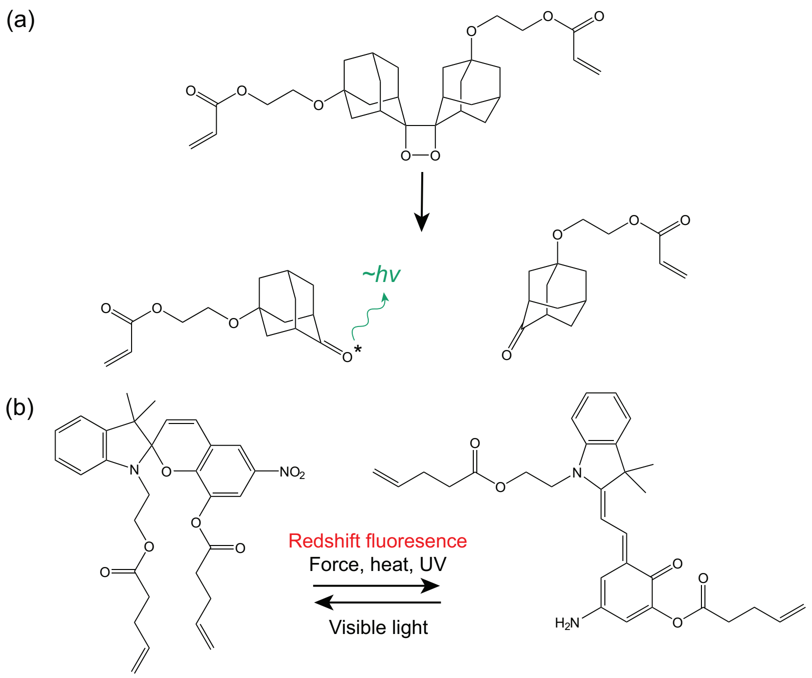

Figure 1.16 – **(a)** Chemiluminescence from bis(adamantyl)-1,2-dioxetane can be induced mechanically when incorporated in a polymer network[110] **(b)** Transition from spiropyran to merocyanine upon mechanical stress gives a redshift in the emitted fluorescence, giving a readout for the local stress when incorporated in a polymer network[111].

The 1,2-dioxetane chemiluminescent bond rupture sensor was first reported by the Sijbesma group in 2012[110], emitting blue light upon mechanical failure of the oxygen ring, see Figure 1.16a. The blue light can be redshifted towards yellow emission using various acceptors, using (FRET). Since the report in 2012, this bond rupture probe has been used in several studies, some of which will be introduced and discussed here.

The dioxetane probe was used to study bond rupture of glassy poly(methyl methacrylate) (PMMA) polymer networks upon solvent ingression[112]. In this study bursts of dioxetane emission were observed, quantified as $10^9 - 10^{11}$ bonds broken in each burst, after calibration. The number of bonds broken and the crack opening size both increased with higher crosslinking density, observed with a camera and by the naked eye, respectively.

The dioxetane probe has also been used to study bond rupture in thermoplastic elastomers[113]. In this study, an increase of dioxetane emission was observed for increasing strain rate. In addition, the dioxetane emission was found to be proportional to the molecular weight which in turn is proportional to the stress response.

Furthermore, the dioxetane probe has shown to be effective to study the Mullins effect, history-dependent stress-softening first observed in rubbers by Bouasse and Carrière in 1903[114]. A study performed by Clough *et al.*, where silica-filled rubbers are strained cyclically to higher degree, has shown that the amount of light emitted by the dioxetane bond rupture sensor is proportional to the cumulative hysteresis energy[115]. In addition, bond rupture was observed during unloading of the samples, possibly due to a delay in force transmission to the dioxetanes, mediated by the silica filler-particles[II].

Lastly, the dioxetane probe has also shed light on the fracture process for toughened elastomers, where single networks (SN), double networks (DN) and triple networks (TN) of (pre-notched) glassy acrylate samples were tensile tested[59]. Furthermore, in line with the previous example[115], the amount of light emitted by the dioxetane bond rupture sensor is proportional with the cumulative hysteresis energy, tested with un-notched samples[59]. In addition, the network toughness was shown to be tunable by varying the composition of the first, second and third network. In notched samples, fracture was shown to be localized around the notch due to high stress localization in a region in front of the crack tip. From SN to DN to TN, the area over which the bonds were observed to break was increasing.

Spiropyran is a stress sensor that changes conformation to merocyanine when stressed above ∼240 pN, fluorescing at a longer wavelength[116, 117], see Figure 1.16b. As such, the sensor is used to study (high) mechanical stresses in polymeric materials. Some examples of these studies will be introduced and discussed here.

In the first example, spiropyran is used in glassy PMMA polymers, toughened with 7.3 wt% core-shell rubber nanoparticles, to study local stresses around the tip of a notch upon slow uniaxial extension leading to crack propagation[118]. The stress profile of the mechanosensor was

observed to be circular ahead of the crack tip. The crack propagation occurred on the timescale of seconds, given that the frame rate was 5 seconds and samples fractured over the course of some 10-20 frames. Importantly, samples were both prestretched and not prestretched before notching, and the prestretching was shown to enhance the fluorescent signal from the mechanosensor, suggesting that polymer alignment is important for the observed signal. The importance of polymer alignment for spiropyran to merocyanine conversion is also discussed in work reported by O'Bryan *et al.*[119]. In this work, polymer alignment is achieved by stretching the poly(ϵ-caprolactone) films by hand, and the absence of this step lead to a 'response very minor by comparison to pre-stretched samples' upon stretching these samples to failure with Dynamic Mechanical Analysis[119]. In addition, work reported by Lee *et al.* shows information on the back-conversion time from merocyanine to spiropyran[120]. After UV-induced or stress-induced (strain = 2.0) conversion from spiropyran to merocyanine, the half-time conversion back to the spiropyran state is 30 minutes and 38 minutes, respectively, tested with Polyurethane samples.
Lastly, spiropyran can also act as a warning for the general material user, preventing deformation of rubbers too much such that this deformation leads to material failure. This has been shown in an elegant way by the Craig group, by incorporating the word STOP in a Sylgard 184 and Ecoflex (Smooth-On, PA, USA) composite material, showing the word STOP after spiropyran to merocyanine conversion at near-failure[121].

An important note for using mechanosensors as stress, strain or failure reporters is that crack propagation in polymeric materials typically occurs at relatively high speeds, ranging from ~1 m/s for soft polyacrylamide gels[122] to ~1000 m/s for highly crosslinked rubbers[123]. LEFM, introduced in Section 1.4.1, predicts that the energy release rate G relates to the crack propagation velocity v via

$$G(l, v) = \Gamma(v) \simeq \frac{\sigma^2}{E} l \left(1 - \frac{v}{c_R}\right) \tag{1.34}$$

with l the crack length and c_R the Rayleigh wave-speed[124]. Based on this relation, cracks propagate slower for materials with lower elastic modulus. As a practical consequence, to study fracture in polymer networks, image acquisition in experiments typically should be over 1 kHz to obtain information from mechanosensors at useful temporal resolution.

1.4.4 Fracture of mechanically heterogeneous materials

So far, this Chapter has introduced the chemical and physical properties of polymers (Section 1.1), mechanical properties of materials and several techniques to obtain these at a range of length scales (Section 1.2), heterogeneity and methods to control it (Section 1.3), and, finally, an overview of fracture mechanics and methods developed in the past decade to study fracture at the micro to nano scale using mechanosensors (Section 1.4). This provides the ingredients needed to study the influence of mechanical heterogeneity on material fracture. This Section will give an overview of reports in literature on the role of a materials mechanical heterogeneity on the fracture mechanism.

Experimentally, there have been studies that attempt to identify the role of mechanical heterogeneity in the fracture mechanism, by controlling and/or quantifying the heterogeneity. For example, in a study performed by Garcimartín *et. al*, the acoustic emission caused by fracture of the heterogeneous materials plaster, chipboard wood, and fiberglass is followed[125]. Here, a sample is placed in a sealed chamber where a pressure difference can be applied, in order to exert a force on the material. During the test, sound is recorded at four positions around the sample, and from the relative time at which a sound signal is picked up, a position of fracture can be determined. It is found that microcracks cluster around the final major crack.

In another study performed by Vanel *et al.* the fracture of a crack propagating trough a piece of paper with two distributions of holes, creating heterogeneity, is studied by applying a constant deformation[126]. In the first distribution, the spacing between the holes was constant, whereas in the second the spacing alternated between a shorter and longer distance, keeping the period constant and equal to the first distribution. It was found that the rupture dynamics is slower for the first distribution, although the critical rupture threshold is comparable. The results show that the crack is accelerated more with shorter hole spacing, suggesting that the probability of cracks and voids merging decays with increasing separation between the cracks.

In the past decade, the emergence of techniques such as 3D printing and laser-cutting have enabled the production and examination of mm-scale beam networks, with precise control of the network architecture. Experiments performed by Berthier *et al.*[127] on laser-cut 2D acrylic samples show that low-connectivity samples show a ductile-like fracture, and high-connectivity samples show a brittle-like fracture mechanism. Furthermore, the crack width is observed to decay with the mean coordination number <z>. The latter is also observed in a study by Driscoll *et al.*[128], where the crack width is shown to be inversely proportional to material rigidity. In another study where the network was created with 3D printing, it was shown that the orientation of the applied strain influences the fracture mechanism, ductile or brittle, for heterogeneous materials[129]. However, the system size could play a role here, as is shown by (off-lattice) simulations performed by Tauber *et al.*[130]. Here, it is shown that (connectivity or threshold) disorder scales with the system size, and this sets where the fracture mechanism transitions from ductile to brittle. In addition, this study shows that the number of broken bonds is a function of the system percolation, with the maximum around the isostatic point. However, what is the fracture mechanism at this intermediate degree of heterogeneity?

A lattice model study by Sekhawat *et al.* in 2013 predicts three different fracture scenarios[131];

1. For low disorder, stress localization leads to nucleation of a single crack which eventually fractures the material.
2. For large disorder, catastrophic failure follows after percolation of diffuse damage that merge and eventually fractures the material.
3. For intermediate disorder, the model predicts a two-step failure process, where first intermittent bursts of bond rupture events, also called avalanches, are followed by the formation and growth of a dominant crack. However, it remains an open question whether heterogeneity's promote or obstruct material failure.

Testing this theory requires control over the mechanical heterogeneity of the material, and microscopic understanding of the fracture mechanism. However, to our knowledge, there are no reports in literature where the role of network architecture on fracture mechanics of polymeric materials with a controlled and heterogeneous network structure on the sub-mm scale, obtained with for example photolithography as elucidated in Section 1.3.2, is studied.

1.5 Research Questions

The goal of the research conducted in this PhD was to study the properties of mechanical heterogeneous material and, afterwards, the role of mechanical heterogeneity on the fracture mechanism of material failure. To do so, the first step is to produce a material with controlled mechanical heterogeneity, see Section 1.3.2, giving rise to the first step in this research, with associated research questions:

Step 1: Production of a mechanically heterogeneous material

- Can we produce a material in which the mechanical heterogeneity is controllable?
- Is this material compatible with mechanosensors, such that these tools can be used to study failure?

Let's assume that in this research a material is produced that is mechanically heterogeneous. In order to study the relation to fracture, the exact local mechanical landscape has to be known in order to link the fracture process to the heterogeneous structure. A commonly used technique to obtain information on the local polymer density is light scattering[132]. However, this technique would not be able to estimate the local mechanical heterogeneity in case there are two types of crosslinkers with a different bond energy strength. Section 1.2.2 gives examples of measurement techniques that can be used to probe the local mechanics of a material, a direct measure for the mechanical heterogeneity of a material. This gives rise to the second step, with associated research questions:

Step 2: Mechanical understanding of the produced mechanically heterogeneous material

- Can we accurately determine the mechanical profile of the mechanically heterogeneous material produced in step 1?
- Can we use mechanical understanding of heterogeneous materials for practical purposes as well?

After the heterogeneity can be controlled and understood, the fracture process and the relation to heterogeneity can be studied in step three. Some research questions that are debated in literature and were aimed to answer at the beginning of the project are:

Step 3: Study the role of mechanical heterogeneity in material failure

- How do cracks nucleate in materials when subjected to a very localized, or heterogenous, stress?
- How does a mechanically heterogeneous material fracture when it is subjected to too much stress or strain?
- More particularly, do experiments confirm the three different fracture scenarios for mechanically heterogeneous materials as predicted by simulations (see Section 1.4.4)?
- Does the material toughness increase or decrease as a function of heterogeneity?

The research questions that are posed in step 3 are, in fact, quite ambitious. Therefore, the work presented in this thesis should be read as an initiation, or nucleation, of clarifying the role of heterogeneity on the (microscopic) fracture process in polymer networks.

1.6 Thesis Outline

Below, a short summary for each chapter is provided to outline their contributions to the general aim of the Thesis. The Thesis contains two parts. The first part, Chapters 2-4, contains chapters on development, characterization and a practical application of mechanically heterogeneous materials. The second part, Chapters 5-7, contains chapters on fracture mechanics of soft synthetic materials, of which some are mechanically heterogeneous.

Part I of this thesis will start with Chapter 2, presenting a method to produce a mechanically heterogeneous material using inhomogeneous UV-lithography of a photopatternable polymer network on the millimeter-scale, programmable on the $\sim$micrometer scale. Based on this length scale, a method is developed to produce mechanical maps of materials, by spatially obtaining the mechanical response using an in-house developed multi-point indentation setup.
Chapter 3 will build further on this work, by recognizing that a local mechanical response of a heterogeneous material will convolve, i.e. blur, the recorded read-out. This Chapter aims to deconvolve this response into the expected local mechanical property, a process much like image deblurring when the image is acquired with a moving camera or from a moving object.
The final Chapter in Part I, Chapter 4, gives an example of where this technique of mapping local mechanical heterogeneity can be used practically by mapping meat and meat analogues and quantifying the resemblance of their mechanical landscape by means of an auto-correlation technique called Moran's *I*.

Part II of this thesis will start with Chapter 5, in which the mechanoluminescent probe dioxetane, which emits a photon when this crosslinker is broken, is used to study puncture mechanics of single and double networks with varying probe size and probe velocity. For these parameters, the amount of broken bonds is calculated, after calibration with thermoluminescence, and interpreted during fracture nucleation and propagation.
In Chapter 6, delayed failure of elastomers will be examined, using the mechanoluminescent probe spiropyran which fluoresces when a mechanical threshold on the molecule is exceeded, see Section 1.4.3. By imaging the sample at high, sub-millisecond, frame rate and capturing the fluorescent signal around the catastrophic failure event, it is observed that the fluorescent signal from the spiropyran starts to rise only in the order of milliseconds before the catastrophic failure of the material, whereas the simultaneously obtained LSSI readout, see Section 1.2.2, shows that the material start to deform in the order of seconds before the material fails catastrophically, as observed before by van der Kooij *et al.*[58].

Finally, Chapter 7 holds a general discussion on the research presented in this thesis, placing the results in a broader context and providing a future outlook on follow-up research that could address research questions that were not answered in this project, as well as presenting newly risen research questions.

Bibliography

[1] Mikko J Alava, Phani KVV Nukala, and Stefano Zapperi. Statistical models of fracture. *Advances in Physics*, 55(3-4):349–476, 2006.

[2] Ted L Anderson. *Fracture mechanics: fundamentals and applications*. CRC press, 2017.

[3] Isaac Newton. *Sir Isaac Newton's mathematical principles of natural philosophy and his system of the world*. Univ of California Press, 1962.

[4] Jay R Lund and Joseph P Byrne. Leonardo da vinci's tensile strength tests: Implications for the discovery of engineering mechanics. *Civil Engineering Systems*, 18(3):243–250, 2001.

[5] Rahul Rakshit and Alok Kumar Das. A review on cutting of industrial ceramic materials. *Precision Engineering*, 59:90–109, 2019.

[6] Flake C Campbell. *Elements of metallurgy and engineering alloys*. ASM International, 2008.

[7] Amit Bhaduri. *Mechanical properties and working of metals and alloys*, volume 264. Springer, 2018.

[8] Salvatore Torquato and HW Haslach Jr. Random heterogeneous materials: microstructure and macroscopic properties. *Appl. Mech. Rev.*, 55(4):B62–B63, 2002.

[9] Kemal Arda Günay, Patrick Theato, and Harm-Anton Klok. Standing on the shoulders of hermann staudinger: Post-polymerization modification from past to present. *Journal of Polymer Science Part A: Polymer Chemistry*, 51(1):1–28, 2013.

[10] Michael Rubinstein, Ralph H Colby, et al. *Polymer physics*, volume 23. Oxford university press New York, 2003.

[11] Hermann Staudinger. Uber polymerisation. *Ber. dtsch. chem. Ges.*, 53:1073–1085, 1920.

[12] Yuan Yuan, Wei Yuan, and Yulan Chen. Recent advances in mechanoluminescent polymers. *Science China Materials*, 59(6):507–520, 2016.

[13] Christian Harito, Listya Utari, Budi Riza Putra, Brian Yuliarto, Setyo Purwanto, Syed ZJ Zaidi, Dmitry V Bavykin, Frank Marken, and Frank C Walsh. The development of wearable polymer-based sensors: Perspectives. *Journal of The Electrochemical Society*, 167(3):037566, 2020.

[14] Jinwoo Lee, Dongkwan Kim, Heayoun Sul, and Seung Hwan Ko. Thermo-haptic materials and devices for wearable virtual and augmented reality. *Advanced Functional Materials*, 31(39):2007376, 2021.

[15] Roland Geyer, Jenna R Jambeck, and Kara Lavender Law. Production, use, and fate of all plastics ever made. *Science advances*, 3(7):e1700782, 2017.

[16] PlasticsEurope. Plastics – the Facts 2019. Technical report, 2019.

[17] L Mwaikambo. Review of the history, properties and application of plant fibres. *African Journal of Science and Technology*, 7(2):121, 2006.

[18] BWB Holman and AEO Malau-Aduli. A review of sheep wool quality traits. *Annual Review & Research in Biology*, 2(1):1–14, 2012.

[19] AU Ude, RA Eshkoor, R Zulkifili, AK Ariffin, AW Dzuraidah, and CH Azhari. Bombyx mori silk fibre and its composite: a review of contemporary developments. *Materials & Design*, 57:298–305, 2014.

[20] Giuseppe Bellussi and Carlo Perego. Industrial catalytic aspects of the synthesis of monomers for nylon production. *Cattech*, 4(1):4–16, 2000.

[21] Thingujam Jackson Singh and Sutanu Samanta. Characterization of kevlar fiber and its composites: A review. *Materials Today: Proceedings*, 2(4-5):1381–1387, 2015.

[22] Edward N Peters. *Plastics: thermoplastics, thermosets, and elastomers*. Wiley-Interscience, New York, 2002.

[23] Elisabeth Eckert, Frank Münch, Thomas Göen, Ariawan Purbojo, Johannes Müller, and Robert Cesnjevar. Comparative study on the migration of di-2-ethylhexyl phthalate (dehp) and tri-2-ethylhexyl trimellitate (totm) into blood from pvc tubing material of a heart-lung machine. *Chemosphere*, 145:10–16, 2016.

[24] European union - a european strategy for plastics in a circular economy. `https://eur-lex.europa.eu/legal-content/EN/TXT/?qid=1516265440535&uri=COM:2018:28:FIN`. Accessed: 2020-09-02.

[25] United nations environment program - the global partnership on marine litter”. `https://www.unenvironment.org/explore-topics/oceans-seas/what-we-do/addressing-land-based-pollution/global-partnership-marine`. Accessed: 2020-09-02.

[26] Pawankumar Rai, Srishti Mehrotra, Smriti Priya, Edgard Gnansounou, and Sandeep K Sharma. Recent advances in the sustainable design and applications of biodegradable polymers. *Bioresource technology*, page 124739, 2021.

[27] FL; National Oceanic U.S. National Park Service; Mote Marine Lab, Sarasota and Atmospheric Administration Marine Debris Program. Marine debris decomposition times. `https://www.whoi.edu/fileserver.do?id=107364&pt=2&p=88817`. Accessed: 2020-09-02.

[28] Bruce Alberts, Alexander Johnson, Julian Lewis, Martin Raff, Keith Roberts, and Peter Walter. Molecular biology of the cell: Reference edition. 2007.

[29] Gilbert N Lewis. The atom and the molecule. *Journal of the American Chemical Society*, 38(4):762–785, 1916.

[30] Peter Atkins and Loretta Jones. *Chemical principles: The quest for insight*. Macmillan, 2007.

[31] Masahide Terazima, Yui Nogami, and Toshihiro Tominaga. Diffusion of a radical from an initiator of a free radical polymerization: a radical from aibn. *Chemical Physics Letters*, 332(5-6):503–507, 2000.

[32] Manmeet Kaur and AK Srivastava. Photopolymerization: A review. *Journal of Macromolecular Science, Part C: Polymer Reviews*, 42(4):481–512, 2002.

[33] Sebastian Seiffert and Joris Sprakel. Physical chemistry of supramolecular polymer networks. *Chemical Society Reviews*, 41(2):909–930, 2012.

[34] Hanne M van der Kooij, Arijana Susa, Santiago J García, Sybrand van der Zwaag, and Joris Sprakel. Imaging the molecular motions of autonomous repair in a self-healing polymer. *Advanced materials*, 29(26):1701017, 2017.

[35] Ch SSR Kumar and Avinash M Nijasure. Vulcanization of rubber. *Resonance*, 2(4):55–59, 1997.

[36] Rudolf Pfaendner. How will additives shape the future of plastics? *Polymer degradation and stability*, 91(9):2249–2256, 2006.

[37] Annemieke Ten Brinke. *Silica reinforced tyre rubbers*. Twente University Press, 2002.

[38] Daniel V Schroeder. An introduction to thermal physics, 1999.

[39] Paul J Flory. *Principles of polymer chemistry*. Cornell University Press, 1953.

[40] CI Addison, AA Louis, and JP Hansen. Influence of solvent quality on polymer solutions: A monte carlo study of bulk and interfacial properties. *The Journal of chemical physics*, 121(1):612–620, 2004.

[41] Isaac C Sanchez and Robert H Lacombe. Statistical thermodynamics of polymer solutions. *Macromolecules*, 11(6):1145–1156, 1978.

[42] Jean-Pierre Hansen and Ian Ranald McDonald. *Theory of simple liquids: with applications to soft matter*. Academic Press, 2013.

[43] W Nunes dos Santos, JA De Sousa, and R Gregorio Jr. Thermal conductivity behaviour of polymers around glass transition and crystalline melting temperatures. *Polymer Testing*, 32(5):987–994, 2013.

[44] TCB McLeish. Tube theory of entangled polymer dynamics. *Advances in physics*, 51(6):1379–1527, 2002.

[45] PG De Gennes. Dynamics of entangled polymer solutions. i. the rouse model. *Macromolecules*, 9(4):587–593, 1976.

[46] Dow Corning. Sylgard 184 silicone.

[47] Seok Woo Lee and Seung S Lee. Shrinkage ratio of pdms and its alignment method for the wafer level process. *Microsystem technologies*, 14(2):205–208, 2008.

[48] Sungjune Park, Kunal Mondal, Robert M Treadway III, Vikash Kumar, Siyuan Ma, James D Holbery, and Michael D Dickey. Silicones for stretchable and durable soft devices: beyond sylgard-184. *ACS applied materials & interfaces*, 10(13):11261–11268, 2018.

[49] Denisse Ortiz-Acosta. Sylgard® cure inhibition characterization. Technical report, Los Alamos National Lab.(LANL), Los Alamos, NM (United States), 2012.

[50] Shinsuke Murakami, Masahiro Oguchi, Tomohiro Tasaki, Ichiro Daigo, and Seiji Hashimoto. Lifespan of commodities, part i: The creation of a database and its review. *Journal of Industrial Ecology*, 14(4):598–612, 2010.

[51] FP Beer, ER Johnston Jr, JT Dewolf, and DF Mazurek. Mechanics of materials, sixth edit edition, 2012.

[52] F Beer, E Johnston, and J DeWolf. Mechanics of materials, 5th si edition. *Stress*, 1(10):1–12, 1999.

[53] Valentin L Popov. *Contact mechanics and friction*. Springer, 2010.

[54] Clive R Siviour and Jennifer L Jordan. High strain rate mechanics of polymers: a review. *Journal of Dynamic Behavior of Materials*, 2(1):15–32, 2016.

[55] James Freeman Steffe. *Rheological methods in food process engineering.* Freeman press, 1996.

[56] J Sprakel, E Spruijt, MA Cohen Stuart, NAM Besseling, MP Lettinga, and J Van Der Gucht. Shear banding and rheochaos in associative polymer networks. *Soft Matter*, 4(8):1696–1705, 2008.

[57] Jian Ping Gong, Yoshinori Katsuyama, Takayuki Kurokawa, and Yoshihito Osada. Double-network hydrogels with extremely high mechanical strength. *Advanced materials*, 15(14):1155–1158, 2003.

[58] Hanne M van der Kooij, Simone Dussi, Gea T van de Kerkhof, Raoul AM Frijns, Jasper van der Gucht, and Joris Sprakel. Laser speckle strain imaging reveals the origin of delayed fracture in a soft solid. *Science advances*, 4(5):eaar1926, 2018.

[59] Etienne Ducrot, Yulan Chen, Markus Bulters, Rint P Sijbesma, and Costantino Creton. Toughening elastomers with sacrificial bonds and watching them break. *Science*, 344(6180):186–189, 2014.

[60] Jianhua Zhang, Yuanyuan Miao, Qiong Zhang, Yawen Sun, Lei Wu, and Yongzhen Peng. Mechanism of stable sewage nitrogen removal in a partial nitrification-anammox biofilm system at low temperatures: microbial community and eps analysis. *Bioresource technology*, 297:122459, 2020.

[61] Morten Rybtke, Louise Dahl Hultqvist, Michael Givskov, and Tim Tolker-Nielsen. Pseudomonas aeruginosa biofilm infections: community structure, antimicrobial tolerance and immune response. *Journal of molecular biology*, 427(23):3628–3645, 2015.

[62] Ronald F Gibson. A review of recent research on nanoindentation of polymer composites and their constituents. *Composites Science and Technology*, 105:51–65, 2014.

[63] Li-Heng Cai, Thomas E Kodger, Rodrigo E Guerra, Adrian F Pegoraro, Michael Rubinstein, and David A Weitz. Soft poly (dimethylsiloxane) elastomers from architecture-driven entanglement free design. *Advanced Materials*, 27(35):5132–5140, 2015.

[64] Daniel Kiracofe and Arvind Raman. On eigenmodes, stiffness, and sensitivity of atomic force microscope cantilevers in air versus liquids. *Journal of Applied Physics*, 107(3):033506, 2010.

[65] David P Allison, Ninell P Mortensen, Claretta J Sullivan, and Mitchel J Doktycz. Atomic force microscopy of biological samples. *Wiley Interdisciplinary Reviews: Nanomedicine and Nanobiotechnology*, 2(6):618–634, 2010.

[66] Kipom Kim and Omar A Saleh. A high-resolution magnetic tweezer for single-molecule measurements. *Nucleic acids research*, 37(20):e136–e136, 2009.

[67] Graeme A King, Federica Burla, Erwin JG Peterman, and Gijs JL Wuite. Supercoiling dna optically. *Proceedings of the National Academy of Sciences*, 116(52):26534–26539, 2019.

[68] Jan Gieseler, Juan Ruben Gomez-Solano, Alessandro Magazzù, Isaac Pérez Castillo, Laura Pérez García, Marta Gironella-Torrent, Xavier Viader-Godoy, Felix Ritort, Giuseppe Pesce, Alejandro V Arzola, et al. Optical tweezers: A comprehensive tutorial from calibration to applications. *arXiv preprint arXiv:2004.05246*, 2020.

[69] Hao Shen, Lawrence J Tauzin, Rashad Baiyasi, Wenxiao Wang, Nicholas Moringo,

Bo Shuang, and Christy F Landes. Single particle tracking: from theory to biophysical applications. *Chemical reviews*, 117(11):7331–7376, 2017.

[70] LG Wilson, AW Harrison, AB Schofield, J Arlt, and WCK Poon. Passive and active microrheology of hard-sphere colloids. *The Journal of Physical Chemistry B*, 113(12):3806–3812, 2009.

[71] RR Brau, JM Ferrer, H Lee, CE Castro, BK Tam, PB Tarsa, P Matsudaira, MC Boyce, RD Kamm, and MJ Lang. Passive and active microrheology with optical tweezers. *Journal of Optics A: Pure and Applied Optics*, 9(8):S103, 2007.

[72] David Briers, Donald D Duncan, Evan R Hirst, Sean J Kirkpatrick, Marcus Larsson, Wiendelt Steenbergen, Tomas Stromberg, and Oliver B Thompson. Laser speckle contrast imaging: theoretical and practical limitations. *Journal of biomedical optics*, 18(6):066018, 2013.

[73] Laszlo Takacs. The historical development of mechanochemistry. *Chemical Society Reviews*, 42(18):7649–7659, 2013.

[74] Yinjun Chen, Gaëlle Mellot, Diederik van Luijk, Costantino Creton, and Rint P Sijbesma. Mechanochemical tools for polymer materials. *Chemical Society Reviews*, 2021.

[75] Lucile Michels, Vera Gorelova, Yosapol Harnvanichvech, Jan Willem Borst, Bauke Albada, Dolf Weijers, and Joris Sprakel. Complete microviscosity maps of living plant cells and tissues with a toolbox of targeting mechanoprobes. *Proceedings of the National Academy of Sciences*, 117(30):18110–18118, 2020.

[76] Nico Bruns, Katarzyna Pustelny, Lisa M Bergeron, Timothy A Whitehead, and Douglas S Clark. Mechanical nanosensor based on fret within a thermosome: Damage-reporting polymeric materials. *Angewandte Chemie*, 121(31):5776–5779, 2009.

[77] Johnathan N Brantley, Constance B Bailey, Joe R Cannon, Katie A Clark, David A Vanden Bout, Jennifer S Brodbelt, Adrian T Keatinge-Clay, and Christopher W Bielawski. Mechanically modulating the photophysical properties of fluorescent protein biocomposites for ratio-and intensiometric sensors. *Angewandte Chemie*, 126(20):5188–5192, 2014.

[78] Roger Y Tsien. The green fluorescent protein. *Annual review of biochemistry*, 67(1):509–544, 1998.

[79] S James Remington. Green fluorescent protein: a perspective. *Protein Science*, 20(9):1509–1519, 2011.

[80] Hande E Cingil, Ingeborg M Storm, Yelda Yorulmaz, Diane W te Brake, Renko de Vries, Martien A Cohen Stuart, and Joris Sprakel. Monitoring protein capsid assembly with a conjugated polymer strain sensor. *Journal of the American Chemical Society*, 137(31):9800–9803, 2015.

[81] Helena Teles, Paulina J Skrzeszewska, Marc WT Werten, Jasper van der Gucht, Gerrit Eggink, and Frits A de Wolf. Influence of molecular size on gel-forming properties of telechelic collagen-inspired polymers. *Soft Matter*, 6(19):4681–4687, 2010.

[82] Diederik WR Balkenende, Souleymane Coulibaly, Sandor Balog, Yoan C Simon, Gina L Fiore, and Christoph Weder. Mechanochemistry with metallosupramolecular polymers. *Journal of the American Chemical Society*, 136(29):10493–10498, 2014.

[83] Juliette Slootman, Victoria Waltz, C Joshua Yeh, Christoph Baumann, Robert

Göstl, Jean Comtet, and Costantino Creton. Quantifying rate-and temperature-dependent molecular damage in elastomer fracture. *Physical Review X*, 10(4):041045, 2020.

[84] Taesoo D Lee and Abasifreke U Ebong. A review of thin film solar cell technologies and challenges. *Renewable and Sustainable Energy Reviews*, 70:1286–1297, 2017.

[85] Christelle Lopez and Olivia Ménard. Human milk fat globules: polar lipid composition and in situ structural investigations revealing the heterogeneous distribution of proteins and the lateral segregation of sphingomyelin in the biological membrane. *Colloids and Surfaces B: Biointerfaces*, 83(1):29–41, 2011.

[86] Reinforced concrete and importance of rebar. `https://basiccivilengineering.com/`. Accessed: 2021-11-15.

[87] Geology in. `http://www.geologyin.com/2015/12/what-are-earths-layers.html`. Accessed: 2021-01-19.

[88] Jaap M Evers, Richard G Haverkamp, Stephen E Holroyd, Geoffrey B Jameson, Duncan DS Mackenzie, and Owen J McCarthy. Heterogeneity of milk fat globule membrane structure and composition as observed using fluorescence microscopy techniques. *International Dairy Journal*, 18(12):1081–1089, 2008.

[89] Xiao Ma, Victoria Beltran, Georg Ramer, Georges Pavlidis, Dilworth Y Parkinson, Mathieu Thoury, Tyler Meldrum, Andrea Centrone, and Barbara H Berrie. Revealing the distribution of metal carboxylates in oil paint from the micro-to nanoscale. *Angewandte Chemie International Edition*, 58(34):11652–11656, 2019.

[90] Lukáš Fiala, Jan Toman, Jan Vodička, and Václav Ráček. Experimental study on electrical properties of steel-fibre reinforced concrete. *Procedia Engineering*, 151:241–248, 2016.

[91] Giorgio Carta, Michele Brun, and Antonio Baldi. Design of a porous material with isotropic negative poisson's ratio. *Mechanics of materials*, 97:67–75, 2016.

[92] Theodore Manouras and Panagiotis Argitis. High sensitivity resists for euv lithography: A review of material design strategies and performance results. *Nanomaterials*, 10(8):1593, 2020.

[93] Hang Yin, Yonghui Ding, Yao Zhai, Wei Tan, and Xiaobo Yin. Orthogonal programming of heterogeneous micro-mechano-environments and geometries in three-dimensional bio-stereolithography. *Nature communications*, 9(1):1–7, 2018.

[94] Jungwook Kim, James A Hanna, Myunghwan Byun, Christian D Santangelo, and Ryan C Hayward. Designing responsive buckled surfaces by halftone gel lithography. *Science*, 335(6073):1201–1205, 2012.

[95] Walter Kauzmann and Henry Eyring. The viscous flow of large molecules. *Journal of the American Chemical Society*, 62(11):3113–3125, 1940.

[96] Tuan Q Nguyen and Hans-Henning Kausch. *Flexible polymer chains in elongational flow: Theory and experiment*. Springer Science & Business Media, 2012.

[97] C Kirsch. Die theorie der elastizitat und die bedurfnisse der festigkeitslehre. *Zeitschrift des Vereines Deutscher Ingenieure*, 42:797–807, 1898.

[98] Charles Edward Inglis. Stresses in a plate due to the presence of cracks and sharp corners. *Trans Inst Naval Archit*, 55:219–241, 1913.

[99] Costantino Creton and Matteo Ciccotti. Fracture and adhesion of soft materials: a review. *Reports on Progress in Physics*, 79(4):046601, 2016.

[100] RS Rivlin and A Gr Thomas. Rupture of rubber. i. characteristic energy for tearing.

Journal of polymer science, 10(3):291–318, 1953.

[101] Michael May, Harichandana Channammagari, and Philipp Hahn. High-rate mode ii fracture toughness testing of polymer matrix composites–a review. *Composites Part A: Applied Science and Manufacturing*, 137:106019, 2020.

[102] HJ Kwon and P-YB Jar. Fracture toughness of polymers in shear mode. *Polymer*, 46(26):12480–12492, 2005.

[103] GR Irwin. Linear fracture mechanics, fracture transition, and fracture control. *Engineering fracture mechanics*, 1(2):241–257, 1968.

[104] James Gordon Williams. Fracture mechanics of polymers. *Ellis Horwood Limited, Market Cross House, Cooper St, Chichester, West Sussex, PO 19, 1 EB, UK, 1984. 302*, 1984.

[105] John D. Clayton. *Nonlinear Fracture Mechanics*, pages 1–7. Springer Berlin Heidelberg, Berlin, Heidelberg, 2018.

[106] G Liu and AN Gent. A triangular double cantilever beam test for measuring adhesive or cohesive fracture energy. *The Journal of Adhesion*, 38(1-2):79–88, 1992.

[107] Yingtian Yu, Bu Wang, Young Jea Lee, and Mathieu Bauchy. Fracture toughness of silicate glasses: insights from molecular dynamics simulations. *MRS Online Proceedings Library (OPL)*, 1757, 2015.

[108] EH Andrews. Rupture propagation in hysteresial materials: stress at a notch. *Journal of the Mechanics and Physics of Solids*, 11(4):231–242, 1963.

[109] GJ Lake and AG Thomas. The strength of highly elastic materials. *Proceedings of the Royal Society of London. Series A. Mathematical and Physical Sciences*, 300(1460):108–119, 1967.

[110] Yulan Chen, AJH Spiering, S Karthikeyan, Gerrit WM Peters, EW Meijer, and Rint P Sijbesma. Mechanically induced chemiluminescence from polymers incorporating a 1, 2-dioxetane unit in the main chain. *Nature chemistry*, 4(7):559, 2012.

[111] Jess M Clough, Jasper van der Gucht, Thomas E Kodger, and Joris Sprakel. Cephalopod-inspired high dynamic range mechano-imaging in polymeric materials. *Advanced Functional Materials*, 30(38):2002716, 2020.

[112] Jess M Clough, Jasper Van Der Gucht, and Rint P Sijbesma. Mechanoluminescent imaging of osmotic stress-induced damage in a glassy polymer network. *Macromolecules*, 50(5):2043–2053, 2017.

[113] Yulan Chen and Rint P Sijbesma. Dioxetanes as mechanoluminescent probes in thermoplastic elastomers. *Macromolecules*, 47(12):3797–3805, 2014.

[114] Henri Bouasse and Zéphyrin Carrière. Sur les courbes de traction du caoutchouc vulcanisé. In *Annales de la Faculté des sciences de Toulouse: Mathématiques*, volume 5, pages 257–283, 1903.

[115] Jess M Clough, Costantino Creton, Stephen L Craig, and Rint P Sijbesma. Covalent bond scission in the mullins effect of a filled elastomer: real-time visualization with mechanoluminescence. *Advanced Functional Materials*, 26(48):9063–9074, 2016.

[116] Gregory R Gossweiler, Tatiana B Kouznetsova, and Stephen L Craig. Force-rate characterization of two spiropyran-based molecular force probes. *Journal of the American Chemical Society*, 137(19):6148–6151, 2015.

[117] Douglas A Davis, Andrew Hamilton, Jinglei Yang, Lee D Cremar, Dara Van Gough, Stephanie L Potisek, Mitchell T Ong, Paul V Braun, Todd J Martínez,

Scott R White, et al. Force-induced activation of covalent bonds in mechanoresponsive polymeric materials. *Nature*, 459(7243):68–72, 2009.

[118] Asha-Dee N Celestine, Brett A Beiermann, Preston A May, Jeffrey S Moore, Nancy R Sottos, and Scott R White. Fracture-induced activation in mechanophore-linked, rubber toughened pmma. *Polymer*, 55(16):4164–4171, 2014.

[119] Greg O'Bryan, Bryan M Wong, and James R McElhanon. Stress sensing in polycaprolactone films via an embedded photochromic compound. *ACS applied materials & interfaces*, 2(6):1594–1600, 2010.

[120] Corissa K Lee, Douglas A Davis, Scott R White, Jeffrey S Moore, Nancy R Sottos, and Paul V Braun. Force-induced redistribution of a chemical equilibrium. *Journal of the American Chemical Society*, 132(45):16107–16111, 2010.

[121] Meredith H Barbee, Kunal Mondal, John Z Deng, Vivek Bharambe, Taylor V Neumann, Jacob J Adams, Nicholas Boechler, Michael D Dickey, and Stephen L Craig. Mechanochromic stretchable electronics. *ACS applied materials & interfaces*, 10(35):29918–29924, 2018.

[122] Jay Fineberg and Eran Bouchbinder. Recent developments in dynamic fracture: some perspectives. *International Journal of Fracture*, 196(1-2):33–57, 2015.

[123] Wolfgang G Knauss. A review of fracture in viscoelastic materials. *International Journal of Fracture*, 196(1-2):99–146, 2015.

[124] Tamar Goldman, Ariel Livne, and Jay Fineberg. Acquisition of inertia by a moving crack. *Physical Review Letters*, 104(11):114301, 2010.

[125] Angel Garcimartin, Alessio Guarino, Ludovic Bellon, and Sergio Ciliberto. Statistical properties of fracture precursors. *Physical Review Letters*, 79(17):3202, 1997.

[126] Osvanny Ramos, P-P Cortet, Sergio Ciliberto, and Loïc Vanel. Experimental study of the effect of disorder on subcritical crack growth dynamics. *Physical review letters*, 110(16):165506, 2013.

[127] Estelle Berthier, Jonathan E Kollmer, Silke E Henkes, Kuang Liu, Jennifer M Schwarz, and Karen E Daniels. Rigidity percolation control of the brittle-ductile transition in disordered networks. *Physical Review Materials*, 3(7):075602, 2019.

[128] Michelle M Driscoll, Bryan Gin-ge Chen, Thomas H Beuman, Stephan Ulrich, Sidney R Nagel, and Vincenzo Vitelli. The role of rigidity in controlling material failure. *Proceedings of the National Academy of Sciences*, 113(39):10813–10817, 2016.

[129] Maryam Hanifpour, Charlotte F Petersen, Mikko J Alava, and Stefano Zapperi. Mechanics of disordered auxetic metamaterials. *The European Physical Journal B*, 91(11):1–8, 2018.

[130] Justin Tauber, Aimée R Kok, Jasper Van Der Gucht, and Simone Dussi. The role of temperature in the rigidity-controlled fracture of elastic networks. *Soft Matter*, 16(43):9975–9985, 2020.

[131] Ashivni Shekhawat, Stefano Zapperi, and James P Sethna. From damage percolation to crack nucleation through finite size criticality. *Physical review letters*, 110(18):185505, 2013.

[132] Fany Di Lorenzo, Johannes Hellwig, Regine von Klitzing, and Sebastian Seiffert. Macroscopic and microscopic elasticity of heterogeneous polymer gels. *Acs Macro Letters*, 4(7):698–703, 2015.

PART I:

Mechanical characterization of mechanically heterogeneous polymer networks

Part I of this will be about mechanical characterization of mechanical heterogeneous materials. First, chapter 2 will introduce the technique developed and used in this research to mechanically characterize mechanical heterogeneous materials. Subsequently, chapter 3 shows that there is more to this fairly simple technique, as the mechanical response of a mechanically heterogeneous material is heterogeneous as well, leading to blurring of the obtained mechanical information. Finally, chapter 4 will exemplify this technique applied in the emerging field of plant-based synthetic meat analogues.

Chapter 2

Mechanical mapping of heterogeneously crosslinked polymer networks

We present the development of a multi-position indentation setup capable of spatially mapping mechanically heterogeneous materials. A detailed description of the indentation instrumentation is first provided, emphasizing force sensitivity, noise reduction and signal fidelity. Afterwards, we present indentation experiments on soft hydrogels that are submerged in water, and show how the large contributions to the measured force due to the air-water surface tension can be avoided. The displacement field of the indented hydrogel is visualized using fluorescently coated microspheres embedded in the hydrogel, allowing simultaneous mapping of the stress and strain fields for a soft polymer network. We then fabricate a polymer network with patterned elasticity using half-tone UV lithography and map the elastic modulus with the multi-position indentation instrument. The applied UV pattern is found back in the measured elastic modulus map, showing the capability of the multi-position indentation setup to map mechanically heterogeneous polymer networks.

This chapter is published as:

J.N.M. Boots, R. Fokkink, J. Van der Gucht and T.E. Kodger
“Development of a multi-position indentation setup: mapping soft and patternable heterogeneously crosslinked polymer networks”
Review of Scientific Instruments , 90 (1) , 015108 (2019)

2.1 Introduction

Polymeric materials have become indispensable to everyday life, due to their widespread applications. The properties of polymer materials are determined by their molecular structure and connectivity. Contrary to crystalline materials, polymers have an intrinsically disordered structure, which is characterized by heterogeneities that are frozen in during preparation of the materials. The amplitude and typical length scale of these heterogeneities can be particularly large for hydrogels, i.e. polymer networks swollen in water, where coupling between the crosslinking reaction and the local monomer density can lead to large spatial variations in crosslink density, especially when the gel is close to the critical gel point[1, 2, 3, 4, 5]. Biological hydrogel systems such as collagen and fibrin biopolymer networks also contain mechanical heterogeneities on larger length scales due to local variations in polymer density[6,7]. These heterogeneities have a large effect on the mechanical response of the materials, as they lead to non-affine deformations[8] and stress localization in regions where cracks may eventually nucleate[9,10]. More recently, several groups have tried to exploit heterogeneity to design materials with a desired mechanical response[11, 12, 13, 14, 15].

It is clear from these examples that there is a need for characterization methods that can probe the properties of the material locally. Examples of conventional methods to probe the mechanical properties of polymer materials include rheology or Dynamic Mechanical Analysis (DMA), which measure average properties of a specimen[16,17], and Atomic Force Microscopy (AFM), which effectively probes the surface of a specimen and not the bulk and practically cannot probe regions that are larger than a hundred square micrometers[6,18,19]. A technique that can be used to measure mechanical heterogeneities on larger length scales (μm-cm) is indentation, in which a spherical probe is pushed against the sample and the resulting normal force is measured[20,21]. By performing indentations at multiple positions, a spatially resolved elasticity map can be obtained. However, to fully characterize the mechanics in a heterogeneous soft material, information on the distribution of stresses within the material is crucial. This requires measurement of the strain field in the material under indentation, and calls for the incorporation of imaging possibilities.

To realize this, we present a spatially high-precision and mechanically sensitive multi-position indentation set-up, which, due to its flexible design, can be easily integrated with imaging capabilities. We show how this combination can be used to independently determine the local Young's modulus and Poisson ratio of the material. In addition, we describe how the method can be used to characterize materials submerged in a fluid, where the effects of buoyancy and capillary forces need to be accounted for.

The structure of this article is as follows: first, we discuss the principles of the indentation experiment and a detailed description of the instrument; second, we show data on the indentation of submerged hydrogels; third, we show the combination of indentation with fluorescence microscopy to measure the displacement field in hydrogels using fluorescently labeled microspheres; and lastly, we show mechanical mapping of a micro-patterned polydimethylsiloxane (PDMS) network that directly demonstrates the benefit of the built multi-position indentation instrument.

2.2 Contact Mechanics

A mechanical test that is suited to probe mechanical properties of a material locally is indentation. In an indentation experiment, a probe connected to a load cell is lowered onto a sample, and the resulting normal force is measured as shown in figure 2.1. The load cell measures a local mechanical response of the material over an area that is determined by the size of the indenting sphere. Hertzian contact theory relates the indentation force between a rigid sphere and a semi-infinite elastic substrate to the mechanical properties of that substrate:

$$F = \frac{4}{3} R^{1/2} \delta^{3/2} \frac{E}{1-\nu^2} \tag{2.1}$$

where F is the measured (normal) force, δ the indentation depth, R the radius of the probe, E the elastic modulus, and ν Poisson's ratio of the elastic body. Here we use a stainless steel probe with an elastic modulus that is orders of magnitude larger than that of the measured polymer samples. The work presented in this article is performed solely with spherical probes, avoiding the mandatory alignment of the probe with the surface of the substrate that is necessary for other configurations such as conical, cylindrical and flat probes[21]. Note that in the presence of adhesive (van der Waals) forces between the probe and the sample one should consider the adhesive contact theory developed by Johnson, Kendall and Roberts, commonly known as JKR theory[22]. Additionally, corrections for finite sample-thickness may be necessary. As shown elsewhere[23], these corrections depend on the ratio $\sqrt{R\delta}/h$ with h the thickness of the sample. Here, we have ensured that in all measurements $\sqrt{R\delta}/h < 0.1$, for which these corrections are negligibly small.

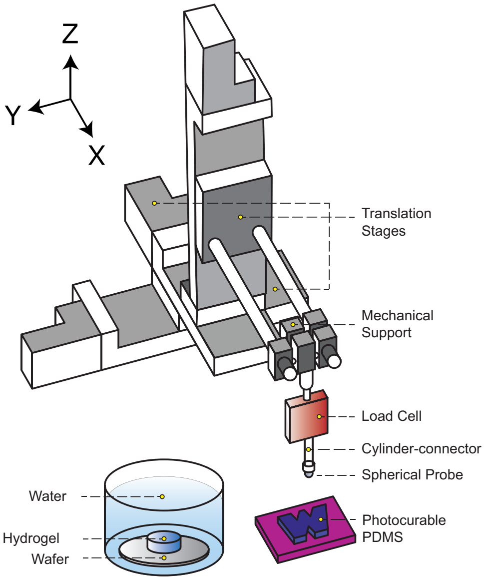

Figure 2.1 – 3D schematic representation of the experimental instrument. Three translation stages are mounted on top of one another to enable movement of the load cell (red) and the attached probe in three dimensions. Mechanical support is achieved with right-angle clamps (Thorlabs RA90/M), which ensures an orthogonal angle with the sample surface by eliminating rotational degrees of freedom. Two samples are tested; photo-patterned PDMS and hydrogels submersed in water, placed on a silicon wafer that was glued to the bottom of a beaker.

2.3 The multi-position spherical indentation instrument

Indenting a 2D polymeric substrate at multiple positions requires a force sensor that can be moved not only in the vertical ($\hat{z}$) direction, but also in the lateral ($\hat{x}$-$\hat{y}$) directions. To achieve this, three translation stages (M-403.6DG, Physical Instruments), with a minimal incremental movement of 0.2 μm and a total travel range of 15 cm, are used to move the load cell in three directions, as shown in figure 2.1. Each translation stage is controlled by communicating to a control box (C-663.12 Mercury Step Stepper Motor Controller, 1 Axis) with Matlab[24]. The movement of the translation stages and readout of the load cell are performed step-wise.

We use FUTEK load sensors (FSH02667, 20 gram limit, non-submersible or QSH00618, 100 gram limit, submersible) that are connected to an analog amplifier (SG-3016, ICP DAS) which communicates with the computer via a digital acquisition device (USB-6001, National Instruments), see figure 2.2a. An RC-filter is used to filter out high frequency electrical noise, as shown in figure 2.2b. The load cell is sampled every millisecond and an average is taken over a thousand samplings. The filtered voltage signal is then converted to the measured force, after calibration with standard weights.

2.4 Indentation of submerged hydrogels

We first test our set-up by measuring the elasticity of soft hydrogels. Hydrogels contain large amounts, up to 99.9 mass %, of water[25], resulting in low elastic moduli, especially when the crosslink density is close to the critical gel point.

To measure these low elastic moduli, a sensitive load cell is required. However, indentation of a hydrogel in air leads to a contribution in the measured force from the air-water surface tension, γ_{LG}, which is approximately 70 mN/m. Since hydrogels contain mostly water by mass, their surface tension is similar to this[26], which means that for soft hydrogels the capillary force will dominate the elastic restoring force. Therefore, the

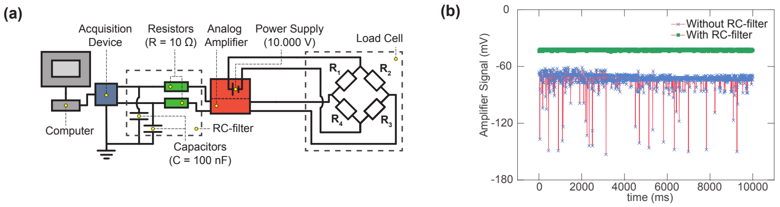

Figure 2.2 – **(a)** A schematic of the electrical circuit. The load cell is powered by a stable voltage of 10.000 V supplied by the analog amplifier. Thermo-sensitive strain gauges in the Wheatstone bridge are placed oppositely perpendicular and parallel of the tension and compression axes of the load cell, where the latter will respond to an applied load. The stable input voltage is compared to the change in voltage due to compression of the two parallel oriented resistors. A Voltage output is returned to the amplifier and passed onto the differential input of a data acquisition device (f_{max} = 10 kHz) through a RC-filter to filter out high frequency noise (R = 10Ω and C = 100 nF, f_c = 159 kHz). **(b)** The voltage measured with and without the RC-filter; the former is offset +30 mV for visualization purposes.

hydrogels must be submerged in water while measuring the normal force. Unfortunately, the most sensitive commercially available load cells cannot be submersed into a solvent. To obtain maximal force resolution, we first perform indentation experiments on soft hydrogels submersed in water with a highly sensitive commercially available non-submersible load cell. This means that the cylindrical connector between the load cell and the probe (see figure 2.1) traverses the air/water interface, which results in a capillary contribution to the measured force due to the meniscus of the air-water interface at the surface of the cylindrical connector. Moreover, it means that the buoyancy force changes when the height of the part of the cylinder that is submerged in water changes.

Upon indenting a submerged hydrogel sample, a force-distance curve is obtained as shown in figure 2.3. The raw data is obtained with the more sensitive 20g-limit non-submersible load cell and requires corrections for the capillary force and for the buoyancy force.

For a perfectly smooth surface characterized by an equilibrium contact angle θ, the capillary force F_c adds a constant contribution to the measured force, given by

$$F_c = \gamma_{LG}\ell\cos\theta \tag{2.2}$$

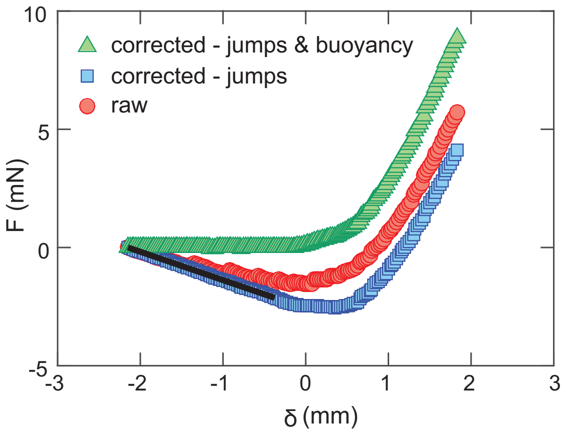

Figure 2.3 – Indentation of a 10 w/v % poly(acrylamide) gel, crosslinked with 1.0 w/w % N,N'-methylenebisacrylamide, measured with a non-submersible load cell and with a probe of radius $R = 2$ mm. Shown is a single force versus distance curve, i.e. no repeats, for: raw data (red circles); data corrected for jumps in the force (blue squares); data corrected for buoyancy, where the black line indicates a fit of the data before contact used for the correction (green triangles).

where ℓ is the circumference of the cylindrical connector. In practice, however, roughness or chemical heterogeneity of the surface leads to contact angle hysteresis and contact line pinning[27]. This is evident from figure 2.4a and c, where the position of the air-water interface and the contact angle at the cylinder surface are shown as a function of time during a single indentation cycle. Clearly the contact angle is not constant during indentation, so that also the capillary force varies in time (figure 2.4e). The intermittent movement of the contact line due to repeated pinning and unpinning at the cylinder surface then leads to jumps in the measured force curve. Indeed, the jumps observed in the raw force curves shown in figure 2.3) have the same magnitude as those observed in figure 2.4e.

One solution to reduce the magnitude of the jumps in the measured normal force is to eliminate surface irregularities that cause the changes in contact angle. We have attempted to do this by coating the cylinder-connector with a complex coacervate through a sequential layer by layer application of poly(diallyldimethylammonium chloride) and

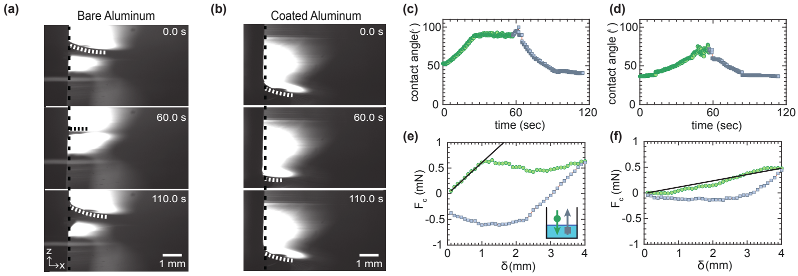

Figure 2.4 – ($\hat{x}$,$\hat{z}$)-Snapshots of the air-liquid interface and the surface of the cylinder-connector for **(a)** bare aluminum and **(b)** aluminum coated with complex coacervates (phase contrast images). In between snapshots, the cylinder-connector was moved 4 mm down and up again at a velocity of 1 mm/s, with 80 force-samplings each of 1 second and ~0.5 second processing time for a total of 120 seconds. Snapshots are taken under a small $\sim 20^\circ$ angle. The dotted white/black lines indicate the pinning of the air/water interface at the cylinder-connector. The contact angles in **(c)** and **(d)** are obtained by selecting an intensity threshold for each frame at the indicated vertical lines. The force-distance curves in **(e)** and **(f)** show the capillary force measured by the non-submerged load cell in the absence of a hydrogel, after correcting for buoyancy according to equation (2.3).

poly(styrenesulfonate) in a 1M NaCl solution, increasing the hydrophilicity. As shown in figure 2.4b, d, this indeed reduces the contact angle hysteresis and the resulting variations in the capillary force (figure 2.4f).

However, even with this coating contact angle hysteresis is still present, so that the jumps in the force curve cannot be eliminated completely. This means that we must correct for the jumps in the force by shifting the measured normal force accordingly after each jump, which is done here by taking the value of the point prior to the jump and adding the difference between the two preceding points: $F_n = F_{n-1} + (F_{n-1} - F_{n-2})$, where n is the index of the data point that must be corrected.

The second correction that we must apply to the data in figure 2.3 is for the buoyancy force, which arises when an object moves through a fluid thereby displacing the fluid. This force, F_b, is dependent on the height of the cylindrical connector in the fluid with respect to the fluid's surface[28]:

$$F_b = -\rho_F g A \Delta h \qquad (2.3)$$

in which ρ_F is the density of the fluid, g is the gravitational acceleration, A is the cross-sectional area of the cylinder and Δh is the total height of the part of the cylinder that is submersed in the fluid. The latter increases linearly as the probe is moved down, leading to a linear relation between the buoyancy force and the indentation depth δ. We can thus correct for the buoyancy force simply by extrapolating the initial part of the force curve where the probe is only moving through the liquid and not yet in contact with the hydrogel (black line in figure 2.3).

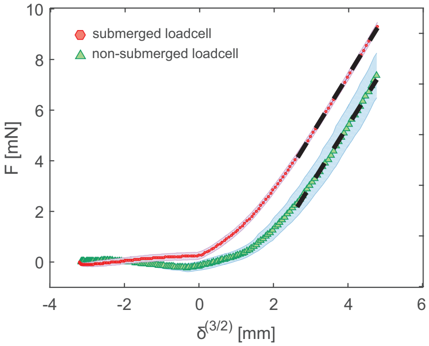

Figure 2.5 – Indentation of a 10 w/v % Poly(acrylamide) network cross-linked with 1.0 w/w % N,N'-Methylenebisacrylamide, measured with a non-submersible and submersible load cell and a probe of radius $R = 2$ mm. Both measurements are repeated 5 times at a single position on the network, where the first cycle corresponds to the data shown in figure 2.3. The mean of these 5 repeats are plotted along with the corresponding standard deviation, shown with shaded error bars. The dotted black lines indicate linear fits, according to Hertzian contact theory, using slopes $a_{submerged} =$ 75.58 N/m$^{(3/2)}$ and $a_{non-submerged} =$ 74.58 N/m$^{(3/2)}$, from which the moduli E can be obtained using equation (2.1), giving $E_{submerged} = 951$ Pa and $E_{non-submerged} = 938$ Pa assuming $\nu = 0.5$.

The simplest approach to avoid the dynamic contact angle and buoyancy corrections is to utilize a submersible load cell. Raw data for a 100g-limit submersible load cell is shown in figure 2.5 with neither of the above corrections for buoyancy and contact angle hysteresis, plotted together with the corrected data from figure 2.3. We find excellent agreement for the moduli; the obtained elastic moduli $E_{submerged} = 951$ Pa and $E_{non-submerged} = 938$ Pa assuming $\nu = 0.5$, measured in the swollen state, are in good agreement with values reported elsewhere[29]. Note that the shaded error bars, representing the standard deviation from

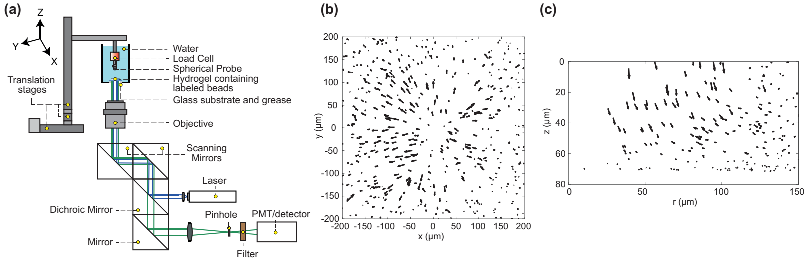

Figure 2.6 – **(a)** Schematic representation of the multi-position indentation setup combined with a Nikon C2 confocal microscope used to measure the 3D displacement field in a hydrogel. Laser light is directed to the sample using a dichroic mirror and scanning mirrors. The objective has a 20x magnification with a limited working distance of 1 mm. The emitted light is red shifted by the fluorescent microspheres and passes the dichroic mirror and a long pass emission filter. **(b)** The (x̂-ŷ) projected 3D displacement field of fluorescently labelled microspheres with a diameter of 1.3 μm in a hydrogel, which move due to an applied indentation with a stainless steel sphere of 500 μm in diameter; radial symmetry indicates the indentation location. The arrows show the displacement over which a bead is tracked. **(c)** The (r̂-ẑ) projected 3D displacement of the same data as in (b).

5 repeated measurements on a single position on the network, are small for data obtained with the submerged load cell while the error bars are substantially larger for the data taken with the non-submersible load cell. Hence, even for this soft polymer network, the non-submersible load cell is more than sufficiently sensitive to accurately determine the modulus of the material.

2.5 Multi-position indentation and fluorescence microscopy

While the measured indentation force gives a very good estimate of the local mechanical properties of the material, much more detailed information can be obtained by simultaneously measuring the displacement field within the sample. In particular for heterogeneous samples, which are characterized by large non-affine strains and strongly localized displacements, information on the strain field is crucial for a correct interpretation of the indentation data. Therefore, we combine our indentation setup with displacement imaging. As we will show below, the displacement maps obtained in this way can also be used to independently measure the Poisson ratio of the sample.

A common methodology to measure local displacements is by means of embedding a very low volume fraction of fluorescent tracer particles within the material. This approach requires combining fluorescence microscopy and mechanical deformation; indentation readily allows for this modification as both translation and force read-out are present on the topside of the instrument, leaving the entire region below the sample available for modification. Since the displacement field in an indentation experiment will vary both in the $\hat{x}$, $\hat{y}$, and $\hat{z}$-directions, obtaining displacement information in all three dimensions is desirable over obtaining only two dimensional information[30]. Therefore, the indentation setup is mounted on a confocal microscope, as shown in figure 2.6a.

To measure the 3D displacement field in a hydrogel, a polyacrylamide hydrogel similar in composition to the one shown in figure 2.5, but containing a low density of fluorescent polystyrene tracer particles is indented with a spherical probe. The fluorescent beads are displaced due to the indentation with the spherical probe; this motion is analyzed using a locating and tracking algorithm for Matlab[31]. The resulting displacement field is radially symmetric (figure 2.6b) and expands as the indentation depth δ increases. Making use of this radial symmetry, we plot the 3D displacement of the beads in the ($\hat{r}$-$\hat{z}$) plane in figure 2.6c. Clearly, there is not only a displacement component in the $\hat{z}$-direction, but deeper in the sample there is also a component in the $\hat{r}$ direction, which points outward. By comparing the measured displacement field with numerically calculated displacement fields for different values of ν, we can estimate the Poisson ratio of the polyacrylamide hydrogel. In particular, the absence of an inward displacement component indicates that the Poisson ratio of the hydrogel is close to 0.5, which is in good agreement with known values for hydrogels[32]. Indeed, we find a very good agreement between the experimental and theoretical displacement maps for $\nu \approx 0.5$ (see Appendix 2, specifically figure 2.A.2). We thus conclude that the combination of force measurements and displacement mapping allows for an independent measurement of the Young's modulus and Poisson ratio.

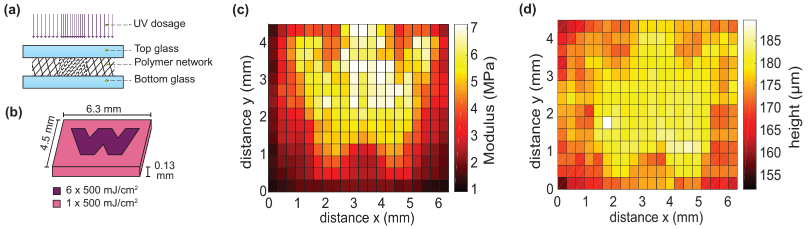

Figure 2.7 – **(a)** Spatially programmed sample preparation; the PDMS, mixed with the photo-initiator, is sandwiched between two glass slides and exposed to different dosages of UV light. This creates a proportional amount of free radicals and thereby a crosslink-gradient across the material, visualized with hatching density. **(b)** The spatial exposure of UV light dosage. **(c)** The multi-position indentation instrument is used to obtain a mechanical map of the material. The used probe has a radius R of 0.5 mm. A force-threshold of 25 mN is used to set the indentation depth δ of the probe into the material. **(d)** The height of the PDMS sample is measured by the multi-position indentation instrument.

2.6 Multi-position indentation of a heterogeneous network

The true power of the multi-position indentation instrument is exemplified by obtaining a mechanical 2D-map of a tunable mechanically heterogeneous polymer network at the millimeter scale. A test material is fabricated composed of a commercially available (methacryloxypropyl)methylsiloxane - dimethylsiloxane copolymer (later on referred to as PDMS) purchased from Gelest in combination with 0.01 w/v % of a free radical photo-initiator (2,2-dimethyl-2-phenylacetophenone), resulting in a photopatternable polymer network[33]. The material is half-tone printed by exposing to a spatially varying intensity of UV light resulting in a spatially varying modulus[13]. To obtain a flat sample, the photopatternable PDMS is sandwiched between two glass slides separated by a 127 µm thick mylar spacer, see figure 2.7a. The glass slides are coated with sacrifical dextran layer, obtained by spincoating a 5 w/v % solution of 450-640 kDa dextran in water at 2000 rpm for 12 seconds. The sacrificial layer is used to detach the polymer film from the glass substrate after UV exposure, a process that takes about 10 days soaking the sample in water and shaking on a lab shaker. Samples are exposed to UV light in a programmed pattern[34], see figure 2.7b; the intensity of UV dosage defines the crosslinking density and therefore the local modulus of the PDMS. Unexposed PDMS is rinsed away with propylene glycol monomethyl ether acetate (PGMEA). An important note, the spatial resolution of UV exposure (2 µm) is above the polymer mesh size ζ, which is estimated from the magnitude of the PDMS modulus to be on the order of 1-10 nm[35], using $\zeta \approx \left(\frac{E}{3k_BT}\right)^{-1/3} \approx$ 1-10 nm. As a result, this resolution is insufficient to control crosslinking at the single polymer length scale. However, naturally heterogeneous materials, such as collagen bundles or physiological tissue, are typically heterogeneous on the same length scale or larger, $1 - 7\mu m$ for collagen[36], than the spatial resolution of patternable PDMS[6,7].

The multi-position indentation method is indeed able to map the mechanical landscape of the PDMS, corresponding to the applied dosage pattern, showing the photo-patternability of the PDMS in combination with the photo-initiator as shown in figure 2.7c. The local modulus is obtained from equation (2.1) with an assumed Poisson's ratio, $\nu = 0.5$. The height of the PDMS sample is also determined by taking the difference between a zero gap measurement taken next to the material, which determines the distance between the probe and the substrate, and the position where the probe contacts the PDMS sample; this height or thickness weakly depends on the UV light dosage to which the sample is exposed as shown in figure 2.7d.

The sharpness of the measured elasticity pattern is limited by factors originating both from the method of sample synthesis and from the indentation methodology. First, photo-initiators illuminated with UV light degrade, yielding free radicals, which crosslink the pendant methacrylate groups of the PDMS polymers. Diffusion of these free radicals will result in blurring of the features; this effect is limited by the relatively high viscosity of the PDMS. Second, broadening of UV light during exposure by both the top glass and the PDMS layer will blur the exposed features; this is reduced by producing samples that are relatively thin with respect to the exposed area, see figure 2.7b. Third, the measured pattern is blurred by the finite size of the probe. The contact radius a of the probe on the substrate depends on the probe size and the indentation depth as $a \approx \sqrt{R\delta} \approx 100$

µm, and the indenter probes the mechanical properties within a region of approximately (twice) this size[21]. A smaller probe size and indentation depth will thus lead to a better spatial resolution. However, this also reduces the measured normal force which will decrease the sensitivity of the measurement, especially for very soft samples.

2.7 Conclusion and Outlook

In this work we have shown that multi-position indentation is a powerful technique to spatially map the elastic modulus of mechanically heterogeneous materials over length scales larger than conventional AFM. In addition, we have shown that the indentation instrument can (i) be used in combination with experiments using fluorescent imaging, a promising combination for future experiments to for example accurately determine Poisson's ratio, and (ii) map samples that are submerged in a solvent. Future challenges to improve the mapping of the elastic modulus involve mechanical deconvolution of the stress field in heterogeneous materials, an area we intend to explore further using finite element simulations. In addition, the sharpness of the patterned heterogeneity can be improved by incorporating a chain-transfer agent that quenches the free radical, preventing crosslinking of the material in unexposed regions. This ability to spatially program the modulus of a polymeric material and map the resulting modulus will allow for a systematic investigation into the role of mechanical heterogeneity on the mechanical performance of materials, such as their toughness and resistance to fracture nucleation.

2.8 Appendix Chapter 2

Combining multi-position indentation with fluorescence microscopy

This Appendix provides additional information on the analysis of the experiment presented in figure 6 of the main text, where multi-position indentation is combined with confocal fluorescence imaging to obtain a three dimensional deformation field in a hydrogel. The hydrogel is a 10 w/v % Poly(acrylamide) network crosslinked with 1.0 w/w % N,N'-

Methylenebisacrylamide, in which fluorescently labelled microspheres with a diameter of 1.3 µm are embedded, and a deformation is applied with a spherical probe with radius R = 500 µm which is connected to a submersible load cell that measures the normal force.

Finite element calculations

We compare the experimental displacement field with numerical calculations for an ideal elastic solid, using axisymmetric finite elements. The material is parameterized by the Young's modulus E and the Poisson ratio v, but the displacement field $\mathbf{u}(r, z)$ for a given indentation depth δ depends only on the Poisson ratio, and not on the Young's modulus. We use second-order (6-node) triangular elements to interpolate the displacement field, using a finite element mesh, such as the one shown in figure 2.A.1. The sample and the probe have the same dimensions as in the experiments, and no-slip conditions are imposed at the lower surface. The indentation is modeled by imposing a fixed displacement at the nodes at the top surface that are within the contact radius, $r < a$, corresponding to the shape of the spherical probe. The equilibrium displacement at the nodes $\mathbf{u}(r, z)$ is then obtained by solving the finite element equations, using a non-linear updated Lagrangian iteration scheme[37]. We then plot the displacement field at fixed query points on a regular grid.

We perform calculations for different values of the Poisson ratio v. Figure 2.A.2 shows a comparison between the experimental displacement field and the displacement field calculated for $v = 0.49$. The experimental and theoretical profiles show very similar features, with a displacement that points mostly downward near the spherical probe, while it has a significant radial component in the outward direction farther away from the probe.

Displacement profiles for different Poisson ratios are shown in figure 2.A.3. While for $v = 0.49$, the radial component u_r always points outward, away from the axis of the indenter, it has an inward component near the top surface for smaller v. This is in agreement with Hertz' theory for a semi-infinite elastic material (infinite thickness), which predicts a radial displacement field at the top surface equal to[38]

$$u_r(r, z = 0) = \left\{ \begin{array}{ll} -\frac{2(1-2\nu)}{3\pi(1-v)} \frac{a}{r} \left[1 - \left(1 - r^2/a^2\right)^{3/2}\right] & (r \leq a) \\ -\frac{2(1-2\nu)}{3\pi(1-v)} \frac{a}{r} \quad (r > a) & \end{array} \right.$$

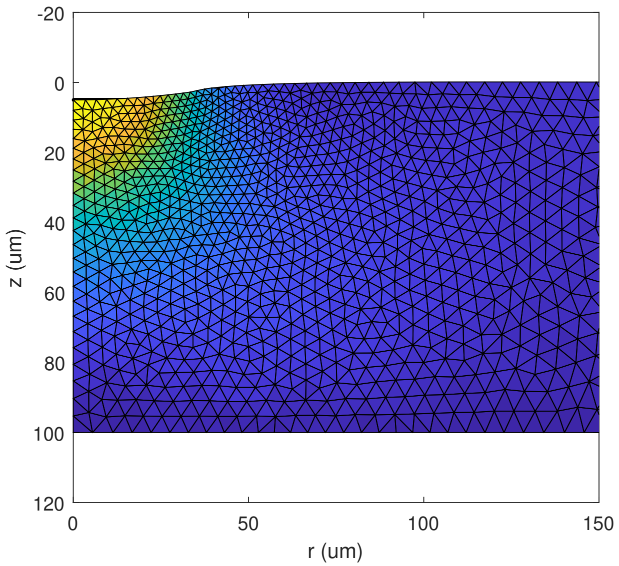

Figure 2.A.1 – The finite element mesh used in the calculations; note that the mesh extends to $r = 500$ μm to avoid boundary effects at the outer edge. Axisymmetric finite elements are used with the symmetry axis at $r = 0$; a fixed displacement is imposed at the top, corresponding to the shape of the spherical probe. No-slip boundary conditions are used at the lower surface. The color scale indicates the magnitude of the displacement $u(r, z)$.

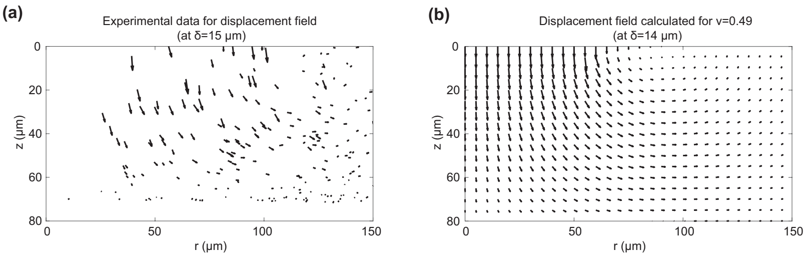

Figure 2.A.2 – A comparison between data obtained from **(a)** experiments and **(b)** finite element simulations (both for $\delta = 15$ μm).

where a is the contact radius, equal to $\sqrt{R\delta}$. For $v = 0.5$ the radial displacement at the top surface ($z = 0$) vanishes, while for $v < 0.5$ it is negative, indicating an inward displacement. In the experimental displacement field, we find no negative radial displacement, indicating that the Poisson ratio in the experiment is close to 0.5.

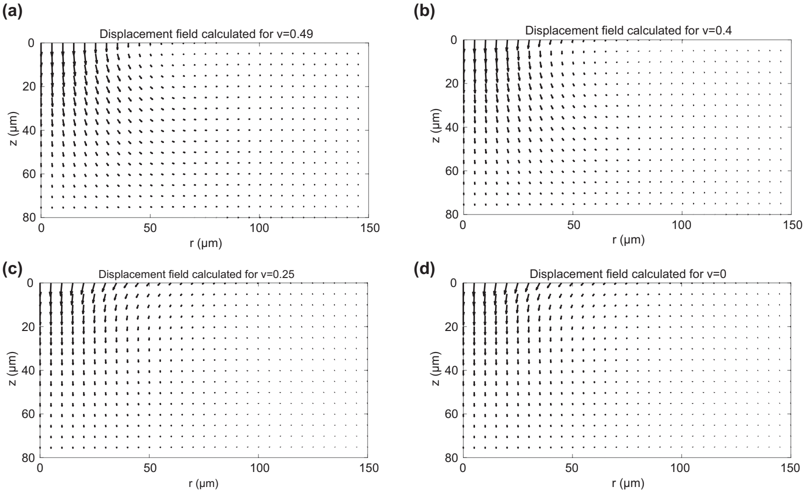

Figure 2.A.3 – Displacement profiles for different values of the Poisson ratio ν for an indentation depth $\delta = 5$ μm. For $\nu = 0.49$, the radial component of $\mathbf{u}$ points outwards, while for smaller ν the bit points inward at the top surface. In the experimental data in SI figure 2.A.2a only outward movement of the beads is observed.

Bibliography

[1] Muhammad Sahimi. Non-linear and non-local transport processes in heterogeneous media: from long-range correlated percolation to fracture and materials breakdown. *Physics Reports*, 306(4-6):213–395, 1998.

[2] Ilknur Yazici and Oguz Okay. Spatial inhomogeneity in poly (acrylic acid) hydrogels. *Polymer*, 46(8):2595–2602, 2005.

[3] SL Vega, MY Kwon, and JA Burdick. Recent advances in hydrogels for cartilage tissue engineering. *European cells & materials*, 33:59–75, 2017.

[4] F Di Lorenzo and S Seiffert. Nanostructural heterogeneity in polymer networks and gels. *Polymer Chemistry*, 6(31):5515–5528, 2015.

[5] Hayfa Souguir and Tristan Baumberger. Inhomogeneity development during slow,

irreversible cross-linking of gelatin. In *Macromolecular Symposia*, volume 329, pages 41–48. Wiley Online Library, 2013.

[6] Eric M Darling, Rebecca E Wilusz, Michael P Bolognesi, Stefan Zauscher, and Farshid Guilak. Spatial mapping of the biomechanical properties of the pericellular matrix of articular cartilage measured in situ via atomic force microscopy. *Biophysical journal*, 98(12):2848–2856, 2010.

[7] Fouad Khatyr, Claude Imberdis, Paul Vescovo, Daniel Varchon, and Jean-Michel Lagarde. Model of the viscoelastic behaviour of skin in vivo and study of anisotropy. *Skin research and technology*, 10(2):96–103, 2004.

[8] Mo Bai, Andrew R Missel, William S Klug, and Alex J Levine. The mechanics and affine–nonaffine transition in polydisperse semiflexible networks. *Soft Matter*, 7(3):907–914, 2011.

[9] Yuval Mulla, Giorgio Oliveri, Johannes TB Overvelde, and Gijsje H Koenderink. Crack initiation in viscoelastic materials. *Physical review letters*, 120(26):268002, 2018.

[10] Ashivni Shekhawat, Stefano Zapperi, and James P Sethna. From damage percolation to crack nucleation through finite size criticality. *Physical review letters*, 110(18):185505, 2013.

[11] Johannes TB Overvelde, James C Weaver, Chuck Hoberman, and Katia Bertoldi. Rational design of reconfigurable prismatic architected materials. *Nature*, 541(7637):347, 2017.

[12] N Gaspar, CW Smith, and KE Evans. Auxetic behaviour and anisotropic heterogeneity. *Acta Materialia*, 57(3):875–880, 2009.

[13] Jungwook Kim, James A Hanna, Myunghwan Byun, Christian D Santangelo, and Ryan C Hayward. Designing responsive buckled surfaces by halftone gel lithography. *Science*, 335(6073):1201–1205, 2012.

[14] David H Gracias. Stimuli responsive self-folding using thin polymer films. *Current Opinion in Chemical Engineering*, 2(1):112–119, 2013.

[15] Mustapha Jamal, Aasiyeh M Zarafshar, and David H Gracias. Differentially photocrosslinked polymers enable self-assembling microfluidics. *Nature communications*, 2:527, 2011.

[16] Li-Heng Cai, Thomas E Kodger, Rodrigo E Guerra, Adrian F Pegoraro, Michael Rubinstein, and David A Weitz. Soft poly (dimethylsiloxane) elastomers from architecture-driven entanglement free design. *Advanced Materials*, 27(35):5132–5140, 2015.

[17] Gowthaman Swaminathan and Kunigal Shivakumar. A re-examination of dma testing of polymer matrix composites. *Journal of Reinforced Plastics and Composites*, 28(8):979–994, 2009.

[18] Maxim E Dokukin and Igor Sokolov. Quantitative mapping of the elastic modulus of soft materials with harmonix and peakforce qnm afm modes. *Langmuir*, 28(46):16060–16071, 2012.

[19] John Ralston, Ian Larson, Mark W Rutland, Adam A Feiler, and Mieke Kleijn. Atomic force microscopy and direct surface force measurements (iupac technical report). *Pure and applied chemistry*, 77(12):2149–2170, 2005.

[20] Erik Rettler, Stephanie Hoeppener, Bernd W Sigusch, and Ulrich S Schubert. Mapping the mechanical properties of biomaterials on different length scales: depth-

sensing indentation and afm based nanoindentation. *Journal of Materials Chemistry B*, 1(22):2789–2806, 2013.

[21] Yuhang Hu, Xuanhe Zhao, Joost J Vlassak, and Zhigang Suo. Using indentation to characterize the poroelasticity of gels. *Applied Physics Letters*, 96(12):121904, 2010.

[22] Valentin L Popov. *Contact mechanics and friction*. Springer, 2010.

[23] Edwin P Chan, Yuhang Hu, Peter M Johnson, Zhigang Suo, and Christopher M Stafford. Spherical indentation testing of poroelastic relaxations in thin hydrogel layers. *Soft Matter*, 8(5):1492–1498, 2012.

[24] MATLAB. *version R2016b*. The MathWorks Inc., Natick, Massachusetts, 2016.

[25] Allan S Hoffman. Hydrogels for biomedical applications. *Advanced drug delivery reviews*, 64:18–23, 2012.

[26] Aditi Chakrabarti and Manoj K Chaudhury. Direct measurement of the surface tension of a soft elastic hydrogel: exploration of elastocapillary instability in adhesion. *Langmuir*, 29(23):6926–6935, 2013.

[27] Bo He, Junghoon Lee, and Neelesh A Patankar. Contact angle hysteresis on rough hydrophobic surfaces. *Colloids and Surfaces A: Physicochemical and Engineering Aspects*, 248(1-3):101–104, 2004.

[28] Douglas C Giancoli. *Physics for scientists and engineers*. Pearson Education International, 2008.

[29] Aleksandra K Denisin and Beth L Pruitt. Tuning the range of polyacrylamide gel stiffness for mechanobiology applications. *ACS applied materials & interfaces*, 8(34):21893–21902, 2016.

[30] Martijn AJ Cox, Niels JB Driessen, Ralf A Boerboom, Carlijn VC Bouten, and Frank PT Baaijens. Mechanical characterization of anisotropic planar biological soft tissues using finite indentation: experimental feasibility. *Journal of biomechanics*, 41(2):422–429, 2008.

[31] Yongxiang Gao and Maria L Kilfoil. Accurate detection and complete tracking of large populations of features in three dimensions. *Optics express*, 17(6):4685–4704, 2009.

[32] E Geissler and AM Hecht. The poisson ratio in polymer gels. 2. *Macromolecules*, 14(1):185–188, 1981.

[33] Kyung M Choi and John A Rogers. A photocurable poly (dimethylsiloxane) chemistry designed for soft lithographic molding and printing in the nanometer regime. *Journal of the American Chemical Society*, 125(14):4060–4061, 2003.

[34] *Durham Magneto Optics Ltd.* MicroWriter ML3 Baby, Durham DH1 3HP, UK.

[35] Fany Di Lorenzo, Johannes Hellwig, Regine von Klitzing, and Sebastian Seiffert. Macroscopic and microscopic elasticity of heterogeneous polymer gels. *Acs Macro Letters*, 4(7):698–703, 2015.

[36] Izabela K Piechocka, Anne SG van Oosten, Roel GM Breuls, and Gijsje H Koenderink. Rheology of heterotypic collagen networks. *Biomacromolecules*, 12(7):2797–2805, 2011.

[37] Klaus-Jurgen Bathe. Finite element procedures prentice-hall. *New Jersey*, 1037, 1996.

[38] Kenneth Langstreth Johnson and Kenneth Langstreth Johnson. *Contact mechanics*. Cambridge university press, 1987.

Chapter 3

Mechanical deconvolution of elastic moduli by indentation of mechanically heterogeneous materials

Most materials are mechanically heterogeneous on a certain length scale. In many applications, this heterogeneity is crucial for the material's function, and exploiting mechanical heterogeneity could lead to new materials with interesting features, which require accurate understanding of the local mechanical properties. Generally used techniques to probe local mechanics in mechanically heterogeneous materials include indentation and atomic force microscopy. However, these techniques probe stresses at a region of finite size, so that experiments on a mechanically heterogeneous material lead to blurring or convolution of the measured stress signal. In this study, finite element method simulations are performed to find the length scale over which this mechanical blurring occurs. This length is shown to be a function of the probe size and indentation depth, and independent of the elastic modulus variations in the heterogeneous material, for both 1D and 2D modulus profiles. Making use of these findings, we then propose two deconvolution methods to approximate the actual modulus profile from the apparent, blurred measurements, paving the way for an accurate determination of the local mechanical properties of heterogeneous materials.

This chapter is published as:

J.N.M. Boots, R. Kooij, T.E. Kodger and J. van der Gucht
“Mechanical deconvolution of elastic moduli by indentation of mechanically heterogeneous materials”
Frontiers in Physics 9: 723768. (2021)

3.1 Introduction

Controlling the mechanical heterogeneity of materials could lead to new innovative materials with interesting properties[1], such as scaffolds for tissue engineering[2], stimuli-responsive materials[3], materials with soft-lithography applications[4] and materials with enhanced lifetime[5]. To design such materials, and to understand their mechanical performance, methods are needed that can accurately measure the spatial variation of mechanical properties. This is challenging, since the mechanical response of a material depends strongly on the length scale at which it is probed[6,7]. The most common method to measure local mechanical properties in heterogeneous materials is indentation, in which an indenter is pushed on a material and the local resistance force to deformation is acquired with a force sensor. Using an appropriate contact model, such as Hertzian contact theory[8], the local elastic modulus E can be obtained from the measured force-displacement relation. However, the indenting probe deforms the material in a region of finite size, so that variations in mechanical properties that occur on length scales that are similar to the size of the deformed region or smaller necessarily appear smoothed out. This is illustrated in Figure 3.1, which shows a material with a sharp gradient in the modulus. Probing the material using spatially-dependent indentation leads to a blurred profile, which is a convolution of the actual modulus profile and the volume of material probed by the indenter. Depending on the size of the probe, this blurring may occur on the nm scale for nano-indentation using atomic force microscopy[9,10,11,12,13], on the μm-scale for micro-indentation[14,15], or on the mm-scale or larger for macroscopic probes[16,1718]. Previous studies have shown that the extent of mechanical blurring depends on the indentation depth[6] and occurs over an area that is at least 3 times the contact area of the probe with the substrate[7]. However, the exact dependence of the mechanical response on the probe size and depth remain unknown. Clearly, the characterization of mechanically heterogeneous materials would benefit from a better understanding of the effects of mechanical blurring, and from ways of improving the spatial resolution of mechanical measurements.

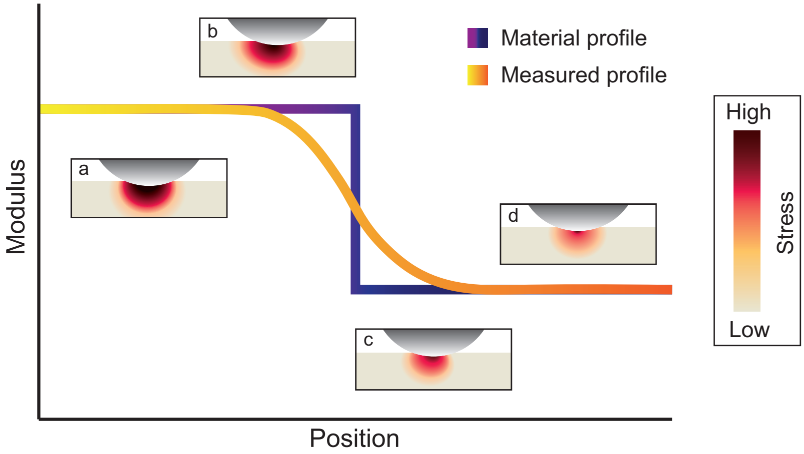

Figure 3.1 – Schematic representation of a material that has a step-wise modulus profile and the resulting modulus profile measured by an indentation experiment at several positions across the modulus interface. The four insets a-d display the heterogeneous stress profiles in the material, color coded for the stress, as the material is indented with, in this example, a spherical probe.

A similar problem occurs in optical imaging, where the captured image is a convolution of the real image and the so-called point spread function, which describes the response of the imaging system to a point force and thereby characterizes the degree of blurring. If the point spread function of an optical device is known, deconvolution methods can be used to deblur the signal and increase the image quality[19,20]. In this work, we explore a similar deconvolution strategy for indentation measurements on mechanically heterogeneous materials. We first identify the mechanical analogue of the point spread function. We do this by performing finite element calculations on materials with a known modulus profile $E(r)$, indented by a spherical probe. From the calculated normal force $F(r)$, we obtain an apparent local modulus $E_a(r)$, which we compare to the real modulus $E(r)$ to assess the degree of blurring and to estimate the mechanical point spread function. We find that the blurring is independent of the magnitude of E, which is a prerequisite for deconvolution to be feasible, since the real modulus is unknown. In addition, we find that the deblurring is set by a combination of the probe radius R and the indentation depth δ, which together determine the length scale over which the probe deforms the material. Based on these findings, we then describe two methods to approximate the real modulus profile E from the apparent moduli E_a measured for different values of R and δ.

3.2 Materials & Methods

3.2.1 Finite Element Method simulations (FEMs)

Finite Element simulations were performed using COMSOL Multiphysics. The 3D stationary structural mechanics module was used to model the indentation of a rigid sphere on a linear elastic substrate. The linear elastic substrate was meshed with small hexahedra swept underneath the spherical probe and coarsely meshed far away from the probe, as shown in Figure 3.2a, and was solved for 43k degrees of freedom. Three probe radii were simulated; 400, 500 and 750 µm. The maximum indentation depth was set at $\delta_{max} = 0.4 \cdot R$ and the step size was 4 µm. The linear elastic substrate was modeled with a fixed constraint at the bottom. Contact between the rigid sphere and the elastic substrate was implemented by the penalty method. Further model details are provided in the Appendix 3. With F obtained from the bottom of the PDMS substrate in the simulations, the apparent modulus E_a was calculated using Hertzian contact theory[8],

$$E_a = \frac{3}{4} R^{-\frac{1}{2}} \delta^{-\frac{3}{2}} F \tag{3.1a}$$

$$E_a = \frac{Y}{(1 - \nu^2)} \tag{3.1b}$$

where Y is the apparent Young's modulus, and ν is Poisson's ratio, which was here taken as 0.45[21].

FEM simulations were performed on a total of four profiles: (i) a 1-dimensional (1D) stepwise modulus profile (ii) 1D sigmoidal profiles with varying widths w (iii) 1D wells with various widths w, and (iv) 2-dimensional (2D) wells with various widths w^2. The modulus profiles were incorporated with a piecewise function in COMSOL's material section using the following relations:

$$E\left(x\right) = E_1 + \left(E_2 - E_1\right) \cdot H\left(x\right) \tag{3.2a}$$

$$E\left(x\right) = E_1 + \frac{\left(E_2 - E_1\right)}{1 + e^{-\left(x\,-\,x_0\right)/w}} \tag{3.2b}$$

$$E\left(x\right) = \frac{\left(E_1 + E_2\right)}{2} + \frac{\left(E_1 - E_2\right)}{2} cos(2\pi\frac{x}{w} + \pi) \tag{3.2c}$$

$$E\left(x, y\right) = E_1 - \left|E_2 - E_1\right| e^{(-\frac{(x - x_0)^2 + (y - x_0)^2}{w^2})} \tag{3.2d}$$

with $E_1 > E_2$, x the position, x_0 the position of the interface and H the Heaviside function defined as:

$$H\left(x\right) = \begin{cases} 0 \text{ for } x - x_0 < 0 \\ 1 \text{ for } x - x_0 > 0 \end{cases}$$

3.3 Results and Discussion

3.3.1 Heterogeneity leads to asymmetric stress profile

FEM simulations are performed on materials with various elastic modulus profiles. Figure 3.2b shows, for the 1D sigmoidal profile with width w = 10.0 mm, the elastic strain energy density profile $u = \frac{U}{V} = \int_0^{\epsilon_f} \sigma \partial \epsilon$. For mechanically heterogeneous materials, the strain energy profile is asymmetric, leading to a convolution in the locally recorded force, which becomes a weighted average of the stress profile. Hence, this calls for a method that converts the convolved profile in a deconvolved profile that approximates the actual material profile, such that mechanically heterogeneous materials can be mapped accurately.

3.3.2 The mechanical point spread function

To find the mechanical point spread function that sets the degree of mechanical blurring, a stepwise profile (Eq 2a) is simulated with FEM. Results in Figure 3.3a,b show that the mechanical blurring is dependent on R and δ. Likely, this is because R and δ set the contact radius $a = \sqrt{R\delta}$ between

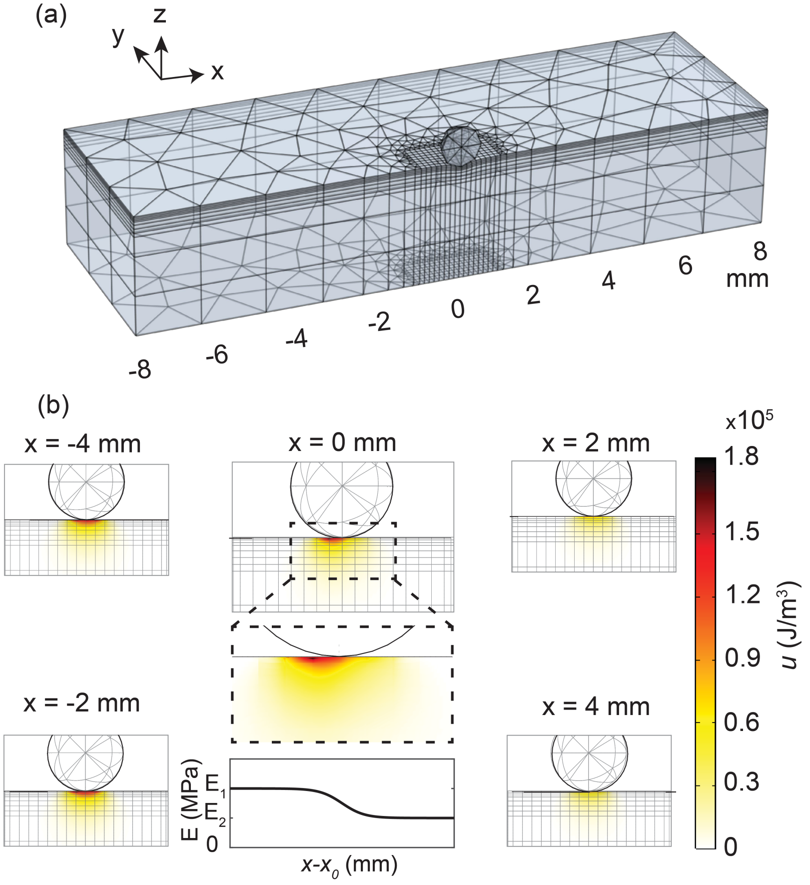

Figure 3.2 – **(a)** Meshing used in the finite element simulations for 1D modulus profiles, where the finely meshed region at the destination moves along with the indentation position. Symmetry in the y-axis is assumed to reduce computation time. **(b)** Elastic strain energy density, u, distribution for indentations at various positions across the interface for a sigmoidal profile (Eq 2b) with width $w = 10.0$ mm, shown with the bottom center plot. The inset of the u profile at the interface, $x = 0$ mm, shows the heterogeneous u profile across the interface, leading to blurring of the recorded stress response in indentation measurements.

the probe and the substrate. The larger a, the larger the area probed by the sphere and the larger the mechanical blurring. At this point, we assume that E_a is a convolution of E and the mechanical blurring function $g(\mathbf{r}-\mathbf{r}')$, with the real modulus at position $\mathbf{r}'$ contributing to the modulus probed at position $\mathbf{r}$, analogous to the point spread function:

$$E_a(\mathbf{r}) = \int_{-\infty}^{\infty} g(\mathbf{r}-\mathbf{r}')E(\mathbf{r}')d\mathbf{r}' \tag{3.3}$$

Next, we assume that the mechanical blurring function $g(\mathbf{r}-\mathbf{r}')$ is a Gaussian function, independent of E:

$$g(x,y) = \frac{1}{\sqrt{\pi}L}e^{-\frac{(x-x_0)^2+(y-y_0)^2}{L^2}} \tag{3.4}$$

where L is a characteristic length that determines the degree of blurring. Equation 3.3 can be solved analytically for the stepwise profile, by inserting Equation 2a and Equation 3.4 in Equation 3.3, resulting in:

$$E_c\left(x\right) = \frac{1}{2}\left(E_1+E_2\right)+\frac{1}{2}\left(E_2-E_1\right)\cdot \mathrm{erf}\left(\frac{x}{L}\right) \tag{3.5}$$

with E_c the convolved elastic modulus, which should approximate E_a. By fitting Equation 3.5 to E_a from the FEM simulations, the characteristic blurring length L can be determined as a function of R and δ. Indeed, the results presented in Figure 3.3c,d show a collapse of E_a when x is rescaled with L obtained from these fits, as expected based on Equation 3.5. Furthermore, to verify whether $L \sim (R,\delta)$, Figure 3.4 shows that L can be fitted with $L = b\cdot(R\delta)^p$. Collapse of L for multiple ${}^{E_1}/_{E_2}$ ratio's shows that L is independent of E. These findings show that our assumption of a Gaussian point spread function works well for deconvolving the mechanical blurring.

Now that we have obtained the mechanical point spread function and its characteristic blurring length L from the analysis of the blurred step profiles, we investigate whether this can be used to deconvolve apparent moduli measured with indentation to obtain a good approximation of the actual modulus profile of heterogeneous materials. We propose two methods to do this.

3.3.3 Deconvolution of 1D profiles

The first method to deconvolve a blurred profile is through extrapolation of E_a to $L = 0$, as at zero indentation depth the material is not deformed and there is no blurring of the mechanical response and, hence, $E_a = E$ in this case. This extrapolation to obtain E_e is shown in Figure 3.5a for a sigmoidal profile with width $w = 10.0$ mm, for several probe positions $x - x_0$. An advantage of this extrapolation method to deconvolve E_a into E_e that approximates E is that the precise shape of $g(\mathbf{r} - \mathbf{r}')$ does not have to be known.

The second method to deconvolve a blurred profile is accomplished with an algebraic deconvolution approach. First, we write the convolution

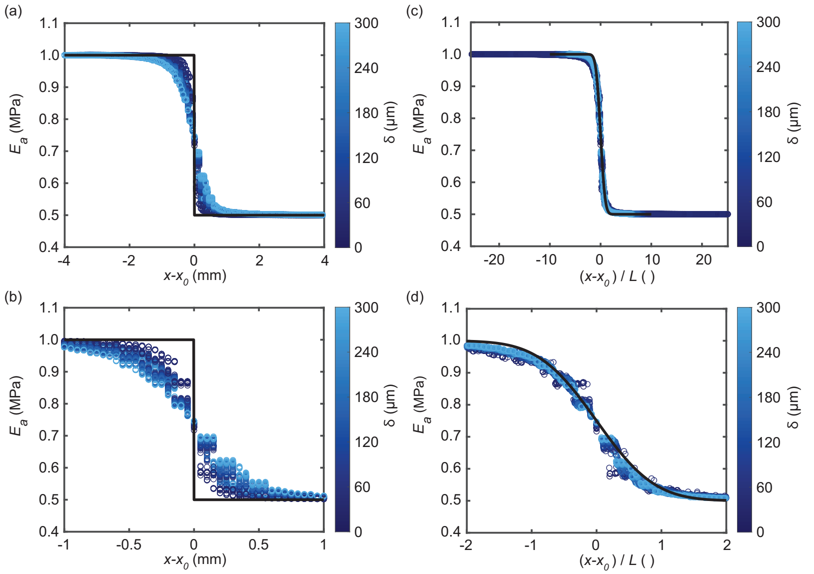

Figure 3.3 – FEM simulation data for a step modulus profile for all three probe radii. **(a)** E_a at all simulated depths δ (color coded) plotted versus the probe position from the interface $(x - x_0)$ for a step profile obtained by Equation 2a (black), with **(b)** a zoom-in of panel (a) showing the data around the interface. **(c)** E_a from panels (a) and (b) plotted versus the probe position from the interface $(x - x_0)$ rescaled with L, where the black line represents E_c from Equation 3.5, with **(d)** a zoom-in of panel (c) showing the data around the interface.

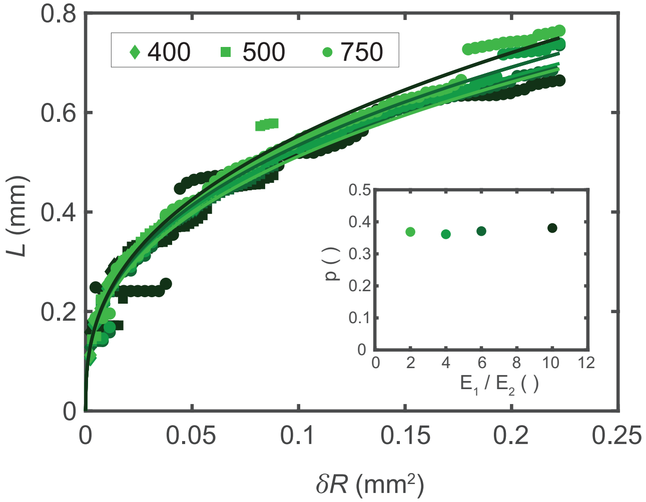

Figure 3.4 – The characteristic length L plotted versus the squared contact radius $a^2 = R\delta$ for all three probe radii, fitted using $L = b \cdot (R\delta)^p$ with prefactor $b = 0.195$ and exponent $p = 0.37$. The legend shows the symbols for the probe radius (μm). The inset shows p versus the ratio between the simulated moduli, with the lower modulus, $E_2 = 0.5$ MPa and $E_1 > E_2$.

as a matrix operation:

$$\mathbf{E_a} = \mathbf{G} \cdot \mathbf{E} \tag{3.6}$$

with **G** a matrix describing the mechanical blurring. Every row of **G** contains coefficients that indicate how much the modulus at position $\mathbf{r}'$ contributes to the modulus probed at position $\mathbf{r}$. These coefficients are determined by $g(\mathbf{r} - \mathbf{r}')$, of which L is known from the simulations on the 1D steplike profile. To obtain the unknown E from the measured E_a we find a least squares solution to Equation 3.6 using an iterative method, Simultaneous Iterative Reconstruction Technique (SIRT) algorithm[22,23]. Further details of this method are provided in the SM.

With the two methods presented above, E_a is extrapolated and deconvolved leading to E_e and E_d, respectively. E_e and E_d convert E_a into an approximation of E, as shown in Figure 3.5b,c for a sigmoidal profile with width $w = 10.0$ mm and a well profile with width $w = 2.0$ mm, respectively. This shows that both presented methods, extrapolation and

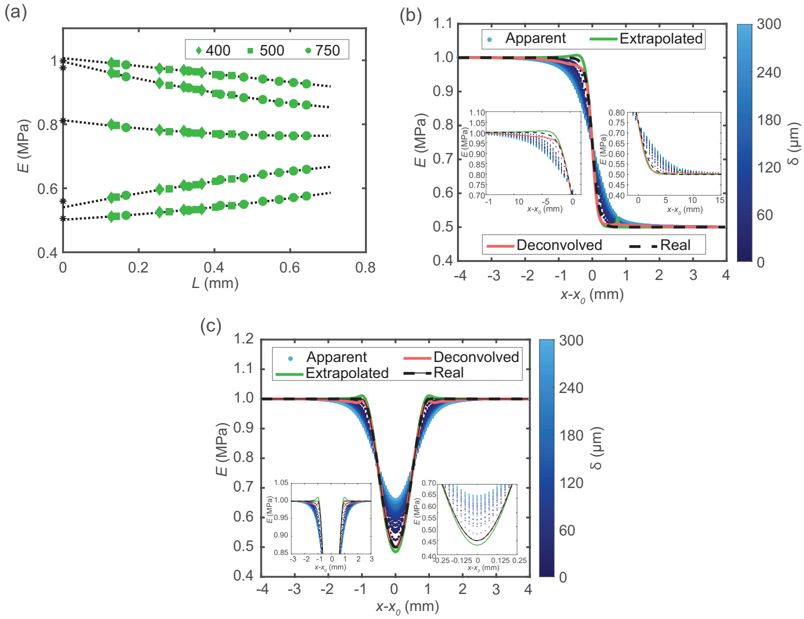

Figure 3.5 – **(a)** E_a plotted versus the L for all three radii simulated for a sigmoidal profile with width $w = 10$ mm. The data are extrapolated using a second order polynomial fit to give an extrapolated modulus E_e at $L = 0$, indicated with an asterisk (*), which approximates the local E. The legend shows the symbols corresponding to R. For visualization purpose, every eighth data point is plotted. **(b)** Elastic moduli plotted versus indentation position around the center of the profile. Insets are zoom-ins. Note that the data shown in both panel (a) and (b) are from a sigmoidal profile with $w = 10.0$ mm. **(c)** Elastic moduli plotted as a function of indentation position for the 1D well profiles for $w = 2.0$ mm, with δ color coded. Insets are zoom-ins.

deconvolution, deblur the stress profile of a heterogeneous elastic profile into an approximation of the actual local elastic modulus.

3.3.4 Deconvolution of 2D profiles

After demonstrating mechanical deconvolution for 1-dimensional (1D) modulus profiles, simulations were performed to showcase the potential of deconvolving a 2-dimensional (2D) modulus profile. In these simulations, the same meshing was used as for the 1D profiles. Symmetry was

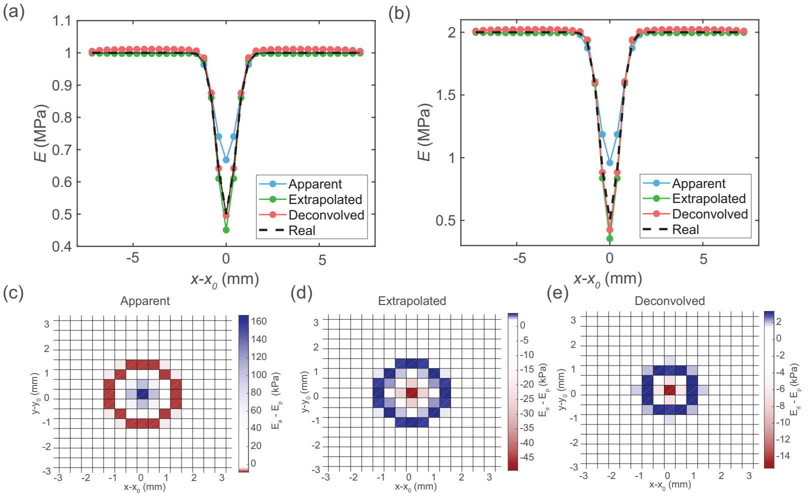

Figure 3.6 – Data of two dimensional modulus profiles of a symmetric well, where one quadrant was simulated. **(a)** All moduli versus probe position plotted as cut line through the center of the well for $E_1 = 1$ MPa and $E_2 = 0.5$ MPa. **(b)** All moduli versus probe position plotted as cut line through the center of the well for $E_1 = 2$ MPa and $E_2 = 0.5$ MPa. **(c)** Surface map of $E_a - E$, **(d)** $E_e - E$, and **(e)** $E_d - E$ for the $E_1 = 1$ MPa and $E_2 = 0.5$ MPa and $w^2 = 0.5$ mm^2 profile. Extrapolation and deconvolution is achieved with L obtained from the 1D stepwise profile (see Figure 3.4).

assumed across $x = x_0$ and $y = y_0$ and, therefore, a quadrant was modeled to reduce computation time.

The discrepancy between the apparent modulus E_a and the actual modulus profile E, shown in Figure 3.6ab, once again demonstrates the necessity for the mechanical deconvolution methodology demonstrated for the 1D profiles. The convolution kernel g and L obtained from the 1D step profile are used to extrapolate and deconvolve E_a.

The results from these simulations show that both the extrapolation and deconvolution methods presented in this work are able to deconvolve both 1D and 2D mechanical profiles, approximating a blurred E_a into profiles close to the actual profile E. Results in Figure 3.3 and 3.4 confirm that mechanical blurring is at least 3 times L, as observed by Bahrami *et al.*[7]. In addition, simulations on two ${}^{E_1}/_{E_2}$ ratio's for 2D wells show that the differences between E_a, E_e and E_d scale approximately with the E_1/E_2 ratio, albeit that larger deviations are found for smaller w, see Figure 3.A.5. Furthermore, like the 1D profile, a sharper modulus profile leads to blurring of E_a, making extrapolation and deconvolution into an approximation of E more challenging. Examples are Figures S3a and S4a, where a sharp, (almost) discontinuous transition in E leads to the Gibbs phenomenon[24] in the deconvolved E_e and E_d; oscillations of the Fourier function at sharp transitions which in imaging is known as the ringing artefact[25]. Nevertheless, the two methods presented allow deconvolution of E_a into an approximate of E.

3.3.5 Towards experimental validation

Our finite element simulations show how indentation measurements on heterogeneous samples lead to mechanical blurring, and how knowledge of the mechanical point spread function can be used to deconvolve the blurred signal to obtain a more accurate modulus profile. , experimental validation is required to transform this proposed method into a reliable practical procedure. To experimentally determine the mechanical point spread function and the associated characteristic length, and to compare this to simulation results shown in Figure 3.4, a material with a precisely known gradient in modulus is needed, ideally a x-dependent step function in modulus. Indentation measurements on this reference sample then allows the determination of the characteristic length in exactly the same way as described in section 3.3.2. Unfortunately, we have not been able to produce such a material of known modulus gradient with the capabilities in our lab, without also creating gradients in the depth-direction or differences in sample height across the modulus step, which made it impossible for us to provide such validation. Our attempts are described in detail in the SM. We hope that this work will inspire others to provide the experimental validation needed to turn our approach into a robust experimental method. We further note that in our approach we have assumed the substrate to be a purely elastic material. While this is justified for elastic solids, such as crosslinked rubbers, care should be taken for viscoelastic soft materials that also have viscous (and therefore rate-dependent) contributions to the mechanical response. Furthermore, since our method is based on linear elasticity, deviations may occur for large indentation depths, where strain hardening may become relevant.

3.4 Conclusion & Future Outlook

The work presented in this paper shows two methods to transform a blurred and measured E_a towards an expected modulus E in FEM simulations in 1D and 2D. This transformation is achieved by using a characteristic length L, which is found to be a function of δ and R. The methods presented to deconvolve a blurred mechanical profile should work on smaller length as well, for example for mechanical maps obtained using spatially resolved AFM-based force spectroscopy[10,11], provided that the material can still be considered as a flat elastic continuum. For this it is necessary to obtain force-distance curves for each position, so that effective modulus data at the same penetration depth can be compared. To validate the extrapolation and deconvolution methods proposed here experimentally, indentation measurements on a material with a precisely known modulus profile are performed. Unfortunately, we did not succeed in obtaining these, but we hope that future work will demonstrate the potential of mechanical deconvolution. We anticipate that the mechanical deconvolution technique presented here can be used to approximate the actual mechanical heterogeneous material from a blurred stress response, leading to more accurate knowledge of local mechanical properties in for example biological systems[12,14], polymeric materials[6,7,15,26] and meat analogues[27].

3.5 Appendix Chapter 3

Finite Element Method (FEM) model settings

In the Finite Element Method simulations, using the linear elastic material model in COMSOL Multiphysics, a steel probe is pushing on a Polydimethylsiloxane (PDMS) substrate. PDMS substrate dimensions are (x,y,z) 16x5x3 mm, with a symmetry on the y-axis, for the 1D profile and 20x20x3 mm for the 2D profile, see Figure 3.A.1. Meshing in the z-direction was swept explicitly with fixes values, increasing in distance from top to bottom. The mesh size on the PDMS substrate of triangulars was 'predefined' as normal and the mesh size of the small squares underneath the probe was 0.25*R. The indentation sphere mesh size was modeled with tetrahedrals of size R. For 1D profiles, the probe x-displacement was 50 µm ranging from 4-12 mm. For 2D profiles, the probe x,y-displacement was 40 µm ranging from 2.8-10 mm, simulating only one quadrant. On the PDMS substrate, linear strains were forced and a fixed constraint was applied on the bottom surface. At the contact interface, a characteristic penalty factor E_{char}, an actual stiffness of a spring inserted between the boundaries, of 1 GPa and a contact pressure penalty factor of 10^{13} N/m^3 set the transfer of stresses between the source (probe) and destination (PDMS block). By default, COMSOL expresses the contact pressure penalty factor as a quotient of a material stiffness-dependent penalty factor, and the overall minimal mesh size of the contact destination. The default setting produced elastic moduli, calculated with Equation 1a from the main article with F obtained from the bottom of the PDMS substrate, deviating too much from the set elastic modulus for the indentation models, so the contact pressure expression was replaced with an empirically established optimal value. E_{char} was optimized to:

1. minimize the deviation for the apparent elastic modulus E_a from the actual modeled elastic modulus E for a homogeneous PDMS block
2. limit the average computation time for a single indentation

Data for the optimization of E_{char} is shown in Figure 3.A.2.

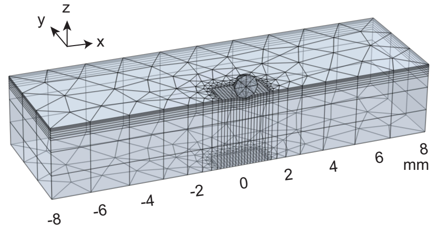

Figure 3.A.1 – Meshing used in the finite element simulations for 1D modulus profiles, where the finely meshed region at the destination moves along with the indentation position. Symmetry in the y-axis is assumed to reduce computation time. This Figure is the same as Figure 3.2a

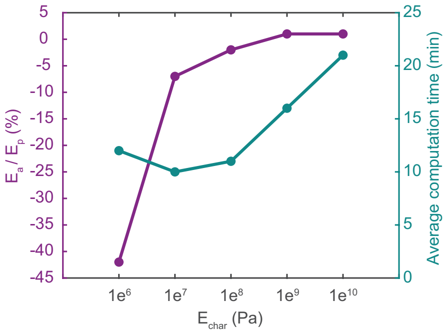

Figure 3.A.2 – The penalty factor E_{char} versus the deviation from the modeled homogeneous E_a calculated with Equation 3.1a to E, and the average computation time for a single indentation.

Details second deconvolution method

The second deconvolution method presented in the main paper uses the Simultaneous Iterative Reconstruction Technique (SIRT)[22,23]. As explained in the Section 3.3.3, the convolution is written as $\mathbf{E_a} = \mathbf{G} \cdot \mathbf{E}$, where $\mathbf{E_a}$ is a vector containing the measured moduli, $\mathbf{E}$ the real moduli, and $\mathbf{G}$ is a matrix that represents the measurement process. An approximation for $\mathbf{E}$, $\mathbf{E_d}$, is found by solving this system in a least-squares sense, by minimizing the norm $||\mathbf{G}\mathbf{E_d} - \mathbf{E_a}||$. We do this using the SIRT algorithm. Starting from an initial guess for $\mathbf{E_d}$($\mathbf{E_d}^{(0)} = \mathbf{E_a}$), we use the following update equation to iteratively find the best solution[28]:

$$\mathbf{E_d}^{(n+1)} = \mathbf{E_d}^{(n)} + \mathbf{C}\mathbf{G}^T\mathbf{R}(\mathbf{E_a} - \mathbf{G}\mathbf{E_d}^{(n)}) \tag{3.7}$$

where $\mathbf{C}$ and $\mathbf{R}$ are diagonal matrices that contain the inverse of the sum of the columns and rows of $\mathbf{G}$, respectively, given by $C_{jj} = 1/\sum_i G_{ij}$ and $R_{ii} = 1/\sum_j G_{ij}$.

All simulated widths for all profiles

Step profile and sigmoidal profile

Results for the step profile and sigmoidal profiles with all widths simulated with COMSOL Multiphysics are presented in Figure 3.A.3. The step profile is defined with Equation 2a from the main article:

$$E\left(x\right) = E_1 + \left(E_2 - E_1\right) \cdot H\left(x_0\right)$$

with $H\left(x_0\right)$ the Heaviside function defined as

$$H\left(x\right) = \begin{cases} 0 \text{ for } x - x_0 < 0 \\ 1 \text{ for } x - x_0 > 0 \end{cases}$$

The sigmoidal profile is defined with Equation 2b from the main article:

$$E\left(x\right) = E_1 + \frac{\left(E_2 - E_1\right)}{1 + e^{-(x - x_0)/w}}$$

1D well profile

Results for the 1D well profile with all widths simulated are presented in Figure 3.A.4. The 1D well profile is defined with equation 2c of the main article:

$$E\left(x,y\right)=E_1-\left|E_2-E_1\right|e^{(-\frac{(x-x_0)^2+(y-x_0)^2}{w^2})}$$

with w^2 is the width of the well.

2D well profile

Results for the 2D well profile with all slopes simulated are presented in Figure 3.A.5. The 2D well profile is defined with equation 2d of the main article:

$$E\left(x,y\right)=E_1-\left|E_2-E_1\right|e^{(-(1/w_2)((x-x_0)^2+(y-x_0)^2))}$$

with w^2 the width of the well size.

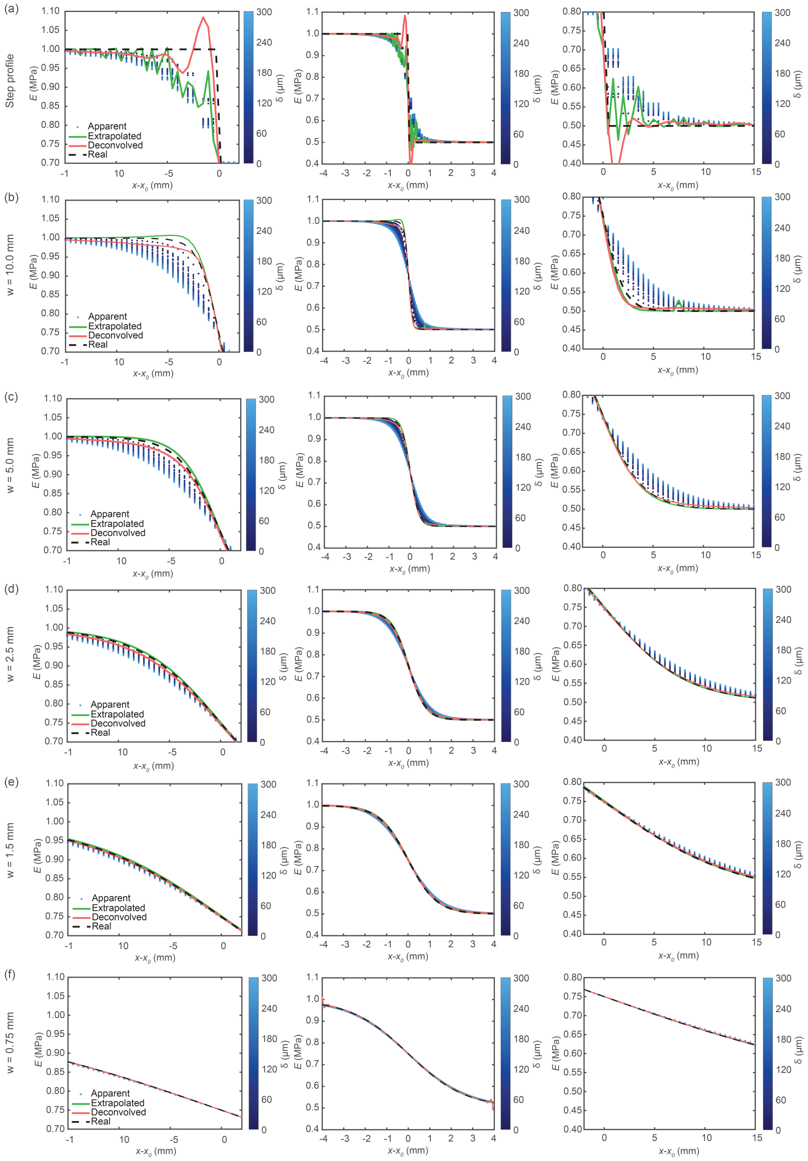

Figure 3.A.3 – Elastic moduli plotted as a function of indentation position for the step profile and sigmoidal profiles with varying slopes, indicated by s on the left, with the indentation depth color coded. Left and right panels are zoom-ins.

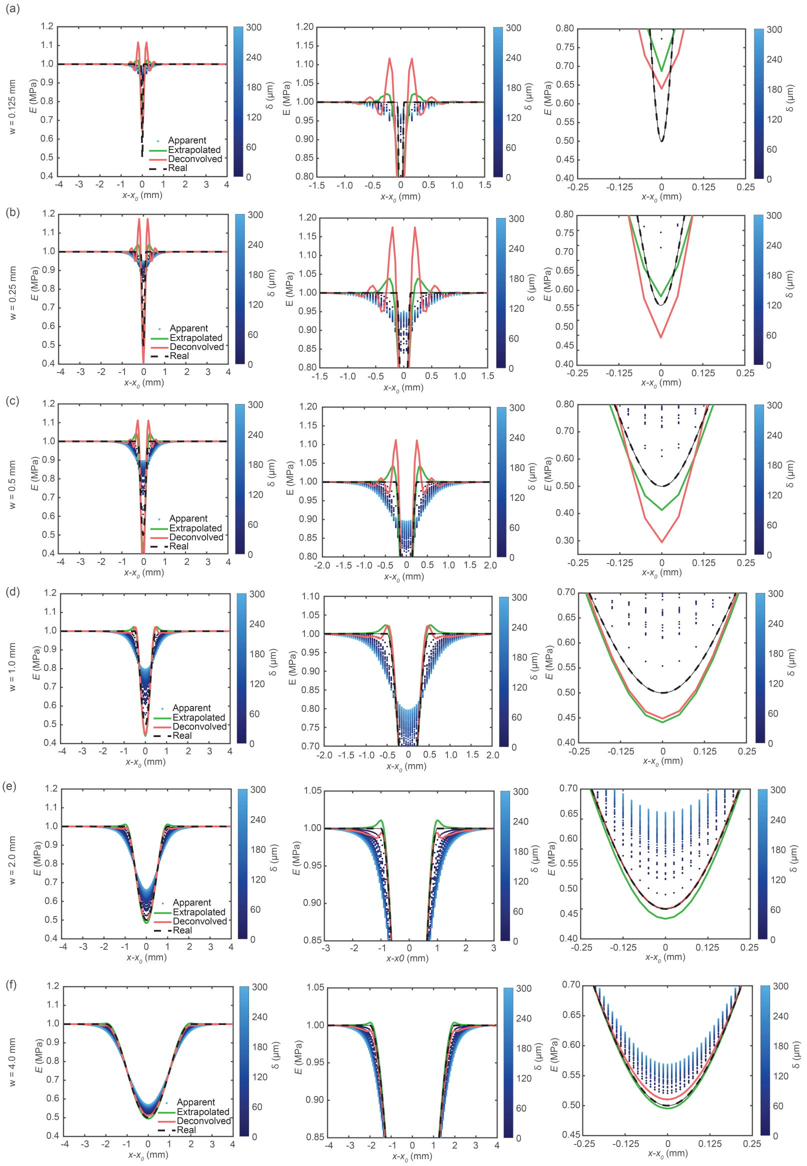

Figure 3.A.4 – Elastic moduli plotted as a function of indentation position for the 1D well profiles with varying well size, indicated by w on the left, and with the indentation depth color coded. Center and right panels are zoom-ins.

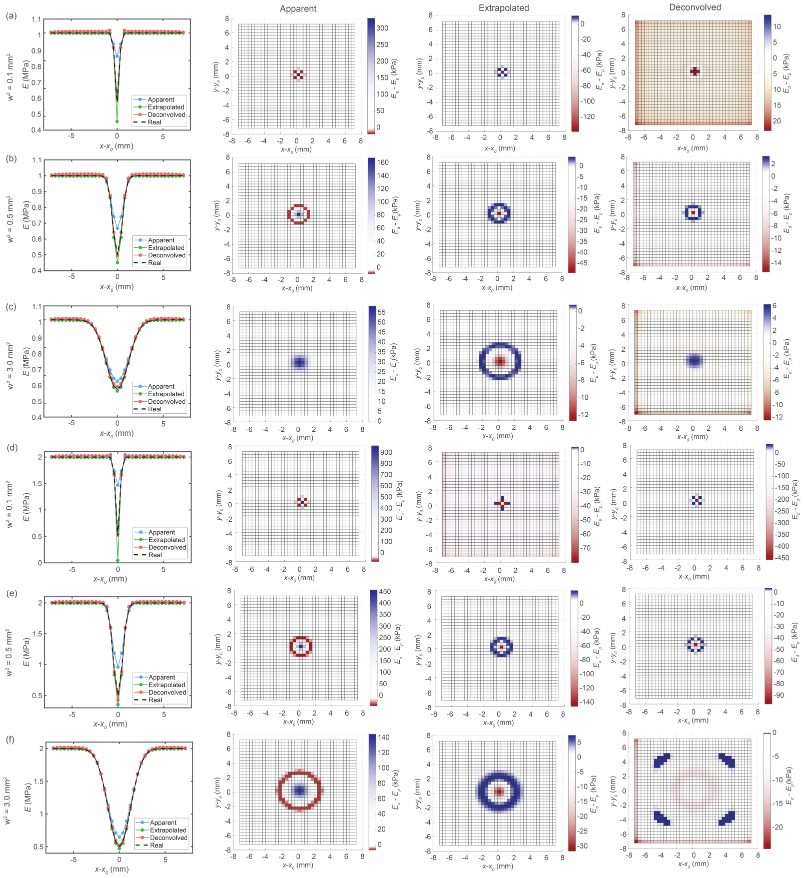

Figure 3.A.5 – Elastic moduli plotted for the 2D well profiles with varying well size, indicated by w^2 on the left, for a cut line trough $y - y_0 = 0$ and 2D surface maps with the difference between the actual modulus profile E and E_a, E_e, E_d, respectively. (a)-(c) is for $E_1 = 1$ MPa and (d)-(f) is for $E_1 = 2$ MPa, where in both $E_2 = 0.5$ MPa.

Towards experimental validation with a steplike profile

Indentation experiments

Using FEM simulations, two methods were introduced, extrapolation and deconvolution, to successfully transform E_a into a profile close to E. To validate the extrapolation and deconvolution methods proposed here experimentally, indentation measurements on a material with a precisely known modulus profile are needed. This section describes the efforts performed to produce this sample, and acquire the mechanical information with an indentation test.

Synthesis of material with stepwise elastic modulus profile

The material with the stepwise modulus profile was produced by using the silicone rubber Sylgard 184[29], see Figure 3.A.6. Sylgard was mixed 7.5:1 base to crosslinking component, stirred, centrifuged for 30 seconds at 2000 rpm, poured in a petridish, vacuum cycled 5 times to remove air bubbles, and left to cure at room temperature for at least 96 hours. Afterwards, a rectangle was cut out using a scalpel and a glass slide with a mylar sheet[30] attached was squeezed into contact with this rectangle to create an empty volume; crucially, mylar does not adhere to silicone rubber enabling removal of the glass slide without tearing of the Sylgard surface. This void was filled with Sylgard 15:1, which has been centrifuged and vacuum cycled as well. The 15:1 Sylgard was cured for at least 96 hours at room temperature, after which the mylar and glass slide lid was easily removed.

Measuring local E with multi-point indentation

The material with stepwise modulus profile was indented using a multi-point indentation setup[18], with slight alterations presented hereafter. The initial 24 μm of the sample was indented with a piezo actuator (Thorlabs, NFL5DP20/M) with 0.24 μm step size, to find the point of contact between the probe and the sample surface δ_0 with high accuracy. Subsequently, the sample was indented further with a stepper motor (M-403.6DG, Physical Instruments) with step size 4 μm until a set force threshold was reached. The probe used for indentation was a spherical probe with radius R = 750 μm. F was measured using a 20g load cell (FUTEK, FSH02667), calibrated using calibration weights, which was connected to an analog amplifier (SG-3016, ICP DAS) and communicates with the computer via a digital acquisition device (USB-6001, National

Instruments). The load cell voltage was sampled every millisecond and an average was taken every 1000 samplings to compute F. All elements were controlled using MATLAB[31].

Results indentation experiment

Unfortunately, E_a was found to vary with δ even for a homogeneous, as is shown by the data presented in Figure 3.A.6a. At distances larger than L, where the stress response is homogeneous, this δ-dependence is not expected according to Equation 1a of the main article. Therefore, the experimentally obtained data could not be used to assess the validity of the extrapolation and deconvolution method to transform E_a into a modulus profile close to E, deconvolving the obtained response inherent to indentation of a material with a mechanically heterogeneous profile. Possible reasons for this depth-dependence of E_a are: modulus-variation in height due to temperature gradients during polymerization with a softer top layer; air-pocket formation in the rubber which was observed upon heating the second Sylgard fill in a 70°C oven overnight, but can still occur at slower polymerization at room temperature; and a height difference in the sample despite using a cover to produce a flat sample, as shown in Figure 3.A.7b, potentially caused by the method used to compress the cover on the sample.

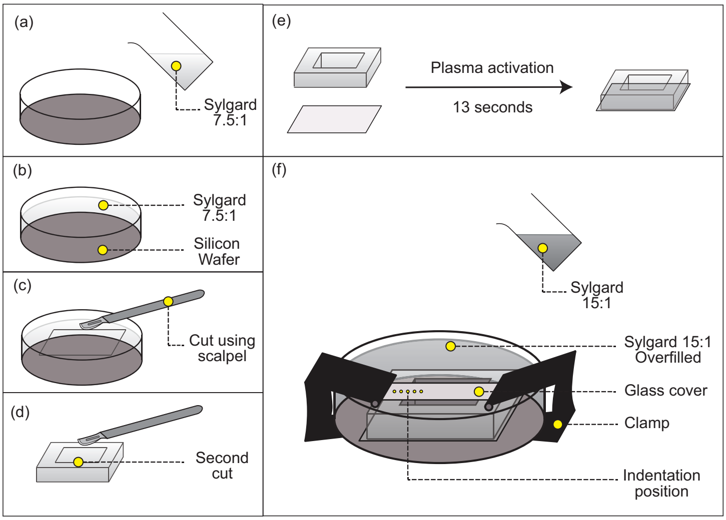

Figure 3.A.6 – Schematic representation of the sample synthesis for the indentation experiments. **(a)** Sylgard 184 with a base:catalyst 7.5:1 poured in a petridish with a silicon wafer at the bottom. **(b)** Sylgard in a petridish, degassed with multiple vacuum cycles and cured at room temperature for a minimum of 96h. **(c)** A scalpel is used to cut out a block of the Sylgard. **(d)** A second cut is made to create a framework of the Sylgard elastic rubber. **(e)** The framework is bonded to glass, which is cleaned with ethanol and deionized water and air dryed, using a plasma cleaner. The plasma treatment is 13 seconds after which the silicon wafer side of the Sylgard framework is bound to the glass. **(f)** A microscopic glass slide is applied on the flat surface between the framework and fixed by clamping, to obtain a flat surface. The framework is filled with a second Sylgard with a lower concentration of catalyst. The minimal curing time is 96h at room temperature, to limit air bubble formation.

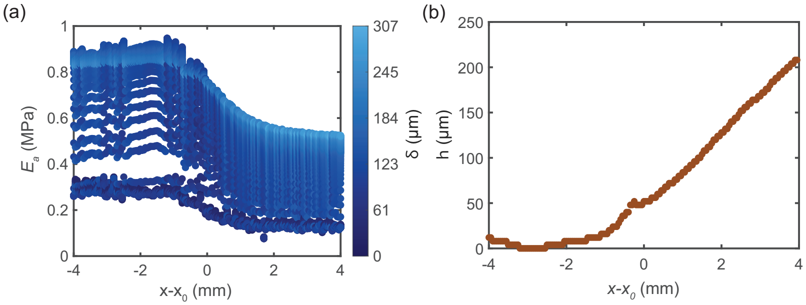

Figure 3.A.7 – **(a)** E_a versus indentation position $x - x_0$, showing that E_a varies with δ **(b)** The height of the sample across the interface, determined by finding the relative probe depth at which F onsets.

Bibliography

[1] Salvatore Torquato and HW Haslach Jr. Random heterogeneous materials: microstructure and macroscopic properties. *Appl. Mech. Rev.*, 55(4):B62–B63, 2002.

[2] Hang Yin, Yonghui Ding, Yao Zhai, Wei Tan, and Xiaobo Yin. Orthogonal programming of heterogeneous micro-mechano-environments and geometries in three-dimensional bio-stereolithography. *Nature communications*, 9(1):1–7, 2018.

[3] Jungwook Kim, James A Hanna, Myunghwan Byun, Christian D Santangelo, and Ryan C Hayward. Designing responsive buckled surfaces by halftone gel lithography. *Science*, 335(6073):1201–1205, 2012.

[4] Kyung M Choi and John A Rogers. A photocurable poly (dimethylsiloxane) chemistry designed for soft lithographic molding and printing in the nanometer regime. *Journal of the American Chemical Society*, 125(14):4060–4061, 2003.

[5] P-P Cortet, Loıc Vanel, and Sergio Ciliberto. Super-arrhenius dynamics for subcritical crack growth in two-dimensional disordered brittle media. *EPL (Europhysics Letters)*, 74(4):602, 2006.

[6] Xu Cheng, Karl W Putz, Charles D Wood, and L Catherine Brinson. Characterization of local elastic modulus in confined polymer films via afm indentation. *Macromolecular rapid communications*, 36(4):391–397, 2015.

[7] Amir Bahrami, Christian Bailly, and Bernard Nysten. Spatial resolution and property contrast in local mechanical mapping of polymer blends using afm dynamic force spectroscopy. *Polymer*, 165:180–190, 2019.

[8] Valentin L Popov. *Contact mechanics and friction*. Springer, Berlin: Springer Berlin Heidelberg, 2010.

[9] Gerd Binnig, Calvin F Quate, and Ch Gerber. Atomic force microscope. *Physical review letters*, 56(9):930, 1986.

[10] Yves F Dufrêne, Toshio Ando, Ricardo Garcia, David Alsteens, David Martinez-Martin, Andreas Engel, Christoph Gerber, and Daniel J Müller. Imaging modes of atomic force microscopy for application in molecular and cell biology. *Nature nanotechnology*, 12(4):295–307, 2017.

[11] Hang Zhang, Junxiang Huang, Yongwei Wang, Rui Liu, Xiulan Huai, Jingjing Jiang, and Chantelle Anfuso. Atomic force microscopy for two-dimensional materials: A tutorial review. *Optics Communications*, 406:3–17, 2018.

[12] Annafrancesca Rigato, Felix Rico, Frédéric Eghiaian, Mathieu Piel, and Simon Scheuring. Atomic force microscopy mechanical mapping of micropatterned cells shows adhesion geometry-dependent mechanical response on local and global scales. *ACS nano*, 9(6):5846–5856, 2015.

[13] Yu M Efremov, AI Shpichka, SL Kotova, and PS Timashev. Viscoelastic mapping of cells based on fast force volume and peakforce tapping. *Soft Matter*, 15(27):5455–5463, 2019.

[14] Johannes Rheinlaender and Tilman E Schäffer. Mapping the mechanical stiffness of live cells with the scanning ion conductance microscope. *Soft Matter*, 9(12):3230–3236, 2013.

[15] Yizhuo Gu, Min Li, Ji Wang, and Zuoguang Zhang. Characterization of the interphase in carbon fiber/polymer composites using a nanoscale dynamic mechanical

imaging technique. *Carbon*, 48(11):3229–3235, 2010.

[16] Edwin P Chan, Yuhang Hu, Peter M Johnson, Zhigang Suo, and Christopher M Stafford. Spherical indentation testing of poroelastic relaxations in thin hydrogel layers. *Soft Matter*, 8(5):1492–1498, 2012.

[17] Marina Czerner, Lucas Sanchez Fellay, Maria Patricia Suarez, Patricia Maria Frontini, and Laura Alejandra Fasce. Determination of elastic modulus of gelatin gels by indentation experiments. 2015.

[18] JNM Boots, R Fokkink, J Van der Gucht, and TE Kodger. Development of a multi-position indentation setup: mapping soft and patternable heterogeneously crosslinked polymer networks. *Review of Scientific Instruments*, 90(1):015108, 2019.

[19] G Dougherty and Z Kawaf. The point spread function revisited: image restoration using 2-d deconvolution. *Radiography*, 7(4):255–262, 2001.

[20] Pinaki Sarder and Arye Nehorai. Deconvolution methods for 3-d fluorescence microscopy images. *IEEE Signal Processing Magazine*, 23(3):32–45, 2006.

[21] Angelina Müller, Matthias C Wapler, and Ulrike Wallrabe. A quick and accurate method to determine the poisson’s ratio and the coefficient of thermal expansion of pdms. *Soft Matter*, 15(4):779–784, 2019.

[22] Peter Gilbert. Iterative methods for the three-dimensional reconstruction of an object from projections. *Journal of theoretical biology*, 36(1):105–117, 1972.

[23] D Wolf, A Lubk, and H Lichte. Weighted simultaneous iterative reconstruction technique for single-axis tomography. *Ultramicroscopy*, 136:15–25, 2014.

[24] David Gottlieb and Chi-Wang Shu. On the gibbs phenomenon and its resolution. *SIAM review*, 39(4):644–668, 1997.

[25] Elias Kellner, Bibek Dhital, Valerij G Kiselev, and Marco Reisert. Gibbs-ringing artifact removal based on local subvoxel-shifts. *Magnetic resonance in medicine*, 76(5):1574–1581, 2016.

[26] Peter Schön, Kristóf Bagdi, Kinga Molnár, Patrick Markus, Béla Pukánszky, and G Julius Vancso. Quantitative mapping of elastic moduli at the nanoscale in phase separated polyurethanes by afm. *European Polymer Journal*, 47(4):692–698, 2011.

[27] JNM Boots, NPK Humblet-Hua, L Tonneijck, R Fokkink, J van der Gucht, and TE Kodger. Characterization of the local mechanical texture of animal meat and meat replacements using multi-point indentation. *Journal of Food Engineering*, 300:110505, 2021.

[28] Per Christian Hansen and Maria Saxild-Hansen. Air tools—a matlab package of algebraic iterative reconstruction methods. *Journal of Computational and Applied Mathematics*, 236(8):2167–2178, 2012.

[29] Dow Corning. Sylgard 184 Silicone Elastomer.

[30] Plastic Color Coded Shim BoPET. *Precision Brand Products, Inc.* 2250 Curtiss Street, Downers Grove, IL 60515, USA.

[31] The Mathworks, Inc., Natick, Massachusetts. *MATLAB version 9.5.0.944444 (R2018b)*, 2018.

Chapter 4

Characterization of the local mechanical texture of animal meat and meat replacements using multi-point indentation

Over consumption of animal meat is a large contributor to environmental change and should be reduced. This reduction can be achieved by replacing high environmental impact animal meat with an alternative produced from plant-based products or innovative \textit{in vitro} techniques that have negligible environmental impact. However, the general public will likely consume only meat replacements that mimic the aesthetic qualities of animal meat, with a challenging parameter to tune being the local mechanical response which defines the food texture. In this work, we present a method to characterize the local mechanics of food by using multi-point indentation to spatially measure the local elastic modulus. The resulting heterogeneous mechanical maps are quantified using the established auto-correlation method Moran's I, which can be used to quantify the resemblance of food texture between samples. The presented technique holds the potential to correlate production parameters such as shear rate and chemical composition with perceived food texture.

This chapter is published as:

J.N.M. Boots, N.P.K. Humblet-Hua, L. Tonneijck, R. Fokkink, J. van der Gucht and T.E. Kodger
"Characterization of the local mechanical texture of animal meat and meat replacements using multi-point indentation"
Journal of Food Engineering, 110505 (2021)

4.1 Introduction

From 2020 to 2050, the world population will rise by an estimated 2 billion[1]. To realize an increase of quality of life and reduce the world's environmental footprint, humanity faces major challenges amongst which is food security. Over the past decades health experts have emphasized the detrimental effects of the over consumption of meat for ethical, health, ecological and environmental reasons[2]. To decrease meat consumption, meat replacements are being developed with two strategies: either with cultured meat, meat produced by *in vitro* cell culture of animal cells, or with plant-based products[3]. Crucial to increase people's willingness to consume meat replacements, the product must mimic the aesthetic qualities of meat such as size, appearance, taste and texture[4].

While mimicking meat flavor is possible, a challenging food quality to tune is texture experienced during mastication which is defined by mechanical properties[5]. To date, there are analytical techniques capable of measuring these mechanical properties of food, such as rheology[6], the Warner-Bratzler Shear Force (WBSF) which measures tenderness, the texture profile analysis (TPA) which measures hardness, springiness, cohesiveness, gumminess and chewiness, and tensile testing which measures mechanical anisotropy[2]. However, all of these methods produce results based on bulk measurements averaging over any spatial heterogeneity, requiring local properties to be indirectly inferred.

In this work, we present a methodology that locally measures the mechanical response of meat or meat replacement, an important oral sensing property[5], through the use of multi-point indentation resulting in spatial mechanical 'maps' of elastic modulus. Lastly we analyze the data and introduce a new parameter, the decay length $\ell_{\frac{1}{2}}$, that represents the magnitude of local mechanical heterogeneity, indicative for the food texture.

4.2 Methods

4.2.1 Multi-point indentation and humidity control

The multi-point indentation setup translates in x, y a capacitive load cell using three translation stages and pushes a spherical probe on a sample to locally measure the normal force, as seen in Figure 4.1. Further technical instrumental details may be found in a previous publication[7]. A force-distance curve is obtained from which a local modulus, $E_{x,y}$, is determined using Hertzian contact theory[8], according to

$$E_{x,y} = \frac{3}{4} \frac{F}{R^{1/2} \delta^{3/2}} \left(1 - \nu^2\right) \tag{4.1}$$

with F the normal force measured by the load cell, R the probe radius, δ the indentation depth and ν the Poisson's ratio of the sample. Using this setup, mechanical maps of several meat types are produced. Mapping a sample placed in air results in poor mapping, since the modulus of the material changes relatively fast due to water evaporation, as samples contain up to 80 volume % of water[9]. Furthermore, the setup takes approximately 1 hour to obtain 50 force-distance curves with an acceptable amount of indentation steps to accurately determine the elastic modulus, thus mapping with reasonable spatial accuracy takes $\sim$24 hours for the samples mapped in this work.

Therefore, to reduce the evaporation rate, meat samples were placed in a custom-built chamber, which contained a piezoelectric water nebulizer, recirculating fan, and dry air source operating at flow rate of $10L/min$, see Figure 4.1. The humidity was controlled using a temporal feedback loop from a Thorlabs TSP01 humidity logger. The change of the Young's modulus in time, $E_{x,y}(t)$, for the meat replacement used in this research was found to be ${}^{\delta E}/_{\delta t}$ = 10 kPa/h during the measurement when using the humidity chamber set at a relative humidity (RH) of 40%, i.e. a non-humidity-controlled environment. Alternatively, at 90% RH, the ${}^{\delta E}/_{\delta t}$ = 3 kPa/h and at 95% RH ${}^{\delta E}/_{\delta t}$ = 1 kPa/h. Controlling the chamber humidity during the measurements decreases the change in sample modulus, but does not completely eliminate water evaporation. Therefore, all further experiments are performed at the maximal achievable 95% RH and room temperature. To correct for this change, the raw data is post-processed, as shown in Figure 4.2h-j.

The evaporative change in modulus is determined by measuring the modulus at the four corners of the scanned area before and after the experiment. Since the experiment proceeds row-by-row, data is corrected in accordance with experimental time at which it was measured, shown in Figure 4.2i. A second post-process is done for a few outliers in the data by spatially averaging these data points with their immediate neighbours. These outliers are caused by communication errors of the translation stages used in the setup with the computer and are displayed in Figure 4.2. The results after this second post-process are shown in Figures 4.2a-g & 4.2j.

An important factor for mechanical structure is the fiber bundle size. For the meat samples tested in this work, individual fiber bundles can be resolved with the naked eye and are, therefore, on the order of 1 mm. To resolve individual fibers, the used spherical probe radius $R = 1$ mm and the probe was moved across the surface for a scan area $A = 20x15$ mm with step size $L = 0.5$ mm in between measurements. Hence, samples are subsampled as shown in Figure 4.2, which was done to limit the change of the modulus due to evaporation. The indentation step size was 20μm with a maximum indentation depth of 500μm or when a set force threshold for the meat type was reached by the load cell, the probe was retracted and moved to the next position.

4.2.2 Meat samples

In this research, the following were mechanically mapped: meat replacement normal and orthogonal to a processing direction, tofu, raw beef, raw chicken, cooked beef and cooked chicken. The model meat analogue contained soy protein isolate (SUPRO® 500E IP, Solae, St Louis MO, USA), vital wheat gluten (Roquette, Lestrem, France), NaCl, and demineralized water. The analog has a fibrous and soft texture with a final dry matter content of about 30% wt with dimensions of approximately 30x25x100 mm^3 (w x h x l) and is prepared using the shear cell technology on a couette-type shearing device[10,11]. All other samples were purchased at a local supermarket and, unless cooked, measured as acquired after cutting to loadable pieces of sample without any other processing. Cooking samples was done in a pan with sunflower oil, flipping the samples over a few times until they resembled consumer meat.

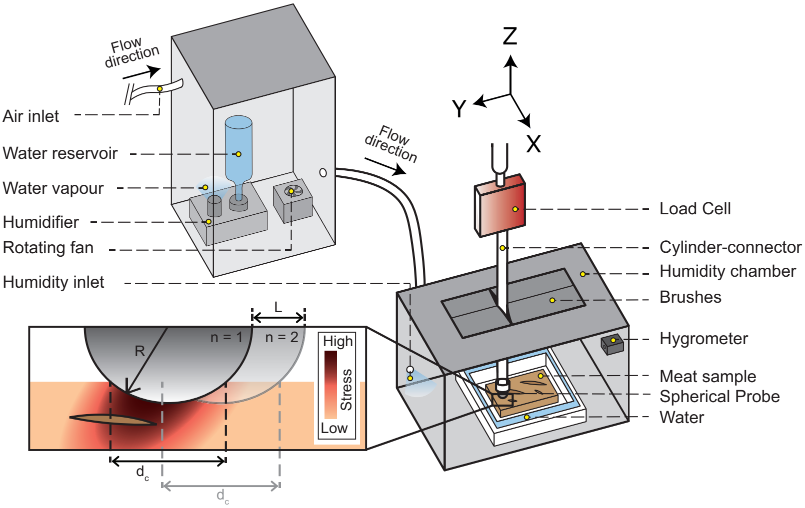

Figure 4.1 – **Experimental setup schematic:** Schematic of the multi-position setup that is used for experiments. The load cell is connected to three translation stages allowing motion in three directions, as indicated by the arrows. The sample is kept in a custom-built humidity chamber to reduce sample evaporation. Water vapour is generated by a custom built humidity-generator, which has an air inlet and a fan, to ensure constant flow of water vapour. The humidity is monitored continuously with a digital hygrometer. The bottom left inset shows indentation with a probe of radius R, a stress profile for indentation number $n = 1$ and the step size L of the probe to $n = 2$. Note that the stress profile is heterogeneous due to the presence of a region of higher modulus within the sample denoted by the outlined region.

4.3 Results

Finding a length-scale for mechanical heterogeneity from mechanical maps of meat

With the multi-point indentation setup, mechanical maps of meat and meat analogues are obtained at the same lateral step size L and total scan area A, shown in Figure 4.2. These mechanical maps are used to quantify a heterogeneous length scale, $\ell_{\frac{1}{2}}$, indicative for the local variation in modulus, by using spatial autocorrelation. A powerful example of spatial autocorrelation is Moran's I, a technique widely used to study spatial data analysis in a variety of topics such as agriculture[12], crime[13], voting[14], and healthcare[15]. Moran's I is defined as:

$$I = \frac{N}{W} \frac{\sum_i \sum_j w_{ij}(x_i - \bar{x})(x_j - \bar{x})}{\sum_i (x_i - \bar{x})^2} \tag{4.2}$$

where I is the Global Moran's I, N is the number of cells, x is the value of $E_{x,y}$ of the cell of interest, $\bar{x}$ is the spatial mean of x, w_{ij} is a spatial weights matrix and W is the sum of all w_{ij}. The value of Moran's I scales from 1 when the sample is fully locally correlated to -1 when fully anti-correlated and 0 when for a random arrangement of the data or decorrelated. The resulting Moran's I for the mechanical maps shown in Figure 4.2 are calculated for two w_{ij} with the open source software GeoDa[16], shown in Figure 4.2k,l. The spatial weights matrix w_{ij} is crucial in determining how the spatial data is correlated and can be defined in multiple ways. In these results, the maps are analyzed by using a 'Queen' connectivity, such that the side and corner sharing neighbouring cells are included in the analysis. Thus a connected weight with no distance weighting and a neighborhood size of 1 is equivalent to,

$$w_{ij} = \begin{pmatrix} 0 & 0 & 0 & 0 & 0 \\ 0 & 1 & 1 & 1 & 0 \\ 0 & 1 & 0 & 1 & 0 \\ 0 & 1 & 1 & 1 & 0 \\ 0 & 0 & 0 & 0 & 0 \end{pmatrix}$$

In addition, the maps are analyzed using w_{ij} of a Queen connectivity

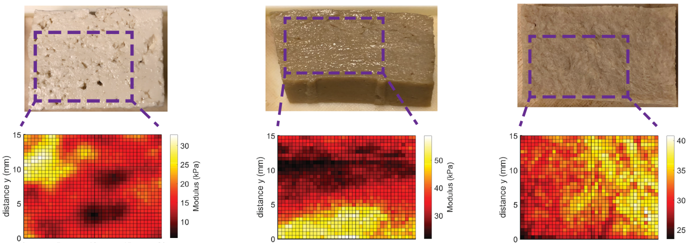

(a) Raw Tofu (b) Meat Replacement (c) Meat Replacement, Orthogonal

(d) Raw Beef (e) Cooked Beef (f) Raw Chicken (g) Cooked Chicken

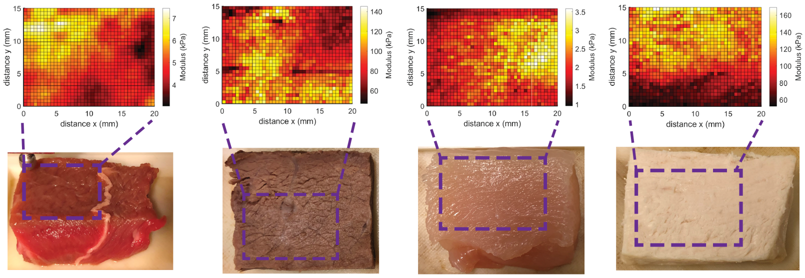

(h) Cooked Chicken, pre-processed (i) Cooked Chicken, post-process 1 (j) Cooked Chicken, post-process 2

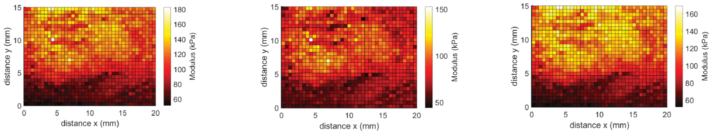

(k) Connected Weight (l) Inverse Distance Weight (m) Decay Length

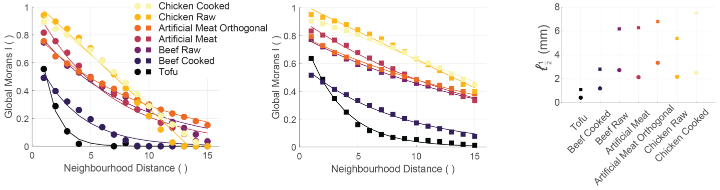

Figure 4.2 – Raw and processed data: (a)-(g) Mechanical maps showing the elastic modulus of the meat samples measured with the multi-position indentation setup. Each map shows the region that is indented by the multi-point indentation setup. Note that the step size L and the total scan area are kept constant. **(h)-(j)** One dataset shown in three different states of the analysis; **(h)** prior to analysis, **(i)** after the first post-process for the change in modulus and **(j)** after the second post-process for the outliers correction. Figures (a)-(g) all show post-process 2 data and figures (g) and (j) are identical. **(k,l)** Global Moran's I plotted versus neighborhood distance for **(k)** a Connected weight and **(l)** an inverse distance weight matrix. **(m)** Shows the decay length, $\ell_{\frac{1}{2}}$, for all the meat (replacement) samples measured for Connected weight (circles) and Inverse distance weight (squares).

combined with an inverse distance weight which for a neighborhood size of 2 is equivalent to,

$$w_{ij} = \begin{pmatrix} 0 & 0 & 0.5 & 0 & 0 \\ 0 & \sqrt{2}/2 & 1 & \sqrt{2}/2 & 0 \\ 0.5 & 1 & 0 & 1 & 0.5 \\ 0 & \sqrt{2}/2 & 1 & \sqrt{2}/2 & 0 \\ 0 & 0 & 0.5 & 0 & 0 \end{pmatrix}$$

Figures 4.2k and 4.2l show the Global Moran's I for both the weights matrices used. Irrespective of the weighting matrix used, Global Moran's I decays as the neighbourhood distance in the correlation increases. This decay correlates to a decreasing local correlation, thus, a length scale for the mechanical heterogeneity: fitting the Global Moran's I data gives a decay length $\ell_{\frac{1}{2}}$ shown in Figure 4.2m. All Global Moran's I data in Figures 4.2k and 4.2l is fitted with an exponential decay function $y = ae^{-bx}$. The decay lengths $\ell_{\frac{1}{2}}$ are calculated with $\ell_{\frac{1}{2}} = \frac{1}{b}\ln(2)\,L$, where L is the step size of the indentation between measurements $L = 0.5$ mm.

4.4 Discussion

All elastic moduli shown in Figure 4.2a-g are calculated from a single indentation using Hertzian Contact Theory, which implicitly assumes a substrate with a homogeneous elastic modulus. However, real experimental samples are mechanically heterogeneous, included those in this work. An inherent consequence of indentation of a mechanically heterogeneous material is blurring of the normal stress response, which leads to blurring of the mechanical map and, therefore, affects the extracted decay length. This normal stress response is blurred over a region larger than the contact area of the spherical probe with the sample, as is depicted in Figure 4.1, and is a function of the probe radius R and indentation depth δ. The size of the indentation area is determined by the contact area of the probe with the surface. In this work, a spherical probe is used, resulting in a contact diameter $d_c = 2\sqrt{R\delta}$, for probes smaller than the thickness of the sample[17] as is the case for all data in Figure 4.2a-g. For the maximum indentation depth reached 500 μm, the contact diameter $d_{c_{max}} \approx 1.4$ mm; thus, each indentation measurement overlaps with the neighbouring indentation measurement, as $d_{c_{max}} > L$ and shown in Figure 4.1. The choice for step size L and scan area A both affect the total duration of the experiment, as the number of modulus scans $n = \frac{A}{L^2}$. Given that the sample modulus changes over time, as elucidated in section 4.2, n should be minimized; A cannot be too big or L too small. A is chosen to comprise several fiber bundles and L is chosen to limit n while still being able to resolve individual fibers, determined by a combination of d_c and L. In the case an intrinsic feature size is unknown, R and L can be varied to determine a feature size. In this work, R, L and A are kept constant, such that all results for the decay length can be compared.

The decay length, $\ell_{\frac{1}{2}}$, obtained by Moran's I analysis of the mechanical maps, holds information on the mechanical structure of the sample. In case Global Moran's I decays rapidly, $\ell_{\frac{1}{2}}$ decreases and the sample is correlated over a short distance. Hence, a large value of $\ell_{\frac{1}{2}}$ is related to a more heterogeneous material and lower value $\ell_{\frac{1}{2}}$ is related to a more homogeneous material. This trend is seen in the data in Figure 4.2. For example, tofu is a commonly used meat substitute that is known for its homogeneous mechanical structure, and therefore a low decay length is expected. Indeed, Figure 4.2m shows that tofu has the smallest $\ell_{\frac{1}{2}}$, implying a higher mechanical homogeneity compared to the other samples. For all other samples, the decay length is dissimilar, indicating a range in the mechanical heterogeneity. For example, $\ell_{\frac{1}{2}}$ for beef is smaller than for chicken; this is likely related to the fiber bundle size, which is larger for chicken.

Additionally, meat samples are anisotropic materials with an elastic modulus dependent on the orientation of the sample. Therefore, the cutting plane of the meat affects the measured elastic modulus. In Figure 4.2b and Figure 4.2c, the sample is cut perpendicular and parallel to the surface, respectively. These mechanical maps clearly show a different structure: In Figure 4.2c, fiber patterns are visible, whereas the map in Figure 4.2b is dominated by an externally applied temperature gradient in the sample production. The resulting $\ell_{\frac{1}{2}}$ captures this heterogeneity with the orthogonal direction being significantly lower than the normal direction, as seen in Figure 4.2m.

Lastly, the magnitude of $\ell_{\frac{1}{2}}$ is dependent on the choice of the w_{ij}, as shown in Figure 4.2m. We chose these two w_{ij} as they are commonly used for spatial correlation analyses, like Moran's I[16]; these w_{ij} are isotropic and not directions. For example, the fiber patterns seen in Figure 4.2c are thus underrepresented in the current isotropic spatial correlation. By contrast, another choice could be a w_{ij} which contains directional orientation with zeros orthogonal to better correlate only in the direction of mechanical anisotropy in the meat samples thus emphasizes this fiber structure; this is of interest for future investigation.

4.5 Conclusion & Future Outlook

The work shown in this paper aims to provide the meat replacement industry with a methodology to quantify the local mechanical resemblance of animal meat to the produced meat replacement. The presented methodology, using a combination of multi-point indentation and Moran's I autocorrelation analysis, shows that a quantitative decay length, that is indicative of local food structure, can be extracted and directly compared between meat replacements and true meat samples.

In future work, the presented elastic moduli maps could be cross-correlated to, for example, local protein content with a bivariant form of Moran's I to find a relation between local food structure and local material content. This local contents information could be obtained using imaging techniques such as Raman microscopy[18]. In addition, to improve the inherently blurred mechanical maps, samples could be indented with probes of multiple radii, to extract decay lengths that hold mechanical information with reduced or even possibly near-zero blurring when the data is extrapolated to an infinitely small probe size.

Appendix Chapter 4: Press Publication

The work presented in this Chapter has also been published in the Wageningen University & Research magazine, Resource, by means of an infographic. The infographic is shown in Figure 4.A.1.

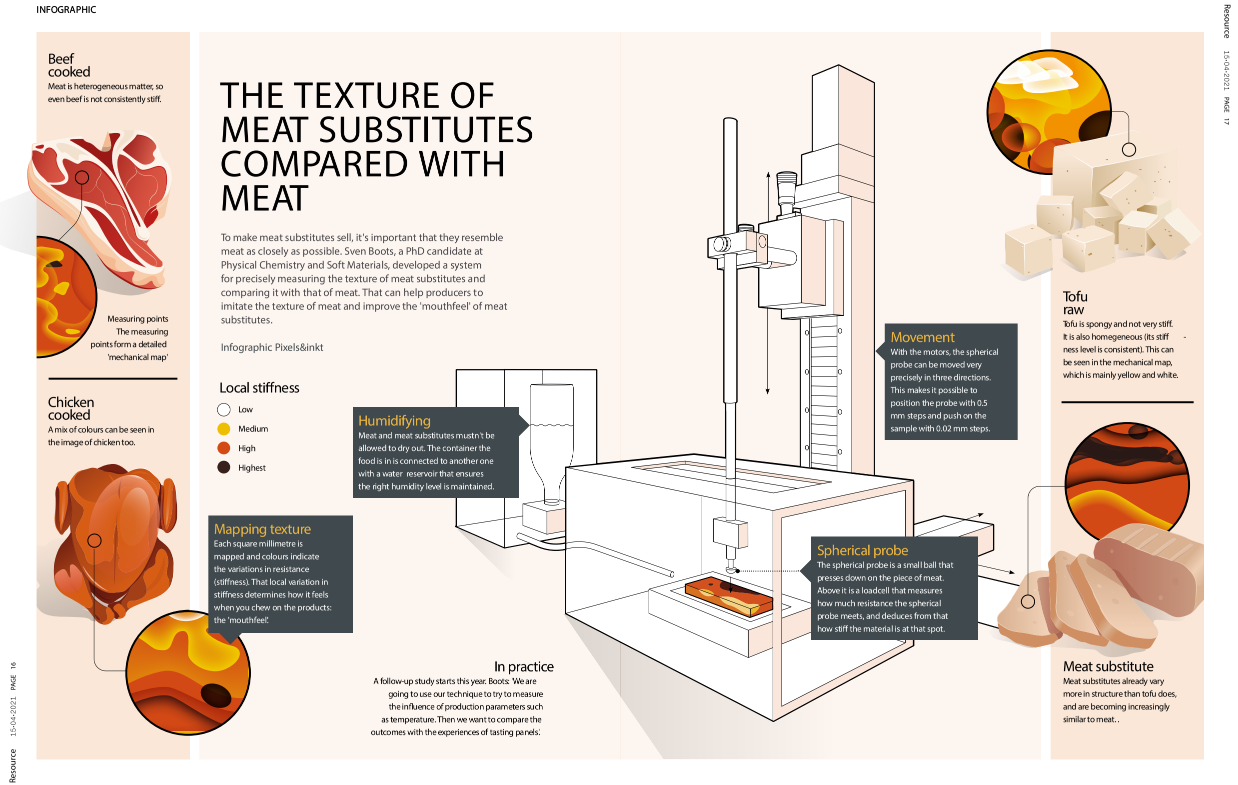

Resource 15-04-2021 PAGE 16

INFOGRAPHIC

THE TEXTURE OF MEAT SUBSTITUTES COMPARED WITH MEAT

To make meat substitutes sell, it's important that they resemble meat as closely as possible. Sven Boots, a PhD candidate at Physical Chemistry and Soft Materials, developed a system for precisely measuring the texture of meat substitutes and comparing it with that of meat. That can help producers to imitate the texture of meat and improve the 'mouthfeel' of meat substitutes.

Infographic Pixels&inkt

Beef cooked
Meat is heterogeneous matter, so even beef is not consistently stiff.

Measuring points
The measuring points form a detailed 'mechanical map'

Chicken cooked
A mix of colours can be seen in the image of chicken too.

Local stiffness

- ○ Low
- 🟡 Medium
- 🟠 High
- ● Highest

Mapping texture
Each square millimetre is mapped and colours indicate the variations in resistance (stiffness). That local variation in stiffness determines how it feels when you chew on the products: the 'mouthfeel'.

Humidifying
Meat and meat substitutes mustn't be allowed to dry out. The container the food is in is connected to another one with a water reservoir that ensures the right humidity level is maintained.

Movement
With the motors, the spherical probe can be moved very precisely in three directions. This makes it possible to position the probe with 0.5 mm steps and push on the sample with 0.02 mm steps.

Spherical probe
The spherical probe is a small ball that presses down on the piece of meat. Above it is a loadcell that measures how much resistance the spherical probe meets, and deduces from that how stiff the material is at that spot.

In practice
A follow-up study starts this year. Boots: 'We are going to use our technique to try to measure the influence of production parameters such as temperature. Then we want to compare the outcomes with the experiences of tasting panels.'

Tofu raw
Tofu is spongy and not very stiff. It is also homogeneous (its stiffness level is consistent). This can be seen in the mechanical map, which is mainly yellow and white.

Meat substitute
Meat substitutes already vary more in structure than tofu does, and are becoming increasingly similar to meat..

Resource 15-04-2021 PAGE 17

Figure 4.A.1 – Publication of an infographic about the project presented in this Chapter in the Wageningen University & Research magazine Resource. Printed with permission of the producer, Pixels&Inkt, Culemborg, Netherlands.

Bibliography

[1] Population Division of the Department of Economic United Nations and Social Affairs. Integrating population issues into sustainable development, including the post-2015 development agenda. 2015.

[2] Birgit L Dekkers, Remko M Boom, and Atze Jan van der Goot. Structuring processes for meat analogues. *Trends in Food Science & Technology*, 81:25–36, 2018.

[3] Sarah PF Bonny, Graham E Gardner, David W Pethick, and Jean-François Hocquette. Artificial meat and the future of the meat industry. *Animal Production Science*, 57(11):2216–2223, 2017.

[4] Jennie I Macdiarmid, Flora Douglas, and Jonina Campbell. Eating like there's no tomorrow: Public awareness of the environmental impact of food and reluctance to eat less meat as part of a sustainable diet. *Appetite*, 96:487–493, 2016.

[5] Laurence Mioche, Pierre Bourdiol, and Sandra Monier. Chewing behaviour and bolus formation during mastication of meat with different textures. *Archives of Oral Biology*, 48(3):193–200, 2003.

[6] Peter Fischer, Michael Pollard, Philipp Erni, Irene Marti, and Stefan Padar. Rheological approaches to food systems. *Comptes Rendus Physique*, 10(8):740–750, 2009.

[7] JNM Boots, R Fokkink, J Van der Gucht, and TE Kodger. Development of a multi-position indentation setup: mapping soft and patternable heterogeneously cross-linked polymer networks. *Review of Scientific Instruments*, 90(1):015108, 2019.

[8] Valentin L Popov. *Contact mechanics and friction*. Springer, 2010.

[9] Elisabeth Huff-Lonergan and A Sosnicki. Water-holding capacity of fresh meat. *Fact Sheet*, 4669, 2002.

[10] Georgios A Krintiras, Javier Gadea Diaz, Atze Jan Van Der Goot, Andrzej I Stankiewicz, and Georgios D Stefanidis. On the use of the couette cell technology for large scale production of textured soy-based meat replacers. *Journal of Food Engineering*, 169:205–213, 2016.

[11] Steven HV Cornet, Dylan Edwards, Atze Jan van der Goot, and Ruud GM van der Sman. Water release kinetics from soy protein gels and meat analogues as studied with confined compression. *Innovative Food Science & Emerging Technologies*, 66:102528, 2020.

[12] Hermann Pythagore Pierre Donfouet, Aleksandra Barczak, Cécile Détang-Dessendre, and Elise Maigné. Crop production and crop diversity in france: a spatial analysis. *Ecological Economics*, 134:29–39, 2017.

[13] Jihoon Chung and Heeyoung Kim. Crime risk maps: a multivariate spatial analysis of crime data. *Geographical analysis*, 51(4):475–499, 2019.

[14] Tony Robinson and Stephen Noriega. Voter migration as a source of electoral change in the rocky mountain west. *Political Geography*, 29(1):28–39, 2010.

[15] Yefu Chen, Junfeng Jiao, Shunhua Bai, and Josiah Lindquist. Modeling the spatial factors of covid-19 in new york city. *Available at SSRN 3606719*, 2020.

[16] Luc Anselin, Ibnu Syabri, and Youngihn Kho. Geoda: an introduction to spatial data analysis. In *Handbook of applied spatial analysis*, pages 73–89. Springer, 2010.

[17] Edwin P Chan, Yuhang Hu, Peter M Johnson, Zhigang Suo, and Christopher M Stafford. Spherical indentation testing of poroelastic relaxations in thin hydrogel

layers. *Soft Matter*, 8(5):1492–1498, 2012.

[18] Huijuan Yang, Wangang Zhang, Teng Li, Haibo Zheng, Muhammad Ammar Khan, Xinglian Xu, Jingxin Sun, and Guanghong Zhou. Effect of protein structure on water and fat distribution during meat gelling. *Food chemistry*, 204:239–245, 2016.

PART II:

Using mechanosensors to obtain detailed microscopic information on material failure

In Part I, a methodology is developed to produce a material with controllable heterogeneity and to characterize this material mechanically (Chapter 2), the blurred characterization is improved upon with finite element method simulations (Chapter 3), and from the mechanical landscape of meat analogues a methodology is developed in which a length scale indicative for the heterogeneity is found, allowing to mechanically quantify texture differences between animal meat and plant-based meat analogues needed to produce meat analogues that mechanically mimic animal meats (Chapter 4).

Part II of this thesis will shift the focus towards microscopic understanding of soft polymer networks, using the 1,2-dioxetane bond to quantify the number of bonds that break in a puncture test in Chapter 5, and the spiropyran bond in combination with LSSI to simultaneously map local stresses and strains spatially and at high time resolution inside an elastomer in Chapter 6.

Chapter 5

Quantifying bond rupture during indentation fracture of soft polymer networks using molecular mechanophores

Understanding the resistance of soft materials to puncture bears relevance to many fields. However, the complex mechanics during deep indentation make it difficult to disentangle how the different dissipation processes contribute to the fracture energy and how this depends on the molecular structure of the material. To investigate this, we perform deep indentation experiments with a flat-ended cylindrical probe on polymer networks containing the covalently incorporated mechanoluminescent bond rupture sensor 1,2-dioxetane. By carrying out the experiments inside an integrating sphere, we are able to quantify the number of ruptured bonds during puncture nucleation and propagation. We find that puncture is associated with significant diffuse damage, both prior to nucleation of the main crack and during crack propagation. Moreover, in agreement with earlier results for uniaxial extension, we show that puncture of double networks leads to strongly enhanced rupture in the pre-stretched sacrificial network, while fracture of the matrix network is much more localized. Finally, we complement the experiments with MD simulations that allow us to link the rupture processes to the distribution of tension in the networks.

This chapter is published as:

J.N.M. Boots, D. W te Brake , Jess M. Clough, J. Tauber, J. Ruiz-Franco, T.E. Kodger, and J. van der Gucht
“Quantifying bond rupture during indentation fracture of soft polymer networks using molecular mechanophores”
Physical Review Materials, 6(2), 025605 (2022)

5.1 Introduction

Soft polymer materials are lightweight and deformable, making them suited candidates for several applications among which are seals[1], tyres[2], vibration dampers, soft robotics[3], haptics[4, 5], and biomedical applications[6, 7]. However, their lifetime in many of these applications is limited by the damage that occurs during deformation or loading. One deformation mode that is particularly prone to cause damage is the indentation with a sharp object, which leads to puncture of the material at high enough forces. Understanding the resistance of soft materials to puncture bears relevance to many fields, including punctures in tyres[8], forensic studies[9], bite mechanics[10], surgery[11] and design of protective clothing[12]. However, compared to the mechanics of fracture in other deformation modes, such as uniaxial extension and uniform compression, puncture mechanics is relatively poorly understood, mostly due to the heterogeneous, strongly localized, and non-linear deformation field that arises during deep indentation and the role of friction and adhesion between the indenter and the material. Recently, Fakhouri, Hutchens and Crosby studied the large strain behaviour of soft elastomers during deep indentation, and they developed a model to predict how the critical indentation force at which puncture starts depends on the size and shape of the indenter[13]. Experimental studies show that the shape of the crack that accompanies puncture is very sensitive to the geometry of the punch tip. While deep indentation with a sharp, conical punch leads to a planar mode-I crack[14], a flat-bottomed cylindrical punch penetrates a soft material by the formation of a ring-shaped mode-II crack that propagates ahead of the indenter tip[15]. A micromechanical model, developed by Shergold and Fleck[16], relates the penetration force to the strain energy stored in the material and the fracture energy needed to propagate the crack. However, it remains unclear how different dissipation processes contribute to the fracture energy and how this depends on the molecular structure of the material. Recent work on the uniaxial extension of elastomers shows that delocalized bond rupture in a large, diffuse zone around the crack tip can greatly enhance the fracture energy[17]. It is unclear, however, to what extent diffuse bond rupture also plays a role in the resistance to puncture and penetration. To make progress in our understanding, and to arrive at a microscopic picture of the puncture process, both for the crack nucleation and propagation stages, there is a clear need for methods that can quantify bond rupture during puncture.

In the past decade, knowledge about molecular scale fracture mechanics gained momentum through mechanochemical tools, such as molecular mechanophores that elicit an optical signal in response to mechanical activation[18, 19]. A particularly powerful mechanophore for fracture studies is the mechanoluminescent probe bis(adamantyl)-1,2-dioxetane[20], which can be covalently incorporated in polymeric materials, for example, by introducing it as a crosslinker in polymer networks produced by free radical polymerisation. The 1,2-dioxetane molecule releases energy in the form of light after being subjected to a thermal or mechanical stimulus that leads to bond rupture (see Figure 5.1a). Upon rupture, the carbon-oxygen ring in the dioxetane crosslinker breaks leading to two adamantones, of which one can be in the excited singlet or triplet state, which in turn can relax to the ground state by fluorescence[21, 22], thereby emitting a photon. Previous work using this mechanophore sheds light on the shape, size and location of the fracture process zone around a propagating crack tip in elastomers subjected to uniaxial tension[17]. These measurements also clearly illustrated the importance of the molecular architecture of the polymer networks, showing strongly enhanced bond rupture in so-called double networks consisting of two interpenetrating polymer networks, thereby providing experimental support for the molecular explanations put forward earlier for the enhanced toughness of such materials[23, 24, 25, 26, 27].

In this work, we use the same dioxetane mechanophores to detect bond rupture during deep indentation and puncture of soft crosslinked polymer materials, both single and double networks. To obtain a truly quantitative measurement of the number of broken bonds, we perform the experiment in an integrating sphere, so that all emitted photons can be detected. By simultaneously measuring the indentation force and the luminescent signal, we relate the mechanical response during different stages of penetration to the underlying molecular events. With the help of numerical mechanical simulations on model networks, this allows us to obtain a more detailed understanding of the microscopic processes occurring during indentation fracture.

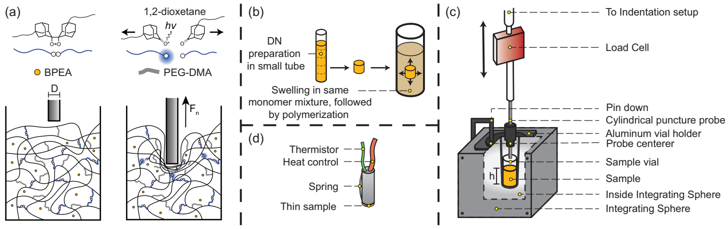

Figure 5.1 – **(a)** Mechanically induced chemiluminescence of a single dioxetane bond (top), BPEA fluorophore and PEG-DMA crosslinker (center), and schematic representation the rupture of multiple dioxetane crosslinkers and some PEG-DMA crosslinkers in a strained polymer network during a deep indentation with a flat-bottomed cylindrical punch of diameter D (bottom). Photons emitted by bond scission events enable quantification of bond rupture during puncture. **(b)** Schematic of the synthesis scheme for the double network (DN): the first network is swollen in the same monomer mixture, which is then polymerized. **(c)** Schematic representation of the puncture experiment, conducted in an integrating sphere. The vial[28] containing the sample was held in place with an aluminum vial holder. After the sample vial was loaded, a 3D printed probe centerer was placed on top of the aluminum vial holder, ensuring puncture to occur in the lateral center of the sample. The puncture was done with custom-made cylindrical rods with flat bottoms of varying size, which were connected to a load cell to measure the force as a function of penetration depth. **(d)** Schematic of the heating element that was used for the heating experiments. Note the spring on the left of the element, which is a key factor that enables a secure position of the probe in the sample vial.

5.2 Materials & Methods

5.2.1 Materials

We prepare networks made of poly(hexyl methacrylate), which is crosslinked using crosslinkers that can be mechanoluminescent (dioxetane-DMA) or optically inactive (PEG-DMA). Hexyl methacrylate (HMA) and polyethyleneglycoldimethacrylate (PEG-DMA, Mn=550 g/mol) were purified on an alumina column before use. Bismethacrylate functionalized bis(adamantyl)-1,2-dioxetane (dioxetane-DMA) was synthesized based on a previously published procedure[20], albeit with a different crosslinking functionality: see Appendix 5.5 for details. 2,2'-azobis(2-methylpropionitrile) (AIBN), a thermal free radical initiator, and 9,10-bis(phenylethynyl)anthracene[29] (BPEA), a fluorophore that redshifts the dioxetane emitted photons[29]) were purchased from Sigma Aldrich and TCI chemicals and used without purification.

5.2.2 Synthesis of polymer networks

Single Network (SN) - Samples with different degree of crosslinking were synthesized, containing either a mixture of dioxetane-DMA to PEG-DMA in a ratio 1:3 as crosslinkers or with dioxetane-DMA as the only crosslinker, in this work indicated with a fraction f=0.25 or f=1 of the crosslinkers is a mechanoluminescent dioxetane molecule, respectively. For the synthesis of f=0.25 networks, dioxetane-DMA (3.5 mg, 0.006 mmol) and AIBN (2.0 mg, 0.012 mmol) were mixed with 0.06 mL BPEA, stock solution of 2.5 g/L in toluene (λ_{abs} = 455 nm, λ_{em} = 486 nm)[30] and HMA (0.50 mL, 2.5 mmol) and PEG-DMA (0.0096 mL, 0.019 mmol) were added, resulting in a stoichiometry of HMA:PEG-DMA:dioxetane-DMA 99:0.75:0.25. Networks with f=1 were made in the same way, except that 14 mg (0.024 mmol) dioxetane-DMA was added and no PEG-DMA, resulting in a stoichiometry of HMA:dioxetane-DMA 99:1. These solutions were degassed with N_2 for 10 minutes. The mixture was allowed to polymerize in the oven at 70°C for 2h. Before removing the cap, the solution was allowed to cool down and left at room temperature (RT) for 2 hours to continue the polymerization. Any remaining volatiles were removed at 70°C under vacuum overnight, slightly shrinking the samples. To maximize contact of the sample with the bottom of the vial, samples were centrifuged at 5000 rpm for 5 minutes, resulting in samples with a height of ~15 mm with negligible shrinkage due to the centrifugation. Yet, a small void between sample and the sides of the vial remained present for most samples.

All experiments reported here were performed with the same batch of dioxetane, ensuring that the luminescent properties were equal for all puncture tests.

Double Network (DN) - First, the first network of the double network is synthesized in an NMR tube with a diameter of 3.9 mm, following the protocol of the single network, see Figure 5.1b. The resulting network is cut in pieces with a height of 7 mm using a scalpel. Then, the network was swollen for two days in a monomer mixture containing HMA (0.30 mL, 1.52 mmol), PEG-DMA (0.007 mL, 0.015 mmol), AIBN (0.001 mg, 0.007 mmol) and 0.033 ml of a 2.5 g/L solution of BPEA in toluene, isotropically stretching the chains of the network. The obtained isotropic prestretching[31] was 1.65, see Figure 5.A.5 in Appendix 5.5. After degassing with N_2, the same protocol as for the SN was followed to polymerize the second network to obtain the DN.

5.2.3 Experimental methods

Indentation experiments - Indentation tests were performed using cylindrical punches (with a diameter of 1 or 0.7 mm) with a flat end. The indentation tests were performed with the sample placed in an integrating sphere (Thorlabs, IS200), see Figure 5.1(c). The integrating sphere was connected to an APD detector (ALV-7004 Digital Correlator) with an optical fiber (Thorlabs, FP600URT). An in-house written script was used to record the collected photons at a frequency of 1250 Hz. Movement of the puncture probes and readout of the load cell were controlled using MATLAB[32]. All puncture tests were performed at RT. For the cyclic loading experiments, samples had to be immobilized to prevent movement of the sample during retraction due to adhesive and friction forces between the sample and the puncture probe. Therefore, the vial was fixed with the 3D printed probe centerer, which in turn was pinned down physically with two bars from the top, as shown in Figure 5.1c.

Calibration of the dioxetane emission - To convert the photon count measured in the integrating sphere into the number of broken dioxetane bonds, we performed a calibration experiment in which we heat a sample in the integrating sphere to 230°C using the heating element[33] shown in Figure 5.1d, leading to thermally activated chemiluminescence[34]. We heated the sample for 3000 seconds, at which point the emission has returned to the noise level and all dioxetane bonds have decomposed thermally (see Figure 5.A.8 in Appendix 5.5). By comparing the total thermoluminescent photon count in this heating experiment to the mechanoluminescent photon count in the puncture experiments (both corrected for background noise), we can estimate the number of broken bonds n_b corresponding to a certain photon count c_p:

$$n_b = \frac{\Phi_T}{\Phi_M} \frac{N_{b,T}}{N_{p,T}} c_p \tag{5.1}$$

where $N_{b,T}$ is the total number of dioxetane bonds present in the thermally decomposed reference sample, which are all assumed to break, $N_{p,T}$ the total photon count in the reference experiment, and the ratio Φ_T/Φ_M corrects for the difference in chemiexcitation yield between thermally activated and mechanically activated dioxetane, with $\Phi_T \approx 17\%$[34] and $\Phi_M \approx 9.8\%$[35]. Note that n_b denotes the number of broken bonds during one acquisition interval of 0.8 ms. The cumulative number of broken bonds up to a certain strain $\Sigma n_b(\delta)$ can then be obtained by integration. We assume that the photon capture efficiency is not affected by the presence of the puncture probe or heating element, because both are made from materials that reflect most of the light. Furthermore, while the different sizes of the probe and the heating element might influence the leakage of photons from the integrating sphere slightly, the overall photon leakage is so small that these differences are expected to be negligible. More details about the calibration can be found in Appendix 5.5.

5.2.4 Simulations

Single Network (SN) - We model the polymer network using a two-dimensional network model. We start by placing monomers on a triangular network of $N \times N$ nodes with $N = 170$, and lattice spacing l_0. Neighbouring monomers are then connected to each other with a probability $p_1 = 0.7$, and dangling bonds, which are elastically inactive, are removed from the network. Between each connected pair of nodes, a polymer chain of $N_m = 6$ connected monomers are inserted, resulting in an overall crosslink density of 8.7%. Here, crosslinkers are defined as nodes that connect at least three chains.

The excluded volume interaction is described by the Weeks-Chandler-Andersen (WCA) potential to mimic excluded volume, defined as[36]

$$V_{WCA}(r) = \begin{cases} 4\epsilon\left[\left(\frac{\sigma}{r}\right)^{12} - \left(\frac{\sigma}{r}\right)^{6}\right] + \epsilon \text{ if } r \leq 2^{1/6}\sigma \\ 0 \qquad\qquad\qquad\qquad\qquad \text{otherwise} \end{cases}, \tag{5.2}$$

where σ is the diameter of a monomer, used as the unit length, and ϵ controls the energy scale. The networks were equilibrated in two steps, using NPT-ensemble simulations with a Nosé-Hoover thermostat[37]. In the first step, we equilibrate the network without allowing for bond rupture, by using a finite extensible nonlinear elastic (FENE) potential for the bonds between bonded neighbouring monomers, expressed as[38]

$$V_{FENE}\left(r\right) = -\epsilon k_F R_0^2 ln\left[1 - \left(\frac{r}{R_0\sigma}\right)^2\right], \tag{5.3}$$

where $k_F = 15\epsilon/\sigma^2$ is the dimensionless spring constant and $R_0 = 1.5\sigma$ is the maximum extension of the bond. The mass of all particles is m, and hence, here and in the following, we express all quantities in reduced units: $[T] = \epsilon/k_B$ for the temperature, $[P] = \epsilon\sigma^{-2}$ for the pressure, and $[t] = \sqrt{m\sigma^2/\epsilon}$ for time, where k_B is the Boltzmann constant. In this mode, the energy minimum is found at $r_{min} = 0.96$. We fix $P = 0.0$ and $T = 1.0$, allowing anisotropic fluctuations of the periodic simulation box during 10^6 steps.

Next, we change the potential to a quartic potential, which allows us to model fracture processes in a realistic way[39, 40]:

$$V_Q\left(r\right) = k_Q\left(r - R_c\right)^3\left(r - R_c - B_1\right) \tag{5.4}$$

where R_c is the cut-off radius that establishes the maximum bond length. Bonds break irreversibly if the bond length r exceeds R_c. We consider several different types of bonds in our simulations, with parameters as specified in Table I (plots of the different potentials can be found in Fig. S6b). In particular, the mechanoluminescent dioxetane crosslinkers used in the experiments are known to have a lower rupture force than the other covalent bonds in the polymer network. We therefore denote the bonds in the main chain of the polymers and of the non-dioxetane crosslinkers as ‘strong’ bonds, while the dioxetane bonds are denoted as ‘weak’ bonds; three types of weak bonds, varying in rupture force as governed by the parameter k_Q, are considered (see Table I). The parameter B_1 is fixed at -0.7425 and $R_c = 1.5$ in all cases. The energy minimum is closer to $r_{min} = 0.96$, which is also the same as that for the FENE potential, so that any artificial stress accumulated after the change of the potential is minimized. However, before starting the indentation simulation, the network is re-equilibrated in the same way with the new potential. Note that bonds can in principle break during the second equilibration step, but we did not observe any bond rupture.

Bond type	k_Q	V_{min}	F_{max}
Strong	4751	-153	486
Weak-I	4251	-136	435
Weak-II	3651	-117	373
Weak-III	2351	-75	241

Table 5.1 – Four different quartic potentials V_Q used with four different values of the parameter k_Q. The bond energy (the minimum of the potential) and the rupture force (calculated as the maximum value of $\mathrm{d}V_Q/\mathrm{d}r$) are also listed for each potential (in reduced units).

Double Network (DN) - Double networks (DN) are modelled by adding a second type of polymers between the crosslinkers defined previously in the single network. We choose a connectivity of $p_2 = 0.55$ for this second network (denoted DN-II), which ensures that the second network is fully percolated, but has a lower crosslink density than the first network, as is also the case in experimental DNs[41]. In the experimental networks, the prestress in the first network (denoted DN-I) resulting from the swelling step causes bonds in the first network to be more prone to rupture than those in the second network. Here, we account for this by assigning a weaker potential ('weak-III', see Table I) to the crosslinks in the first network and a 'strong' potential to the crosslinks in the second network. The networks are equilibrated again in two steps, similar to the SN.

Indentation simulations - The indentation of the networks is simulated in the NVT-ensemble using Langevin dynamics. Here, the friction coefficient of the monomers is fixed at $\xi_F = 1.0$. Periodic boundary conditions are considered in the horizontal direction (perpendicular to the direction of indentation), while reflective walls are used at the top and bottom edges. The indenter is modeled as a collection of $N_x \times N_y$ overlapping spherical particles of diameter $\sigma_I \geq 10\sigma$ (see Fig. S6c) that interact with the monomers by the WCA potential previously defined. This set of particles behaves as a rigid solid moving with a velocity $\mathbf{v}_I = -|v|\hat{e}_y$, where $|v| = 0.01$ and $\hat{e}_y$ is the unit vector in the y-direction. The indentation force is measured by averaging the force exerted on the particles at the bottom of the indenter (which we denote as the sensor). We compare several indenter widths, $D = 22\sigma, 32\sigma, 44\sigma$, and 68σ.

Equilibration and puncture simulations are carried out using the

LAMMPS simulation package[42] with a simulation time step $\Delta t = 0.002$. The results are averaged over two system realizations for each set of parameters. Additional information is shown in Appendix 5.5.

5.3 Results & Discussion

5.3.1 Puncture of single networks

To allow for quantification of the number of broken bonds during puncture, we prepare HMA polymer networks in which a fraction f=0.25 of the crosslinkers is a mechanoluminescent dioxetane molecule (Figure 5.1a). We then perform indentation experiments with a flat-bottomed cylindrical punch of diameter D inside an integrating sphere, while simultaneously measuring the force F_n as a function of indentation depth δ (Fig. 1c). This set-up does not allow us to obtain spatial information about the rupture of bonds; however, it does enable us to collect all photons emitted by ruptured dioxetane bonds, which is required for obtaining quantitative information about the number of broken bonds.

A typical force-distance curve is shown in Figure 5.2a (top panel). The force curve is non-linear, with a pre-puncture response indicating a stiffness that increases with depth. Our data are in good agreement with previous work that reported a transition from a linear response $F_n \sim \delta$ at small depth to a quadratic response $F_n \sim \delta^2$ for deeper indentation (see Figure 5.A.9), which could be explained by modelling the material as a Neo-Hookean solid[13]. For small depth ($\delta < D$), the force response for a cylindrical punch in given by[43, 44]:

$$F_n = DE^*\delta \tag{5.5}$$

where $E^* = E/(1-\nu^2)$ with E the Young's modulus of the material and ν the Poisson ratio, which is $\nu \approx 0.5$ for the nearly incompressible polymer networks that we use. From the initial slope of the force-depth curve we then find a Young's modulus on the order of 2 MPa for our samples (Figure 5.3a).

At a critical depth δ_c, the indenter pierces through the surface of the material and the force drops abruptly. As the indenter continues to move down after a crack has nucleated, the force reaches a quasi-steady state,

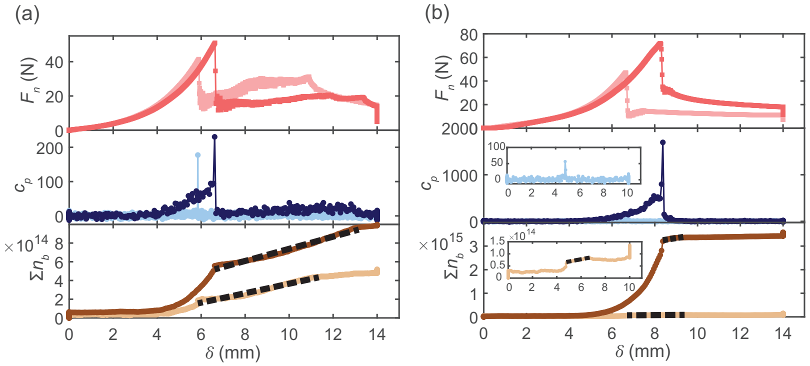

Figure 5.2 – The normal force F_n measured by the bulk load cell (top), the photon counts c_p recorded by the detector (middle) and the cumulative number of bonds broken Σn_b (bottom) as a function of the probe depth δ, for **(a)** a SN indented with a probe with $D = 1$ mm at $v = 2$ mm/s and, in lighter color in the background, $D = 1$ mm, and $v = 0.5$ mm/s, **(b)** DN-I with $D = 1$ mm at $v = 2$ mm/s and, in lighter color in the background, DN-II with $D = 1$ mm at $v = 2$ mm/s. Λ is deduced from the slope of the linear fits, indicated with dotted lines. Insets in the middle and bottom plots in panel b show the DN-II network at different y-axis scale. Please note the different scales on the vertical axes between panels a and b.

which is significantly lower than the force at which the initial puncture takes place. In this stage of steady penetration, a ring-shaped crack propagates ahead of the indenter as it moves down[16]. Clearly, the force required to propagate the crack is smaller than the force required for nucleation.

The dioxetane emission c_p collected by the integrating sphere allows us to detect the rupture of bonds during the different stages of penetration. As shown in Figure 5.2a (central panel), the dioxetane emission rises already before puncture occurs, and then shows a sharp peak during crack nucleation, indicating a large and abrupt rupture cascade accompanying crack nucleation. After the crack has nucleated, the photon count reaches a steady, but non-zero value, which reflects bond rupture as the crack propagates.

To convert the photon count into the number of broken bonds, we perform a calibration experiment using a reference sample in which dioxetane bonds are decomposed thermally inside the integrating sphere, as described in detail in the Methods section and in Appendix 5.5. The cumulative number of broken bonds Σn_b as the probe penetrates the sample as a function of depth is shown in Figure 5.2a, bottom panel. Again, we clearly see that bond rupture starts well before the main puncture event (which occurs at $\delta_c = 6.5$ mm for the experiment with a probe velocity of 2 mm/s and at $\delta_c = 5.8$ mm for a probe velocity of 0.5 mm/s). After the crack has nucleated, the cumulative bond rupture count increases linearly with δ, which agrees well with the idea of a crack that propagates steadily as the indenter moves down. From the slope of the curve, $\Lambda = \partial \Sigma n_b / \partial \delta$, we can estimate the width of the fracture zone. Assuming that the puncture occurs by forming a ring-shaped crack with a diameter that is comparable to the diameter D of the indenter[16], the surface area of the crack is $\pi D d$ with d the length of the crack, which is assumed to increase proportionally to δ. From this, we estimate the number of ruptured dioxetane bonds per unit crack area for this network as $\Sigma = \Lambda/\pi D = 1.4 \times 10^{19}$ m^{-2} for $v = 2$ mm/s, where the value of Λ is an average over 28 independently measured samples prepared in the same way. We can compare this number to the number that would be expected for a sharp crack surface as occurs for ideal brittle fracture, in which all bonds break in one single fracture plane; this can be estimated as $\Sigma_0 = f/(\xi^2)$ with ξ the average distance between crosslinks and where the factor f denotes the fraction of dioxetane crosslinkers relative to the total number of crosslinks, in this case equal to 0.25. We note that some of the crosslinkers may have reacted only at one end. In our estimate of Σ_0, we have implicitly assumed that the relative proportion of such inactive crosslinkers is the same for the dioxetane and PEG crosslinkers. Estimating ξ as $\xi \approx (E/3k_BT)^{-1/3}$, as expected from classical rubber theory, we find $\xi = 1.7$ nm, and $\Sigma_0 = 8.8 \times 10^{16}$ m^{-2}. Comparing Σ and Σ_0 we can define an enhancement factor α, which specifies the increase in bond rupture compared to the ideal brittle case

$$\alpha = \frac{\Sigma}{\Sigma_0} = \frac{\Lambda \xi^2}{f \pi D} \tag{5.6}$$

For the present case, $\alpha \approx 160$, indicating that the fracture zone extends over a zone that is much wider than the mesh size, which also implies a large increase in the fracture energy. As is evident from post-mortem images of punctured samples, shown in Fig. 16S, this may be due to a wide and diffuse crack surface, to microcracks that radiate out from the main crack, or to irregularities in the crack shape.

We then repeated these measurements for a different probe diameter

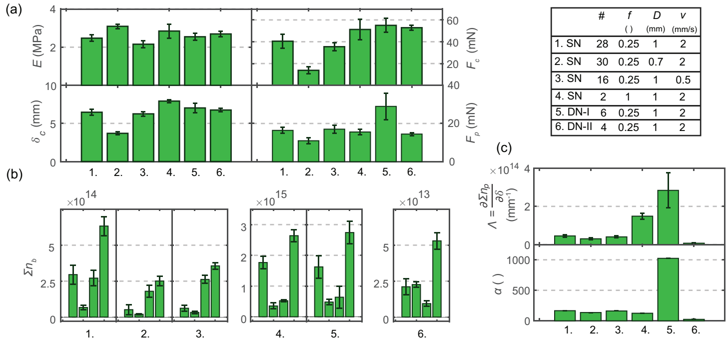

	#	f ( )	D (mm)	v (mm/s)
1. SN	28	0.25	1	2
2. SN	30	0.25	0.7	2
3. SN	16	0.25	1	0.5
4. SN	2	1	1	2
5. DN-I	6	0.25	1	2
6. DN-II	4	0.25	1	2

Figure 5.3 – **(a)** Bar plots of mechanical data; the elastic modulus E, the critical puncture depth at the main failure event δ_c, the critical normal force recorded by the bulk load cell at the puncture event F_c and the force during crack propagation F_p. **(b)** Bar plots showing the number of broken bonds before, during and after the main failure event n_{prior}, n_{main}, n_{post} and their sum $\Sigma n_b = n_{prior} + n_{main} + n_{post}$, from left to right within each of the samples. Please note the varying scales on the y-axes. **(c)** The number of broken bonds per unit crack length Λ and the enhancement factor α (Equation 5.6). The numbers indicate different samples and conditions as specified in the table at the top-right; ($\#$) denotes the number of independent measurements for each configuration, (f) denotes the fraction of crosslinkers that is mechanoluminescent, (D) denotes the probe diameter and v the probe velocity.

and indentation velocity (Figure 5.3). For an indenter with a smaller diameter, $D = 0.7$ mm, we find that the critical penetration depth for rupture becomes roughly a factor of 1.75 lower, while the corresponding force decreases with a factor of 2.9 (Figure 5.3a-2). This is in reasonable agreement with findings by Fakhouri, Hutchens and Crosby[13], who found $\delta_c \sim D$ and $F_c \sim D^2$. The force F_p during the propagation stage is roughly 1.4 times smaller for the smaller probe, which corresponds to an increase in indentation pressure ($4F_p/\pi D^2$) by a factor 1.4 times, in qualitative agreement with earlier findings[16]. The number of bonds that break prior to and during the main puncture event are significantly smaller than for the larger probe (Figure 5.3b-2), which indicates that crack nucleation is a much more localized event for this smaller probe size. For the propagation stage, we find that the number of bonds per unit crack length Λ decreases approximately proportionally to D, which means that the enhancement factor α, which characterizes the crack sharpness (Equation 5.6), is very similar to the one found for the larger probe (Figure 5.3c-2).

Decreasing the velocity does not lead to a large change in the critical puncture depth and force (Figure 5.3a-3). However, when looking at the broken bonds, we observe that the number of ruptured bonds prior to crack nucleation decreases by approximately a factor of 5 (Figure 5.3b-3). Apparently, the reduction in indentation velocity allows for additional stress relaxation mechanisms that reduce bond rupture. In the propagation stage, however, the effect of the velocity is much smaller, as can be seen from the enhancement factor α which decreases only by a factor 1.03 (Figure 5.3c-3). Remarkably, the effect of probe velocity on bond rupture is much smaller during the crack propagation stage than during crack nucleation. Apparently, the dissipative processes around the crack front are less rate-dependent in this velocity range than those involved prior to rupture; the origin of this difference is not clear.

The samples that we considered so far were crosslinked using a mixture of PEG-DMA and dioxetane DMA crosslinkers, with f=0.25. Since the dioxetane crosslinkers are weaker than other covalent bonds, the introduction of dioxetane linkers may affect the bond rupture process. To investigate this, we have also prepared samples with dioxetane crosslinkers only (f=1). As shown in Figure 5.3a-4, the type of crosslinker does not have a significant effect on the Young's modulus, the critical puncture strain and force, and the force required for crack nucleation. As expected, the number of dioxetane bonds that break in these samples is higher than in the mixed sample for the same indenter diameter and indentation velocity (Figure 5.3b-4 and 13S). In particular, the number of bonds that break before (n_{prior}) and during (n_{main}) the main puncture event is 5-6 times higher than for the mixed sample. Considering that the number of dioxetane bonds is four times higher in these samples, this suggests that the higher fraction of weak dioxetane bonds facilitates bond rupture. Such an enhancement is not observed during the propagation stage, as the enhancement factor α (Equation 6) is somewhat lower than for the sample with mixed crosslinkers (Figure 5.3c-4), indicating a slightly sharper crack surface for the sample with only dioxetane crosslinkers.

5.3.2 Puncture of double networks

In the last decade, it has become clear that the resistance to fracture of a polymer material can be enhanced significantly by creating so-called double networks (DNs)[23]. In particular, tough DN elastomers have been made by swelling a first network in a liquid consisting of monomers that are then polymerized to form the second network[17, 25]. The first network (also called the sacrificial network), thus carries prestress due to the swelling and therefore tends to fracture before the second network (the matrix). This leads to large damage zones (microcracks) in the first network, which are held together by the intact matrix chains. Hence, the increased toughness is believed to result from the large number of sacrificial bonds that rupture upon fracture[17, 25, 40, 41].

Here, we use our experimental set-up to study puncture of double network elastomers. We prepare DNs as described previously[17], while incorporating dioxetane crosslinkers (at f=0.25) either in the first network (DN-I) or in the second (DN-II), see the Methods section. The force-depth curve for the DNs is very similar to that for the single networks, showing a significant increase in the stiffness with increasing strain, followed by an abrupt drop as the sample punctures (Figure 5.2b, top panel). The critical depth and force and the elastic modulus are also comparable to those for the SNs (Figure 5.3a-5,6), with the latter in line with a previous report[31]. The force for crack propagation is a bit higher in DN-I than for the single networks, which could be due to a higher toughness[14]; however, this is not the case for DN-II. Possibly, the crosslinking reaction in DN-II was less efficient than in DN-I, which could have caused this difference in propagation force. While the force response may not be very distinctive, the dioxetane emission is strongly increased for DNs with the dioxetane in the first network (see Figure 5.2c, and Figure 5.3b-5), both before and after the main puncture event. This confirms the hypothesis for the toughening of DNs due to extra bond rupture in the sacrifical network. By contrast, for DN-II, which has the dioxetane in the second network, the emission is much lower than for the SNs (Figure 5.3b-6), indicating very limited bond rupture in the matrix network. A similar behaviour is seen in the propagation phase, where the parameters Λ and α are much higher than for the SNs if the dioxetane is in the first network, while they are much lower when the dioxetane is in the second network (Figure 5.3c-5,6). Note, however, that for the DNs the propagation phase (as signified by the linear increase of Σn_b versus δ) extends only for a small range of depths; already long before δ reaches its maximum value, the bond rupture levels off and reaches a plateau, indicating that the crack propagation is halted. This is in contrast to the SNs, where bond rupture proceeds until the indenter is nearly at the bottom of the vial. This arrest of the crack propagation is confirmed by post-mortem images in Figure 5.A.16, which clearly show that the crack only proceeded through roughly half of the sample. This arrest of the crack is probably caused by the higher toughness of these materials, which prevents further crack propagation if not enough energy can be released.

Cyclic indentation of DNs - As shown above, most samples show significant bond rupture prior to the nucleation of a macroscopic crack. This accumulated damage should result in significant hysteresis and softening upon repeated loading, already before puncture occurs. We investigate this hysteresis for the DN-I sample, for which the photon emission is highest, by performing repeated indentation cycles at progressively increasing maximum depth δ_m, with 5 cycles for each depth (see Figure 5.4a). For this sample, macroscopic crack nucleation occurs in the first cycle of the series with $\delta_m = 14$ mm, as indicated by the large peak in the dioxetane emission. However, significant emission can be detected already in the earlier cycles, indicating damage accumulation preceding fracture, similar to what we observed in the steady penetration data. As shown in Figure 5.4b, this accumulated damage leads to a softening of the material. In fact, this softening strongly resembles earlier observations on double networks under uniaxial tension, which were ascribed to the so-called Mullins effect[25]: in the later cycles, the indentation force is significantly lower on restraining below the maximum previously applied depth, see Figure 5.A.10. The area enclosed between the first loading to a certain depth and the reloading to that same depth is a measure for the irreversibly dissipated energy due to the accumulated damage. Note that this hysteresis energy is much smaller than the hysteresis between the approach and retract curves, which also includes viscoelastic dissipation and friction and adhesion between the probe and the material.

The corresponding dioxetane emission is shown in Figure 5.4c. Significant emission is detected only when δ_m exceeds 9 mm. The material does already soften at lower indentation depths, as shown in Figure 5.4b, but apparently this is not accompanied by significant emission. Possibly this is because the number of ruptured bonds in these cycles is too low to cause

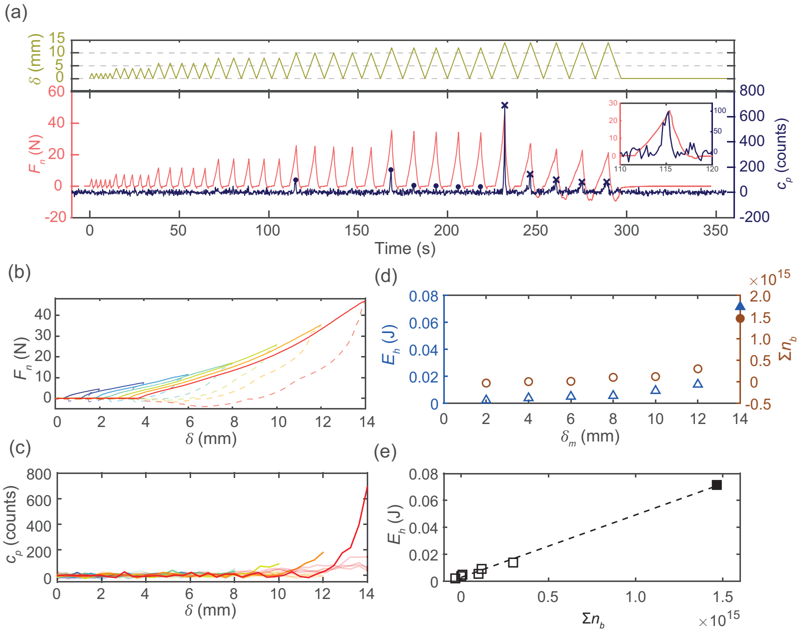

Figure 5.4 – **(a)** Cycling indentation tests of double network DN-I, showing the the depth δ (top) and the resulting force F_n in red and photon count c_p in blue (bottom) as a function of time. Circles and crosses indicate cycles where c_p exceeds the noise level before and after the main fracture event, respectively. The inset shows the first cycle with significant photon count. **(b)** Force-distance loops showing the first cycle of every depth; full curve is the approach and dashed curve the retract curve. **(c)** Photon counted by the detector c_p for all cycles with the first at each d_m plotted with zero transparency and the other four with some transparency. **(d)** The hysteresis energy E_h ($\triangle$) and the cumulative number of broken bonds Σn_b ($\circ$) both summed over 5 cycles at a maximum applied puncture depth δ_m, plotted versus δ_m. **(e)** E_h vs. Σn_b both summed over 5 cycles at δ_m with the dashed line a linear fit, with the slope indicating the energy dissipated per broken dioxetane bond. Filled data points indicate data after the main fracture event.

emission beyond the noise level. For deeper indentation, the dioxetane emission increased with increasing maximum depth. The emission in the first cycle at each δ_m is much higher than that in subsequent cycles, however. Moreover, significant light was emitted only when the depth reached a value that it had not yet reached before, indicating that few additional bonds were broken upon indenting again to the same depth. These data are in very good agreement with earlier observations of bond rupture during repeated tensile loading of filled elastomers[45].

To investigate the relation between the irreversible softening of the material and the number of broken bonds in more detail, we determine both the cumulative hysteresis energy E_h, determined by integrating the approach force over the indentation depth and taking the difference between subsequent cycles, and the cumulative number of broken dioxetane bonds Σn_b, both summed over all 5 cycles at a maximum depth δ_m (using the same calibration as used before). The two are plotted as a function of the depth δ_m in Figure 5.4d, while Figure 5.4e shows the relation between the cumulative number of broken bonds and the total hysteresis energy. We find a linear relation between E_h and $\Delta\Sigma n_b$ in Figure 5.4e. We can obtain the energy dissipated per ruptured dioxetane bond from a linear fit to the data in Figure 5.4e, giving a value of approximately 2.8×10^4 kJ/mol. Comparing this to the energy required to mechanically rupture a dioxetane bond, which has been estimated to be around 50 kJ/mol[45], we see that roughly 0.2 % of the dissipated energy is directly caused by rupture of the dioxetane bonds, similar to an earlier report for uniaxial loading of a filled elastomer[45]. The additional dissipation can be explained in part by the Lake Thomas theory for polymer fracture[46], which explains the enhanced fracture energy of polymers by the fact that stretching a polymer strand stores energy in all backbone bonds in the strand; rupture of one of the bonds then releases all this energy. Furthermore, the current methodology only reports rupture of dioxetane bonds, whereas other bonds, i.e. the PEG-DMA and the HMA backbone, also have to break around the tip, leading to an underestimation of the total number of ruptured bonds during the hysteresis tests. Lastly, it is very likely that additional dissipation mechanisms (such as friction or viscoelastic effects) contribute to the hysteresis energy[47]. We note that mechanical hysteresis is sensitive to the size of the sample; since in our experiments the sample thickness is not orders of magnitude larger than the indentation depth, the values we find are likely to be influenced by boundary effects.

5.3.3 Simulations

To obtain a more microscopic insight into the puncture process, we perform Molecular Dynamics (MD) simulations of the indentation process, using two-dimensional bead spring networks with quartic potential bonds (see Methods). During the simulations, we monitor the force exerted by the probe on the network F, as well as the cumulative number of broken bonds Σn_b. We first consider networks in which all bonds have the same potential ('strong bonds', see Table 1), indented by probes of different diameter (Figure 5.5a). In agreement with the experimental observations, we find that F first rises non-linearly due to elastic response of the material, and then drops abruptly as the probe punctures the material. After the drop the force reaches a steady value around which it fluctuates as the probe moves further downward. Similarly to the experimental force curves (Figure 5.3a), the critical depth δ_c and force F_c at rupture and the propagation force F_p increase as the probe diameter increases. The evolution of the number of broken bonds Σn_b (Figure 5.5a, lower panel) also follows a similar trend as observed experimentally (Figure 5.2a): Bond rupture starts already before the main puncture event, then increases significantly around the peak force (as seen by the increase in slope) before reaching a more or less constant slope within the crack propagation phase. Both the number of broken bonds before and during the main fracture event, and the slope Λ of the curves in the propagation phase increase with increasing probe diameter (see Figure 5.A.19 and 5.A.20), in agreement with the experimental results shown in Figure 5.3b and c.

Figure 5.5b shows snapshots that highlight the distribution of tension in the polymer chains underneath the indenter for indentation depths around and after the peak force, with stretched bonds shown in red. Just before crack nucleation ($\delta \sim \delta_c$), the stretched bonds form long 'force chains' around the probe. Bond rupture then partially relaxes these force chains, and after crack nucleation the distribution of stretched bonds is more irregular, although the force chains can still be observed in right panel in Figure 5.5b. We note also that the stretched bonds occur predominantly a small distance ahead of the indenter, so that the crack also propagates ahead of the probe. Remarkably, the rupture can be postponed by increasing D, which can be explained by the presence of stretched bonds occupying areas farther away from the front of the indenter, indicating thus a delocalization of stress (see Figure 5.A.21). Analyzing the distribution of broken bonds, we find that bond rupture occurs underneath the indenter, while the rest of the network remains undamaged (Figure 5.5c). Similar scenarios are found for different diameter probes and for different

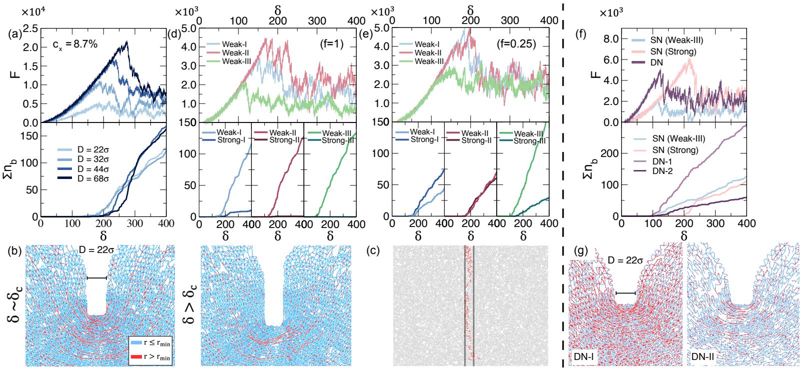

Figure 5.5 – **(a)** Force F and cumulative number of bonds broken Σn_b as a function of the probe depth δ for SN's with crosslinker concentration $c_x \sim 8.7\%$. **(b)** Snapshots of the SN with $c_x \sim 8.7\%$ and $D = 22\sigma$, at $\delta \sim \delta_c$ and $\delta < \delta_c$. **(c)** Broken bond position regarding the rest network. The vertical lines indicate the size D of the probe. **(d)** F and Σn_b as a function of δ for SN's with 100 % of crosslinks with weak bonds, punctured with a probe size $D = 22\sigma$. **(e)** Same information for SN's with 25 % of crosslinks with weak bonds. **(f)** F and Σn_b for a DN punctured with a probe of $D = 22\sigma$, having DN-I $c_x \sim 8.7\%$. Here, we compare the mechanical response of the DN with the single DN-I in the cases where the bonds are defined as strong (*SN-Strong*) or weak (*SN-Weak*). Likewise, Σn_b is split in broken bonds on DN-I and DN-II, respectively. **(g)** Snapshots showing the distribution of stretched bonds (red color) on the DN-I and DN-II.

degrees of crosslinker, as shown in Appendix 5.5 in Figure 5.A.22. We note, however, that the propagation of the crack is likely to occur in a different way than in the experiments, because the simulations are performed for two-dimensional networks, where a ring-shaped crack cannot develop. Moreover, while the experimental probes are many orders of magnitude larger than the mesh size of the networks, in the simulations the difference is only one order of magnitude, so that the probe is comparatively sharper in the simulations.

Next, we consider networks consisting of mixtures of strong and weak bonds, to mimic the networks that contain dioxetane crosslinkers, which are known to be weaker than other covalent bonds. Since the relative rupture force of dioxetane bonds compared to other covalent bonds is not precisely known, we consider three different weak potentials, as specified in Table 1. In the case where all crosslinkers are weak bonds while the backbone bonds are strong (f=1), we find that the rupture force first increases as the strength of the weak bonds increases, although the Weak-II case here shows a slightly higher peak force than Weak-I (Figure 5.5d). We believe, however, that the difference in peak force between Weak-I and Weak II is within the simulation error, because the stochastic nature of crack nucleation leads to relatively large differences in the moment of fracture, especially for these relatively small systems. Likewise, the large majority of bonds that break are (weaker) crosslinks, although for the weak-I potential, whose rupture force $F_{max} = 435$, being the smallest difference with the strong bonds also some backbone bonds are ruptured. In the case where only 25 % of the crosslinks are weak bonds (f=0.25), we observe that the exact nature of the potential has less influence on the puncture process (Figure 5.5e). Thus, for the weakest crosslinks, weak-III, characterized to have $F_{max} = 241$, rupture occurs predominantly at the weakest links, but upon reducing the difference in strength, we see more and more strong bonds that rupture (see also Figure 5.A.19). This shift illustrates the balance between the localization of stresses in the network and the strength of the bonds in determining the pattern of bond rupture: in the presence of a significant amount of very weak bonds (weak-III), fracture occurs predominantly by rupture of weak bonds, and hence the location of these weak bonds determines how cracks propagate. On the other hand, for the weak-I case, for which the difference in bond strength is smaller, the distribution of mechanical stress becomes more important, and thus strong and weak bonds have roughly the same probability to break. Comparing Figures 5.5d and 5.5e, we can see that for Weak-III, the number of broken weak bonds depends only weakly on their relative fraction in the network f, while for Weak-I, the number of broken weak bonds increases strongly as f goes from 0.25 to 1. The latter is closer to our experimental findings in Figure 5.3b, where the number of broken dioxetanes was found to increase more or less proportionally to f. This suggests that the difference in bond strength between the dioxetane bonds and the other bonds is relatively modest.

Finally, we perform simulations on the puncture of double networks. As explained in the methods section, we account for the pre-stretch in the first network DN-I (also called sacrificial network) by assigning a weaker potential (of type weak-III) to the crosslinks in this network. As shown in Figure 5.5f, we find that puncture of the DN occurs at roughly the same indentation depth as for the single network obtained by only considering DN-I, while the propagation force after crack nucleation is similar to that found for the strong network DN-II. Similarly to the experimental DNs (Figure 5.2b), we find a strongly enhanced number of broken bonds in the first network DN-I, while the number of broken bonds in the second network DN-II is reduced (Figure 5.5f, lower panel). The number of ruptured bonds in DN-I is also higher than that in a single network with the same topology and bond potential, which indicates that the enhanced rupture is not due to presence of weaker bonds, but due to the interplay between the two networks. To further illustrate that, we present snapshots showing the distribution of tension in the two parts (at $\delta \sim \delta_c$) of the DN in Figure 5.5g. Clearly the stresses are much more delocalized in DN-I, with stretched chains occurring in a much larger region than for the single networks. This delocalization of stress is the origin of the enhanced bond rupture in DN-I, and hence, it translates in a higher width fracture zone on the DN-I (see Figure 5.A.24). We note, finally, that the reduction of the number of broken bonds in DN-II compared to DN-I is much less pronounced in the simulations (Figure 5.5f) than in the experiments (Figure 5.2b). This difference could be due to the simplifying approximations in our model, such as our approach to account for pre-stretch in the first network by assuming a weaker potential, the limited system size, and the fact that our simulations are carried out in 2D instead of 3D. Alternatively, bond rupture in the experimental DN-II may be underestimated by incomplete polymerization and crosslinking in the second network due to the constraints imposed by the first network.

5.4 Concluding remarks

In this work, we have used mechanoluminescent molecular probes to obtain a detailed and quantitative insight in the bond rupture processes that occur during puncture of polymer materials. We have demonstrated that significant bond rupture occurs already before the probe penetrates the surface of the material and a drop in indentation force can be seen. Once the probe has pierced through the surface, further penetration proceeds by the propagation of a ring-shaped crack. By quantifying the number of broken bonds in this stage, it is clear that this crack is associated with a damage zone of significant size. Furthermore, we have shown that the puncture of double network involves a strongly enhanced rupture of bonds in the first, sacrificial network. By comparing to computer simulations of model networks, we find that this is due to a delocalization of the stresses in a large zone around the indenter.

We anticipate that the methods presented here can be used to address multiple interesting scientific questions such as the effects of indenter geometry, network topology, crosslink density, plasticizers, and visco-elastic stress relaxation on puncture mechanics. Finally, while the use of the integrating sphere prevents us from obtaining spatial information, it may be possible to map out the spatial distribution of bond rupture events during puncture by using a high-sensitivity camera.

5.5 Appendix Chapter 5

Materials & Methods

Synthesis of dioxetane-DMA crosslinker

5,5'/7'-bismethacrylate- 5,5'/7'-dihydroxyethylenoxy- adamantylideneadamantane 1,2-dioxetane (dioxetane-DMA) was synthesized based on the protocol by[20], but using a different crosslinking functionality, see Figure 5.A.1. To a solution of hydroxyl bifunctionalized bis(adamantyl)-1,2-dioxetane (0.4 g, 0.95 mmol) and triethylamine (1.5 mL) in dry THF (18 mL) was added dropwise a dry THF solution (20 mL) of methacryloyl chloride (0.157 ml, 1.94 mmol) at 0°C. After stirring at room temperature for 24 h, the solution was poured into water (50 mL) and extracted with diethyl ether (2×30 mL). The combined organic layers were washed with a saturated sodium bicarbonate solution (2x50 mL), water (50 mL), dried over anhydrous Na_2SO_4 and evaporated under reduced pressure to obtain dioxetane-DMA.

The ^{1}H-NMR and ^{13}C-NMR spectra of the dioxetane-DMA crosslinker are shown in Figure 5.A.2 and 5.A.3, repectively.

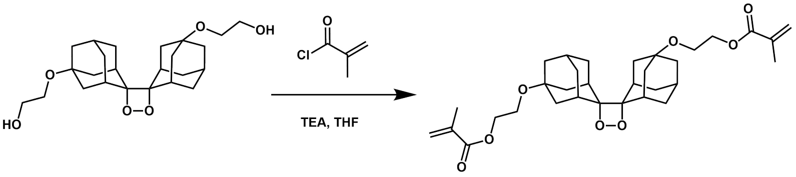

Figure 5.A.1 – Synthetic scheme of dioxetane-dimethacrylate crosslinker.

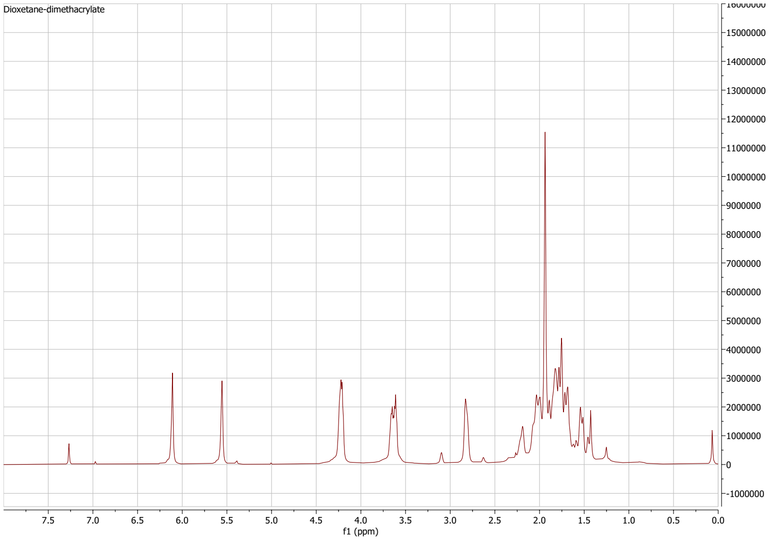

Figure 5.A.2 – ^{1}H-NMR spectrum of 5,5'/7'-bismethacrylate- 5,5'/7'-dihydroxyethylenoxy- adamantylideneadamantane 1,2-dioxetane in $CDCl_3$. Some degradation into ketone during oxidation step (2.6 ppm) and unoxidized adamantylidene-adamantane (3.1 ppm).
^{1}H-NMR (400 MHz, $CDCl_3$): δ 6.12 [s, 2H], 5.57 [s, 2H], 4.22 [m, 4H], 3.66 [m, 4H], 2.83 [br, 4H], 1.44-2.30 [m, 32H]. Some degradation into ketone during oxidation step (2.6 ppm) and unoxidized adamantylidene adamantane (3.1 ppm).

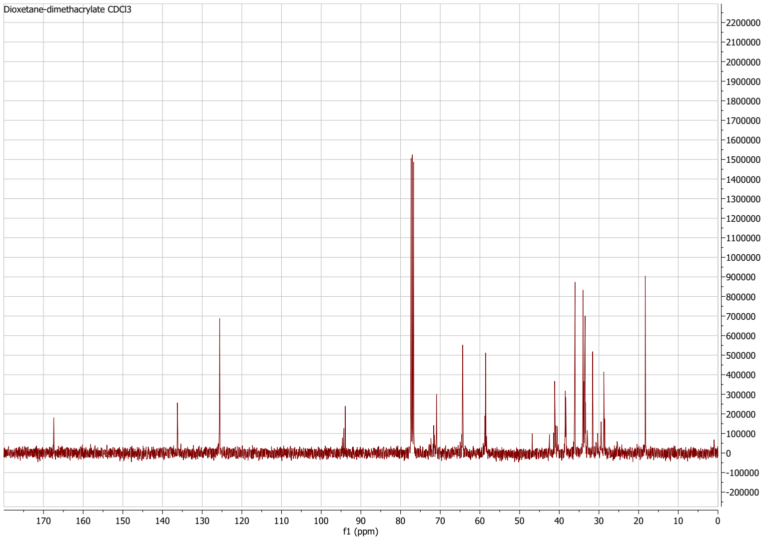

Figure 5.A.3 – ^{13}C-NMR spectrum of 5,5'/7'-bismethacrylate- 5,5'/7'-dihydroxyethylenoxy- adamantylideneadamantane 1,2-dioxetane in $CDCl_3$.
^{13}C-NMR (400 MHz, $CDCl_3$): δ 167.42, 136.24, 125.60, 125.57, 94.64, 94.27, 93.95, 72.34, 71.64, 71.54, 70.94, 64.57, 64.43, 64.36, 64.27, 64.24, 58.76, 58.68, 58.57, 58.48, 41.43, 41.15, 40.89, 40.56, 40.45, 38.51, 38.47, 38.36, 36.16, 36.03, 34.07, 34.02, 33.97, 33.90, 33.77, 33.64, 33.58, 33.49, 33.40, 31.60, 28.77, 28.73, 28.54, 28.51, 18.31.
Description ^{13}C-NMR peaks: 167 (*C*=O), 136 (MAcr, C-*C*=C), 125, (MAcr, C-C=*C*), 94 (Diox, (C-*C*-O-O)), 71 (Adamantone-ethylene glycol, C-C-*C*-O), 64+58 (ethylene glycol), 28-46 (adamantane), 18 (MAcr -CH_3).

Preparation double networks

Figure 5.A.4 and 5.A.5 show the preparation steps and swelling ratio of Double Networks (DNs), respectively.

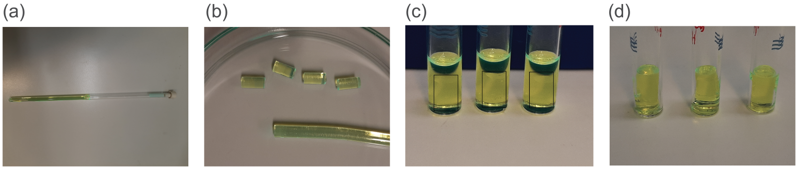

Figure 5.A.4 – Preparation of a Double Network. **(a)** DN-I is polymerized in a NMR tube, **(b)** cut with a specific length, **(c)** the first network, present in the black boxes, is swollen in a degassed solution containing the compounds for DN-II, and finally **(d)** polymerized to obtain the Double Network.

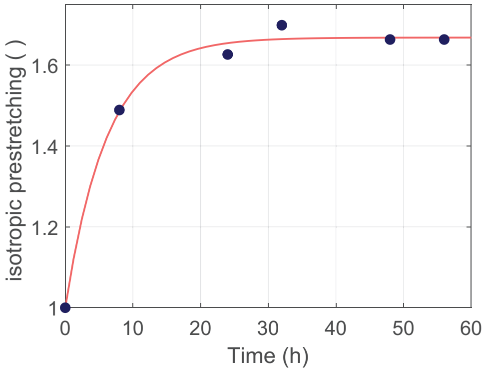

Figure 5.A.5 – Isotropic prestretching, i.e. the cubic root of the swelling ratio[31] which is obtained with the final weight over initial weight, of a double network, measured over time.

Bond scission calibration

As explained in this Chapter, the dioxetane-DMA crosslinker is incorporated in polymer networks to study bond scission in puncture and hysteresis tests. To calibrate the dioxetane photon emission c_p to the number of broken bonds n_b, equation 5.1 is used:

$$n_b = n_{prior} + n_{main} + n_{post} = \frac{\Phi_T}{\Phi_M}\frac{N_{b,T}}{N_{p,T}}c_p \tag{5.7}$$

where n_{prior}, n_{main}, and n_{post} are the number of broken bonds before, during and after the puncture event, respectively. $N_{b,T}$ is a known quantity from the sample preparation. $N_{p,T}$ is obtained in reference experiments, presented in Section 5.5, by cleaving all the bonds by means of thermoluminescence, as the 1,2-dioxetane bond will cleave rapidly[21] when heated above ∼200 °C. With that, c_p can be converted in n_b.

Samples are heated using a Resistive Cartridge Heater as a heating element (Thorlabs, HT15W). The heating element was equipped with a spring developed in-house, see Figure 1d of the main article, to ensure contact between the heating element and the vials (VWR International, product number 1-NWV-C) that fit the opening of the integrating sphere. The heating element was controlled with a Universal Temperature Process Controller (Omega, CN142).

Simulations

We generate polymer networks by diluting triangular lattices of $N \times N$ nodes with spacing l_0. Here, a fraction p_1 of all possible nearest-neighbor bonds is present. Then, dangling ends are eliminated in the network, and bonds are substituted with monomers of diameter σ. The resulting network denominated as SN (see Fig. 5.A.6S(a.I)) is submitted to an equilibration process using the FENE potential, as we explain in the main. Finally, the potential is changed to the Quartic potential, shown in Fig. 5.A.6S(b) by the red curve, and a second equilibration step is performed before the puncture simulations. In cases where we consider a weaker interaction for bonds formed between crosslinkers and monomers, we choose all these bonds, i.e. $p_x = 100\%$, or the $p_x = 25\%$ of them randomly and apply one of the potentials defined as weak, shown in Fig. Fig. 5.A.6S(b).

To study the mechanical response of a DN's under puncture, a second network is generated by using the position of the nodes resulting from the SN. Likewise, the fraction of all possible nearest-neighbor bonds, now defined as p_2, is fixed in the range $0.55 \leq p_1 \leq p_2$. In particular, we use $p_2 = 0.55$. A schematic of the assembly process and the resulting network after applying the equilibration step with the FENE potential are shown in Fig. 5.A.6S(a.II). Then, to capture the mechanical properties of the double networks, the interaction of the second lattice (DN-2) is switched to be stronger than in the first one (DN-1), as indicated in Fig. 5.A.6S(b) by the red and blue colors, respectively. In this way, bonds in DN-1 will be broken at a lower energy cost, mimicking the pre-stress induced during the assembly of the double networks in the laboratory.

In Fig. 5.A.6S(c) we represent the intruder used for applying the puncture. This object is represented by superimposing particles of a diameter $\sigma_I \geq 10\sigma$. The set of these particles behaves like a rigid solid that moves at a constant velocity $\mathbf{v}_I = -|v|\hat{e}_y$, where $|v|$ is the speed and $\hat{e}_y$ is the Cartesian component in the y-axis. Likewise, the intruder and the polymeric network interact using a WCA interaction. Then, during puncturing, we calculate the force exerted by the first row of particles on the network, highlighted in black in Fig. 5.A.6S(c).

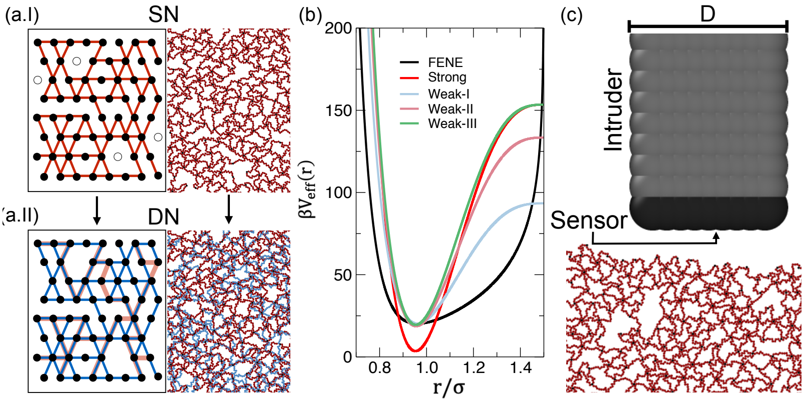

Figure 5.A.6 – **(a)** Modeling of a single (a.I) and double (a.II) network. On the left is a triangular lattice formation, where black and empty dots indicate crosslinkers and vacant positions once dangling ends are removed for the single network. Blue and red bonds correspond to the weak and strong networks, respectively. On the right, we present snapshots of the polymer systems during the equilibration process. **(b)** Potential interactions used for the equilibration and puncture simulations. **(c)** Modeling of the intruder of width D, where the black-colored particles refer to the region on which we measure the force applied on the network, called "sensor."

Results

Reference experiment: obtain $N_{p,T}$ using thermoluminescence

Figure 5.A.8 shows a picture taken of a SN sample showing thermoluminescence on a hot plate at ~230 °C. This shows that thermoluminescence of the dioxetane-DMA bond indeed produces photons.

An equivalent test was done in an integrating sphere to calibrate the number of photons emitted by the sample in puncture and hysteresis tests c_p to the number of bonds broken n_b, see Equation 1, by recording the total number of photons that a sample could emit $N_{p,T}$. $N_{p,T}$ is acquired with thermoluminescence of a thin piece of sample in an integrating sphere by recording the sample photon emission until a steady state is reached and all the bonds are broken, see Figure 5.A.8 (a,b). The half-time to decay of the 1,2-dioxetane molecule at ~200 °C is reported to be on the order of $\sim 1 \times 10^3$ sec[22]. The data presented in Figure 5.A.8 (a,b) also shows this order of magnitude half-time to decay for the 1,2-dioxetane molecule. For the thermoluminescent control tests, a thin piece if sample is taken to ensure that thermal conduction is sufficient to cleave all mechanoluminescent bonds. To account for the difference in sample volume between puncture tests and heat experiments, a weight conversion for the puncture test, w_p, to the control test, w_c, is used, which is multiplied with $N_{p,T}$. The set temperature of the heating probe is increased step-by-step and photon emission started between 190-230°C. The inset shows the Proportional Integral Derivative (PID) loop of the heating element, which is activated for about 3 seconds every 10 seconds. The detected photon counts are averaged using a sliding window with the interval of the PID loop. The photon count-level does not decrease to the initial dark count noise level of the detector. Instead, an additional control experiment showed that the heating element itself is responsible for photon counts when heated above 190 °C, see Figure 5.A.8 (c). Therefore, $N_{p,T}$ is determined as the summation of the counts between 180-750 seconds, with the noise level, determined between 2500-2900 seconds, deducted, resulting in the counts indicated by the blue shaded areas in Figure 5.A.8 (a,b). For the SN's with both crosslinkers present, $N_{p,T} = 2.685 \pm 0.577 \times 10^7$ counts, and for the SN with only the dioxetane-DMA crosslinker present, $N_{p,T} = 1.717 \pm 0.029 \times 10^8$ counts. $N_{p,T}$ is assumed to be proportional to the amount of dioxetane-DMA present in the network. Therefore, the $N_{p,T}$ for the DN's tested in puncture and hysteresis tests was assumed to be equal to the $N_{p,T}$ for the SN's with both crosslinkers present.

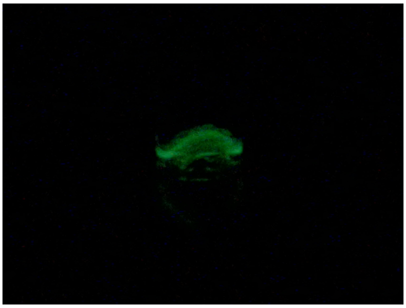

Figure 5.A.7 – Picture of test experiment showing heat induced chemiluminescence: thermoluminescence. Sample is heated on a hotplate to $\sim 220°$C to induce dioxetane bond scission, leading to green light emission.

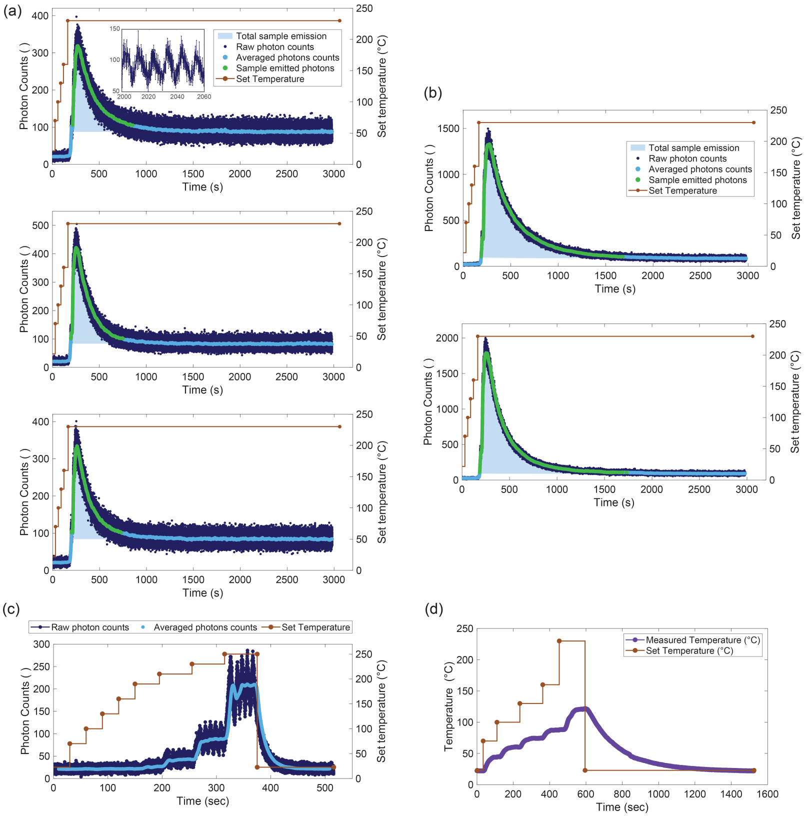

Figure 5.A.8 – Photon emission of a thin flat piece of sample heated by a heating element, to induce thermal cleavage of all the dioxetane bonds present for a SN with **(a)** both the dioxetane-DMA and PEG-DMA crosslinker, and **(b)** with only the dioxetane-DMA crosslinker. The inset in (a) top shows the PID loop of the heating element. After cooling samples with both crosslinkers (a), samples retain mechanical integrity, implying the higher activation energy for the PEG-DMA crosslinker. **(c)** Control experiment where the light detector detects photons while the heating element is heating silicon oil and thus in the absence of a luminescent probe. **(d)** A second control experiment where a sample is heated with the same temperature used in panels (a) and (b) and the temperature on the bottom of the vial is measured with an infrared thermometer (PCE Instruments, product number PCE-IR 51).

Puncture Mechanics

Figure 5.A.9 shows the mechanical response of SNs with both the PEG-DMA and dioxetane-DMA crosslinker at f = 0.25, punctured with a probe with diameter D = 1.0 mm (and D = 0.7 mm for panel (b)), a crosslinker concentration X = 1 mol% and at a probe velocity v = 2.0 mm/s. The mechanical response observed in the puncture tests of these SNs is similar to previously described puncture mechanics[13]; Figure 5.A.9 (b) shows the power 1 relation $\frac{F}{F_c} \sim \left(\frac{\delta-\delta_0}{\delta_c}\right)$ at small depths transitioning into a power 2 relation at larger depths, and Figure 5.A.9 (b) shows $F_c \sim R^2$ for a flat cylindrical probe.

The critical stress σ_c, obtained from $\sigma_c = \frac{F_c}{R^2}$, was found to be 0.152 MPa, based on the linear fit in 5.A.9 (b). It should noted that this fit is based on only three points; the origin and mean data for puncture tests with probe sizes $D = 1.0$ mm and $D = 0.7$ mm. Photon emission was only detected for a range of probe sizes, with both an upper and lower limit. The lower limit was set by the stiffness of the HMA sample, as the forces reached would bend a puncture probe with $D < 0.7$ mm. The upper limit was set by F_c, which was not reached for puncture probes with $D >$ 1.0 mm.

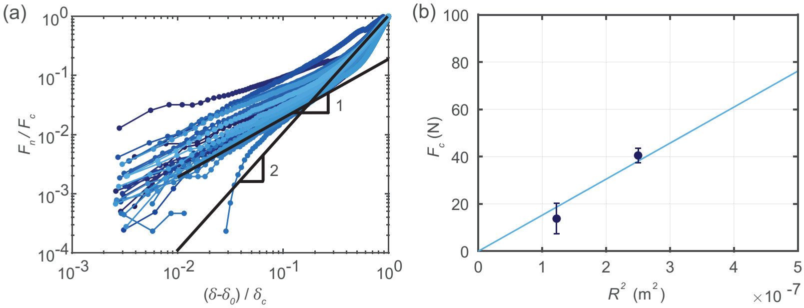

Figure 5.A.9 – Mechanical data for SN's showing **(a)** the normal force normalised with the critical force versus the depth normalized with the critical depth, and **(b)** the averaged critical force at failure versus the squared probe radius.

Hysteresis energy

Figure 5.A.10 shows force-distance curves of the hysteresis test presented in Figure 5.4, here with all the approach and retraction curves. In addition, the inset is a zoom-in of the dashed box, showing the irreversible stress-softening upon cyclical loading. Figure 5.A.11 shows data similar to Figure 5.4d, but here showing the number of broken bonds and the dissipated energy per cycle q rather than summed over all 5 cycles per maximum depth.

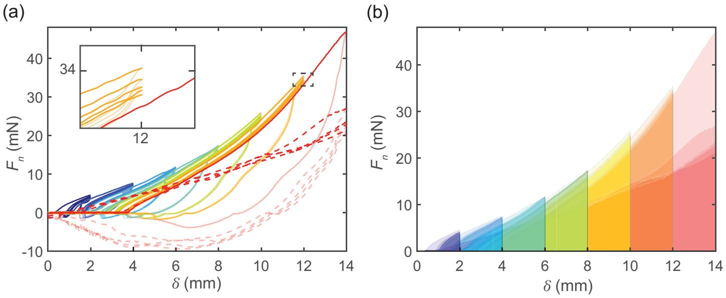

Figure 5.A.10 – **(a)** Force-distance loops of hysteresis test on a DN with both the PEG-DMA and the dioxetane-DMA crosslinker, showing loops before (——) and after (- - -) the puncture event, and the retraction curves in reduced opacity. The inset shows stress irreversible stress-softening due to bond ruptures, with an increase in d_m leading to subsequent stress-softening as well. **(b)** Force-distance curves of the same hysteresis test showing with the shaded area the hysteresis energy $E_h = F_n \cdot \delta_s$, where d_s is the step size of the stepper motor.

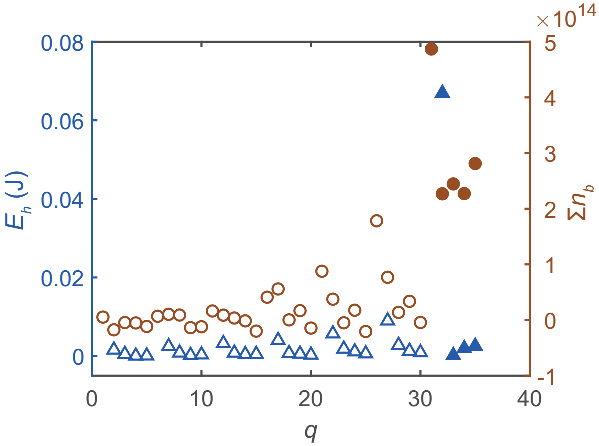

Figure 5.A.11 – The hysteresis energy ΣE_h ($\triangle$) and the cumulative number of broken bonds Σn_b ($\circ$) for each cycle q plotted versus q. Filled data points indicate data after the main fracture event.

Puncture tests

Figure 5.3 holds multiple bar plots that show data on some interesting parameters deduced from the puncture tests with various experimental procedures and for various samples. These parameters are defined as shown in the list below, of which some parameters are clarified by Figure 5.A.12;

- δ_c: the critical puncture depth at F_c.
- F_c: the maximum force before the material fails, indicated with a red X.
- F_Δ: from the maximum force before the material fails, indicated with a red X, until the the first force datapoint after a clear drop and before the force start to fluctuate due to crack propagation, indicated with a second red X in the inset and in Figure 5.A.11 (a).
- n_{main}: from 1 c_p datapoint before the top blue X until 1 c_p datapoint after the top blue X, indicated by the left green asterisk (*).
- n_{post}: from the left * to the right green *.
- n_{prior}: from the left blue cross (X) until 2 c_p datapoints before the top blue X.
- t_p: from the time corresponding to the left blue X until the top blue X.

Figure 5.A.12 also shows the 'onset' time at which bonds start to break prior to the puncture event t_p, in panel (c). t_p is larger for DN-I compared to DN-II, which is valid as the second network is not prestretched like the first network, but since n_b is lower as well, more of the initial photons might be lost in the noise of the detector. This effect can be seen comparing samples 1. and 4., where sample 4. contains solely dioxetane-DMA crosslinker, and 1. the PEG-DMA crosslinker as well. So the fact that 4. onsets before 1. could have to do with simply more mechanoluminescent probes being present, increasing the likelihood that the noise level is exceeded at an earlier stage. However, this could also (partly) be allocated to the fact that more of the weaker dioxetane-DMA bonds, i.e. with lower activation energy, are present leading to more bond rupture.

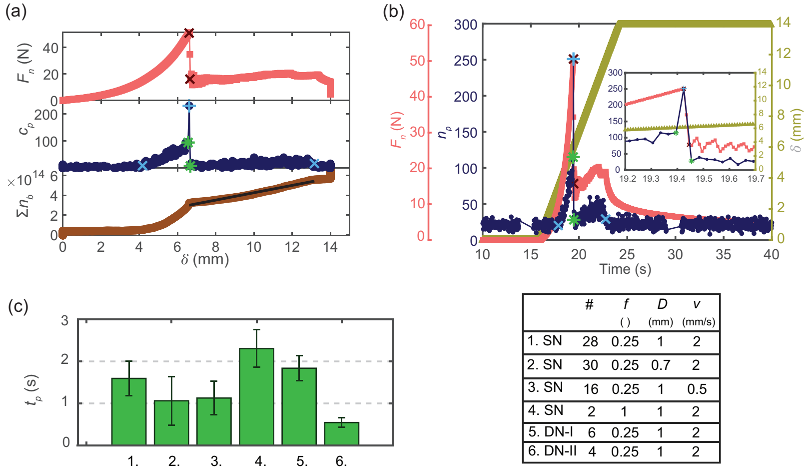

	#	f ( )	D (mm)	v (mm/s)
1. SN	28	0.25	1	2
2. SN	30	0.25	0.7	2
3. SN	16	0.25	1	0.5
4. SN	2	1	1	2
5. DN-I	6	0.25	1	2
6. DN-II	4	0.25	1	2

Figure 5.A.12 – **(a)** The same data as Figure 3 of the main article, now with symbols overlayed that indicate how some parameters of interests are extracted from the data. **(b)** Time-synchronized raw data of the puncture experiment shown in panel (a). X's are determined manually for all puncture tests. **(c)** The time prior t_p to the puncture events where the first photons, detectable above the threshold limit, are recorded for all datasets. The bottom-left legend numbers the type of network (subscript), experimental settings (D, X, v) and number of puncture tests performed ($\#$) for each configuration from 1.-6., shown at the x-axis of panel (c). The subscript d denotes the dioxetane-DMA crosslinker, the p the PEG-DMA crosslinker.

Figures 5.A.13, 5.A.14 and 5.A.15 show the normal force F_n measured by the load cell, the photons c_p emitted by broken dioxetane bonds as recorded by the detector, and the cumulative number of bonds broken Σn_b for all the puncture tests performed in this study, respectively. The findings from these Figures 5.A.13-5.A.15 are averaged in Figure 5.3.

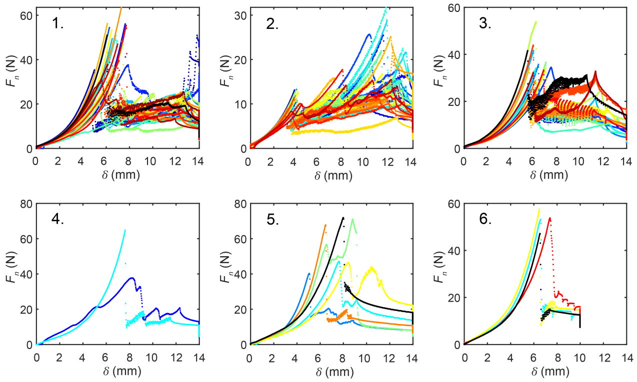

	#	*f* ( )	*D* (mm)	*v* (mm/s)
1. SN	28	0.25	1	2
2. SN	30	0.25	0.7	2
3. SN	16	0.25	1	0.5
4. SN	2	1	1	2
5. DN-I	6	0.25	1	2
6. DN-II	4	0.25	1	2

Figure 5.A.13 – The measured normal force F_n for all the puncture tests performed in this study. The black data is the data shown in Figure 5.2. Note that the y-axis scale varies, for visualization purposes.

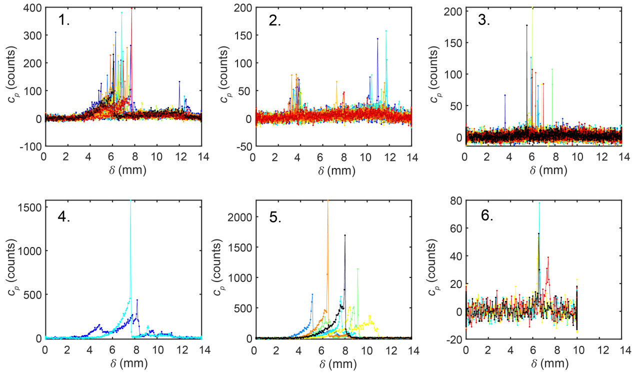

	#	*f* ( )	*D* (mm)	*v* (mm/s)
1. SN	28	0.25	1	2
2. SN	30	0.25	0.7	2
3. SN	16	0.25	1	0.5
4. SN	2	1	1	2
5. DN-I	6	0.25	1	2
6. DN-II	4	0.25	1	2

Figure 5.A.14 – The emitted photons c_p for all the puncture tests performed in this study. The black data is the data shown in Figure 5.2. Note that the y-axis scale varies, for visualization purposes.

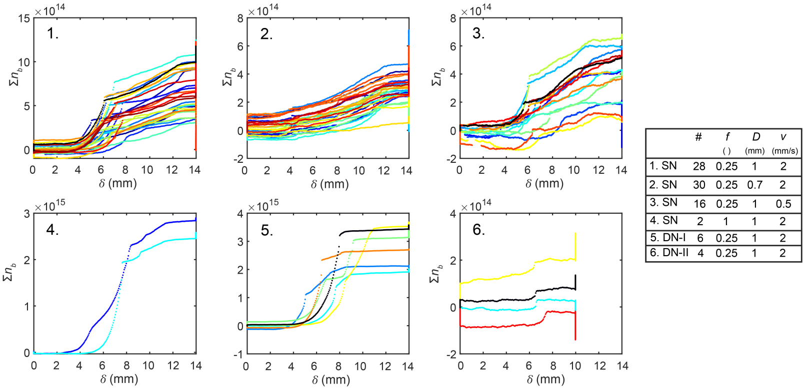

	#	*f* ( )	*D* (mm)	*v* (mm/s)
1. SN	28	0.25	1	2
2. SN	30	0.25	0.7	2
3. SN	16	0.25	1	0.5
4. SN	2	1	1	2
5. DN-I	6	0.25	1	2
6. DN-II	4	0.25	1	2

Figure 5.A.15 – The cumulative bonds broken Σn_b for all the puncture tests performed in this study. The black data is the data shown in Figure 5.2t. Note that the y-axis scale varies, for visualization purposes.

Post mortem fracture area estimation from images

The post mortem fracture area A was estimated from images. Images were acquired from back-illuminated samples and photographed with a CMOS camera (Thorlabs, DCC1545M), while the vial containing the sample was submerged in decalin, to refractive-index match the sample. The area A was obtained by cropping a box around the black-area and summing the black pixels in this box by applying an intensity-threshold, see Figure 5.A.16. An important note is that the acquired image is taken from the largest surface area, selected by eye, by rotating the vial. While we are taking a 2D projection to define A which is an underestimation of the actual A, however, these results are relative to each other. A better estimation of A could be acquired with higher precision by for example tomography or confocal laser scanning microscopy where the crack opening is filled with a fluorescent dye.

Note that, as predicted by the Flat-bottomed punch penetration model by Shergold and Fleck[16], the radius of the opening decreases after retraction of the puncture probe.

Sample number	1.	2.	5.
A **(mm²)**	34.28 ± 2.83	11.45 ± 2.22	7.88 ± 1.59

Table 5.A.1 – Post-mortem fracture areas (mm^2) obtained with Bright Field imaging, with the sample number indicating the sample as shown in the legend of e.g. Figure 5.A.16.

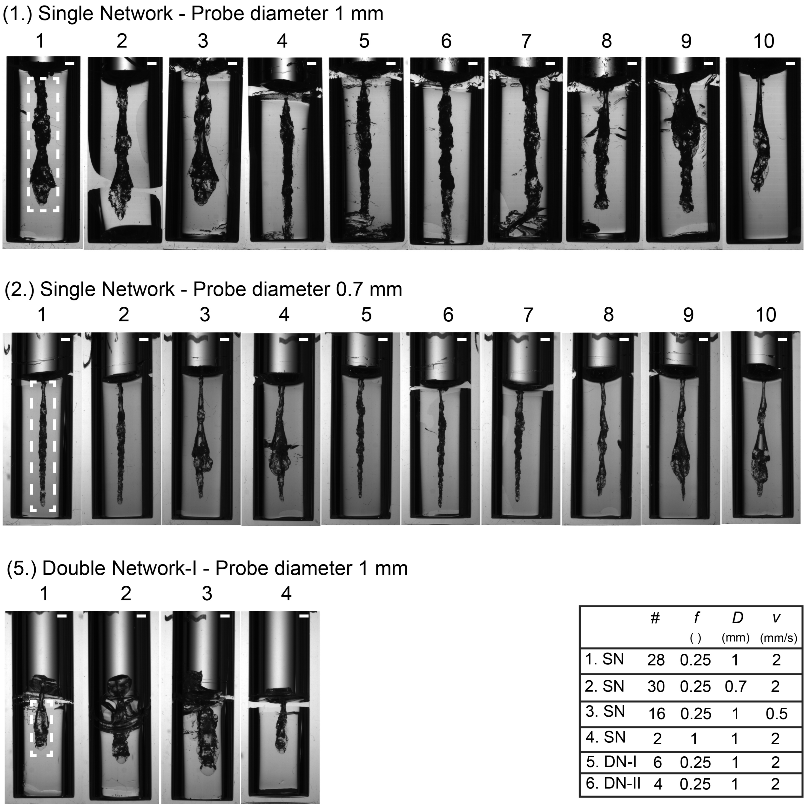

	#	*f* ( )	*D* (mm)	*v* (mm/s)
1. SN	28	0.25	1	2
2. SN	30	0.25	0.7	2
3. SN	16	0.25	1	0.5
4. SN	2	1	1	2
5. DN-I	6	0.25	1	2
6. DN-II	4	0.25	1	2

Figure 5.A.16 – Post-mortem puncture surface images of samples (1.), (2.) and (5.). Samples were imaged with a CMOS camera (Thorlabs, DCC1545M), while the vial containing the sample was submerged in decalin, to refractive-index match the sample. The dotted-box overlay on the samples 1 show the crop used to determine A. The scale bar on the top-right of each picture represents 1 mm.

Video - Hysteresis test DN

Video 1 (V1) shows a hysteresis test on a DN with only the PEG-DMA crosslinker. Videos are acquired with the same setup as the images acquired for the post mortem fracture area, see the previous subsection. Figure 5.A.17 presents the same force-distance curve as V1, showing loops before (—–) and after (- - -) the puncture event. Please note the relatively slow stress relaxation after the last deformation is applied in the video, hinting that stress relaxation due to dissipation processes is an important parameter in the mechanics of double networks.

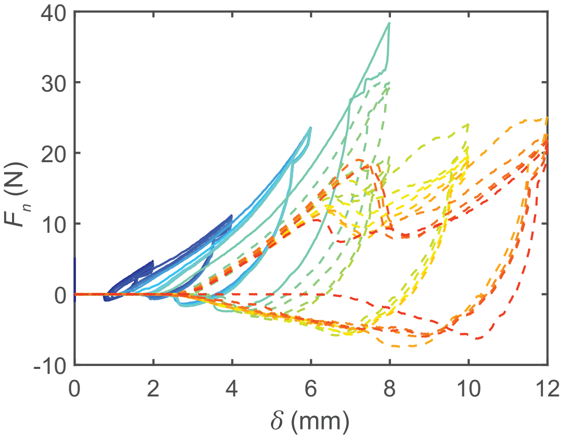

Figure 5.A.17 – Force-distance loops of hysteresis test on a DN with only the PEG-DMA crosslinker, tested outside the integrating sphere.

Simulations

We study the mechanical behavior of a SN as a function of crosslinker concentration c_x. These results are shown in Fig. 5.A.18 for $c_x = 2.3\%$ and $c_x = 4.8\%$. In correspondence with the case of $c_x = 8.7\%$, shown in main, there is a dependence on D as well as on c_x. In particular, by fixing D and decreasing c_x, we observe how the probe needs to go deeper to induce the fracture, because the chain length increases. As we have already discussed, the contour length L and D becomes comparable by reducing the c_x. This correlation between lengths would explain the fact that F tends to overlap with D when $c_x = 2.3\%$.

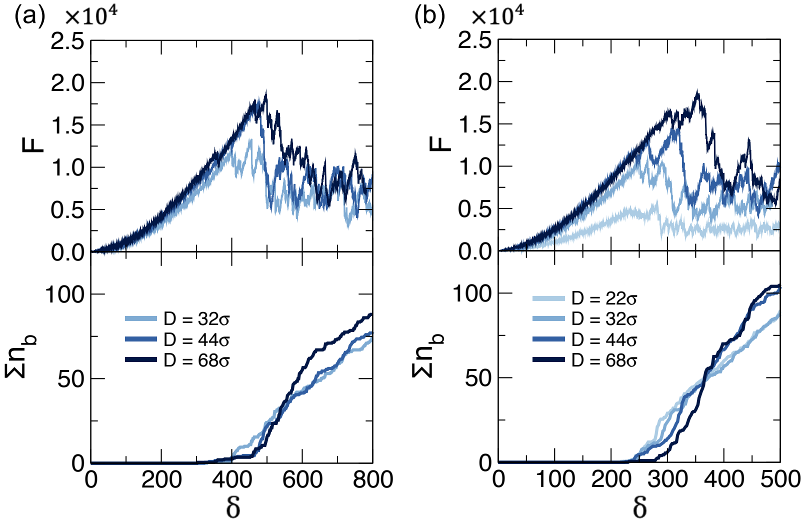

Figure 5.A.18 – Force F and cumulative number of bonds broken Σn_b as a function of the probe depth δ for a SN with crosslinker concentration **(a)** $c_x = 2.3\%$ and **(b)** $c_x = 4.8\%$ for different size of the probe D.

In Fig. 5.A.19, we present bar plots regarding the number of broken bonds before, during, and after the main failure event n_{prior}, n_{main}, n_{post} and their sum Σn_b. In particular, Fig. 5.A.19(a) shows the results for a SN with crosslinker concentration $c_x = 8.7\%$ as a function of the size probe D. On the other hand, Fig. 5.A.19(b) presents results from a network consisting of mixtures of weak and strong bonds being punctured by an indenter.

We estimate the width of the fracture zone Λ by computing the slope of the cumulative number of bonds broken bonds. In the case of a SN

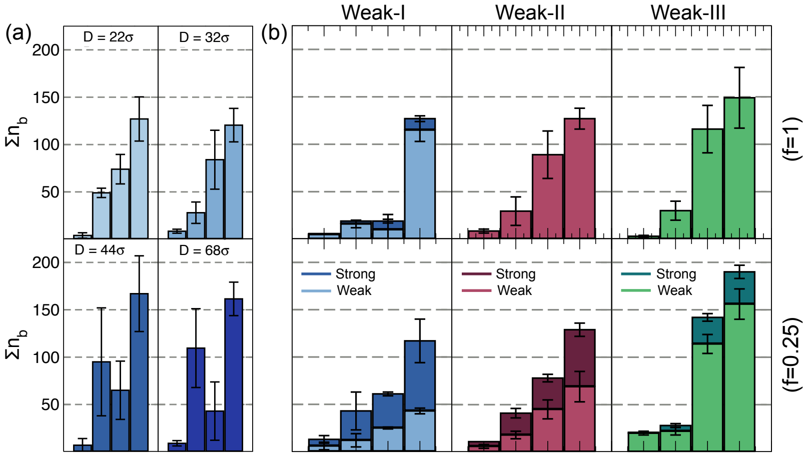

Figure 5.A.19 – Bar plots showing the number of broken bonds before, during, and after the main failure event n_{prior}, n_{main}, n_{post} and their sum $\Sigma n_b = n_{prior} + n_{main} + n_{post}$, from left to right. (**a**) SN with $c_x = 8.7\%$ as a function of the size probe D. (**b**) SN with $c_x = 8.7\%$ punctured with a intruder of $D = 22\sigma$, considering all crosslinkers are weak bonds ($f = 1$) and only 25% of the crosslinks are weak bonds ($f = 0.25$).

with $c_x = 8.7\%$, represented in Fig 5.A.20(a), Λ increases with D, in agreement with the experimental observations. Likewise, the fracture is highly influenced by the 25% of the crosslinks that are weak, as we can see in Fig 5.A.20(b).

Fig. 5.A.21 represents the distribution of tension in the polymer chains as a function of D and c_x, manifesting that, by increasing D, the presence of stretched bonds expands beyond the front of the intruder. Likewise, by increasing c_x, long 'force chains' are formed, indicating a more homogeneous stress distribution. The presence of these long chains causes network rupture to take place for higher δ_c by increasing c_x.

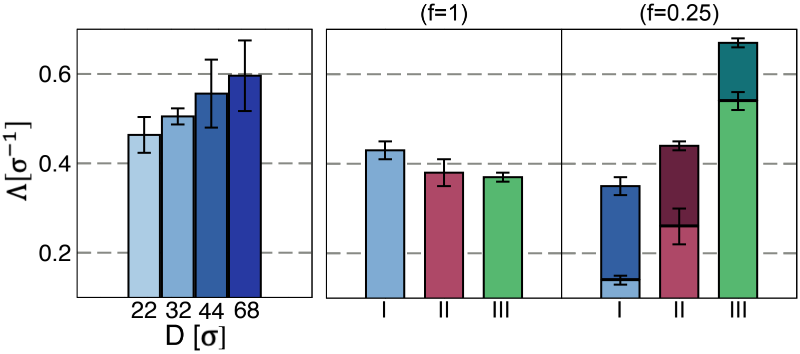

Figure 5.A.20 – (**a**) The number of broken bonds per unit crack length Λ for a SN with $c_x = 8.7\%$ as a function of the size probe D. (**b**) Λ for a SN with $c_x = 8.7\%$ punctured with a intruder of $D = 22\sigma$, considering all crosslinkers are weak bonds ($f = 1$) and only 25% of the crosslinks are weak bonds ($f = 0.25$). Here, light and dark colors refer to weak and strong bonds, respectively.

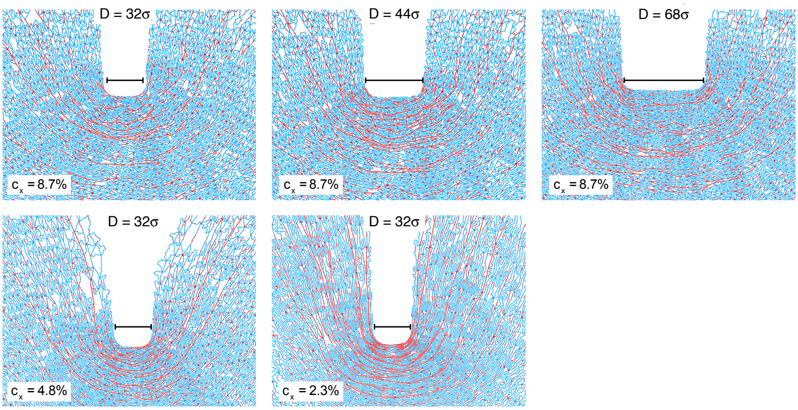

Figure 5.A.21 – Snapshots of the SN with different c_x and D, at $\delta \sim \delta_c$. Blue color indicates compressed bonds ($r \leq r_{min}$), whereas red color highlights streched ones ($r > r_{min}$).

Fig. 5.A.22S shows the broken bond position regarding the rest network. Here, we highlight the polymer chain that undergoes bond breaking in red, thus rendering it mechanically inactive. At the same time, we represent the chains of the network that do not suffer rupture in gray.

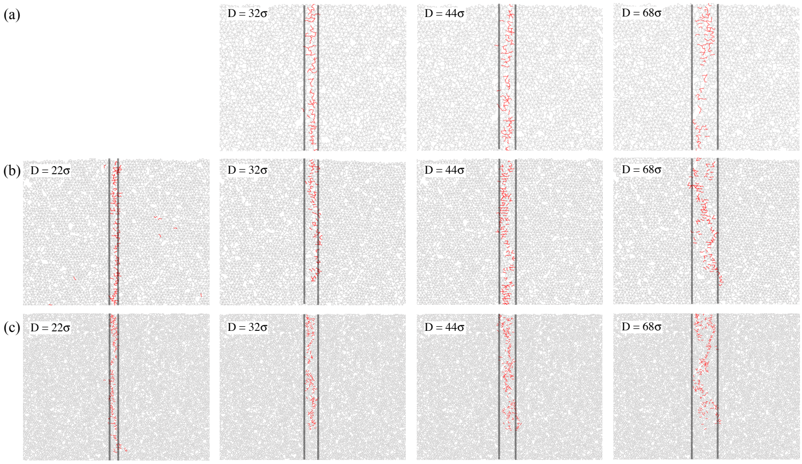

Figure 5.A.22 – Broken bond position regarding the rest SN at different $D = 22\sigma, 32\sigma, 44\sigma$ and 68σ for **(a)** $c_x = 2.3\%$, **(b)** $c_x = 4.8\%$ and **(c)** $c_x = 8.7\%$. The vertical lines indicate the size D of the probe.

Finally, we show the results corresponding to the double network in Fig. 5.A.23(a) and Fig. 5.A.23(b), where DN-1, which interacts by the weak-I, has $c_x = 2.3\%$ and 4.8%, respectively, and we have fixed D/L between the different DN's. As already discussed in Section 5.3.3 for $c_x = 8.7\%$, the penetration required to induce crack propagation, δ_c, is determined by DN-1, whereas DN-2 sets the value of F_c. Likewise, the onset of the crack propagation, determined by F_c, occurs when bonds in the DN-2 network begin to break (see Σn_b in Fig. 5.A.23(a)). Furthermore, we study the spatial distribution of the broken bonds on DN-1 and DN-2, showing the high density of broken bonds located on DN-1.

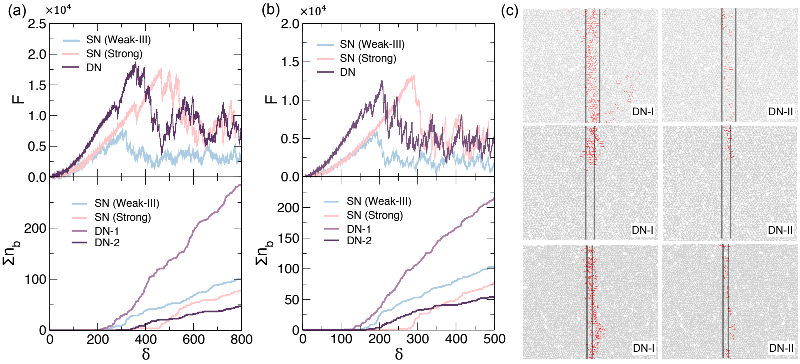

Figure 5.A.23 – Force F and cumulative broken bonds Σn_b as a function of the probe depth δ for DN's. **(a)** DN-1 with $c_x = 2.3\%$ and $D = 68\sigma$. **(b)** DN-1 with $c_x = 4.8\%$ and $D = 32\sigma$. Here, we compare the mechanical response of the DN with the single DN-1 in the cases where the bonds are defined as strong (*SN-Strong*) or weak (*SN-Weak*). Likewise, Σn_b is split in broken bonds on DN-1 and DN-2, respectively. **(c)** Broken bond position regarding the rest DN, for $c_x = 2.3\%$ (top), $c_x = 4.8\%$ (middle) and $c_x = 8.7\%$ (bottom), distinguishing between broken bonds on DN-1 and DN-2. The vertical lines indicate the size D of the probe.

In Fig. 5.A.24, we represent n_{prior}, n_{main}, n_{post}, and Σn_b for a DN punctured with a probe of $D = 22\sigma$, having DN-1 $c_x = 8.7\%$. We observe that the higher number of broken bonds occurs in DN-1 at any stage of the network rupture process. This phenomenon is translated in a higher fracture zone on DN-1.

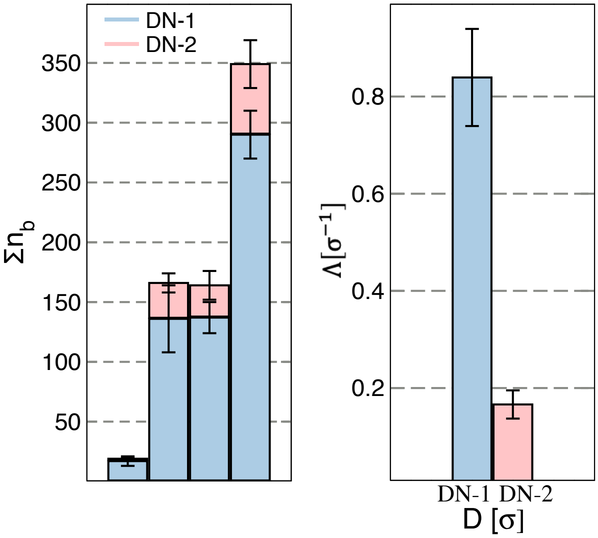

Figure 5.A.24 – Bar plots showing the number of broken bonds before, during, and after the main failure event n_{prior}, n_{main}, n_{post} and their sum $\Sigma n_b = n_{prior} + n_{main} + n_{post}$ and the number of broken bonds per unit crack length Λ for a DN punctured with a probe of $D = 22\sigma$, having DN-1 $c_x = 8.7\%$. Here, we split these quantities on DN-1 and DN-2, respectively.

5.6 List of symbols Chapter 5

List of experimental symbols

A - fracture area obtained from post-mortem images.
c_n - Photon count noise level.
c_p - Photon counts acquired by the detector.
D - Probe diameter.
δ - Applied puncture depth.
δ_c - Critical puncture depth at F_c.
δ_m - Maximum applied puncture depth.
E - Elastic modulus.
E_h - Hysteresis energy.
F_c - Maximum force before the material fails.
F_n - Normal force as measured by the bulk load cell.
$F_\triangle$ - The force drop during the main failure event
n_b - Number of bonds broken dioxetane-DMA bonds in puncture or hysteresis test.
Σn_b - Cumulative number of bonds broken in puncture or hysteresis test.
n_{main} - number of bonds broken during a puncture event.
n_{post} - number of bonds broken after a puncture event.
n_{prior} - number of bonds broken before a puncture event.
$N_{b,T}$ - Total number of dioxetane-DMA bonds present in the polymer network, known from the synthesis.
$N_{p,T}$ - Total number of photons that can be emitted by a sample in a puncture or hysteresis test.
R - Probe radius.
t_p - Time at which $c_p > c_n$, and bonds start breaking before the puncture event.
v - Probe velocity.
w_c - Weight of the sample in the control test.
w_p - Weight of the sample in the puncture test.
X - Crosslinker concentration.

List of numerical symbols

B_1 - Distance (Quartic interaction).
B_2 - Distance (Quartic interaction).

c_x - Crosslinker concentration.
Δt - Simulation time step.
Δ_y - Displacement of a particle on the y-axis.
δ - Puncture depth.
δ_c - Critical puncture depth at F_c.
D - Probe width.
ϵ - Energy scale.
F_c - Maximum force before the material fails.
F_{max} - Rupture force.
L_x - Simulation box length in x-axis.
L_y - Simulation box length in y-axis.
L - Contour length.
l_0 - Mesh size.
k_B - Boltzmann constant.
k_F - Dimensionless spring constant (FENE interaction).
k_Q - Dimensionless spring constant (Quartic interaction).
m - Particle mass.
$N \times N$ - Number of crosslinkers.
$N_x \times N_y$ - Number of particles in x- and y-axis regarding the probe.
P - Pressure.
p_1 - Probability that two nearest-neighbor are bonded in a single and first (DN-I) network.
p_2 - Probability that two nearest-neighbor are bonded in a second network (DN-II).
σ - Particle diameter, defining the lenght scale.
σ_I - Particle diameter reconstructing the probe.
R_0 - Maximum bond extension (FENE interaction).
R_c - Maximum bond extension (Quartic interaction).
r_{min} - energy minimum position.
Σn_b - Cumulative number of bonds broken.
T - Temperature.
U_0 - Energy (Quartic interaction).
$\mathbf{v}_I$ - Velocity vector regarding the intruder.
$|v|$ - Probe speed.
ξ_F - Friction coefficient for the Langevin equation.

Bibliography

[1] Karan Sotoodeh. A review of valve stem sealing to prevent leakage from the valve and its effect on valve operation. *Journal of Failure Analysis and Prevention*, 21(1):9–16, 2021.

[2] Faez Alkadi, Jeongwoo Lee, Jun-Seok Yeo, Seok-Ho Hwang, and Jae-Won Choi. 3d printing of ground tire rubber composites. *International Journal of Precision Engineering and Manufacturing-Green Technology*, 6(2):211–222, 2019.

[3] Carmel Majidi. Soft-matter engineering for soft robotics. *Advanced Materials Technologies*, 4(2):1800477, 2019.

[4] Harshal A Sonar, Aaron P Gerratt, Stéphanie P Lacour, and Jamie Paik. Closed-loop haptic feedback control using a self-sensing soft pneumatic actuator skin. *Soft robotics*, 7(1):22–29, 2020.

[5] Shuo Li, Hedan Bai, Robert F Shepherd, and Huichan Zhao. Bio-inspired design and additive manufacturing of soft materials, machines, robots, and haptic interfaces. *Angewandte Chemie International Edition*, 58(33):11182–11204, 2019.

[6] Hun-Jin Jeong, Hyoryung Nam, Jinah Jang, and Seung-Jae Lee. 3d bioprinting strategies for the regeneration of functional tubular tissues and organs. *Bioengineering*, 7(2):32, 2020.

[7] Sara Cascone and Gaetano Lamberti. Hydrogel-based commercial products for biomedical applications: A review. *International Journal of Pharmaceutics*, 573:118803, 2020.

[8] Federico Cecchini, Valeria Cherubini, Mahrukh Sadaf, Francesco Fabbrocino, and Francesca Nanni. Design of a puncture-resistant composite shell comprising a non-newtonian core. *Polymer Testing*, 67:494–502, 2018.

[9] Brittany Wong, Jules A Kieser, Ionut Ichim, Michael Swain, Vicki Livingstone, Neil Waddell, and Michael Taylor. Experimental simulation of non-ballistic wounding by sharp and blunt punches. *Forensic science, medicine, and pathology*, 4(4):212, 2008.

[10] Susmita Das, Sukumar Laha, and Animangsu Ghatak. A co-operative effect of closely spaced intruding objects puncturing into a soft solid. *Soft matter*, 10(32):6059–6067, 2014.

[11] Allison M Okamura, Christina Simone, and Mark D O'leary. Force modeling for needle insertion into soft tissue. *IEEE transactions on biomedical engineering*, 51(10):1707–1716, 2004.

[12] R Fangueiro, R Carvalho, D Silveira, N Ferreira, C Ferreira, F Monteiro, and S Sampaio. Development of high-performance single layer weft knitted structures for cut and puncture protection. *Journal of Textile Science and Engineering*, 5(225):2, 2015.

[13] Sami Fakhouri, Shelby B Hutchens, and Alfred J Crosby. Puncture mechanics of soft solids. *Soft Matter*, 11(23):4723–4730, 2015.

[14] Oliver A Shergold and Norman A Fleck. Experimental investigation into the deep penetration of soft solids by sharp and blunt punches, with application to the piercing of skin. *Transactions of the ASME*, 127:838, 2005.

[15] A. Stevenson and K. Ab Malek. On the puncture mechanics of rubber. *Rubber*

Chemistry and Technology, 67:743–760, 1994.

[16] Oliver A Shergold and Norman A Fleck. Mechanisms of deep penetration of soft solids, with application to the injection and wounding of skin. *Proceedings of the Royal Society of London. Series A: Mathematical, Physical and Engineering Sciences*, 460(2050):3037–3058, 2004.

[17] Etienne Ducrot, Yulan Chen, Markus Bulters, Rint P Sijbesma, and Costantino Creton. Toughening elastomers with sacrificial bonds and watching them break. *Science*, 344(6180):186–189, 2014.

[18] Juliette Slootman, Victoria Waltz, C Joshua Yeh, Christoph Baumann, Robert Göst, Jean Comtet, and Costantino Creton. Quantifying and mapping covalent bond scission during elastomer fracture. *arXiv preprint arXiv:2006.09468*, 2020.

[19] Gabriel E. Sanoja, Xavier P. Morelle, Jean Comtet, C. Joshua Yeh, Matteo Ciccotti, and Costantino Creton. Why is mechanical fatigue different from toughness in elastomers? the role of damage by polymer chain scission. *Science Advances*, 7(42):eabg9410, 2021.

[20] Yulan Chen, AJH Spiering, S Karthikeyan, Gerrit WM Peters, EW Meijer, and Rint P Sijbesma. Mechanically induced chemiluminescence from polymers incorporating a 1, 2-dioxetane unit in the main chain. *Nature chemistry*, 4(7):559–562, 2012.

[21] Jan C Hummelen, Theo M Luider, Hans Wynberg, et al. Functionalized adamantylideneadamantane 1, 2-dioxetanes: investigations on stable and inherently chemiluminescent compounds as a tool for clinical analysis. *Pure and Applied Chemistry*, 59(5):639–650, 1987.

[22] JC Hummelen, Th M Luider, and H Wynberg. *Thermochemiluminescence immunoassay*. University of Groningen, Stratingh Institute for Chemistry, 1988.

[23] Jian Ping Gong, Yoshinori Katsuyama, Takayuki Kurokawa, and Yoshihito Osada. Double-network hydrogels with extremely high mechanical strength. *Advanced materials*, 15(14):1155–1158, 2003.

[24] Yoshimi Tanaka, Rikimaru Kuwabara, Yang-Ho Na, Takayuki Kurokawa, Jian Ping Gong, and Yoshihito Osada. Determination of fracture energy of high strength double network hydrogels. *The Journal of Physical Chemistry B*, 109(23):11559–11562, 2005.

[25] Rebecca E Webber, Costantino Creton, Hugh R Brown, and Jian Ping Gong. Large strain hysteresis and mullins effect of tough double-network hydrogels. *Macromolecules*, 40(8):2919–2927, 2007.

[26] Hugh R Brown. A model of the fracture of double network gels. *Macromolecules*, 40(10):3815–3818, 2007.

[27] Yoshimi Tanaka. A local damage model for anomalous high toughness of double-network gels. *EPL (Europhysics Letters)*, 78(5):56005, 2007.

[28] VWR. Vwr international b.v., amsterdam. Product number 1-NWV-C.

[29] Masaaki Mitsui, Yuya Kawano, Ryoya Takahashi, and Hiroki Fukui. Photophysics and photostability of 9, 10-bis (phenylethynyl) anthracene revealed by single-molecule spectroscopy. *RSC advances*, 2(26):9921–9931, 2012.

[30] DR Maulding and Bernard G Roberts. Electronic absorption and fluorescence of phenylethynyl-substituted acenes. *The Journal of Organic Chemistry*, 34(6):1734–1736, 1969.

[31] Pierre Millereau, Etienne Ducrot, Jess M Clough, Meredith E Wiseman, Hugh R Brown, Rint P Sijbesma, and Costantino Creton. Mechanics of elastomeric molecular composites. *Proceedings of the National Academy of Sciences*, 115(37):9110–9115, 2018.

[32] The Mathworks, Inc., Natick, Massachusetts. *MATLAB version R2018b*, 2018.

[33] PCE Instruments, PCE Brookhuis B.V., Enschede, The Netherlands. *PCE-IR 51.*

[34] Gary B Schuster, Nicholas J Turro, Hans C Steinmetzer, A Paul Schaap, Gary Faler, Waldemar Adam, and JC Liu. Adamantylideneadamantane-1, 2-dioxetane. chemiluminescence and decomposition kinetics of an unusually stable 1, 2-dioxetane. *Journal of the American Chemical Society*, 97(24):7110–7118, 1975.

[35] Jess M Clough and Rint P Sijbesma. Dioxetane scission products unchanged by mechanical force. *ChemPhysChem*, 16(16):3565–357, 2014.

[36] John D Weeks, David Chandler, and Hans C Andersen. Role of repulsive forces in determining the equilibrium structure of simple liquids. *The Journal of chemical physics*, 54(12):5237–5247, 1971.

[37] Glenn J Martyna, Michael L Klein, and Mark Tuckerman. Nosé–hoover chains: The canonical ensemble via continuous dynamics. *The Journal of chemical physics*, 97(4):2635–2643, 1992.

[38] Kurt Kremer and Gary S Grest. Dynamics of entangled linear polymer melts: A molecular-dynamics simulation. *The Journal of Chemical Physics*, 92(8):5057–5086, 1990.

[39] Ting Ge, Flint Pierce, Dvora Perahia, Gary S Grest, and Mark O Robbins. Molecular dynamics simulations of polymer welding: Strength from interfacial entanglements. *Physical review letters*, 110(9):098301, 2013.

[40] Justin Tauber, Lorenzo Rovigatti, Simone Dussi, and Jasper Van Der Gucht. Sharing the load: Stress redistribution governs fracture of polymer double networks. *Macromolecules*, 54(18):8563–8574, 2021.

[41] Jian Ping Gong. Why are double network hydrogels so tough? *Soft Matter*, 6(12):2583–2590, 2010.

[42] Steve Plimpton. Fast parallel algorithms for short-range molecular dynamics. *Journal of computational physics*, 117(1):1–19, 1995.

[43] Anthony C Fischer-Cripps. *Introduction to contact mechanics*, volume 101. Springer, 2007.

[44] Kenneth Langstreth Johnson. *Contact mechanics*. Cambridge university press, 1987.

[45] Jess M Clough, Costantino Creton, Stephen L Craig, and Rint P Sijbesma. Covalent bond scission in the mullins effect of a filled elastomer: real-time visualization with mechanoluminescence. *Advanced Functional Materials*, 26(48):9063–9074, 2016.

[46] GJ Lake and AG Thomas. The strength of highly elastic materials. *Proceedings of the Royal Society of London. Series A. Mathematical and Physical Sciences*, 300(1460):108–119, 1967.

[47] Teresa T Duncan, Joel M Sarapas, Adrian P Defante, Kathryn L Beers, and Edwin P Chan. Cutting to measure the elasticity and fracture of soft gels. *Soft Matter*, 16(38):8826–8831, 2020.

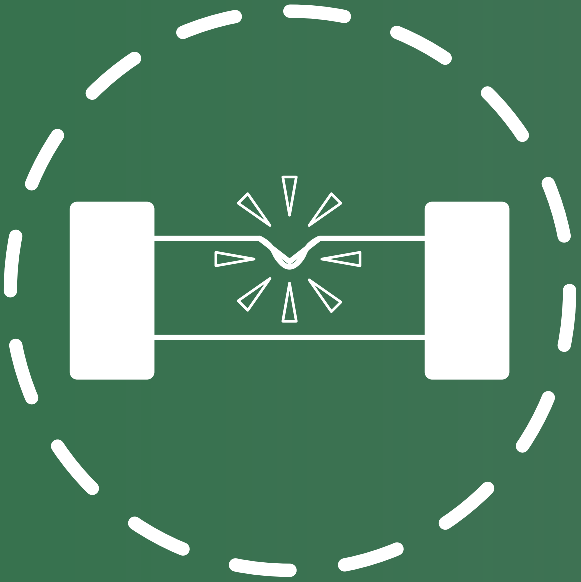

Chapter 6

Simultaneous stress and strain readout during delayed failure of a soft solid

In this preliminary study, the sudden and unexpected delayed failure of elastomers is studied on a microscopic level by simultaneously acquiring microscopic strain and stress using a combination of Laser Speckle Strain Imaging (LSI) and the covalently coupled crosslinker mechanosensor spiropyran. Macroscopically, there is no warning for this abrupt subcritically loaded failure. Yet, our results show that at the millisecond timescale, which is obviously a timescale faster than practically susceptible in everyday life, the bulk stress gradually drops. Microscopically, the results we obtain for strain are in alignment with a previous observation and we build on those by observing that the stress activates at a much shorter time scale than the strain, most likely due to the difference in sensitivity of the sensors. This sensitivity also results in a different spatial activation profile, where the more sensitive LSI signal activates more symmetrical around the notch compared to the spiropyran activation.

Manuscript in preparation as:

J.N.M. Boots, R. Antonelli, D.W. te Brake, R. van Zwieten, H. van der Kooij, T.E. Kodger, J. Sprakel and J. van der Gucht
"Simultaneous stress and strain readout during delayed failure of a soft solid"

6.1 Introduction

Loading solids below their critical fracture stress can still lead to highly unpredictable and sudden failure after a period of time, known as delayed failure. This type of failure is of major concern as this is observed in a wide range of solids, such as ceramics[1], ductile metals[2], heterogeneous (porous) media[3, 4], plastics[5], two-dimensional crystals[6], and a range of soft materials[7, 8, 9, 10, 11]. At the macroscopic level, there is no warning of imminent failure. At the microscopic level, however, previous work by van der Kooij *et al.* has shown that up to a few seconds before the fracture is macroscopically detectable, small-scale deformations emerge around the position of crack nucleation[12]. These deformations were observed using Laser Speckle Strain Imaging (LSSI), a imaging technique in which the dynamics of multiple scattered light is obtained at ∼kHz time interval, allowing to resolve displacements to as small as 0.2 nm[12]. Photons composing a coherent light source, in our case a 532nm laser beam, impinge onto the sample, with each photon diffusing and scattering into the material. In this process each photon accumulates a different phase due to different travelled paths. When exiting the sample in the direction of the camera, the overall difference in phases will be summed up to produce a speckle pattern image. If the sample is dynamic, the speckle pattern will fluctuate in time. The information contained in these fluctuations reveals the dynamic properties of the sample[13]. The observations with LSSI appear to be consistent with kinetics predicted by the erosion hypothesis[9, 10], which considers crack nucleation as the result of a self-accelerating cascade of molecular bond ruptures at the stress localization point[9]. Eventually, this crack nucleating cascade will result in crack propagation. However, a full picture of the mechanics preceding fracture nucleation at the nucleation site until fracture propagation, which would include a microscopic picture describing stress accumulation, is yet to be developed.

In the past decade, knowledge about microscopic scale mechanics increased significantly through mechanochemical tools, such as molecular mechanophores that provoke an optical signal in response to mechanical activation. A particularly useful mechanophore for mechanical studies at the microscopic scale is spiropyran, which can be covalently incorporated in polymeric materials by introducing it as a crosslinker in polymer networks produced by free radical polymerisation[14]. Spiropyran changes conformation to merocyanine upon being stressed above ∼240 pN, fluorescing at a longer wavelength[15, 16]. Previous work using this mechanophore reported the back-conversion time from merocyanine to spiropyran[17]. After UV-induced or stress-induced conversion from spiropyran to merocyanine, the half-time conversion back to the spiropyran state is 30 minutes and 38 minutes, respectively, tested on polyurethane samples, implying that the spiropyran sensor acts as a cumulative stress reporter. In another report, spiropyran has been used in glassy PMMA polymers to study local stresses around the tip of a notch upon slow uniaxial extension leading to crack propagation[14]. The stress profile of the mechanosensor was observed to be circular ahead of the crack tip. However, the mechanics in the glassy polymer varies significantly from that of the elastomer reported earlier with LSSI[12], considering differences in mechanical processes between the materials such as viscoelasticity. In this work, we present the simultaneous readout of small-scale deformations and the accumulation of stress around the site of crack nucleation by using LSSI and the spiropyran stress sensor during delayed failure experiments, respectively. Concomitantly, we record the macroscopic stress on the full sample by means of a load cell. By simultaneously measuring the macroscopic and microscopic mechanics, we relate the mechanical kinetics to the length scales at which they are probed.

6.2 Materials & Methods

6.2.1 Materials

All reactants were purchased from Sigma Aldrich or TCI and used as received. Solvents were purchased from Biosolve and used as received. TiO_2 particles, with a diameter of ∼ 30 nm and coated with silicone oil, were purchased from US Research Nanomaterials. PDMS Sylgard 184 was purchased from Dow Corning.

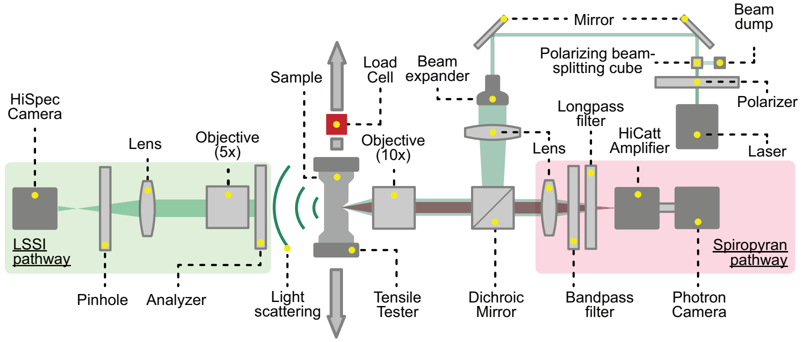

Figure 6.1 – Schematic representation of the combined spiropyran fluorescence and forward-scatter LSSI setup to simultaneously visualize strain (left optical pathway) and stress (right optical pathway) precursors, respectively. Elastomer samples are illuminated with a coherent plane light wave, which both fluoresces the spiropyran crosslinker and multiply scatters from embedded TiO_2 nanoparticles.

6.2.2 Synthesis of spiropyran-divinyl crosslinker

The protocol to synthesize spiropyran-diol is adapted from literature[18]. Spiropyran-diol (3.0 g, 8.14 mmol, 1 equiv) and 4-dimethylaminopyridine (0.099 g, 0.814 mmol, 0.1 equiv.) were dissolved in dry dichloromethane (40 mL) in an oven dried round bottom flask. The dark green suspension was stirred and 4-pentenoic anhydride (3.20 mL, 17.51 mmol, 2.15 equiv) was added dropwise, with 15 min between each addition. The reaction was stirred overnight, resulting in a magenta-purple solution. The mixture was extracted with concentrated sodium bicarbonate solution (1 x 75 mL), 1 N hydrochloric acid (1 x 75 mL), water (2 x 75 mL) and brine (1 x 75 mL) before drying over sodium sulfate. Finally the crude purple oil was recrystallized from hexane and green-yellow spiropyran-divinyl (SP-divinyl) crystals are obtained.

6.2.3 Synthesis of polymer networks

A stock mixture of Sylgard base (125 g), SP-divinyl (125 mg) in 1.25 ml toluene, TiO_2 Si-coated (250 mg) was made to which the Sylgard crosslinker was added 5:1, base:crosslinker, from which all elastomer samples were produced. This viscous mixture was homogenized by stirring, vacuum cycled 3 three times in 1 hour to remove air bubbles and poured in a 3D printed mold creating a Single Edge-Notched Beam (SENB), see Appendix 6.5 for details on the dimensions. The samples were placed in a dessicator applying 4 vacuum cycles for 10 minutes each to remove any remaining air bubbles, and cured overnight in the oven at 70°C. A total of 30 samples were tested in this study.

6.2.4 Experimental setup

Micromechanical maps of the stress and strain were obtained with a custom-built SP-LSSI setup. Elastomer samples are loaded in a strain-controlled tensile tester operated with two actuators (Z825BV, Thorlabs) and the bulk force was recorded with a load cell (FUTEK, LSB200, 100 lb). Samples were illuminated at the tip of the notch with a coherent light beam (Cobolt Samba, 1.5 W, λ = 532 nm), orthogonal to the sample strain direction, fluorescing the spiropyran and multiply scattering the TiO_2 nanoparticles.

The laser intensity, which at full power would degrade the sample, is controlled by a combination of an half wave plate, mounted on a rotational stage (Thorlabs KPRM1E), and a polarizing beam splitter cube. The rotation of the half wave plate changes the polarization from fully vertical, to a combination of horizontal and vertical, depending on the rotational angle. The next optical component, the beamsplitter, divides the beam in a vertical and an horizontal component. The latter is directed to a beam dump, thus reducing the net intensity. The beam is than directed into a 10x beam expander (Thorlabs GBE10-A), and immediately after through a focusing lens. The next optical component is a dichroic mirror: it acts as a mirror for the laser beam, thus deflecting it to the objective and the sample, but it allows the other frequencies to go through. In particular it allows the frequencies emerging from the spiropyran fluorescence, to reach the camera sensor in the backscatter direction.

After the dichroic, the beam is directed into a 10x objective, and focused, with a radius of $\sim$1mm, on the sample notch. The forward scattered light is collected to perform LSSI measures, the backscattered light collected to perform the stress signal. On the forward scattering strain-representing optical pathway, see Figure 6.1(left), the first optical component is an analyzer. This component, placed in front of the camera objective in a cross-polarization configuration, ensures the photons that are scattered

few times, thus conserving the initial polarization, to be blocked.
The property of the light to be in the multiple scattering regime, is fundamental to obtain a good LSSI measure. We want to be sure to collect only light that has explored the sample enough to be considered in a diffusive, multiply scattered, regime. Afterwards, the beam is expanded with an objective, and focused on a HiSpec 1 camera (Fastec Imaging, acquisition rate of 0.5, 4 or 5 kHz).
In the backscattered stress-representing optical pathway, see Figure 6.1(right), the fluorescence signal from the spiropyran sensor was captured with a SA-X2 camera (Photron, acquisition rate of 12 kHz), with the signal amplified by a HiCatt Image Intensifier (Lambert Instruments). The camera's were synchronized and triggered with a pulse generator (Quantum Composers). Upon fracture of the sample, the drop in force triggered a 5V signal to both camera's to stop the ring-buffer acquisition, storing the failure event in the camera's memory.

6.3 Results & Discussion

6.3.1 Macroscopic mechanics during delayed failure

Obtaining a comprehensive mechanical picture preceding delayed material failure requires the mechanics to be tracked both macroscopically and microscopically. Here, we first discuss the macroscopic bulk stress acquired by the load cell during delayed failure. The delayed failure time t_d for the samples tested was observed to decrease as more deformation was applied on sample, as is to be expected, see Figure 6.A.2a. Furthermore, the critical applied strain ϵ_c,at which samples failed, is linearly connected to the critical stress σ_c, see Figure 6.A.2b, as expected when the material fails in the linear elastic regime. Focusing on one of the samples tested, Figure 6.2a,b show that the macroscopic bulk stress appears to drop almost instantly, explaining that this type of failure is experienced as sudden. However, taking a closer look at the stress decay reveals that, rather than an abrupt drop in stress during the material failure, a gradual decrease in stress over the course of milliseconds is observed, as shown in Figure 6.2c. Pin-pointing the stress at which the sample starts propagating a crack was not possible exactly based on time-synchronisation with the current data. Alternatively, tracking of the crack propagation velocity would provide this critical stress, back calculated from the point at which the stress has become zero at complete failure of the sample. Figure 6.A.3 in the SI shows an extrapolation of the crack tip opening displacement (COTD) from the spiropyran data as tracked within the field of view. The crack propagation speed found is in the order of $\sim$ m/s, in line with observations by van der Kooij *et al.*[12] and 2 to 3 orders of magnitude lower than the speed of sound in the material ($\sim$km/s)[19]. Based on the COTD extrapolation, crack propagation starts a few milliseconds before the bulk stress starts to decrease, indicated with the green X in the inset of Figure 6.2. Therewith, the spiropyran sensor was used to show that the decay in the bulk stress coincides with the start of crack propagation. Next, the stress sensor spiropyran will be used to study the stresses around the fracture nucleation site preceding crack propagation.

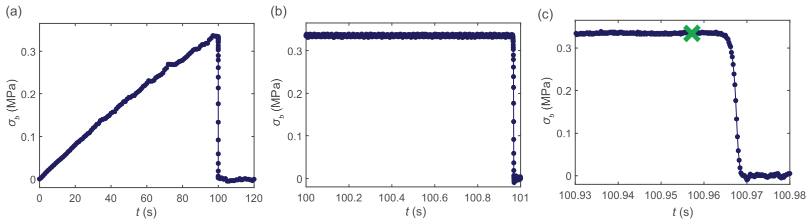

Figure 6.2 – **(a)** Bulk stress σ_b as acquired by the load cell during the entire uniaxial extension of the elastomer. **(b)** σ_b during the second at which the material fails, where the drop in stress still appears to occur sudden. **(c)** σ_b around the failure of an elastomer, with the green cross (X) indicating the time at which the crack starts propagating and the sample catastrophically opens.

6.3.2 Microscopic mechanics during delayed failure

The stress sensor provides the cumulative stress σ_c experienced by the polymers, presented by an increasing fluorescent signal that corresponds to an increasing number of merocyanine bonds switched to the spiropyran state. The uniaxial tensile tests are performed on Single Edge-Notched Beams (SENB), where stresses and strains are well known to concentrate around the notch[20]h. Therefore, the field of view the camera's used to acquire a fluorescent signal from the stress sensor and the multiple scattering light from the TiO_2 tracer beads is focused around the center of the notch.

Comparing mechanosensor kinetics

Previous work by van der Kooij *et al.* has shown that up to a few seconds before the fracture is macroscopically visible, small-scale deformations emerge around the position of crack nucleation[12]. As such, d_2 activation acts as a precursor for material failure. In the current study, we acquire the small-scale deformation activation time t_ϵ, the time at which d_2 activation onsets, from the maps obtained with the d_2 autocorrelation function:

$$d2(t, x, y, \tau) = \frac{\langle [I(t, x, y) - I(t + \tau, x, y)]^2 \rangle}{\langle I(t, x, y) \rangle \langle I(t + \tau, x, y) \rangle} \tag{6.1}$$

d_2 activation is observed to initiate at a locus of about 40-50 squared micrometers localized 50-100 micrometers from the sample edge. Figure 6.3a shows the d_2 activation of the corresponding pixels tracked over multiple seconds. At 6.3 seconds before failure, d_2 exceeds 15 % of the initial level, and the corresponding time is determined to be t_ϵ. The magnitude of d_2, however, is strongly dependent on τ. In previous work[12], $\tau = 0.5$ ms was used. Using this τ resulted in a t_ϵ significantly lower than the actual activation time determined by studying a video of the raw speckle images. It is observed that t_ϵ extracted from the d_2-time histograms is close to the onset extracted from the raw speckle images for τ = 0.1 s. We can explain this difference considering the scattering properties and the physical size of the sample. As reported in[21], the number of scattering events in the sample is proportional to $(L/l^*)^2$, with L the sample thickness and l^* the photon transport mean free path determined independently as described in Appendix 6.5, and the characteristic time scale for the decay of the autocorrelation function, in the case of forward scattering, equals $\tau_0(L/l^*)^2$. In the previous study[12], this ratio was $(L/l^*)^2 \approx (5000/50)^2 \approx 10000$, while it is $(L/l^*)^2 \approx (2000/150)^2 \approx 177$ in the present case. The ratio of these quantities is quantitatively close to the ratio of the two correlation times, explaining the apparent discrepancy. Using τ = 0.1 s, we observe similar order of magnitude d_2 activation kinetics compared to the previous study, i.e. small-scale deformations emerge some seconds before the crack starts propagating.

To study the degree of similarity in activation time between the small-scale deformation activation t_ϵ and micromechanical stress activation

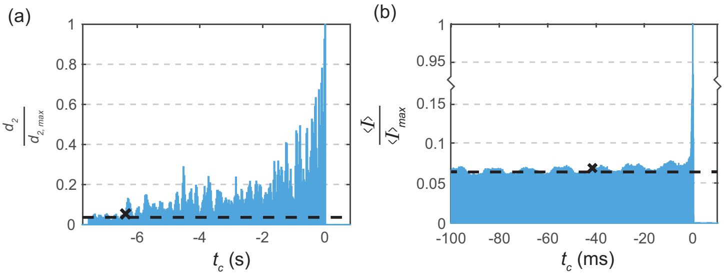

Figure 6.3 – **(a)** The d_2 normalized to the maximum d_2 versus critical time t_c at which the sample starts propagating a crack, with $\tau = 0.1$ s. The black cross (X) indicates the time at which the d_2 signal exceeds 15% of the normalized noise level (- - -). **(b)** The instantaneous spiropyran fluorescence intensity normalized to the maximum intensity versus critical time t_c at which the sample starts propagating a crack. The black cross (X) indicates the time at which the spiropyran signal exceeds 15% of the normalized noise level (- - -).

time t_σ, we determine t_σ from the spiropyran fluorescence signal with the following procedure. First, the mean fluorescence intensity over a square ROI of 1.5x1.5 mm is acquired, with the center at the crack nucleation site. This ROI encapsulates the fluorescence intensity when the intensity is highest, which for all samples tested is at the last frame before the crack starts propagating. After determining a noise level before the fluorescence signal increases, and correcting any fluctuations in the intensity due for e.g. the laser pulsing by using a moving average, an activation time t_σ for the fluorescence signal can be deduced from the samples by locating the time at which the threshold is exceeded, see Figure 6.3. The activation time found for the sample presented in Figure 6.3b is about 43 ms.

The activation times for all samples tested in this study, both for LSSI and spiropyran, are reported in Fig 6.A.5. The observed difference in activation time for the two micromechanical sensors is 2-3 orders of magnitude. There could be two reasons for this large difference in activation time; (1) the spiropyran sensor requires a relatively high onset stress to redshift the fluorescence causing the observer to only acquire the micromechanical stress at relatively high stresses, and (2) strain accumulates only in the order of tens of milliseconds before the crack starts propagating. The former seems to be more plausible, as an increase in small-scale deformation should go hand-in-hand with an increase in local stress, making the latter implausible.

Spatial activation (a)symmetry

In the previous section, we have established that the kinetics observed with LSI and spiropyran differs 2-3 order of magnitude. However, any spatial differences were disregarded. To study the degree of similarity in spatial activation between the two micromechanical sensors, Figure 6.4 shows the spiropyran fluorescence intensity and LSSI d_2 maps for 5 time frames, in panels (a) and (d), respectively. From these maps, the degree and activation length l of micromechanical stress and small-scale deformations are quantified in spatial bins of 15° originating at the crack tip. The data presented in Figure 6.4 suggests that the micromechanical stress signal is more asymmetric than the micromechanical strain. For example, comparing Figures 6.4b and 6.4e bottom panels, d_2 activation is almost symmetric around 0°, which represents the crack propagation direction, whereas the spiropyran stress activation is much more asymmetric. Clearly, there is a spatial difference in activation between the two sensors. The crack tip is offcenter to the center of the notch, as pinpointed by the arrow in Figure 6.4a at t_c = -0.0833. This offset of the crack tip locus from the center of the notch is observed in roughly half of the 30 samples tested in this study. The stress activates more towards the center of the notch, which is located to the top of the current field of view, based on the course of the notch shape. In the sample without any imperfections, stress localization is expected to occur at the center of the notch, as showcased with Finite Element Method (FEM) simulations in Figure 6.A.6a-d. In this example, the stress is symmetric around the center of the notch and shows the shape of a bow-tie. However, when a SENB with a small imperfection is simulated, as shown in Figure 6.A.6e-g, the stress profile at the sample edge drastically changes as it becomes more irregular due to stress concentration around the imperfection. Yet, at lower stresses, a symmetric bow-tie shape is still present. Therefore, the (a)symmetric profile differences observed between the LSI and spiropyran signal can, just like the observed difference in kinetics, be allocated to the difference in sensitivity of the sensor, as the SENB samples are inherently likely to posses imperfections in the network topology around the notch.

The d_2 activation profile shown in Figure 6.4d differs in shape from the profile found in the study by van der Kooij *et al.*[12], where d_2 activation was observed around the full crack tip, whereas the data in the current study mainly shows d_2 activation at the sample edge. FEM simulations show that this difference could be allocated to the difference in notch shape in the tested samples, as the stress profiles does depend on the notch shape, see Figures 6.A.6c and 6.A.6i for a round and rectangular notch shape, respectively. The stress profile from the FEM simulations suggest that for the rectangular profile, the stress at the expected crack propagation direction, i.e. downwards into the sample, is higher compared to the rounded notch. Most likely, stress localization, which strongly depend on the sample topology, is the main reason for this difference.

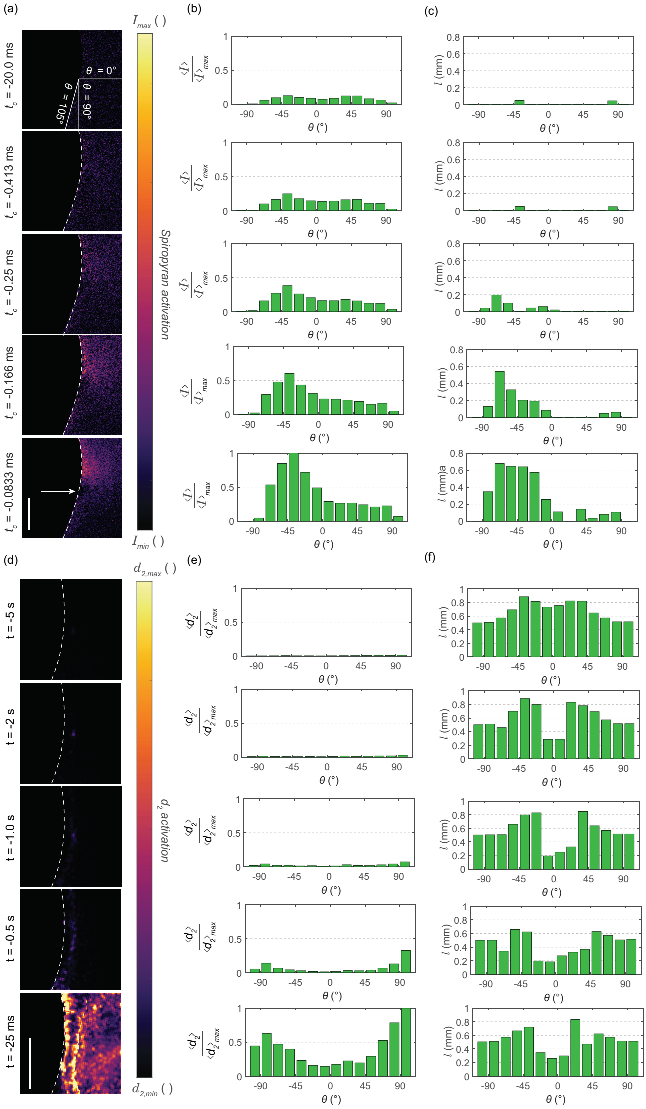

Figure 6.4 – This figure shows the simultaneous acquisition of micromechanical stress, obtained from spiropyran fluorescence, in panels (a)-(c) and small-scale deformations, obtained with LSSI, in panels (d)-(f). **(a)** The spiropyran fluorescence intensity for 5 time frames before $t_c = 0$, which is the first frame where fracture propagation is observed. $\theta = 0°$ corresponds to the crack propagation direction and originates at the crack tip. The arrow in t_c = -0.0833 ms point at the crack nucleation site. **(b)** Normalized mean intensity versus binned angles θ around the crack tip, indicated in panel (a) with the boxes at t_c = -0.20 ms. **(c)** The activation length l over which spiropyran is activated from the crack tip versus the angle θ **(d)** d_2 activation maps around the notch at 5 times prior to $t_c = 0$. **(e)** Normalized d_2 activation versus binned angles. **(f)** The activation length l over which d_2 is activated from the crack tip versus the angle θ. Scale bars represent 0.5 mm.

6.4 Concluding remarks

In this work, we have studied the simultaneous micromechanical strain and stress accumulation during delayed failure at high temporal resolution in elastomers. At the macroscopic level, we have demonstrated that the bulk stress gradually decays when the crack starts propagating at the crack tip. Microscopically, the activation time acquired by the two techniques shows a 2-3 order in magnitude difference, most likely due to the difference in sensitivity between the techniques. This sensitivity difference has also been found to cause difference in the spatial profile of the two sensors, where the spiropyran shows an asymmetric, and LSI a symmetric profile.

In the current study, quantifying the amount of accumulated stress is challenging, as the fast camera used to acquire the spiropyran fluorescence is monochromotic, whereas multichromaticity is preferred[22]. Performing a follow-up study in the future would ideally be performed with the multichromatic Photron Fastcam SA-X2, as this would allow for the quantification of the micromechanical stress from the spiropyran molecule. Yet, in the present study an increased redshift, i.e. increased merocyanine fluorescent signal after filtering the spiropyran signal, does correlate with an increased cumulative stress.

Furthermore, to disentangle the opening of the crosslink “cages” in the elastomer[23] imposed by an externally applied deformation to bond rupture in the d_2 autocorrelation maps, hysteresis tests could be performed. In such tests, the applied strain on the sample is to be relaxed after d_2 activation is detected, which can be acquired at real time by using a fourier transform[24], at a time interval t_r between d_2 activation and sample relaxation. By varying t_r, the resistance of the material to subsequent equal levels of applied strain for n cycles can be tested, allowing for disentanglement of the increased d_2 activation by opening of the crosslink “cages” in the elastomer and bond rupture, where the latter is assumed to increasingly grow as the sample approaches crack propagation. Hence, an increase in t_r is expected to lead to catastrophic failure at lower n. Such an observation would support the hypothesis that bonds rupture by a cascade of events in the seconds before material failure when d_2 activation emerges.

Finally, the method presented in this work could be used in future work to simultaneously acquire spatio-temporal information on the micromechanical stress and deformation for materials with different properties, such as double networks and materials in which the plasticity is varied.

6.5 Appendix Chapter 6

Materials & Methods

Delayed failure experiments on elastomers with the simultaneous read-out of micromechanical stress and small-scale deformations were performed on Single Edge-Notched Beam (SENB). The molds for these beams were 3D printed with an Ultimaker 3, and the dimensions are shown in Figure 6.A.1.

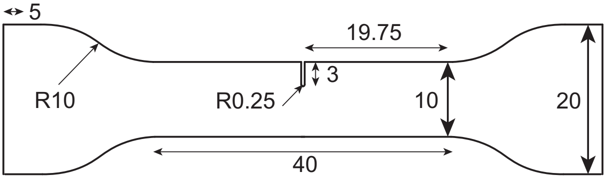

Figure 6.A.1 – Top view of the Single Edge-Notched Beam (SENB), showing the dimensions in millimeters. The sample thickness was 2.5 mm.

l^* - calibration

To obtain a valuable LSI measure one must ensure that the light has scattered enough times inside the material. We do this by calculating the light transport mean free path, namely l^*, and comparing it to the sample size. In the present case, the sample ratio between the thickness, $\sim 2.5mm$, and a measured $l^* = 150 \pm 5$ μ m, is above the limit of $\mathcal{O}(3)$ reported in literature[25].

The measure was obtained in forward scattering geometry. As reported in literature it is possible to know the l^* of a sample, given the knowledge of a reference l^*[26]. For this study we took the reference as polystyrene spherical particles, with radius of 200 nm, concentration ϕ=1 % , and $l^* = 130$ μm. For this calculation, we built an additional setup following the procedure reported in[27]. A laser beam (Changchun New Industries, model MGL-FN-532, 1W, $\lambda = 532$ nm) is guided to the sample cell, in a direction orthogonal to the cuvette surface. After exploring the sample the exiting light is recorded in transmission with a photon-multiplier on the other side of the sample. We measure the light transmitted through the reference sample, and through the sample of unknown l^*. Once the static transmission values are known, we can calculate the l^* of the unknown sample by means of[21, 27]:

$$T = \frac{I}{I_0} = \frac{5l^*/3L}{1 + 4l^*/3L} \tag{6.2}$$

with T the transmission, I and I_0 the initial and transmitted intensities of the laser light, respectively, L the sample thickness and l^* the photon transport mean free path.

Results & Discussion

Macroscopic mechanics during delayed failure

In this study, simultaneous micromechanical information from two techniques is acquired during delayed failure of notched elastomers. The delayed failure time t_d is plotted versus the critical applied strain ϵ_c in Figure 6.A.2a, showing that at high ϵ_c values t_d is lower. Furthermore, ϵ_c is observed to scale linearly with the measured critical stress σ_c, shown in Figure 6.A.2b.

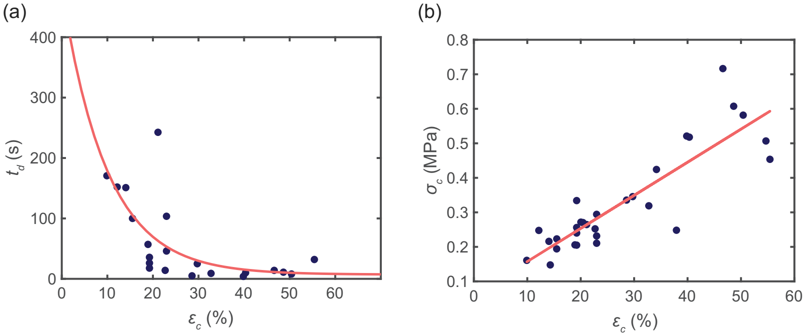

Figure 6.A.2 – **(a)** Critical strain at failure ϵ_c plotted versus the delayed failure time t_d, fitted with an exponential decay function. **(b)** ϵ_c plotted versus the critical stress at failure σ_c, fitted with a linear fit.

To estimate the time at which the sample starts to fail in Figure 6.2, the position of the crack tip is tracked to obtain the crack opening tip distance (COTD). By extrapolating COTD outside the field of view, see Figure 6.A.3, and assuming COTD continues to increase which we assume to be valid here as the maximum velocity reached is a reasonable 1 m/s for this type of material as mentioned in Section 6.3.1, the time of failure is determined.

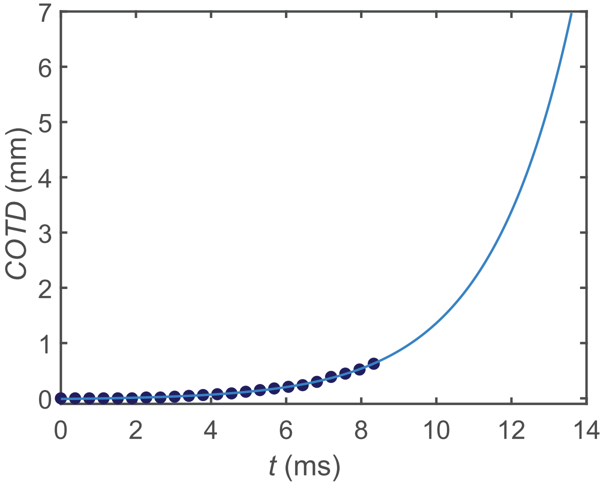

Figure 6.A.3 – The crack opening tip distance (COTD) plotted versus time. The blue datapoints (●) are obtained from the spiropyran fluorescent signal, limited by the field of view. To estimate the time it takes for the crack to propagate trough the sample, the exponential function $a + b \cdot e^{(c \cdot x)}$ is fitted to extrapolate the data.

In Section, 6.3.2 the micromechanical kinetics and spatial activation of the two sensors are discussed. The applied strain ϵ_a, measured bulk stress σ_b during the experimental time t for this particular sample are shown in Figure 6.A.4. The activation times t_σ and t_ϵ for the spiropyran fluorescence and LSI d_2 activation are extracted for multiple samples tested in this study, as shown in Figure 6.A.5. All datapoints in Figure 6.A.5 are in the top left quadrant, indicating that the $t_\epsilon > t_\sigma$.

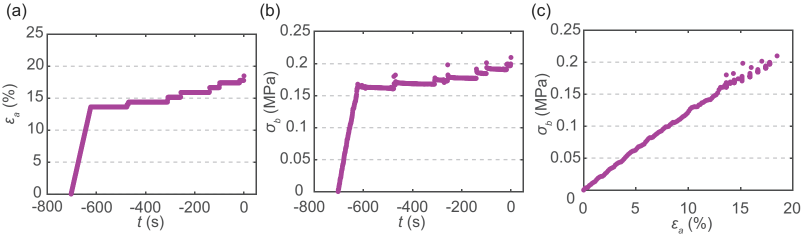

Figure 6.A.4 – Bulk data for the sample presented in Figure 4 of the main text, showing **(a)** time (t) vs. applied strain (ϵ_a), **(b)** t vs. bulk stress σ_b and **(c)** ϵ_a vs. σ_b. The sample shows little delayed failure time t_d and strain softening after the initially applied 15 % strain.

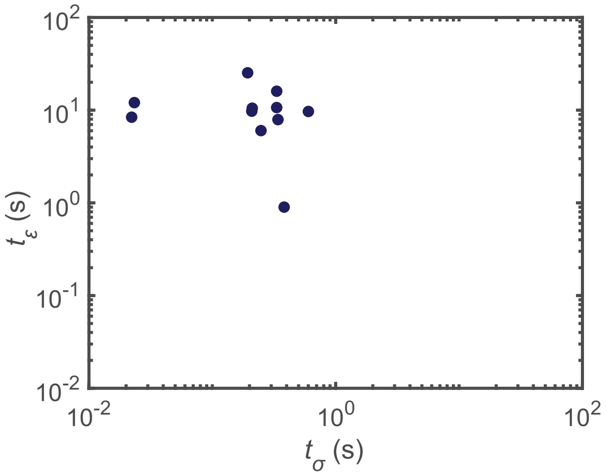

Figure 6.A.5 – Activation times for the microscopic stress sensor (horizontal axis) versus the microscopic strain sensor (vertical axis) for part of the samples tested in this study, showing that the LSSI shows activation at 2-3 orders of magnitude before the spiropyran. Samples where the activation time exceeded the running-buffer limited acquisition memory of the cameras were excluded.

To complement the spatial information obtained with the two micromechanical sensors, Finite Element Method (FEM) simulations were performed using COMSOL Multiphysics, see Figure 6.A.6. The 3D stationary structural mechanics module was used to model the uniaxial extension of a PDMS elastomer with a Young's modulus of 2 MPa by 120 % of the initial length. The linear elastic Single Edge-Notched Beam (SENB) was solved for 156k degrees of freedom.

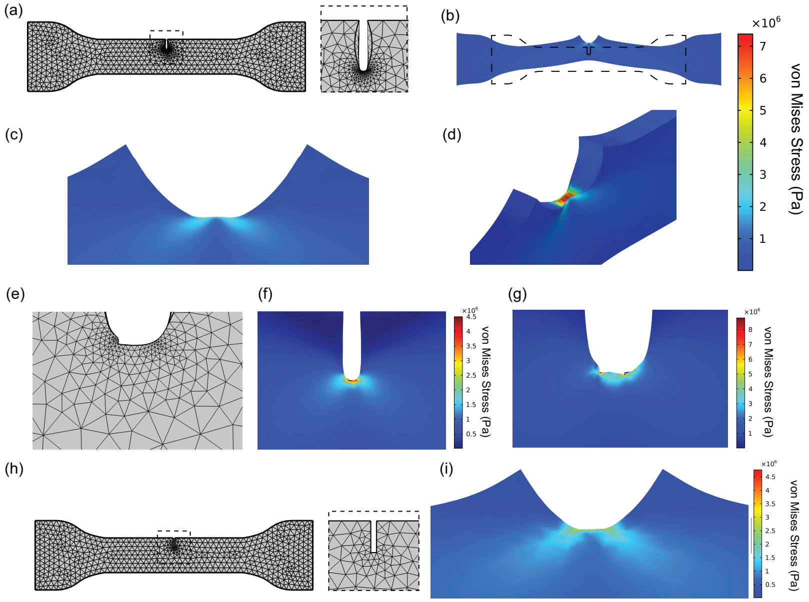

Figure 6.A.6 – FEM simulations where a SENB linear elastic material was **(a)** meshed with 'extremely fine' tetrahedrals, which is a pre-defined physics controlled setting. The inset shows the rounded notch shape, also used in the experiments in this work **(b)** Side view of the sample, showing the sample size before extension in dashed lines and the sample extended color coded with the von Mises stress in the colorbar. **(c)** Zoomed-in side view of the von Mises stress around the notch. **(d)** Zoomed-in 3D view of the von Mises stress under an angle, with scene light activated, showing that the sample, tip in the thickness-plane, curves and thins at the notch, potentially creating a lensing effect. **(e)** Meshing of a SENB with a small imperfection left of the notch center. **(f)** Zoomed-in side view of the von Mises stress around the notch. **(g)** Further zoom-in of panel f. Note the difference in maximum value in the colorbar between panels f and g. **(h)** Simulation of a SENB with a rectangular notch shape, shown in detail by the zoom-in. **(i)** The von Mises stress profile for the SENB with the rectangular notch profile.

Bibliography

[1] Robert Danzer, Tanja Lube, Peter Supancic, and Rajiv Damani. Fracture of ceramics. *Advanced engineering materials*, 10(4):275–298, 2008.

[2] Young Soo Chun, Kyung-Tae Park, and Chong Soo Lee. Delayed static failure of twinning-induced plasticity steels. *Scripta materialia*, 66(12):960–965, 2012.

[3] A Guarino, S Ciliberto, A Garcimartın, M Zei, and R Scorretti. Failure time and critical behaviour of fracture precursors in heterogeneous materials. *The European Physical Journal B-Condensed Matter and Complex Systems*, 26(2):141–151, 2002.

[4] Noushine Shahidzadeh-Bonn, Philippe Vié, Xavier Chateau, Jean-Noël Roux, and Daniel Bonn. Delayed fracture in porous media. *Physical review letters*, 95(17):175501, 2005.

[5] Olivier Lengliné, Renaud Toussaint, Jean Schmittbuhl, Jean E Elkhoury, JP Ampuero, Ken Tore Tallakstad, Stéphane Santucci, and Knut Jørgen Måløy. Average crack-front velocity during subcritical fracture propagation in a heterogeneous medium. *Physical Review E*, 84(3):036104, 2011.

[6] L Pauchard and H Meunier. Instantaneous and time-lag breaking of a two-dimensional solid rod under a bending stress. *Physical review letters*, 70(23):3565, 1993.

[7] Daniel Bonn, Hamid Kellay, Michaël Prochnow, Karim Ben-Djemiaa, and Jacques Meunier. Delayed fracture of an inhomogeneous soft solid. *Science*, 280(5361):265–267, 1998.

[8] Paulina J Skrzeszewska, Joris Sprakel, Frits A de Wolf, Remco Fokkink, Martien A Cohen Stuart, and Jasper van der Gucht. Fracture and self-healing in a well-defined self-assembled polymer network. *Macromolecules*, 43(7):3542–3548, 2010.

[9] Joris Sprakel, Stefan B Lindström, Thomas E Kodger, and David A Weitz. Stress enhancement in the delayed yielding of colloidal gels. *Physical review letters*, 106(24):248303, 2011.

[10] Stefan B Lindström, Thomas E Kodger, Joris Sprakel, and David A Weitz. Structures, stresses, and fluctuations in the delayed failure of colloidal gels. *Soft Matter*, 8(13):3657–3664, 2012.

[11] Xiao Wang and Wei Hong. Delayed fracture in gels. *Soft Matter*, 8(31):8171–8178, 2012.

[12] Hanne M van der Kooij, Simone Dussi, Gea T van de Kerkhof, Raoul AM Frijns, Jasper van der Gucht, and Joris Sprakel. Laser speckle strain imaging reveals the origin of delayed fracture in a soft solid. *Science advances*, 4(5):eaar1926, 2018.

[13] Pavel Zakharov and Frank Scheffold. Advances in dynamic light scattering techniques. In *Light Scattering Reviews 4*, pages 433–467. Springer, 2009.

[14] Asha-Dee N Celestine, Brett A Beiermann, Preston A May, Jeffrey S Moore, Nancy R Sottos, and Scott R White. Fracture-induced activation in mechanophore-linked, rubber toughened pmma. *Polymer*, 55(16):4164–4171, 2014.

[15] Gregory R Gossweiler, Gihan B Hewage, Gerardo Soriano, Qiming Wang, Garrett W Welshofer, Xuanhe Zhao, and Stephen L Craig. Mechanochemical activation of covalent bonds in polymers with full and repeatable macroscopic shape recovery. *ACS Macro Letters*, 3(3):216–219, 2014.

[16] Douglas A Davis, Andrew Hamilton, Jinglei Yang, Lee D Cremar, Dara Van Gough, Stephanie L Potisek, Mitchell T Ong, Paul V Braun, Todd J Martínez, Scott R White, et al. Force-induced activation of covalent bonds in mechanoresponsive polymeric materials. *Nature*, 459(7243):68–72, 2009.

[17] Corissa K Lee, Douglas A Davis, Scott R White, Jeffrey S Moore, Nancy R Sottos, and Paul V Braun. Force-induced redistribution of a chemical equilibrium. *Journal of the American Chemical Society*, 132(45):16107–16111, 2010.

[18] Jess M Clough, Jasper van der Gucht, Thomas E Kodger, and Joris Sprakel. Cephalopod-inspired high dynamic range mechano-imaging in polymeric materials. *Advanced Functional Materials*, 30(38):2002716, 2020.

[19] Jean K Tsou, Jie Liu, Abdul I Barakat, and Michael F Insana. Role of ultrasonic shear rate estimation errors in assessing inflammatory response and vascular risk. *Ultrasound in medicine & biology*, 34(6):963–972, 2008.

[20] Costantino Creton. 50th anniversary perspective: networks and gels: soft but dynamic and tough. *Macromolecules*, 50(21):8297–8316, 2017.

[21] David J Pine, David A Weitz, Paul M Chaikin, and Eric Herbolzheimer. Diffusing wave spectroscopy. *Physical review letters*, 60(12):1134, 1988.

[22] Yinjun Chen, C Joshua Yeh, Yuan Qi, Rong Long, and Costantino Creton. From force-responsive molecules to quantifying and mapping stresses in soft materials. *Science advances*, 6(20):eaaz5093, 2020.

[23] Tetsuharu Narita, Alexandra Knaebel, Jean-Pierre Munch, Miklós Zrínyi, and Sauveur Jean Candau. Microrheology of chemically crosslinked polymer gels by diffusing-wave spectroscopy. In *Macromolecular Symposia*, volume 207, pages 17–30. Wiley Online Library, 2004.

[24] J Buijs, J van der Gucht, and J Sprakel. Fourier transforms for fast and quantitative laser speckle imaging. *Scientific reports*, 9(1):1–9, 2019.

[25] Luis Fernando Rojas-Ochoa, David Lacoste, Ralf Lenke, Peter Schurtenberger, and Frank Scheffold. Depolarization of backscattered linearly polarized light. *JOSA A*, 21(9):1799–1804, 2004.

[26] PD Kaplan, Ming Hsii Kao, AG Yodh, and David J Pine. Geometric constraints for the design of diffusing-wave spectroscopy experiments. *Applied Optics*, 32(21):3828–3836, 1993.

[27] Claudie Bonnet, Milena Corredig, and Marcela Alexander. Stabilization of caseinate-covered oil droplets during acidification with high methoxyl pectin. *Journal of agricultural and food chemistry*, 53(22):8600–8606, 2005.

Chapter 7

General Discussion

This thesis started with introducing three steps necessary to address research questions regarding the role of mechanical heterogeneity on material fracture; (1) development of a mechanically heterogeneous material; (2) verifying and understanding the mechanical landscape; (3) taking a step forward in understanding the fracture process in mechanically heterogeneous materials. In the research conducted in this thesis, presented in Chapters 2-6, we addressed these research questions by means of both experimental work and computer simulations. Although we managed to answer some questions during this research, many new research questions arose. In this final chapter, we will reflect on this research by taking a helicopter view on our findings, linking them to a wider scientific context, and answer the initial research questions where we can. We also look beyond, providing methods that were explored in this work and combining knowledge gained from the research in this thesis with knowledge from literature, developing a vision to answer some of the still open and new research questions in the future, thereby paving the way towards further research and applications.

7.1 Discussion on research performed during this thesis

7.1.1 Discussion thesis Part I

Part I of this thesis is centered around indentation. At the beginning of this project, indentation was chosen as a method to mechanically characterize heterogeneous materials, as other frequently used methods to mechanically characterize materials, such as rheology and tensile testing, probe bulk properties, incapable of obtaining mechanical information at multiple positions in samples. Other experimental techniques that can be used to obtain mechanical properties, see Section 1.2.2, probe mechanics at relatively small length scales ($< \mu$m), making them incompatible with the methods used in this research to produce heterogeneous materials (e.g. photolithography and 2D printing, see Section 1.3.2). This subsection will reflect on the work performed with indentation, discussing Chapters 2-4 subsequently.

In **Chapter 2**, a mechanically heterogeneous material, (methacryloxypropyl)methylsiloxane - dimethylsiloxane copolymer, in combination with 0.01 w/v % of a free radical photo-initiator (2,2-dimethyl-2-phenylacetophenone), is produced based on a protocol described by Choi and Rogers[1], shown to be photocurable at the µm-length scale with a scanning electron microscope. With that, step 1 of this research, see Section 1.6, was performed; a mechanically heterogeneous material was obtained. However, the mechanically heterogeneous profile of the material has to be verified and understood, as described in step 2 of this research. After all, does photolithography of the material used indeed result in mechanical heterogeneity? To verify this, a multi-point indentation setup was built to perform indentation tests at multiple positions across the sample. Analysis of the force-distance curves with Hertzian Contact Theory results in a local elastic modulus, leading to a mechanical map of the sample. Indeed, the material presented in Chapter 2 was shown to be photopatternable, as the imprinted illumination led to the expected mechanical profile. However, the resulting mechanical map is less sharp than the imprinted profile, which could be caused by blurring occurring during the polymerization or by the fact that indentation probes the mechanical response over a finite distance. This was the reason to investigate the physical origin of this blurring in Chapter 3.

The work presented in **Chapter 3** shows that mechanical blurring present in mechanical maps obtained with indentation is a function of the indentation depth and the probe size; the further a material is compressed, the larger the area over which stresses are probed. Using finite element method simulations, we have shown that the blurred or convolved response can be deconvolved using two methods; extrapolation to zero indentation and deconvolution using the SIRT method. With these methods, 1-dimensional (1D) and 2D modulus profiles can be described more accurately and the role of mechanical heterogeneity on fracture can be better understood as well. However, experimental verification of the simulations proved to be challenging. In fact, many efforts were made to experimentally verify the simulations work; multiple methodologies were attempted to create a sample with a mechanically heterogeneous stepwise profile (e.g. plasma bonding two separately cured Sylgard 184 blocks with different elastic modulus and halftone photolithography of photopatternable PDMS[2]), the probe was moved sequentially with a piezo actuator and stepper motor to find the point of contact with the sample with higher accuracy and the components of the in-house built multi-point indentation setup (load cell, stepper motor and piezo actuator) were calibrated multiple times to rule out experimental errors. Unfortunately, the obtained modulus profiles, analyzed with Hertzian Contact Theory, consistently showed a dependence on the indentation depth. The reason that Hertzian Contact Theory was used is because the samples are assumed to be frictionless, the adhesion is assumed to be negligible compared to the obtained stresses and the strains are assumed to be in the linear regime[3]; assumptions that we consider to be valid for polydimethylsiloxane samples. Possible reasons for this depth dependence are mentioned in Chapter 3: skin-formation, modulus-variation in height, air-pocket formation and surface tilt. Future research capable of producing a sample that overcomes these issues could experimentally verify the results from the simulations. Even though experimental verification of the simulations results is not obtained, the work presented in Chapter 3 does present a methodology to more accurately describe the mechanical profile of mechanically heterogeneous materials obtained with contact mechanics testing.

Chapter 4 presents an application of mechanically heterogeneous materials characterized with the multi-point indentation setup. The goal is to help the food industry to improve meat analogues based on a quantitative comparison of the mechanical profile. The methodology, based on spatial auto-correlation analysis of the mechanical maps with Moran's *I*, shows the potential of creating a quantitative comparison between meat analogues and animal meat by introducing a decay length. The method as presented in Chapter 4 takes approximately 24 hours to obtain a mechanical map of 1200 (40x30) points. Ideally, this experiment duration is reduced to diminish drying of the samples. After publication of this work in a journal, a follow up study was started, see next paragraph, where the speed of the experiment has been doubled approximately. This was done by retracing the probe only a fixed distance, equal to the position on the sample step size and, hence, assuming that the sample tilt is $< 45^\circ$ within a row. After a row is completed, the probe is retracted to the initial height, making sure that the point of contact between the probe and the sample is not missed. Further reduction of the experiment time could be obtained by continuous readout of the load cell in the background, something attempted during the design of this methodology as well. Unfortunately, these attempts failed due to challenges with programming the simultaneous control of the continuous load cell readout and probe movement with the stepper motor.

In a future study, which recently started in the PCC group where the research presented in this thesis was conducted, the processing parameters, such as temperature and shear rate, but also contents of the meat analogue, such as salts, water and proteins, will be varied to study the effect on the decay length. In case this methodology shows a connection between the processing parameters and the decay length, the processing parameters can be optimized to create a meat analogue that holds a similar decay length to animal meat, mimicking the texture of animal meat with meat analogues. The next step would be to connect the decay length from meat analogues to sensory panels, scoring the mouthfeel of consuming these analogues. In case there is a direct link between decay length and acceptance of the meat analogue by the sensory panel, in time meat analogues could be produced without sensory panels but rather produced directly based on the quantifiable decay length which would mimic animal meat.

To summarize, in Part I of this thesis, a photopatternable (methacryloxypropyl)methylsiloxane - dimethylsiloxane copolymer was produced and mapped in Chapter 2, the mechanical profile was described more accurately with the methodology described in Chapter 3, and as an application the mechanical maps where used to deduce a length scale from meat samples, enabling quantification of the mechanical texture of animal meats and meat analogues, helping the food industry towards production of meat analogues that mechanically mimic animal meat, based on a quantifiable parameter in Chapter 4. With that, Part I addresses steps 1 & 2 of the initial research plan, described in Section 1.6.

7.1.2 Discussion thesis Part II

Part II of this thesis explores the use of mechanosensors in polymer networks to study microscopic processes during fracture.

Chapter 5 presents a study where the mechanoluminescent molecular probe 1,2-dioxetane is used to obtain a detailed and quantitative insight into the bond rupture processes that occur during puncture of polymer materials. While the materials tested could be considered as homogeneous, of course above a certain length scale somewhat larger than the mesh size, the applied stress is very localized and, therefore, can be considered as heterogeneous. The work shows that a significant number of bonds rupture before critical puncture of the material, which is signalled by a drop in the bulk force acquired by the load cell and a simultaneous spike in bond rupture. After this puncture, the probe continues to penetrate the sample by propagation of a ring-shaped crack. By quantifying the number of rupturing bonds during this propagation stage and showing that this number is higher than the number of bonds expected for a sharp surface (i.e. in case of brittle failure), the damage zone is associated with diffuse failure of a significant size. Furthermore, puncture in double networks shows that, as generally assumed, the majority of the bonds rupture in the first, sacrificial, network. Comparison with MD computer simulations shows that the latter is due to delocalization of the stresses in a large zone around the indenter.

The study also compares the found value for the dissipated energy during hysteresis tests with the energy required for the 1,2-dioxetane molecule to break, which is based on an indirect comparison between mechanically ruptured dioxetane bonds in a PDMS networks and thermally ruptured dioxetane bonds[4]. The latter can be obtained with higher accuracy in a future study, for example with single molecule force spectroscopy experiments[5], basically extending one such crosslinker with an atomic force microscope and acquiring the force-distance curve up to failure.

As a next step, the presented methodology could be performed with a highly sensitive camera, potentially equipped in combination with a signal amplifier such as the experimental setup in Chapter 6, providing spatial information as well. In that way, the damage zone of ruptured bonds could be acquired, both for single and double networks. This information could be used to, for example, shed light on which potential to use in the MD simulations.

Another next step would be to use our methodology, which provides temporal-numeral bond rupture information, to study the role of mechanical heterogeneity on material failure. Here, I propose a method to achieve this goal. The network could be polymerized by means of halftone UV polymerization, as done in the study by Ducrot *et. al*[6], creating layers of crosslinking degree in height, see Figure 7.1. A limitation of this approach is the inherent blurring of the crosslinking concentration at the illumination interfaces due to light scattering and diffusion of free radicals.

In case a network with reproducible mechanical architecture is synthesized and characterized, e.g. by means of multi-point indentation as described in Chapter 2, temporal-numeral bond rupture information can be obtained from a DN with alternating crosslinking degree in the first network (where most bonds rupture, as shown in Chapter 5). Particularly, the number of bonds broken can be related to the elastic modulus and elastic modulus difference between the layers in the first network. Subsequently, these values can be compared to the value found in Chapter 5, which would be essentially the homogeneously crosslinked first network, to obtain the difference in energy dissipated per ruptured bond. In case any differences are found, a next logical step would be to

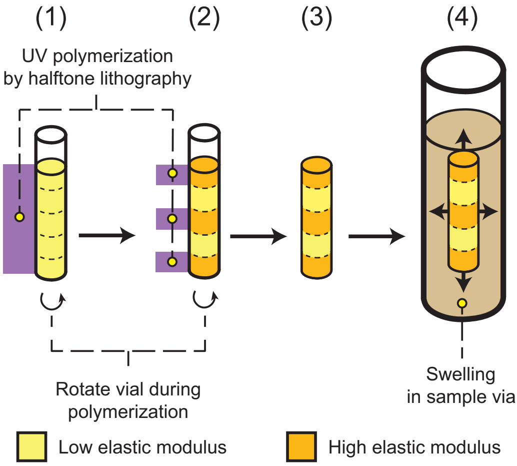

Figure 7.1 – Proposed 4-step sample preparation scheme for a composite double network with alternating elastic modulus in the first network. In step 1, the full material is exposed with UV light. In step 2, only parts are exposed for a second time, giving these parts of the network more crosslinks and, therefore, higher elastic modulus. In step 3, the vial is broken. In step 4, the first networks is swollen the almost the same monomer solution as the second network, with the difference that the first network contains the dioxetane bond rupture sensor and the second network does not.

vary the thicknesses of the first networks, in order to study whether the total energy required to puncture the material is changed. Again, the dioxetane sensor will provide detailed temporal-numeral bond rupture information for each first network layer.

In **Chapter 6**, the mechanosensor spiropyran is used together with Laser Speckle Strain Imaging (LSSI) in an elastomer to simultaneously obtain stress and small-scale deformations from elastomers subjected to uniaxial tension, respectively. The results show that the time scale at which small-scale deformations begin to emerge are, in alignment with a previous study by van der Kooij *et al.*[7], on the order of seconds before the sample starts propagating a crack, whereas the stress onsets in the order of milliseconds before the sample starts propagating a crack. In hindsight, the experiments performed could have been optimized in order to address additional research questions. For example, a more systematic study on the failure time vs. applied strain would ideally be performed in a follow-up study, in order to (1) acquire datasets where the applied strain is not increased during the waiting time (as the applied strain is chosen to break the samples in the order of 1-1800 seconds), and (2) study the relation of stress accumulation, (amount and timescale) to the applied strain. The applied strain is known to scale with the delayed failure time, as also shown in Figure 6.A.2 in Section 6.5. With such systematic data available from future work, the potential stochasticity present in delayed failure can be studied by comparing the stress activation time prior to crack propagation versus the delayed failure time and applied critical stress. Furthermore, the experiment would have benefited from time synchronisation of the bulk load cell and cameras. In the present study, time synchronization of the camera's is conducted by overlaying the timeframe at which the crack starts propagating, and the bulk load cell is not time-synchronized at all. Moreover, the non-averaged up to 10 kHz force readout of the load cell should be stored in a future study for the acquisition in which the force drops to near-zero, to exactly pin-point the moment at which the spiropyran sensor fluorescence intensity increases in correspondence with the bulk stress, rather than back calculating from the frame where the crack starts propagating.

In the current study, the number of spiropyran bonds activated could not be quantified from the monochrome fluorescence signal. Doing so would require a multichromatic signal[8], which could be obtained with the color sensitive equivalent of the camera used, i.e. the Photron Fastcam SA-X2 color camera. For the present study, this camera was not available, but a future study would benefit from this effort as in that case the micromechanical stress can be quantified.

While the methodology presented in Chapter 6 shows a way to simultaneously acquire micromechanical stress and strain, it does not provide the possibility of quantifying the number of bonds broken such as presented in Chapter 5. Therefore, a full fracture mechanics picture could be acquired by incorporating the 1,2-dioxetane crosslinker into the elastomers studied in Chapter 6 as well. Practically, this means that changes will have to be made both on the chemical side and the experimental side compared to the methodology used in Chapter 6, both of which should be feasible. Chemically, the 1,2-dioxetane crosslinker functional group would have to be changed from bis-methacrylate functionalized to bis-vinyl functionalized, such as a study by Clough *et al.*[4]. Experimentally, an additional dichroic mirror would have to be placed after the objective on the LSI-signal acquiring signal, where an extra camera would acquire the 1,2-dioxetane photon emission. With this extra camera in place, the spatio-temporal information on broken dioxetane bonds could be acquired. With this information, the micromechanical stress and strain accumulation could be linked to bonds breaking in the material around the notch, potentially confirming the erosion hypothesis introduced in Chapter 6. The temporal dioxetane bond rupture information is expected to be closer to the spiropyran than the LSSI signal, as bond rupture requires a significant accumulation of stress and strain. The idea of adding bond rupture sensors to the current methodology, that allows for simultaneous acquisition of microscopic stress and strain, will be complemented with the possibility to study mechanical heterogeneity as well in Section 7.2.2.

Lastly, the current methodology, improved with the above suggestions, could be used in the future to study micromechanical processes preceding delayed failure for other materials with different mechanical properties as well, such as tougher materials (e.g. double or triple networks), more brittle or ductile materials, or materials with fillers that acts as plasticizers. By doing so, mechanical properties can be coupled to micromechanical processes preceding delayed failure, potentially leading to new insights in how to forecast and/or reduce delayed failure.

7.2 Towards fracture of mechanically heterogeneous materials

The work presented in this thesis in Chapters 2-4 shows the production and characterization of mechanically heterogeneous materials. In these Chapters, the research questions posed in steps 1 & 2 in Section 1.5 are addressed. Next, the target was to develop a systematic study, in which the stochastic nature of fracture could be addressed and where parameters (e.g. mechanical heterogeneity, toughness, ductility, visco-elasticity, poro-elasticity) could be systematically tuned and probed to study their role in fracture mechanics. While the first research question in step 3 in Section 1.5 is addressed in Chapter 5, the other research questions were only explored in preliminary work. To initiate this effort, Chapters 5 and 6 shows work with two mechanosensors to obtain microscopic information on the fracture process of a material with the eventual goal to study the role of mechanical heterogeneity in fracture mechanics. Moreover, in this subsection, the preliminary work of two novel approaches will be presented that were designed during this PhD project to address the remaining research question posed in step 3 in Section 1.5. Here, these two approaches, their advantages, limitations, and future potential, are discussed.

7.2.1 Further approaches initiated during this thesis

(1) Fracture in macrofluidic channels

In the first methodology, mechanically heterogeneous samples were being pushed hydraulically on a wedge inside a macrofluidic device, inspired by the work of the Bouchaud lab[9], enabling the acquisition of fracture events repeatably with samples with identical programmed heterogeneity (see Figure 7.2). This goal was inspired by the fact that fracture is a stochastic process, largely dependent on the presence of possible local weak spots present in the material creating stress concentration, see Chapter 1. Therefore, to study the fracture process of a mechanically heterogeneous polymer network, many repeated experiments would be needed to accurately describe this process. The idea was to produce heterogeneously crosslinked polymer networks and load them one after the other in a fluidic device, where samples would be pushed on a bifurcation wedge to fracture them, shown by the schematic in Figure 7.2. Loading the samples in these devices required, from a practical point of view, the samples to have a size on the order of millimeters, to manually handle and load the samples. The applied hydraulic pressure would be recorded throughout the experiment, giving information about the energy required at fracture by means of Newton's third law.

With this high statistics data, i.e. high speed images with corresponding applied hydraulic pressure, acquired, the aim was to address some of the research questions postulated at the start of this thesis, given in Section 1.5. Additionally, research questions regarding crack directionality, crack tip velocity and crack arrest could be addressed. Examples of these research questions with associated network topologies are showcased in Figure 7.2;

1. Sample (a) shows a mechanically homogeneous sample; what does

the fracture process look like in this reference material with zero heterogeneity? Acquiring this data and compare it to type of change in network topology will expose the role of the mechanical heterogeneity.

2. Sample (b) shows a sample in which fracture directionality could be tested; will the crack direct around the high modulus center region? In addition, the modulus ratio could be varied in order to study whether this ratio plays a role in redirecting/contouring[10] and/or bifurcating/pinning[11] the crack front.

3. Sample (c) shows a sample with alternating strips in modulus could be tested; is the crack tip velocity dependent on the modulus? Based on equation 1.34 derived with LEFM in Section 1.4.3 an inversely proportional relation is to be expected.

4. Sample (d) shows a thicker strip orthogonal to the sample motion; is the crack arrested by a high modulus region? Again, how does this eventual arrest depend on the relative difference in elastic modulus?

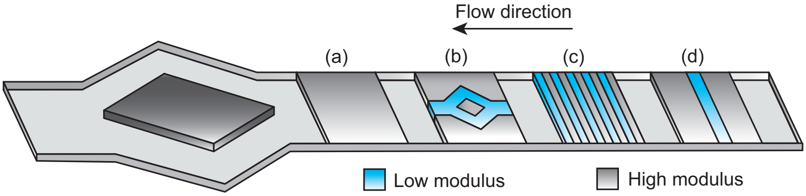

Figure 7.2 – Schematic of the mechanically heterogeneous material profiles that could be tested with a fluidic fracture geometry.

Studying fracture mechanics as a function of heterogeneity requires control over the heterogeneity. Controlling heterogeneity was achieved with UV-lithography, based on the protocol described in Chapter 2, using (methacryloxypropyl)methylsiloxane - dimethylsiloxane copolymer in combination with a photo-initiator. In this system, the local UV dosage sets the amount of local crosslinking. Hence, varying this dosage across the sample results in a mechanically heterogeneous material. In our lab, the UV intensity could be spatially controlled up to a resolution of 2 μm, set by the device used to create the UV dosage[12]. This was sufficient to imprint heterogeneity in samples on the size of milimeters, practically required for loading in the macrofluidic test channels. As the size of polymers in on the order of 1-100 Angstrom, it is important to point out that the heterogeneity is controlled at a length scale where many $(\sim\ 10^{2-5})$ polymers are exposed and thus not at the single polymer level.

The dataset shown in Figure 7.3 is representative of the stage that was accomplished for this methodology. Figure 7.3 shows the distance from the tip of the wedge to the back-end of the sample loaded and the applied pressure over time. From this data, some fracture parameters could be studied, such as critical pressure, fracture energy (see equation 1.28), fracture toughness (see equation 1.29 with the modulus measured by indentation as described in Chapter 2), and fracture propagation speed. Subsequently, the goal was to vary the elastic modulus and to study the influence on these fracture parameters. However, there are some prerequisites in this experiment to accurately describe this failure process:

1. There should be no leakage between the channel and sample for two reasons; (i) the energy required to fracture samples is much harder to achieve in case some of the applied pressure is wasted on leakage, and (ii) Newton's third law could not be used anymore to relate the hydraulic pressure to the critical fracture stress, as the latter part of this equilibrium should be combined with the pressure lost with the leaking solvent. Hence, the energy required to fracture the sample would be unknown. Attempts to limit this were pursued by minimizing the height difference between the channel and samples, as described in Appendix 7A.
2. The wedge should stay intact and the deformation should be negligible during the fracture test, as only in this case the stress is concentrated and the fracture process can be described with models that assume stress concentration, see Section 1.4. In addition, deflection or delamination of the wedge tip would hinder actual fracture of the sample.

The data presented in Figure 7.3 shows that up to fracture, the above prerequisites hold. After some 24 seconds, the crack length increases and the crack starts to open up further as the sample is fracturing. After some 35 seconds, crack opening is halted when the sample breaks in the top

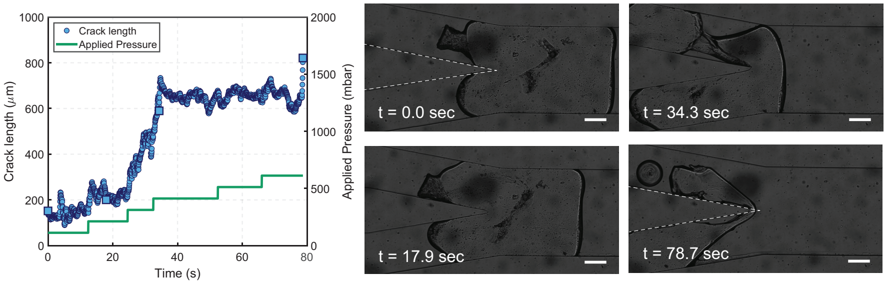

Figure 7.3 – Crack length and applied pressure over time for a homogeneously exposed photopatternable polymer network, and snapshots corresponding to the square datapoints for the crack length. The top and bottom snapshots have the wedge tip superimposed with a dashed white line. Scale bar is 200 μm.

bifurcated channel, enabling fluid to bypass the sample, dropping the pressure applied on the sample. Therefore, the pressure was increased to continue the opening of the crack. However, the snapshot at t = 78.4 seconds shows that the sample has moved beyond the tip of the wedge, implying that it has delaminated the channel wedge. In addition, the shape of the crack does not remain fully sharp but rather deflects, as can be seen in the t = 17.9 sec and t = 34.3 sec snapshots.

At this point, it was hypothesized that the difference in fracture toughness between the sample tested and the channel wedge, see equation 1.29, was insufficient to fracture the samples while maintaining the integrity of the wedge throughout a fracture experiment. To increase this difference, there were a few options that were explored, briefly summarized here:

1. The elastic modulus of the samples was lowered by decreasing the UV dosage used to decrease the number of activated free radicals and consequently lower the amount of crosslinks in the samples.
2. The modulus of the macrofluidic channels was increased by:
    - 2.1. changing the ratio of Sylgard 184 from 10:1 to 5:1
    - 2.2. producing macrofluidic channels out of a material that has a higher elastic modulus than Sylgard 184. Here, it was attempted to produce these with SU8-100, as the elastic modulus of

SU8 is 2-3 orders of magnitude higher compared to Sylgard 184[13]. The SU8 channeled where sealed using a glass slide with Norland UV glue spincoated on it, curing the glue after contact. Unfortunately, these channels did not seal properly and were leaking fluid when the pressure was raised above 0.2 bars.

3. The ductility of the samples was decreased by swelling the samples in ethyl acetate for 48 hours, removing any non-percolated polymer chains that act as fillers and therefore are able to absorb energy and increase ductility. After swelling, ethyl acetate was removed from samples by submerging them in acetone and water for 24 hours, subsequently, deswelling the samples.

However, even after optimizing the difference in fracture toughness between the sample and channel, the above mentioned issues were not solved. Hence, it was concluded that the method as presented here was incapable of performing fracture tests that would enable a systematic study of the fracture process of mechanically heterogeneous fracture in polymer networks. Nevertheless, the method to fracture soft polymer networks in macroluidic devices with repeatably loadable samples explored in this work could inspire others to improve the method and make it capable of performing the fracture tests. Here, four ideas are explored that could bring this goal a step closer:

1. To decrease the possibility of solvent leaking around samples before it has fractured, making mechanical analysis of the fracture mechanism impossible as energy balance is violated, samples could be made more brittle or experiments could be performed on different materials which are more brittle, keeping in mind that in order to study mechanical heterogeneity the heterogeneity needs to be controllable.

2. The elastic modulus of the macrofluidic channels could be enhanced by choosing a different material out of which the channels are made. As attempted during this research, this material could be SU-8. Work presented by Zhang *et al.*[14] shows a method to plasma-seal SU8 with Sylgard 184, using N_2 plasma treatment of the Sylgard 184. Channels made with this method should have

a fracture toughness that is at least an order of magnitude higher than Sylgard 184, significantly increasing the possibility of the fracture test to work. Another advantage is that the user keeps the flexibility of easy altering of the channel design, simply by creating a master with a different layout.

3. The fluidic device could be fabricated with glass or quartz chip using an isotropic wet etching process (Dolomite Microfluidics, UK), significantly increasing the capability of the channel to resist deformation and/or delimitation of the wedge tip. Downsides of this method are the higher cost and the lower flexibility of changing the design of the fluidic device.

4. The fracture toughness of the samples could be lowered by choosing a different polymer. The challenge is that in order to study the relation between heterogeneity and fracture, the heterogeneity has to be programmable. In work presented in 2018 by Yin *et al.*[15], a PEGDMA hydrogel with a reported stiffness on the order of 10 kPa, 1-2 orders of magnitude lower than the photopatternable polymer network used in this work, was reported that is also photopatternable. Crucially, the sample height change for increased stiffness parts shows a slight increase of 2%. This polymeric material could serve as a model system to study fracture of heterogeneous materials, although manually loading of such soft sample might prove challenging.

(2) Fracture in macroscopic beam networks using photoelasticity

In the second methodology, designed to systematically control and measure the heterogeneity of a material during fracture, the system size of the network was up-scaled, allowing for full control over the network topology, and therewith heterogeneity. The big advantage is that at these length scales the network topology is easily controlled by means of 3D printing beam networks and, hence, the role of the network topology can be coupled to the fracture site. Examples of fields where such beam networks are studied include metamaterials[16] and studies that mimic biological fibrous networks[17]. An inherent consequence of this approach is that a mm-cm scale beam mimics a single connection in a polymer network, while in fact these beams consist of many polymers. Generally, computer simulations can accurately describe the mechanics of 2D beam networks. However, the time domain is often challenging to describe in models, as assumptions have to made on visco-elastic relaxation processes leading to models that might not capture the real situation. Therefore, the goal was to use cm-scale 2D beam networks as model systems to study the time-dependent phenomenon fatigue, i.e. the systematic build-up of microfractures upon cyclical subcritical deformation of a material which eventually leads to catastrophic failure. Particularly, the aim was to cyclically deform the network and link stress and strain information of every beam to the fracture process, potentially to forecast the cycle and failure location in networks based on the topology of the network using graph theory. The strain information was obtained by taking bright field images of the beam network as it was being deformed, simply by calculating the change in beam length after applied bulk deformation. The stress information was obtained using the well-known principle of photoelasticity[18].

Photoelasticity is a technique where a birefringent sample of interest is illuminated with polarized light, changing the refractive index upon mechanical deformation. Most crystalline materials are birefringent, whereas only a relatively small fraction of non-crystalline polymeric materials are birefringent[19]. A typical photoelastic response results in so-called fringes, an alternating pattern of black and white intensity corresponding to a difference in principal stresses, observed when a birefringent sample, placed between two polarizers, is illuminated with polarized light. Examples of studies where this photoelastic response has been used include the study of interparticle forces in jamming granular packings[18,19], showing force chains, and the study of auxetic materials[20].

The experimental setup built in this study is capable of simultaneously recording strain and stress, by recording non-polarized and polarized light, respectively, see Figure 7.4a. The sample is produced according to the procedure presented Figure 7.4b. It should be noted that 3D printing of 2D beam networks is associated with downsides as well, including limited resolution at sharp corners and underfilling of the mold, leading to odd shaped samples and irreproducibility problems. Such irreproducibilities could entail changes in sample and/or beam cross-sectional area, influencing mechanical behaviour, or rounded corners, influencing stress concentration. Considering that these irreproducibilities occurred on a

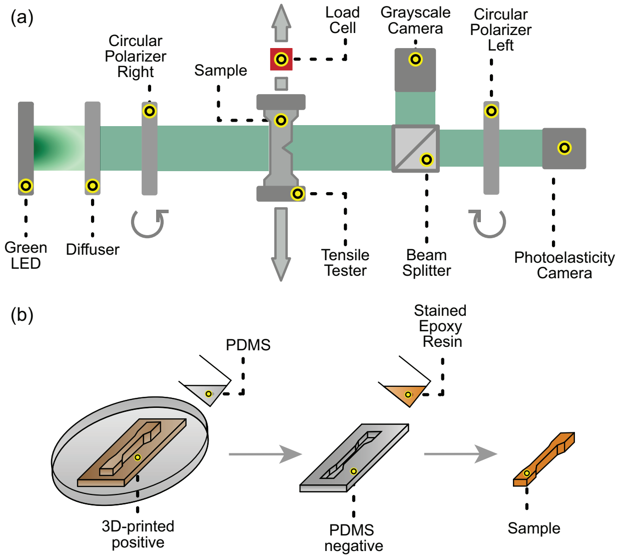

Figure 7.4 – **(a)** Schematic of the experimental setup used to deform samples in a tensile tester and record bright field and photoelastic signal simultaneously **(b)** Synthesis of the 2D beam networks, casting PDMS on a acetone-vapored ABS 3D print, and pouring the photoelastic material in the resulting PDMS mold.

low degree by careful sample preparation, the assumption is made that samples are reproducible. A load cell captures the bulk stress while two oppositely directed actuators, which essentially make the tensile tester, deform the sample. To convert the photoelastic signal into a stress, calibration tests are performed on single beams, for which a calibration from photoelastic signal to stress is shown in Figure 7.5a. The beams in Figure 7.5a show that the photoelastic response, the intensity of the beam, does not increase linearly with the applied strain. Rather, the fringe pattern, i.e. the black and white pattern, at position (x,y) in the sample scales with the sine square of a principal stress difference between the two principal stresses σ_1 and σ_2:

$$I(x,y) = I_0 sin^2\left(\frac{\pi\left(\sigma_1 - \sigma_2\right) hC(\lambda)}{\lambda}\right) \tag{7.1}$$

with h the sample thickness, λ the light wavelength and C(λ) the stress-optic coefficient (a λ-dependent material property)[19,21]. From

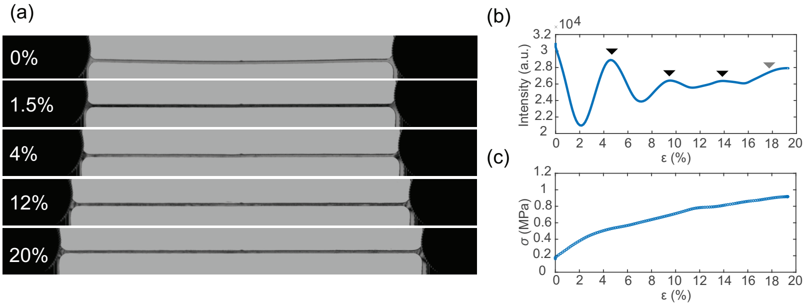

Figure 7.5 – Single beam calibration. **(a)** An increasing applied deformation ϵ of single beam, from top to bottom **(b)** The intensity of the beam plotted versus the applied strain ϵ for the single beam in panel (a) **(c)** The stress as recorded by the bulk load cell plotted versus the applied strain ϵ.

Figure 7.5b,c a so called fringe number, a stress per fringe, is deducted. Fringes are indicated by the arrows in Figure 7.5b, i.e. at the maxima of the intensity vs. applied stain plot, with each interval between arrows a fringe. The combination of Figures 7.5b,c is used to convert the fringe patterns in more complex networks, shown in Figure 7.6, to stresses, a process that is described in detail by means of a flowchart in Appendix 7B. These stresses are then linked to the topology of the network by obtaining information on the beam importance through network theory. Particularly, Geodesic Edge Betweenness Centrality (GEBC) is used to describe importance of beams in the networks, inspired by work of the Daniels group[22], a process that is also described in detail by means of a flowchart in Appendix 7B. GEBC is a value that represents beam importance in a network by finding the shortest path from each beams to all other beams, essentially finding beams through which a relatively high number of shortest paths run. The Daniels group has shown that GEBC can help to forecast the failure location in 2D laser-cut acrylic networks, enabling the exclusion of many unlikely fracture sites[22]. An inherent consequence of laser-cutting materials is the residual stress present in the material after laser-cutting, leading to an unknown steady-state stress profile and irreproducabilities upon repeating the experiment, drawbacks that are not present in the sample preparation presented in the work discussed here.

The networks shown in Figure 7.6 are the 2D beam networks tested in this project. The p-value indicates the fraction of beams that remain

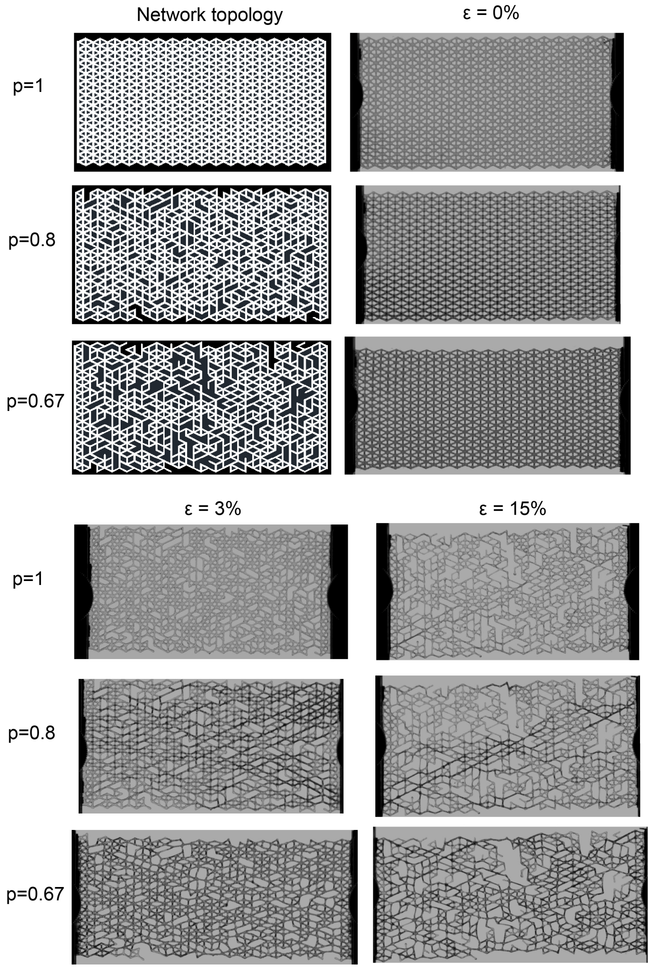

Figure 7.6 – Network topology and photoelastic responses for p=1, p=0.8 and p=0.67 beam networks deformed to three different strains ϵ.

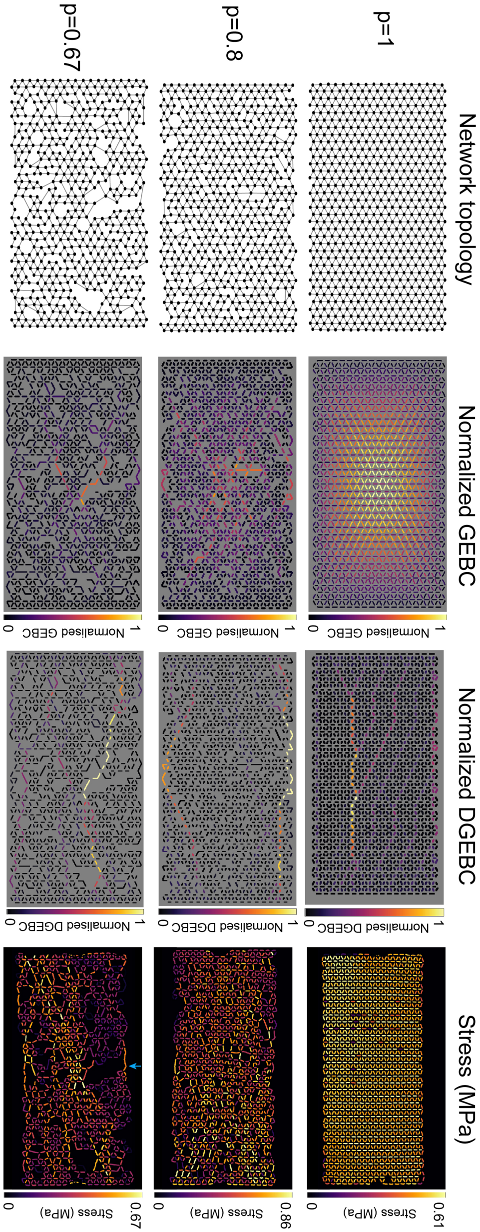

Figure 7.7 – Network topology used for Geodesic Edge Betweenness Centrality (GEBC), Directed Geodesic Edge Betweenness Centrality (DGEBC) and Stress for p=1, p=0.8 and p=0.67 networks. The blue arrow in the bottom left panel indicates the first fracture location after 51 cycles from $\epsilon = 0\%$ to $\epsilon = 15\%$.

present after random removal of beams, excluding the two outer columns of beams on each side. So far, only one configuration for the p-values was tested.

At this point, all the ingredients are in place to link the network topology to the stress and strain buildup. Figure 7.7 shows an overview of the preliminary results that were achieved in this study. The GEBC value shown particularly for the p=1 network does not resemble an expected homogeneous distribution of stress. An explanation is that the GEBC value calculates beam importance by finding the shortest path from all beams to all beams. However, the stress applied to the system is from sink to source, i.e. the sites a deformation is applied to the network, in this case from left-to-right. Therefore, rather than finding the shortest path from all the beams to all other beams, a Directed Geodesic Edge Betweenness Centrality (DGEBC), developed in this study, was used to find the shortest pathway from all sink to source beams, see Figure 7.B.2 in Appendix 7B. The results for DGEBC, also shown in Figure 7.7, do not actually forecast the location of the first fracture event, indicated by the arrow in the bottom right corner, as shown by e.g. the $p = 0.67$ network. Rather, the center pathway indicated in yellow for the p=0.67 network would be the DGEBC-predicted fracture location. A possible explanation could be that in the DGEBC analysis there is merging of some beams, as can be seen by comparing the network topologies between Figures 7.6 and 7.7, causing some pathways to become shorter and, therefore, alter the importance on the centrality scale. This distribution in length could be corrected for in future efforts by allocating so-called weights, i.e. importance, to the beams, a feature incorporated in the MATLAB tool. Yet, the stress data does show a relatively high stress at the location of the first fracture, indicating that these bonds carry stress for almost the top half of the network. Future work could be pursued to overcome the issues with the merging of beams and link geodesic centrality information to local stress and strain of beams to forecast network failure.

To recapitulate, the goal of this work was to study the role of network topology on fatigue and to forecast the location of fracture events. With the current status of this project, the first bond rupture event could not yet be linked to the network topology. In order to achieve this link, the DGEBC analysis would have to be improved and the experiment would have to be repeated for multiple networks at the same p-value, with different randomly deleted beams, to verify an eventual correlation. Furthermore, results show that after the first bond is broken, stress relaxes to the neighbouring beams, as the photoelastic response undergoes some fringes in this area. The challenge is to track this stress relaxation. Attempts to estimate the stress buildup of beams after they had fractured and relaxed their stress, by matching the change in photoelastic response to beams before the beam fracture, were so far unsuccessful. Yet, in case the challenges in the presented methodology are overcome, it could lead to new insights in connecting network topology to local stress and strain information and forecasting the fracture location.

7.2.2 Combining gained thesis knowledge with literature to address open research questions

The work in this thesis paves the way towards a systematic study on the role of mechanical heterogeneity on material failure. Here, at the end of this thesis, lessons learned from the work in this thesis will be combined with some reports in literature, in order to recommend further strategies that could be pursued to couple mechanical heterogeneity to material failure.

Improving compatibility of photopatternable PDMS with mechanosensors
Material failure is governed by complex physical processes, depending on various material properties in the fracture toughness, such as the elastic modulus and the fracture energy, which in turn are set by the (local) polymer structure, the length of the polymer chains, the degree of polymerization, the density and the bond dissociation energy. To study the effect of local polymer structure, i.e. mechanical heterogeneity, on material fracture, one would like to study a particular material with various mechanically heterogeneous profiles using a tool that gives insight in the local physical processes. Section 1.4.3 introduces some of the mechanoluminescent probes that report on polymer strain, stress or even scission, tools that provide valuable information on local physical processes. Each of these probes has limitations, posing associated challenges that result in desirable

properties for the mechanically heterogeneous material. For example, Section 1.2.2 introduces LSSI to obtain an indirect measure for the material strain as bonds rupture localized at the material notch, only observable just before the material fails[7]. In another example, Section 1.4.3 introduces the stress sensor spiropyran, which only activates above a certain force threshold and, therefore, requires the material to resist failure until polymers are stressed above this threshold. As a last example, Section 1.4.3 also introduces the polymer scission reporter dioxetane, emitting a single photon upon scission with a quantum yield of $\sim$10%[23], requiring a minimum numbers of bonds to break before a detector is of high enough sensitivity to acquire the signal. These examples show that not all materials will be suitable for the presented mechanosensors, as stresses reached might be insuffucient to activate the spiropyran sensor or the number of bonds broken might be insufficient to be sensitive to the photon emission signal of the dioxetane sensor. Therefore, a mechanically heterogeneous material has to be able to generate localized stress concentration and/or exceed stresses (spiropyran) before the material fails, and have a minimum number of bonds breaking (dioxetane) as otherwise these sensors can not be used to study the fracture mechanics of the mechanically heterogeneous material. In the mean time, future research might lead to mechanosensors with enhanced sensitivity, such as the Diels-Alder adduct of π-extended anthracene reported by Göstl, Sijbesma, and co-workers[24, 25] used for example to quantify rate- and temperature-dependent molecular damage in elastomer fracture by Slootman *et al.*[26], could reduce part of the aforementioned requirements of the materials to be compatible with the mechanosensor used.

The mechanically heterogeneous material presented in Chapter 2 has the limitation that it is fairly brittle; upon removal of the material out of 3D-printed molds samples frequently failed. Therefore, obtaining stress information from this material, as done from Sylgard 184 samples in Chapter 6, was impossible. To produce a sample with a higher elongation-at-break, the (methacryloxypropyl)methylsiloxane - dimethylsiloxane copolymer was mixed with both solid (silicon dioxide, amorphous, hexamethyldisilazane treated, 13 wt%) and liquid (polydimethylsiloxane trimethylsiloxy terminated, 125-250 cSt) fillers, optimizing the materials ductility; work performed by BSc student Robin Schouten. Unfortunately, the gains in elongation-at-break where insufficient to make the material compatible with activation of the spiropyran sensor. Alternatively, an extra polymer (methacryloxypropyl terminated polydimethylsolixane) could be added to achieve a material with higher elongation-at-break[27]. This material, with a elongation-at-break sufficient to mechanically activate spiropyran and obtain stress information, can then be heterogeneously photo-printed as showcased in Chapter 2, and the same methodology as presented in Chapter 6 could be used to study the stress-strain build relation of mechanically heterogeneous materials. Taking this even a step further, the 1,2-dioxetane crosslinker could be incorporated in this system as well, as this material has shown dissolvability in vinyl-terminated Sylard 184, and should also be dissolvable in the (methacryloxypropyl)mehtylsolixane mixture and/or methacrylate-terminated polydimethylsolixane, allowing for the readout of bond rupture. Importantly, the emission wavelength of the 1,2-dioxetane bond in toluene (λ_{em} = 486 nm) is well below the wavelengths used in the experiment described in Chapter 6. Unfortunately, due to time constraints, these more ductile photopatternable networks were not yet combined with the dioxetane mechanoluminescent probe to study material failure of mechanically heterogeneous materials. In future studies, this would be a highly interesting study to perform, as the dioxetane probes would enable direct visualization of bond rupture locations throughout the fracture process. With the mechanical profile of the material known, obtained with multi-point indentation, the effect of mechanical heterogeneity on fracture can be studied. In case the acquired signal of the dioxetane is below the sensitivity of the camera, an image intensifier could be considered[28], expanding the dynamic range of the camera.

Creating a material with mechanical heterogeneity: Laser cutting
A methodology that could be considered to create a mechanically heterogeneous material is laser cutting, in which laser pulses are used to essentially break polymer bonds at the point where the laser hits by locally heating these bonds. With this technique, 2D beam networks, much like the networks studied in Section 7.2.1 in combination with photoelasticity, can be obtained[22]. The accuracy of this process is dependent on the laser settings (laser power and velocity)[29] and the polymer illuminated[30]. By cutting samples at multiple positions, a polymeric material with desirable heterogeneous structure could be obtained. Repeatability of this topology is obtained by using motorized and computer controlled stages. However, laser cutting does come with limitations, as it requires

optimization of the laser cutter settings for the polymeric material used and it is associated with defects such as microcracks, heat-affected zone and redeposition of material. These limitations will result in slight irrepoducability in the exact network properties, as e.g. the number microcracks will vary from sample to sample. A further limitation is that the mechanical heterogeneity that is obtained is either the materials modulus or zero modulus, i.e. presence or absence of material, while it would be interesting to study mechanical heterogeneity with a (non-zero) grayscale in heterogeneity.

Creating a material with mechanical heterogeneity: Photopatterning of acrylate samples

The dioxetane crosslinker, a mechanoluminescent probe that emits a photon upon scission, has been used to show that from single to double to triple networks an increasing amount of bonds are breaking due to prestretching[6]. In this study, acrylate samples are produced with uniform UV polymerization. In principle, mechanically heterogeneous patterns could be obtained in these network in case the UV pattern used for polymerization in non-uniform. However, unless quenched, the 2-hydroxyethyl-2-methylpropiophenone UV-initiator used will continue to polymerize the network, a process strengthened by the relatively long overnight polymerization time in the current protocol, reducing the effect of the inhomogeneous UV exposure on creating mechanical heterogeneity. Quenching of the UV initiator could be achieved by a shorter polymerization time, bringing the sample into contact with air where oxygen will quench the reaction. Alternatively, adding a small amount of thiols, for example ethanethiol, should quench the reaction as well, making the process as bit more controlled as the concentration of thiols added can be optimized. The non-uniform UV pattern can be readily obtained by illumination trough a photomask or with a spatially translatable UV source[12].

7.3 Perspective on heterogeneous materials

For the past 5 years I have had the privilege of exploring routes to unravel the role of mechanical heterogeneity on material failure experimentally on a microscopic level. This turned out to be a challenging goal to achieve, for which there are a few reasons, including; the chemical and volumetric challenges associated with the usage of mechanosensors, the challenges and limitations associated with the synthesis of mechanically heterogeneous materials and the challenges of designing an experimental methodology that presents the desired scientific output while not being hindered by the before mentioned limitations. Answering the research questions posed at the beginning of this research related to the role of mechanical heterogeneity on material failure requires future research to be conducted. This subsection will, based on the experience gained in these past 5 years, present my perspective on the direction that should be pursued in future studies to experimentally unravel the role of mechanical heterogeneity on material failure on a microscopic level.

My strategy would be to continue with the first approach presented in Section 7.2.1, i.e. using macrofluidics to fracture both mechanically homogeneously and programmed mechanically heterogeneous networks with various network topologies, as this approach holds a number of advantages. Firstly, the volume of material that is required to perform the fracture tests is relatively low and, therefore, beneficial for usage of mechanosensors, as typically these require a relatively large amount of synthesis time. Secondly, this low volume material usage allows for a potential high repeatability of the fracture test, enabling to study the stochastic nature of fracture. Relating the stochastic degree to the network topology and/or other parameters such as overall crosslinking concentration and ductility could hold interesting information about the relation between the parameter changed and the fracture process. For example, in the experiment proposed in Figure 7.2, the crack propagation velocity is expected to scale inversely with the elastic modulus according to equation 1.34. Arguably, decreasing the width of the elastic modulus stripes will lead to an increasing discrepancy between the number of stripes and number of changes in crack propagation speed detected, providing valuable insights into for example crack arrests and crack inertia[31] in mechanically heterogeneous materials. Thirdly, previous work by the Bouchaud lab has shown that material failure testing in macrofluidic devices can also be used to study mode I material failure[9]. This approach might have the advantage that the material deforms to a lower degree before it fails compared to pushing the sample on a wedge. Another important note is that the multi-point indentation setup developed in Chapter 2 is capable of mapping the mechanical profile of these $\sim$mm^2-sized materials, as the step size of the stepper motors is as small as 2 μm. In addition, convolution of the acquired profile can be deconvolved with the work presented in Chapter 3.

To experimentally achieve this goal, some improvements to the efforts during this PhD project are presented in Section 7.2.1, including; producing the macrofluidic channel from SU-8 photoresist instead of PDMS; and choosing the right sample material that is brittle, photopatternable and has the right order of magnitude in elasticity. Another large challenge that would ideally be optimized is the loading of the samples, which in this project was done manually, a tedious procedure. An alternative would be stop-flow lithography, where the running fluid is stopped by setting the hydraulic pressure to zero and exposing the channel upstream of the wedge with UV, polymerizing the material. Prerequisites of this approach are that the running fluid will have to create the polymer network, i.e. the running fluid is the monomer. This monomer should not swell the macrofluidic channel, as this will lead to leakage. Furthermore, after polymerization, the sample swelling kinetics should not be too fast as this will create potential friction between sample and the channel, and this might lead to irreproducability issues, since each time the experiment is repeated the swelling of the sample will slightly vary. In addition, testing DN's might also become challenging with stop-flow lithography, unless the monomer that interpenetrates the first network does not swell this network too much, creating friction with the channel, and this swelling does not take too much time, as the high repeatability of the technique would be negated. Despite these challenges associated with stop-flow lithography, an advantage with stop-flow lithography is that the sample symmetry, desired with manual loading as the orientation of the sample is non-controllable, is no longer necessary.

7.4 Appendix 7A. Macrofluidic tests: Methods

This Appendix explains the protocols developed to perform the test experiment that is presented in Section 7.2.1. To perform the text experiment, the sample and channel height had to correspond to be equal, as the force exerted on the sample is supplied by the fluid pushing on the sample. To reach a pressure sufficient to fracture the sample, and to know that the applied pressure on the fluid equals the pressure experienced by the sample, there should be no fluid leaking between the sample and the channel. The chosen method to produce the samples creates samples with fixed heights. Therefore, the size of the samples produced was verified before attempting to match channels with the same height. Consequently, the method to produce the samples is presented prior to the channel preparation in this Section.

Sample preparation

Sample preparation is done according to the protocol present in Chapter 2[32]. Here, a short description of this protocol will be given as well. The soft polymer networks are synthesized out of a commercially available (methacryloxypropyl)methylsiloxane - dimethylsiloxane copolymer purchased from Gelest in combination with 0.01 w/v % of a free radical photo-initiator (2,2-dimethyl-2-phenylacetophenone), resulting in a photopatternable polymer network[1]. A mechanically heterogeneous profile can be obtained with half-tone printing, by exposing the sample to a spatially varying intensity of UV light resulting in a spatially varying modulus[33]. Flat samples are obtained by sandwiching the photopatternable polymer network between two glass slides separated by a 127 μm thick mylar spacer. Importantly, a key characteristic for polydimethylsiloxane is the relatively low volume change upon polymerization[34]. This is also the reason that the material presented here was chosen as a model system to study mechanical heterogeneity in fluidic channels, as large volumetric changes would lead to running fluid leakage in the channel past the sample. Hence, the height of the samples is set by the spacer used.

Channel preparation

The objective is to produce a macrofluidic channel with a height that would match the ∼130 μm of the photopatternable polymer network samples and a bifurcating channel where the samples could be fractured on the bifurcation wedge. The fluidic channels were synthesized of Sylgard 184 (Dow, USA), by pouring Sylgard on a master produced with SU8-100 photoresist (Microresist, Germany). The SU8 was deposited on 75x50 mm Plain Microscope slides (Corning Incorporated, USA) and subsequently spincoated at a speed of 3100 rpm, pre-baked for 3 minutes at 65°C and 11 minutes at 95°C and, exposed with the ML MicroWriter 3 Baby[12] at a focal depth of 1075 μm and an UV-dosage of 1875 $\frac{mJ}{cm^2}$, and post-baked for 1 minute at 65°C and 10 minutes at 95°C. Subsequently the channels were developed in propylene glycol monomethyl ether acetate (PGMEA, Sigma-Aldrich, Germany) for 15 minutes, replenishing the PGMEA after the first 10 minutes, on a lab shaker. The spincoating speed and UV exposure setting were found by a systematic trial-and-error study, see Table 7.A.1. In addition, the optimal settings were found by observing a grid of small pieces of SU8 photoresist produced at a set spincoating speed and varying the focal depth and UV dosage with a Bright Field Microscope, observing the sharpness of the obtained channels. The bifurcation wedge had an angle of 20°.

The height of the photoresist is a function of the spincoating speed. To measure the height of the photoresist, two method were used. The first technique is multi-point indentation, where the height of an object is determined with force-thresholding by stepwise motion and read-out of the force[32]. To determine the height of the sample with indentation, a probe is lowered onto the sample and onto the substrate on which the sample lies, and the difference in height is calculated. The second technique used to measure the height of the photoresist is taking a z-stack with confocal imaging, where contrast is created by submerging the photoresist in a solution with a fluorescent dye.

The glass side with the photoresist master was placed in a petri-dished and submerged in centrifuged, removing air bubbles after mixing, Sylgard 184 10:1 encapsulant. Afterwards, the petri-dish was vacuum cycled 5 times for 5 minutes to remove any remaining air bubbles present. Then, The microfluidic top was cured overnight in a 50°oven. The next day, the microfluidic roof was simply peeled of the photoresist, which was ready

Spincoat Speed (rpm)	**Focal depth (μm)**	**UV Dosage (mJ/cm^2)**	**Height (μm)**
1750	1137.5	1250	230
2000	1112.5	1625	210
2250	1112.5	1625	170
2400	1250	1250	170
3000	1200	1500	110
2800	1000	1700	130

Table 7.A.1 – Spin-coating and ML MicroWriter 3 Baby[12] settings to obtain a SU8-1000 fluidic device channel with a certain height.

to produce up to 20 channels. To load samples and fluid, PEEK tubing was used, for which holes where punched using a 1 mm diameter biopsy punch. The microfluidic device was sealed with plasma bonding; activating the Sylgard 184 roof by 13 second of plasma activation and adhering it to a 75x50 mm Plain Microscope slide that was rinsed with ethanol and deionized water and dry cleaned. Lastly, the seal was strengthened by heating the device for 15 minutes in 70°oven.

The experiment

The macrofluidic channels were imaged using a microscope (Zeiss, Germany) in bright field imaging. To observe the fracture experiment, a camera was connected to the microscope (Phantom High Speed, USA). The pressure was controlled using an pressure pump with a range between 0-2 bars (Elveflow OB1 MK3+, France). The pressure pump was controlled using a custom-built MATLAB script[35], time stamping the applied pressure such that pressure and images could be synchronized using the time stamp from the camera.

The running fluid used was filtered deionized water. The average elastic modulus, of the batch out of which the example presented in here, was 0.8 MPa, measured with indentation, after UV exposure with 750 mJ/cm^2.

7.5 Appendix 7B. Macroscopic beam networks: Methods

This appendix describes two analysis used in this study; (i) the process of converting the photoelastic response in beam networks to stress, schematically shown by a flowchart in Figure 7.B.1, and (ii) the process of obtaining GEBC and DGEBC values purely based on network topology, schematically shown by a flowchart in Figure 7.B.2.

Photoelastic response to stress
First, datasets are loaded in the MATLAB script. Then, the unpolarized images are skeletonized, branchpoints are deleted and discrete beams are found using MATLAB's Image Processing Toolbox to perform multiple operations on the data. The discrete beams are index and based on least mean squares analysis the label is tracked for all the frames during experiments, as samples are being deformed. To obtain the stress for the beams, the discrete beams are overlayed with the photoelastic data, which is averaged. A reference beams showing multiple fringes is used to extract the photoelastic response for beams during all frames, by using a scaling factor. This scaling factor, shown in Figure 7.B.1, overlays beams with the reference beam by finding the peak values, and multiplies this scaling factor with the stress of the reference to allocate a fringe number to the concerned beam. This process is repeated for all the beams in the network. With the fringe numbers known for all the beams, the stress is determined by using the single beam calibration. Finally, the stress for all the beams in the network is color coded for visualization.

Obtaining GEBC and DGEBC from network topology
The first steps in obtaining the GEBC and DGEBC values, from 2D images to discrete beams, are similar to the procedure described above. These discrete beams are used to either retrieve the GEBC or DEBC value. GEBC is obtained with the Brain Connectivity Toolbox[36], where the binary input matrix is produced based on the overlap between beams with nodes. DGEBC is obtained by listing nodes connections, and from there using MATLAB's graph.m and shortestpaththree.m to find the shortest path for a percolating network in the direction of applied strain.

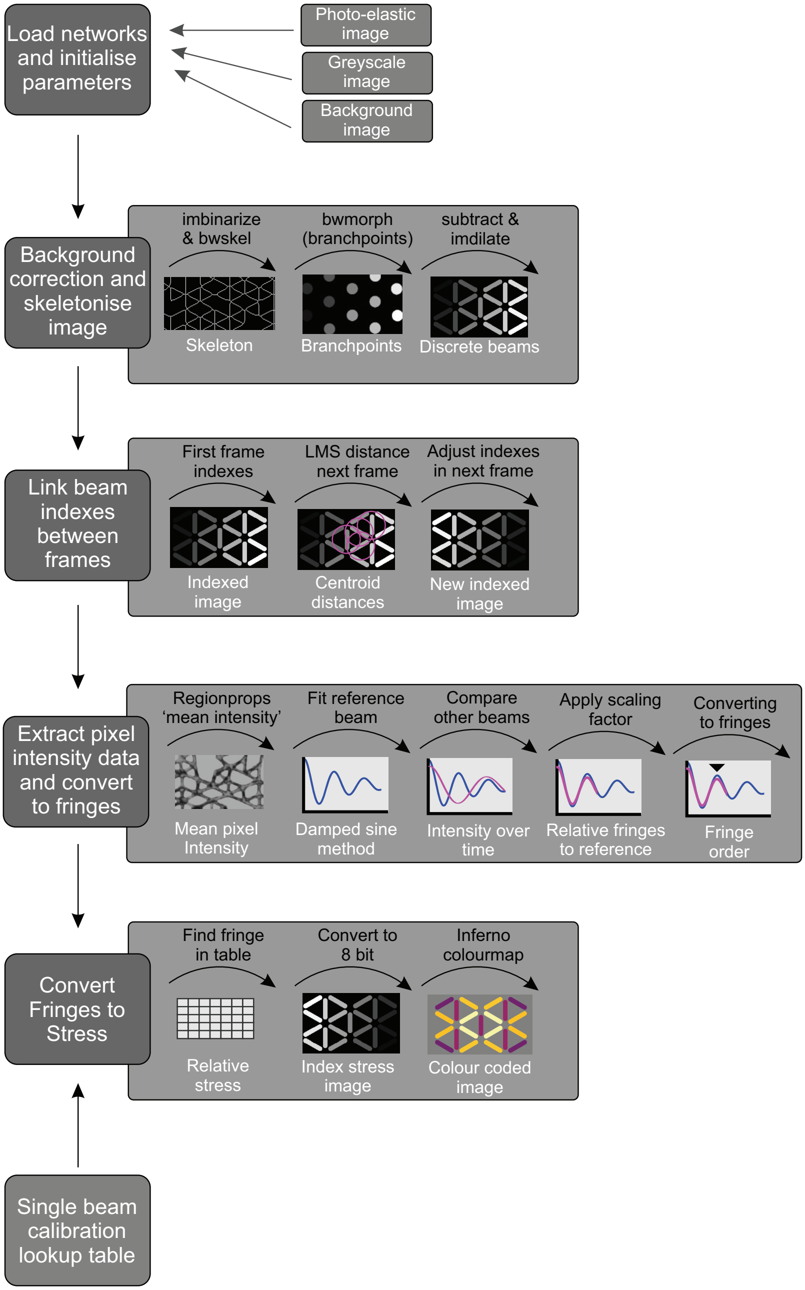

Figure 7.B.1 – Flowchart from photoelastic signal to stress for each beam in a network.

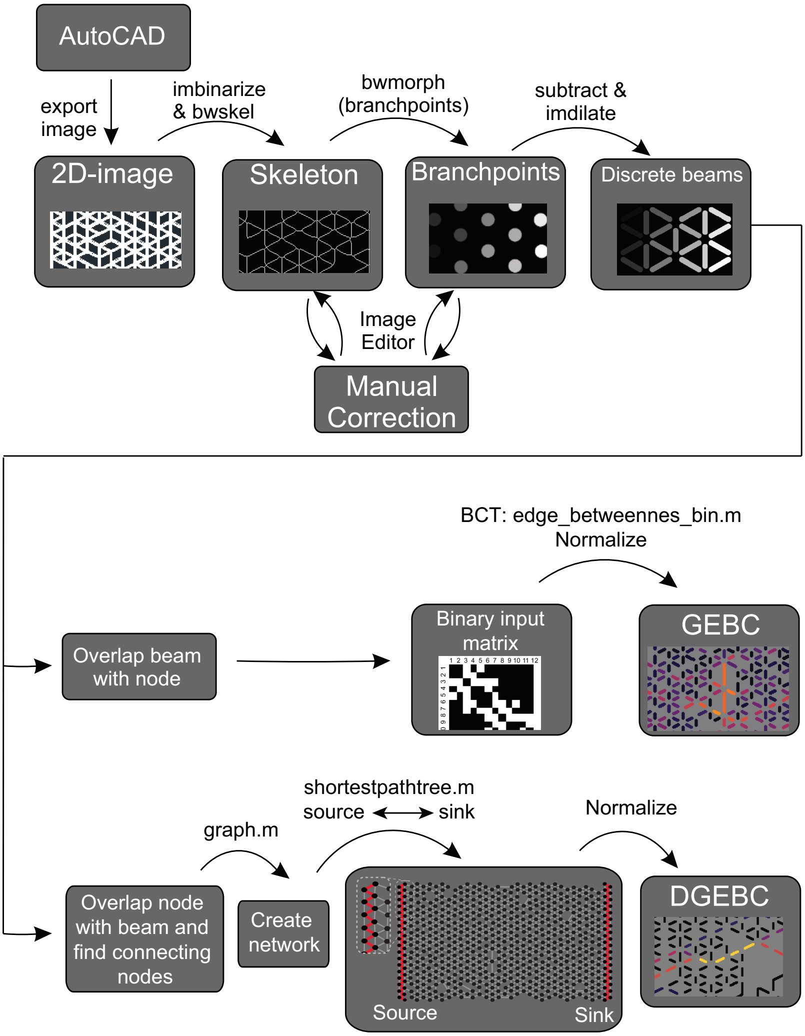

Figure 7.B.2 – Flowchart to obtain GEBC and DGEBC values purely based on network topology. BCT stands for the Brain Connectivity Toolbox used for the analysis[36].

Bibliography

[1] Kyung M Choi and John A Rogers. A photocurable poly (dimethylsiloxane) chemistry designed for soft lithographic molding and printing in the nanometer regime. *Journal of the American Chemical Society*, 125(14):4060–4061, 2003.

[2] Shin-Etsu Chemical Co. Silicones KER-4690 A/B.

[3] Valentin L Popov. *Contact mechanics and friction*. Springer, 2010.

[4] Jess M Clough, Costantino Creton, Stephen L Craig, and Rint P Sijbesma. Covalent bond scission in the mullins effect of a filled elastomer: real-time visualization with mechanoluminescence. *Advanced Functional Materials*, 26(48):9063–9074, 2016.

[5] Megan L Hughes and Lorna Dougan. The physics of pulling polyproteins: a review of single molecule force spectroscopy using the afm to study protein unfolding. *Reports on Progress in Physics*, 79(7):076601, 2016.

[6] Etienne Ducrot, Yulan Chen, Markus Bulters, Rint P Sijbesma, and Costantino Creton. Toughening elastomers with sacrificial bonds and watching them break. *Science*, 344(6180):186–189, 2014.

[7] Hanne M van der Kooij, Simone Dussi, Gea T van de Kerkhof, Raoul AM Frijns, Jasper van der Gucht, and Joris Sprakel. Laser speckle strain imaging reveals the origin of delayed fracture in a soft solid. *Science advances*, 4(5):eaar1926, 2018.

[8] Yinjun Chen, C Joshua Yeh, Yuan Qi, Rong Long, and Costantino Creton. From force-responsive molecules to quantifying and mapping stresses in soft materials. *Science advances*, 6(20):eaaz5093, 2020.

[9] Maxime Lefranc and Elisabeth Bouchaud. Mode i fracture of a biopolymer gel: Rate-dependent dissipation and large deformations disentangled. *Extreme Mechanics Letters*, 1:97–103, 2014.

[10] Sajjad Ahmad, Jean Marc Tulliani, Giuseppe Andrea Ferro, Rao Arsalan Khushnood, Luciana Restuccia, and Pravin Jagdale. Crack path and fracture surface modifications in cement composites. *Frattura ed Integrità Strutturale*, 9(34), 2015.

[11] Swetha Chandrasekaran, Narumichi Sato, Folke Tölle, Rolf Mülhaupt, Bodo Fiedler, and Karl Schulte. Fracture toughness and failure mechanism of graphene based epoxy composites. *Composites Science and Technology*, 97:90–99, 2014.

[12] *Durham Magneto Optics Ltd.* MicroWriter ML3 Baby, Durham DH1 3HP, UK.

[13] Tingge Xu, Jun Hyeon Yoo, Sachin Babu, Samit Roy, Jeong-Bong Lee, and Hongbing Lu. Characterization of the mechanical behavior of su-8 at microscale by viscoelastic analysis. *Journal of Micromechanics and Microengineering*, 26(10):105001, 2016.

[14] Zhiyi Zhang, Ping Zhao, Gaozhi Xiao, Benjamin R Watts, and Changqing Xu. Sealing su-8 microfluidic channels using pdms. *Biomicrofluidics*, 5(4):046503, 2011.

[15] Hang Yin, Yonghui Ding, Yao Zhai, Wei Tan, and Xiaobo Yin. Orthogonal programming of heterogeneous micro-mechano-environments and geometries in three-dimensional bio-stereolithography. *Nature communications*, 9(1):1–7, 2018.

[16] Maryam Hanifpour, Charlotte F Petersen, Mikko J Alava, and Stefano Zapperi. Mechanics of disordered auxetic metamaterials. *The European Physical Journal B*, 91(11):1–8, 2018.

[17] Federica Burla, Justin Tauber, Simone Dussi, Jasper van Der Gucht, and Gijsje H Koenderink. Stress management in composite biopolymer networks. *Nature physics*, 15(6):549–553, 2019.

[18] Trushant S Majmudar and Robert P Behringer. Contact force measurements and stress-induced anisotropy in granular materials. *Nature*, 435(7045):1079–1082, 2005.

[19] Karen E Daniels, Jonathan E Kollmer, and James G Puckett. Photoelastic force measurements in granular materials. *Review of Scientific Instruments*, 88(5):051808, 2017.

[20] Giorgio Carta, Michele Brun, and Antonio Baldi. Design of a porous material with isotropic negative poisson's ratio. *Mechanics of materials*, 97:67–75, 2016.

[21] Max Mark Frocht. Recent advances in photoelasticity and an investigation of the stress distribution in square blocks subjected to diagonal compression. *Trans. ASME*, 53:135–153, 1931.

[22] Estelle Berthier, Mason A Porter, and Karen E Daniels. Forecasting failure locations in 2-dimensional disordered lattices. *Proceedings of the National Academy of Sciences*, 116(34):16742–16749, 2019.

[23] Jess M Clough and Rint P Sijbesma. Dioxetane scission products unchanged by mechanical force. *ChemPhysChem*, 15(16):3565–3571, 2014.

[24] Robert Göstl and RP Sijbesma. π-extended anthracenes as sensitive probes for mechanical stress. *Chemical science*, 7(1):370–375, 2016.

[25] Deniz Yildiz, Christoph Baumann, Annabel Mikosch, Alexander JC Kuehne, Andreas Herrmann, and Robert Göstl. Anti-stokes stress sensing: mechanochemical activation of triplet–triplet annihilation photon upconversion. *Angewandte Chemie International Edition*, 58(37):12919–12923, 2019.

[26] Juliette Slootman, Victoria Waltz, C Joshua Yeh, Christoph Baumann, Robert Göstl, Jean Comtet, and Costantino Creton. Quantifying rate-and temperature-dependent molecular damage in elastomer fracture. *Physical Review X*, 10(4):041045, 2020.

[27] Nirveek Bhattacharjee, Cesar Parra-Cabrera, Yong Tae Kim, Alexandra P Kuo, and Albert Folch. Desktop-stereolithography 3d-printing of a poly (dimethylsiloxane)-based material with sylgard-184 properties. *Advanced materials*, 30(22):1800001, 2018.

[28] Lambert Instruments. *HiCATT: High-speed intensified Camera Attachment*. Leonard Springerlaan 19, 9727KB Groningen, The Netherlands.

[29] J Paulo Davim, Carlos Oliveira, Nuno Barricas, and Marta Conceição. Evaluation of cutting quality of pmma using co 2 lasers. *The International Journal of Advanced Manufacturing Technology*, 35(9-10):875–879, 2008.

[30] F Caiazzo, F Curcio, G Daurelio, and F Memola Capece Minutolo. Laser cutting of different polymeric plastics (pe, pp and pc) by a co2 laser beam. *Journal of Materials Processing Technology*, 159(3):279–285, 2005.

[31] Tamar Goldman, Ariel Livne, and Jay Fineberg. Acquisition of inertia by a moving crack. *Physical Review Letters*, 104(11):114301, 2010.

[32] JNM Boots, R Fokkink, J Van der Gucht, and TE Kodger. Development of a multi-position indentation setup: mapping soft and patternable heterogeneously cross-linked polymer networks. *Review of Scientific Instruments*, 90(1):015108, 2019.

[33] Jungwook Kim, James A Hanna, Myunghwan Byun, Christian D Santangelo, and Ryan C Hayward. Designing responsive buckled surfaces by halftone gel lithography. *Science*, 335(6073):1201–1205, 2012.

[34] Morten Hannibal Madsen, Nikolaj A Feidenhans, Poul-Erik Hansen, Jørgen Garnæs, and Kai Dirscherl. Accounting for pdms shrinkage when replicating structures. *Journal of Micromechanics and Microengineering*, 24(12):127002, 2014.

[35] MATLAB. *version R2016b*. The MathWorks Inc., Natick, Massachusetts, 2016.

[36] Brain connectivity toolbox. `https://sites.google.com/site/bctnet/`. Accessed: 2021-09-08.

Summary

MATERIAL failure is both undesirable and unavoidable. Therefore, ideally, this catastrophic failure event is forecasted or delayed by controlling and understanding this event. Elucidating the conditions under which failure occurs is challenging, due to the interplay between localized damage processes and long-ranged mechanical interactions. For polymeric materials that are being used in, e.g., transportation or packaging, understanding the conditions under which failure occurs is even more challenging due to large deformations, viscoelasticity, and heterogeneity at the microscale. This work focuses on the latter, by controlling and measuring the heterogeneity of soft materials and trying to relate this to material failure. To do so, the first part of this thesis, Chapters 2-4, focus on synthesis of materials with controlled heterogeneity and mechanical characterization of this heterogeneity. The second part of this thesis, Chapters 5-6, explore methods to extract detailed information about localized mechanics and bond rupture required to determine the role of heterogeneity in material failure, using mechanosensors.

In **Chapter 2** we develop a methodology to create a material with controlled heterogeneity, obtained with photolithography. Subsequently, we mechanically characterize this material by means of a home-built multi-point indentation setup which indents a material in a grid-fashion to create a mechanical map. The obtained mechanical map resembles the intended mechanical heterogeneity, although some feature blurring is present. Therefore, in **Chapter 3**, we use finite elements method simulations to explore the length scales involved in this mechanical blurring. The simulations show that a characteristic blurring length can be used as

a correction. However, experimental verification is not obtained due to a height dependence of the elastic modulus.

In **Chapter 4**, we use the developed multi-point indentation setup to find similarities between mechanical maps of meat analogues, in an attempt to present the food industry with a quantitative method to compare the texture of meat analogues with animal meats. By using the commonly used spatial autocorrelation technique Moran's I we find a decay length that resembles the length scales over which the mechanics in meat samples correlate. This decay length can be used to quantify the resemblance between meat analogues with animal meats.

In the second part of the thesis, **Chapter 5** shows the mechanoluminescent crosslinking polymer 1,2-dioxetane being used to quantify bond rupture events in polymer networks during puncture tests. A more detailed understanding of the microscopic processes occurring during indentation fracture is obtained by simultaneously recording the bulk force exerted on the puncture probe, and relating this to the bond rupture events. We find that a significant amount of bonds rupture before the probe penetrates the surface, known as puncture, at which a sharp drop in the force is observed. Further probe penetration proceeds by the propagation of a ring-shaped crack. By quantifying the number of rupturing bonds during this propagation stage and showing that this number is higher than the number of bonds for a cylinder of the probe size (i.e. in case of brittle failure), the damage zone is associated with diffuse failure of a significant size. Furthermore, puncture in double networks shows that the majority of the bonds rupture in the first network, as is generally assumed but had not yet been confirmed in other studies. Comparison with MD computer simulations shows that the latter is due to delocalization of the stresses in a large zone around the indenter.

In **Chapter 6**, we continue previous work performed by our lab, in which laser speckle imaging (LSI) showed that delayed failure of elastomer is preceded by small differential strains well before crack nucleation. Here, we incorporate the stress sensor spiropyran to study the stress accumulation during these moments before crack nucleation. We find that the timescale at which spiropyran onsets is much shorter to the crack nucleation than the small differential strains observed with LSI.

In the final Chapter, **Chapter 7**, we reflect on our findings and presents two additional experimental projects that were started during this project that specifically attempted to address the goal of the project; find the role of heterogeneity in material failure. Even though these projects were not finished completely at the end of the project, they do pave the way towards finding the project goal. Lastly, a perspective on how to achieve this goal experimentally is presented.

LIST OF PUBLICATIONS

- Chapter 2:
  J.N.M. Boots, R. Fokkink, and J. van der Gucht, T.E. Kodger, *Development of a multi-position indentation setup: mapping soft and patternable heterogeneously crosslinked polymer networks*, Review of Scientific Instruments 90 (1), 015108 (2019)

- Chapter 3:
  J.N.M. Boots, R. Kooi, T.E. Kodger, J. van der Gucht, *Mechanical deconvolution of elastic moduli by indentation of mechanically heterogeneous materials*, Frontiers in Physics, 9:723768 (2021)

- Chapter 4:
  J.N.M. Boots, N.P.K. Humblet-Hua, L. Tonneijck, R. Fokkink, J. van der Gucht, T.E. Kodger, *Characterization of the local mechanical texture of animal meat and meat replacements using multi-point indentation*, Journal of Food Engineering, 300, 110505 (2021)

- Chapter 5:
  J.N.M. Boots, D.W. te Brake, Jess M. Clough, J. Tauber, M. Ruiz-Franco, T.E. Kodger, and J. van der Gucht, *Quantifying bond rupture during indentation fracture of soft polymer networks using molecular mechanophores*, Physical Review Materials, 6(2), 025605 (2022)

- Chapter 6:
  J.N.M. Boots, R. Antonelli, D.W. te Brake, R. van Zwieten, H. van der Kooij, T.E. Kodger, J. Sprakel and J. van der Gucht, *Simultaneous stress and strain readout during delayed failure of a soft solid*, In preparation

ACKNOWLEDGEMENTS

During the final internship of my MSc studies at AMOLF I was not sure whether I wanted to pursue a PhD. Would I get the space to make mistakes and to learn from them? Would I get the help I need? Would there be a friendly environment? It was my supervisor at the time, dr. Mulla, who suggested me to apply for a position at the Laboratory of Physical Chemistry and Soft Matter (PCC) at Wageningen University as he did his studies there and told me that the answer to all the above questions is: yes!

He was right. PCC is truly a great place to develop yourself as an academic. Everyone, from staff to support and fellow students, takes the time to share their thoughts and experiences, both scientific and non-scientific, making it an instructive and pleasant environment to work in. Moreover, there is plenty of room for fun moments, for example during the many coffee breaks or the yearly group outings. I'd like to thank everyone at PCC to create this pleasant working atmosphere.

Jasper, thank you for offering me the opportunity to become part of the softbreak project and welcoming me at PCC. I was always impressed with, despite your overflowing agenda, the way that you take time to supervise all the students on a regular basis. I have enjoyed our regular meetings due to the pleasant learning environment and your ability to always make the problems at hand easier to tackle.

Tom, thank you very much for your continuous guidance. You always took the time for yet another conversation, be it about the research project or about random other topics. I have learned a great deal from you: creative thinking on solving practical problems, physical chemistry in general, having fun is important during work, and also being pragmatic from time to time, leading to the famous quote: 'what is better than good, good enough.' I will keep warm memories from all the laughs we had, playing tennis together and having dinner together with Justin and Qimeng at your place.

I would also like to thank Pim, Roel, Jorik en Sam, the BSc and MSc students that I had the privilege to supervise during their internships. It was such a delight to work with all of you, and to share an interest for science and research together. Good luck in the future to all of you.

Mara, Leonie, and Marioes, thanks a lot for always being there to help out with any practical issues. Besides that, I always enjoyed the moments of just walking in your office for a chat.

Remco and Diane, your work is absolutely key to making PCC the great learning environment that it is. Without you always being there to help out with technical (computer or lab) questions, all the students would not be able to perform their research at the current level. Thank you both very much.

Justin, Simone and Raoul, thank you for shared moments as the softbreak team, whether it be in-depth scientific meetings about fracture mechanics, fun moments at campus plaza, or the week we went to the conference in Rolduc together, I enjoyed them all.

Niek, Ram, Huy and Ketan, 6055 was our office. And it was always fun. Playing chess, chatting about random stuff, helping each other with our research endeavors, having dinner together, and sharpshooting the bullseye at the window with the toy gun, I had a great time with you guys. Thanks a lot for all these fun moments.

Everyone at PCC, thank you for creating a great atmosphere to work in. We have shared a lot of memorable moments with coffee breaks, game nights, PhD/postdoc weekends and group outings.

Papa en mama, bedankt dat jullie altijd in mij geloven. Zonder jullie steun had ik waarschijnlijk niet op het punt gestaan dat ik dit 'boekje' had kunnen maken.

Janique, bedankt dat je de vele keren dat ik zat te brabbelen over mijn onderzoek hebt willen aanhoren. Je hebt me altijd gesteund tijdens dit project, en ik hoop dat we elkaar nog heel lang mogen blijven steunen in andere uitdagingen die op ons pad komen.

About the Author

Sven Boots was born on 22 April 1992 in Hoorn, the Netherlands. After receiving his high school diploma from the Martinus College in Grootebroek, he went on to study Physics at the University of Amsterdam, doing a minor Biology in the Bachelor and a Master in Biophysics. Sven concluded his BSc studies with an internship in the Academic Medical Center in Amsterdam studying the blood flow in vascular networks through computer simulations under supervision of Prof. van Bavel, and his MSc studies with an internship at AMOLF studying the interaction of septin on curved lipid membranes under supervision of Prof. Koenderink and dr. Mulla. In 2017, Sven started pursuing his PhD at the Laboratory of Physical Chemistry and Soft Matter at Wageningen University, studying the role of mechanical heterogeneity on material failure by means of experimental work and finite element simulations, under supervision of dr. Tom Kodger and Prof. Jasper van der Gucht. After publicly defending the PhD thesis, Sven will start in a position as a consultant in the energy sector.

OVERVIEW OF COMPLETED TRAINING ACTIVITIES

Discipline specific activities

21st Dutch Soft Matter Meeting	Wageningen (NL)	2016
Physical Chemistry Winterschool	Hans-sur-Lesse (BE)	2017
22nd Dutch Soft Matter Meeting	Delft (NL)	2017
Rheology workshop	VLAG (NL)	2017
24th Dutch Soft Matter Meeting	Leiden (NL)	2017
Physics@Veldhoven (NWO) *	Veldhoven (NL)	2018
DYFP Conference *	Kerkrade (NL)	2018
Soft Matter Design Symposium $^\diamond$	Wageningen (NL)	2018
RPK-B Polymer Physics	Utrecht (NL)	2018
APS March Meeting $^\diamond$	Denver, CO (USA)	2020
Physics@Veldhoven (NWO) $^\diamond$	Veldhoven (NL)	2021

$^\diamond$ Talk * Poster

General courses

VLAG PhD Week	Baarlo (NL)	2017
Poster and Pitching	Wageningen (NL)	2017
Competence Assessment	Wageningen (NL)	2017
Teaching and Supervising Thesis Students	Wageningen (NL)	2017
Adobe InDesign Essentials Training	Wageningen (NL)	2018
WGS PhD Workshop Carousel	Wageningen (NL)	2018
Scientific Writing	Wageningen (NL)	2020
Career Orientation	Wageningen (NL)	2020

Optionals

Writing PhD research proposal	Wageningen (NL)	2017
Advanced Soft Matter	Wageningen (NL)	2017
Group meetings	Wageningen (NL)	2017-2021
Journal club	Wageningen (NL)	2017-2021
Mechanochemistry meetings	Wageningen (NL)	2017-2018
PCC Day Trips to Companies	Venlo (NL)	2018
ERC Meetings	Wageningen (NL)	2019-2021

The research described in this thesis received financial support by the European Research Council (Softbreak, grant agreement 682782).

Original thesis design by Ruben Higler
Cover design by J.N.M. Boots

This thesis is printed by Proefschriftmaken.nl in 80 copies
Please consider the environment before printing the digital version of this thesis